Hydrogen evolution using derivatives of boron or cobalt

Qiuxia Zhao

Université Fédérale
Toulouse Midi-Pyrénées

THÈSE

En vue de l'obtention du

DOCTORAT DE L'UNIVERSITÉ DE TOULOUSE

Délivré par l'Université Toulouse 3 - Paul Sabatier

Présentée et soutenue par

Qiuxia ZHAO

Le 7 octobre 2022

Evolution d'hydrogène à partir de dérivés du bore ou du cobalt

Ecole doctorale : **SDM - SCIENCES DE LA MATIERE - Toulouse**

Spécialité : **Chimie Organométallique et de Coordination**

Unité de recherche :

LCC - Laboratoire de Chimie de Coordination

Thèse dirigée par

Azzedine BOUSSEKSOU et Didier ASTRUC

Jury

M. Didier ASTRUC, Membre invité
M. Jean-René HAMON, Rapporteur
M. Jean-Marie BASSET, Rapporteur
Mme Montserrat GOMEZ, Examinatrice
M. Azzedine BOUSSEKSOU, Directeur de thèse

Jury Members

Dr Azzedine BOUSSEKSOU **Directeur de la thèse**

Directeur du LCC, Université Toulouse III, DRCE2,

M. Jean-Marie BASSET **Rapporteur**

Professeur à l'Université KAUST, Arabie Saoudite et DRCE2 Emérite ENSCP, Université PSL

M. Jean-René HAMON **Rapporteur**

DRCE1, Université de Rennes 1

Mme Montserrat GOMEZ **Président**

Professeur CE, Université de Toulouse III

M. Didier ASTRUC **Membre invité**

Professeur CE Emérite, Université de Bordeaux

Revision:

Page 39: dibonib → diboronic

Page 44: TNMP → TMNP

Page 49: eliciting → confirming

Page 75: remove “however”

Page 77: relocate the caption of **Figure 2.6**

Page 90: add the details of proton signals of the “Click” dendrimer in ^{1}H NMR in **Figure S 2.1**

Page 105: “↔” was revised to be “⇋”

Page 121, line 2: remove “is”

Page 121: add the preparing procedure of PdNP and PtNP

Page 123: $[CoCp_2]^+$, Cl^- → $[CoCp_2]^+Cl^-$

Page 130: relocate **Table 3.1**

Page 138: ass → Mass

Page 139: NMR → ^{1}H NNR

Page 140: add the details of C signals in **Figure S 3.2**

Page 141: add the excepted Mass spectrum of **2H**.

Page 145: relocate the caption of **Table S 3.2**

Page 162: rection → reaction, cleavage → cleave

Page 163: remove the repetition

Page 164: revise the formula of $[Co(\eta^5\text{-}C_5Me_5)(\eta^4\text{-}C_5Me_5H)]$

Page 165: in → ion （in line 7）

Page 168~Page 183: 1,1- diphenylethylene is hydrogenated to be 1,1-diphenylethane. Revise all the spelling mistake of 1,1- diphenylethylene (the original spelling: 1,1- diphenyletheylene) and 1,1- diphenylethane (the original spelling: 1,1- diphenylmethane)

Page 172: 6.18ppm → 1.68ppm

Page 175: 1,1-diphenylethelene → 1,1-diphenylethylene

Acknowledgement

This thesis was completed in the Institute des Sciences Moléculaires (ISM), UMR CNRS N° 5255, University of Bordeaux and the Laboratoire de Chimie de Coordination (LCC) UPR CNRS N° 8241, Université Toulouse III - Paul Sabatier.

I would like to express my sincerest gratitude to my supervisors Prof. Didier Astruc and Dr. Azzedine BOUSSEKSOU for their supports over the last three years. In particular, I am very grateful of having Prof. Didier Astruc as my thesis co-director for his inspiring, patient instruction, insightful criticism and expert guidance on my thesis. His profound knowledge of chemistry, consistent and illuminating instructions, and his contributions of time and ideas, making my Ph.D. experience productive and stimulating. I would like to warmly thank Dr. Azzedine Bousseksou, a prestigious scientist, for his precious administrative and scientific help that have greatly facilitated this thesis.

I am also greatly indebted to the reviewers and jury members of the thesis, Prof. Jean-Marie Basset, Dr. Jean-René Hamon and Prof. Montserrat Gomez, for having accepted to evaluate my work.

High tribute shall be paid to Sergio Moya, Lionel Salmon, Marta Martinez Moro, Eduardo Guisasola Cal, Emerson Coy and Bruno Espuche for their excellent collaborations and analyses on samples.

My sincere gratitude also goes to my former and current colleagues, including Qi Wang, Xiang Liu, Fangyu Fu, Changlong Wang, Naixin Kang, Wenjuan Wang, Yue Liu, Jianyu Wei of the CSH group, and Yuteng Zhang, Yue Zan

of the LCC group. They gave me valuable advices and helped me solve numerous problems in the daily lab life.

I gratefully acknowledge the funding support from the China Scholarship Council for my 3 years of PhD. The Universities of Bordeaux and Toulouse III, and the CNRS are greatly acknowledged for research facilities and funding.

Last but not the least, my gratitude also extends to my family who have been assisting, supporting and caring for me all of my life. Special thanks should also go to all my friends who give me continuous support and encouragement during my thesis.

Table of Contents

Résumé de la thèse en Français

L'hydrogène (H_2) est l'un des combustibles les plus attrayants, en raison de sa densité énergétique gravimétrique élevée et de son sous-produit de combustion non polluant, l'eau.[1-4] Cependant, la plupart du H_2 est actuellement produit par reformage à la vapeur de ressources fossiles, ce qui non seulement consomme des combustibles fossiles avec un faible taux de conversion, mais émet également du CO_2.[5] À cette fin, la production catalytique d'hydrogène à partir de matériaux de stockage d'hydrogène est considérée comme une approche pratique, peu coûteuse et efficace pour répondre aux préoccupations énergétiques et environnementales. Parmi les différents matériaux chimiques de stockage de l'hydrogène, l'ammonia-borane (AB) a suscité un intérêt considérable, car il présente une teneur élevée en hydrogène (19,6 % en poids), une grande stabilité à l'état solide, une non-toxicité et une solubilité dans l'eau.[6-7] En outre, l'hydrolyse du tétrahydroxydibore, $B_2(OH)_4$, est également prometteuse pour le dégagement de H_2. Il a été démontré que les deux atomes d'hydrogène de H_2 sont fournis par l'eau, tandis qu'un atome d'hydrogène provient du l'ammonia-borane et un autre de l'eau dans l'hydrolyse de l'ammonia-borane.[8-9]

Un grand nombre de catalyseurs ont été exploités pour le dégagement d'hydrogène, en particulier les nanoparticules de métaux nobles (MNP), telles que Pt, Pd et Ru, qui possèdent de bonnes propriétés électroniques dans la bande d. En outre, les nanoparticules bimétalliques (BMNP), constituées de deux éléments métalliques distincts, peuvent montrer une synergie positive dans les transformations chimiques catalytiques par rapport à celles de leurs homologues monométalliques, en raison d'une modification électronique et stérique des BMNP.[10-11] En particulier, les BMNP à base d'or sont largement

étudiées en photocatalyse pour leur résonance plasmonique de surface localisée (LSPR) unique, qui sert d'antenne pour convertir les énergies solaires en énergies chimiques.[12] Pour les types de MNP polyvalents, des transporteurs spécifiques sont indispensables pour les confiner au sein des supports et empêcher leur agrégation.

Au début des années 2000, le professeur Didier Astruc, à Bordeaux, a mis au point la synthèse de dendrimères "click" à branchements 1→ 3 et étudié leurs applications en matière de catalyse, de capteurs et d'électronique moléculaire.[13-15] Le travail de thèse s'inscrit dans cette thématique et a notamment porté sur la conception de nanoparticules de métaux de transition stabilisées par des dendrimères "Click" en catalyse. Les complexes organométalliques riches en hydrures, tels que [Co(η^5-C_5H_5)(η^4-C_5H_6)], **1H**, [Co(η^5-C_5Me_5)(η^4-C_5H_6)], **2H**, peuvent également servir de composé robuste pour la réduction et la stabilisation des MNPs. En outre, en transférant un ion hydrure sur un substrat approprié, par exemple une oléfine, à l'aide d'un catalyseur métallique, les complexes organométalliques neutres sont convertis en cation correspondant pour le dégagement d'hydrogène ou l'hydrogénation des oléfines.

Ce manuscrit est composé de trois parties principales, outre le **chapitre 1** qui comporte une introduction générale de la réaction d'évolution de l'hydrogène. Dans le **chapitre 2**, le dendrimère "Click" 1 contenant des ligands 1,2,3-triazole et des terminaisons triéthylène glycol (TEG) a été préparé pour la synthèse d'une série de NPs mono et bimétalliques de métaux de transition. (**Figure 1**) Il est appelé dendrimère "Click" car il est obtenu à partir de la réaction "Click" entre les groupes azido terminaux des noyaux de dendrimères et les dendrons contenant un groupe alcyne à leurs points focaux (ou l'inverse). Grâce aux terminaisons TEG hydrophiles, le dendrimère

"Click" **1** est très soluble en solution aqueuse. Grâce aux cycles triazoles intradendritiques, qui offrent des effets stéréoélectroniques incluant la donicité électronique des ligands et les contraintes stériques drastiques de l'environnement intradendritique, le dendrimère "Click" **1** peut se coordonner librement aux atomes de surface des NP et les activer. Par conséquent, ces polyvalences font des nanoparticules supportées par le dendrimère "Click" **1** un catalyseur efficace pour les réactions d'évolution de l'hydrogène. Les nanoparticules (NPs) de métaux de transition supportées par le dendrimère "Click" **1** ont été produites lors de la réduction des cations métalliques correspondants par $NaBH_4$. (**Figure 1**)

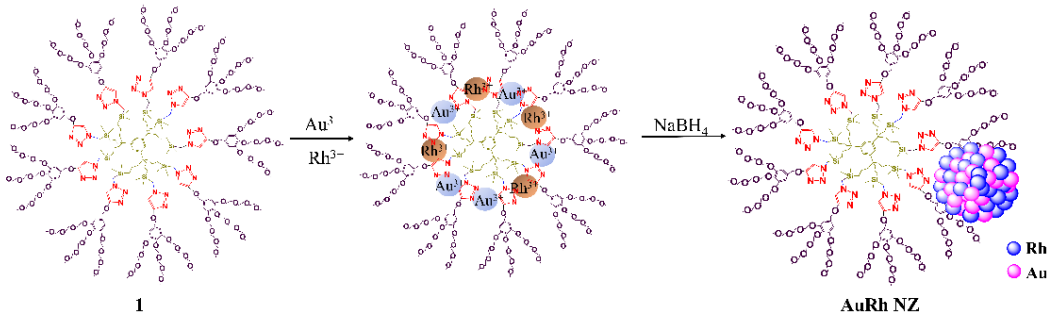

Figure 1. Synthèse de différentes NPs Au-Rh supportées par le dendrimère "click" **1.**

Les mesures TEM ont confirmé la bonne dispersion et la distribution étroite de taille (1,5-3,0 nm) des nanoparticules produites, indiquant l'effet de confinement souhaitable du dendrimère "Click" **1**. Dans l'hydrolyse de $B_2(OH)_4$, les AuNPs et RhNPs monométalliques présentent une efficacité catalytique comparable, montrant une valeur de nombre de tours catalytiques (TOF) de 1500 mol_{H_2} mol_{cat}^{-1} min^{-1} et 570 mol_{H_2} mol_{cat}^{-1} min^{-1}, respectivement. Ensuite, une série de nanoparticules bimétalliques Au-Rh ont été préparées avec des proportions molaires Au/Rh variant de 0,5 à 6. Les nanoparticules

bimétalliques obtenues présentent un effet synergique de type volcanique dans l'hydrolyse catalytique de $B_2(OH)_4$. (**Figure 2**) La composition optimisée, Au_4Rh_1, a montré un TOF 3.4 fois et 8.9 fois supérieur à celui des NZ monométalliques Au et Rh, respectivement. Cette synergie peut être attribuée à l'effet électronique et géométrique de la surface des NPs. Normalement, Rh est considéré comme une espèce métallique supérieure pour la réaction d'évolution de l'hydrogène en raison de son activité d'absorption du substrat,[16] mais elle peut aussi entraîner le blocage des sites actifs, en raison d'une adsorption excessive des substrats ou réactifs (en particulier $B(OH)_3$). Comparativement, Au n'est pas une espèce aussi active dans l'évolution de l'hydrogène. Ainsi, lors de l'introduction d'un métal secondaire dans les NPs bimétalliques Au-Rh, les sites actifs peuvent être transformés par le réarrangement géométrique des atomes d'Au et de Rh. La modification électronique, qui est vérifiée par le spectre XPS, peut également jouer un rôle dans l'optimisation de la performance catalytique des nanocatalyseurs Au-RhNPs.

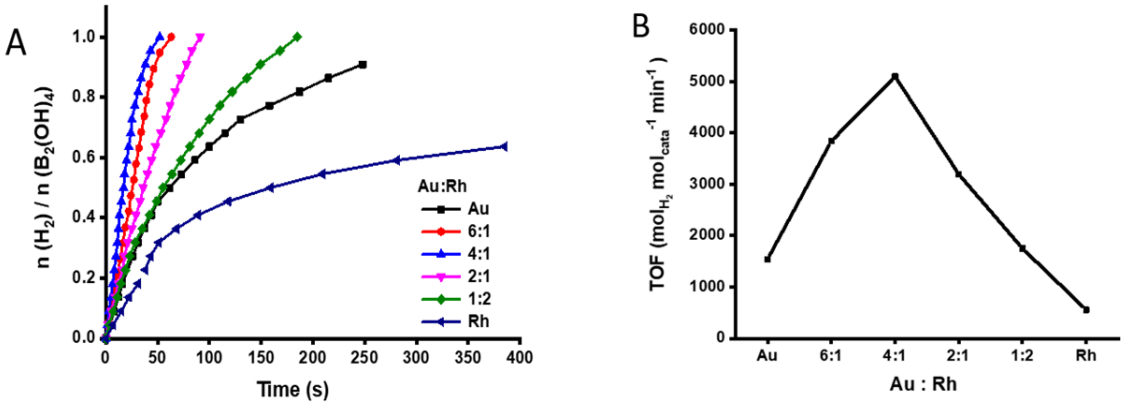

Figure 2. (A) Graphiques de profil temporel de l'évolution de H_2 et (B) valeur TOFs de l'hydrolyse de $B_2(OH)_4$ catalysée par 0.1 mol % de NZs Au-Rh avec différents rapports molaires Au/Rh dans l'obscurité à 25± 1 ˚C**.**

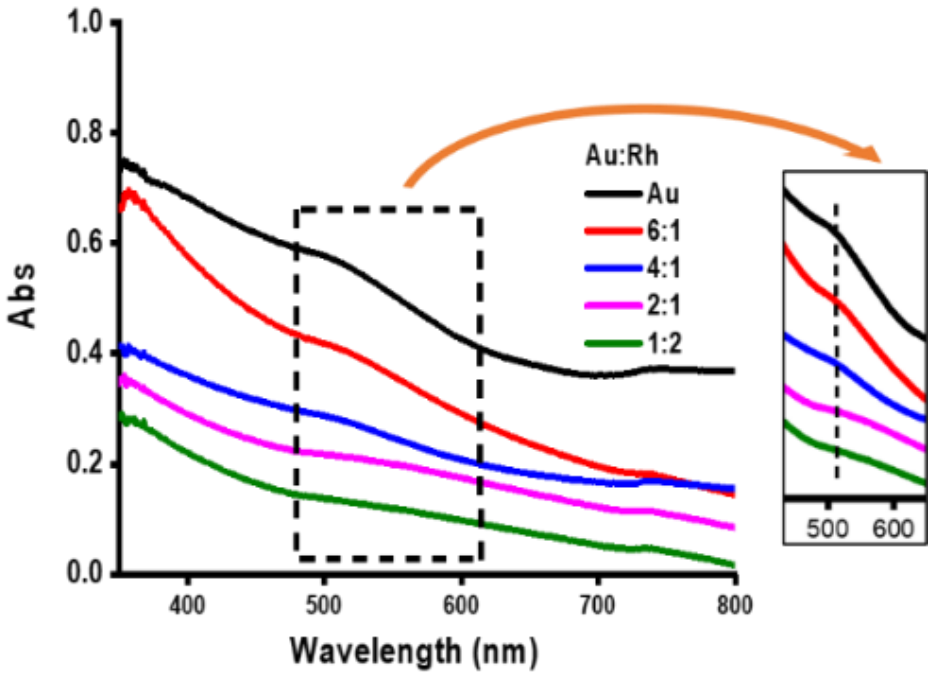

Figure 3. Spectres UV-vis. de Au et Au-Rh NPs

En outre, grâce aux propriétés plasmoniques des NP Au-Rh produites (**Figure 3**), les NP bimétalliques présentent également une amélioration supplémentaire remarquable de l'activité catalytique sous l'éclairage de la lumière visible (**Figure 4**), provoquant ce qui semble être une éjection d'électrons chauds de Au plasmonique vers les substrats adsorbés sur l'atome de Rh voisin et donnant le taux d'amélioration de la lumière le plus élevé de 1.4 pour les NP Au_1Rh_2.

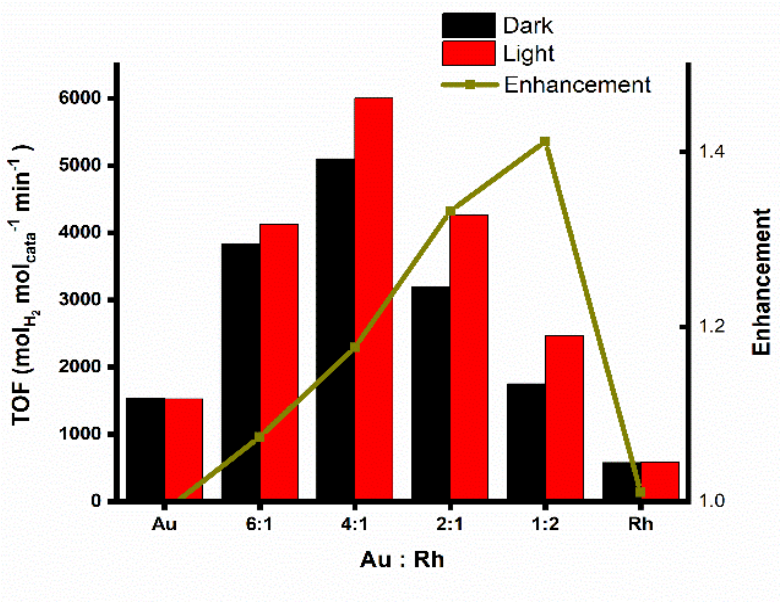

Figure 4. Valeur TOFs et taux d'amélioration (R_L/R_D) de l'hydrolyse de $B_2(OH)_4$ photocatalysée par 0.1 mol % de NPs Au-Rh avec différents rapports molaires Au/Rh à 25± 1˚C.

Les études cinétiques montrent que l'hydrolyse catalytique de $B_2(OH)_4$ est du premier ordre par rapport à la concentration du catalyseur et montrent un ordre zéro dans la quantité de $B_2(OH)_4$. L'expérience isotopique, pour laquelle l'hydrolyse de $B_2(OH)_4$ a été menée dans D_2O plutôt que dans H_2O, a révélé un effet isotopique cinétique (KIE) avec une valeur de kH/kD de 2.52 dans l'obscurité et de 2.94 dans la lumière, indiquant que le clivage de la liaison O-H de l'eau est fortement impliqué dans l'étape déterminant le taux (**Figure 5**).

En outre, pour étudier l'origine des atomes d'hydrogène dans le gaz H_2 produit, une réaction succédant à la formation de H_2 a été conduite *in situ* et *ex-situ* (**Figure 6**) .

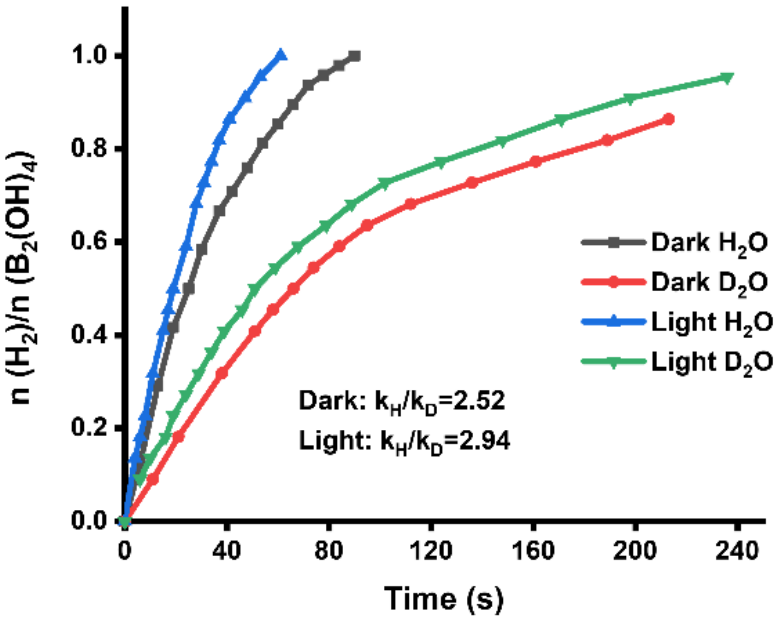

Figure 5. Tracé temporel de l'évolution de l'hydrogène catalysée par 0.1 % molaire d'Au_4Rh_1NPs dans H_2O et D_2O dans l'obscurité et la lumière à 15 ±1˚C.

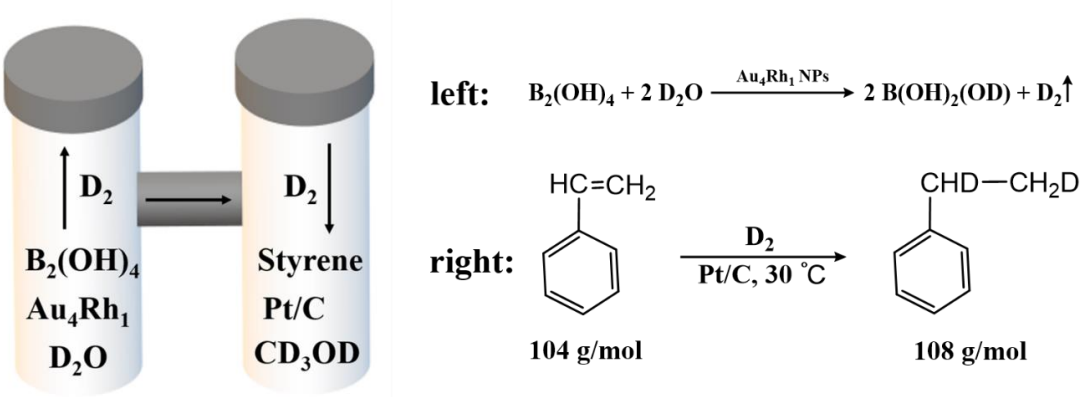

Figure 6. Réaction successive *ex-situ* de déshydrogénation de $B_2(OH)_4$ dans D_2O et d'hydrogénation du styrène dans CD_3OD

Dans la réaction successive (Figure 6), le gaz D_2 a été produit lors de l'hydrolyse de $B_2(OH)_4$ catalysée par Au_4Rh_1 NZ dans D_2O dans le tube de gauche, puis ce gaz a été dirigé vers le tube de droite pour initier l'hydrogénation du styrène dans CD_3OD dans le tube de droite. Le produit dans le tube de droite a été collecté 24 heures plus tard pour être analysé par

spectroscopie ^{1}H RMN et chromatographie en phase gazeuse couplée à la spectrométrie de masse. Le résultat a montré une conversion à 100% du styrène en éthylbenzène. La deutération de l'éthylbenzène produit est vérifiée par l'intégration du pic en ^{1}H RMN, indiquant la formule de l'éthylbenzène comme étant $Ph\text{-}CH_{0.08}D_{1.92}\text{-}CH_{2.71}D_{0.29}$, dans laquelle le nombre total d'atomes D obtenus est de 2. 2 ± 0.2 pour 2 D attendus. Le résultat MS révèle également le pic de masse de l'éthylbenzène deutéré. Ainsi, il est révélé que les deux atomes H dans le H_2 produit proviennent tous deux de l'eau.

Compte tenu de tous les résultats ci-dessus, un mécanisme provisoire est proposé ici pour l'hydrolyse catalytique de $B_2(OH)_4$. Comme le montre la **Figure 7**, dans la première étape du cycle catalytique, $B_2(OH)_4$ est adsorbé sur la surface du catalyseur pour donner l'intermédiaire I. Par la suite, l'intermédiaire II est obtenu suite à l'addition oxydante de la liaison B-B sur la surface métallique.[17] En raison de la déficience en électrons de l'espèce contenant B, c'est-à-dire acide de Lewis, deux molécules de H_2O agissent évidemment comme base de Lewis pour coordonner deux atomes de bore donnant l'intermédiaire III. À ce stade, l'addition oxydante d'une liaison O-H de H_2O est facilitée par la coordination initiale de H_2O aux atomes de bore, ce qui rapproche ces liaisons O-H de la surface du catalyseur. Il en résulte la formation des deux liaisons métal-hydrure NP-H, comme le montrent les expériences réalisées avec D_2O, et la libération de 2 $B(OH)_3$ dont la formation a été démontrée précédemment,[8] donnant l' intermédiaire IV. Enfin, l'intermédiaire hydrure-[M]-hydrure généré IV produit H_2 lors de l'élimination réductrice.[18]

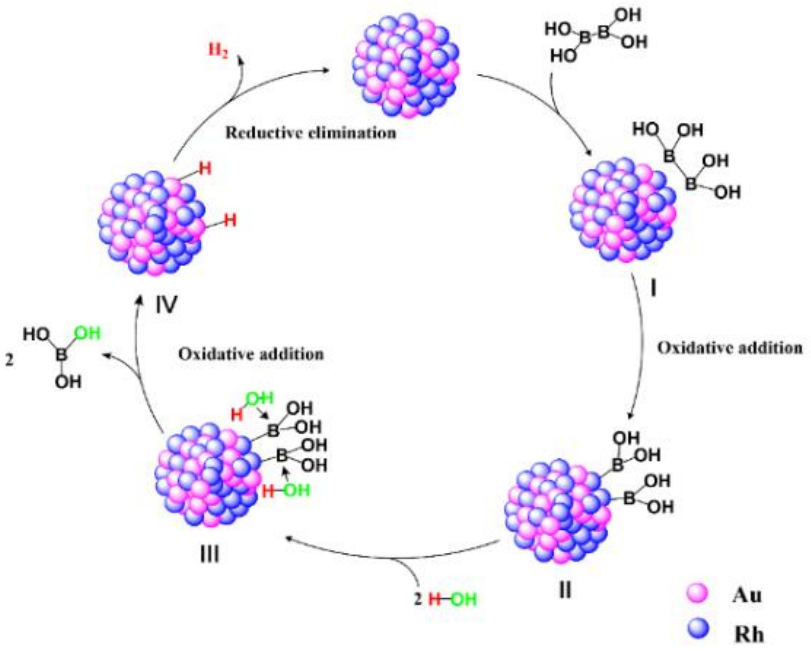

Figure 7. Illustration schématique du mécanisme confirmé de la déshydrogénation de $B_2(OH)_4$ catalysée par les nanozymes catalyseurs Au-RhNP @click dendrimère.

Dans le **Chapitre 3**, les organométalliques neutres riches en atomes H à caractère hydrurique [CoCp(η^4-C_5H_6)] (Cp= η^5-C_5H_5), **1H**, et [CoCp*(η^4-C_5H_6)] (Cp* = η^5-C_5Me_5), **2H**, ont été préparés par réduction des complexes sandwich cationiques correspondants en présence de $NaBH_4$. A titre d'exemple , la préparation de **2H** est illustrée dans la **Figure 8**.

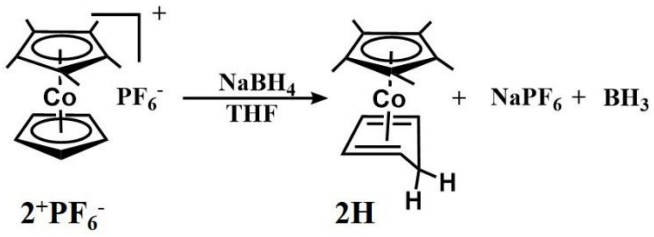

Figure 8. Préparation de **2H** à l'aide de $\mathbf{2^+PF_6^-}$ en présence de $NaBH_4$

Ensuite, les complexes riches en hydrure ont été utilisés à la fois comme réducteurs et stabilisateurs pour une série de nanoparticules de métaux de transition (TMNP), qui sont appelées TMNP (TM = Rh, Pt, Pd) provenant de **1H**, et TMNP* provenant de **2H**. Les catalyseurs TMNP et TMNP* produits ont été appliqués à l'hydrogénation de $B_2(OH)_4$ et à l'hydrolyse de l'ammonia-borane (AB) pour le dégagement d'hydrogène. La déshydrogénation de AB catalysée par TMNP et TMNP* est montrée dans la **Figure 10**; on observe que, pour cette réaction, Rh est le plus actif parmi toutes les métaux. AuNP* peut être actif pour la déshydrogénation de l'AB alors que AuNP est inerte, montrant un meilleur confinement de **2H** que de **1H** pour les nanoparticules métalliques. En ce qui concerne l'efficacité catalytique, RhNP présente un TOF élevé de 165 mol_{H_2} mol_{cat}^{-1} min^{-1}, tandis que la valeur est de 125 mol_{H_2} mol_{cat}^{-1} min^{-1} pour RhNP*, ce qui est un peu plus faible que celle de RhNP.

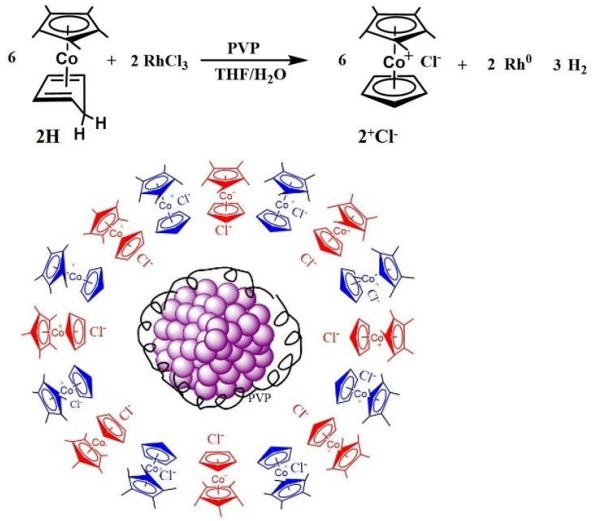

Figure 9. Illustration schématique du catalyseur RhNP* synthétisé lors de la réduction de $RhCl_3$ par [$CoCp^*(\eta^4\text{-}C_5H_6)$]. La couleur rouge montre la coordination de Cl^- au noyau de la NP, et la couleur bleue illustre le chlorure de métallocényle sans coordination, correspondant aux atomes de Rh dans le noyau (qui ne sont donc pas des ions de surface).

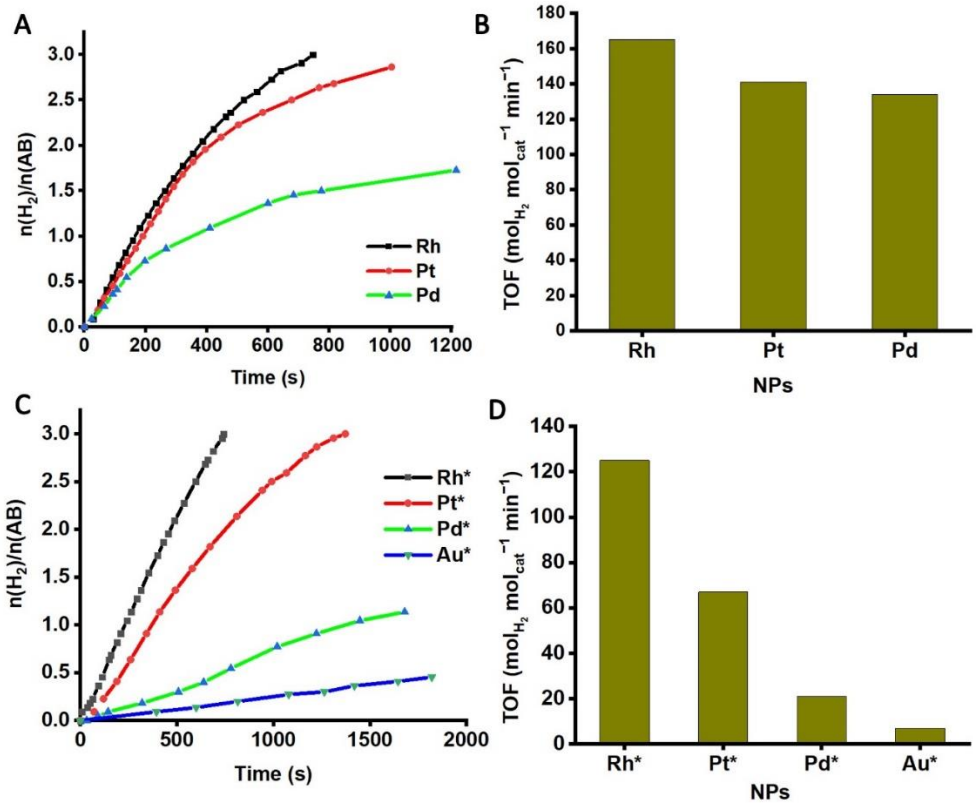

Figure 10. Tracé temporel de l'évolution de H_2 à partir de l'hydrolyse de AB catalysée par TMNP (A) et TMNP* (C). Valeurs TOF de l'hydrolyse de AB catalysée par le TMNP (B) et le TMNP* (D).

La recyclabilité du nanocatalyseur a également été étudiée. Le résultat illustré dans la **Figure 11** révèle que RhNP* montre une grande efficacité pour 3 cycles d'utilisation tandis que RhNP montre une forte baisse de l'efficacité catalytique pour la deuxième utilization. Quant à l'hydrolyse de $B_2(OH)_4$, RhNP* est beaucoup plus actif que RhNP. (**Tableau 1**) Tous ces résultats résumés dans le **Tableau 1** indiquent que le **2H** est un meilleur candidat pour la préparation de nanoparticules métalliques, car RhNP* présente un équilibre entre activité catalytique et stabilité. L'explication de ces résultats réside dans la méthylation des ligands Cp dans les complexes sandwich. Il est bien connu que la perméthylation du ligand Cp stabilise les métallocènes et autres organométalliques en raison de l'influence stéréo-électronique des cinq

substituants méthyles dans Cp*. Dans le complexe **2H**, le ligand Cp* (Cp* = η^5-C_5Me_5) est un donneur d'électrons plus fort que Cp (Cp = η^5-C_5H_5) en raison de l'existence de 5 groupes méthyles libérant des électrons dans Cp*, ce qui augmente la densité électronique du métal central Co. De plus, le volume de Cp* est considérablement plus grand que celui de Cp, offrant une meilleure protection stérique que Cp pour la stabilisation des NP. Par conséquent, après la réduction des précurseurs métalliques, les NP stabilisées par **2**$^+$**Cl**$^-$ sont plus stables que celles stabilisées par **1**$^+$**Cl**$^-$. La meilleure stabilité de RhNP* par rapport à RhNP est une raison supplémentaire expliquant la meilleure recyclabilité obtenue avec RhNP* dans l'hydrolyse de AB, l'agrégation des NPs étant mieux empêchée avec **2**$^+$**Cl**$^-$ qu'avec **1**$^+$**Cl**$^-$. Les meilleures performances catalytiques de TMNP* supporté par **2**$^+$**Cl**$^-$ par rapport au TMNP supporté par **1**$^+$**Cl**$^-$ dans l'hydrolyse catalytique de $B_2(OH)_4$ résultent à la fois de la plus petite taille des NP et de leur meilleure stabilité pendant le processus catalytique. TMNP conduit à des valeurs de TOF plus élevées que TMNP* dans l'hydrolyse AB, ce qui peut être attribué à l'encombrement d'absorption du substrat.

Tableau 1. TOFs comparés pour l'hydrolyse de $B_2(OH)_4$ et AB catalysée par des nanoparticules supportées par **1**$^+$ et **2**$^+$, respectivement.

	TOF $B_2(OH)_4$ hydrolysis		TOF AB hydrolysis	
	TMNP	TMNP*	TMNP	TMNP*
Rh	579	1364	165	125
Pd	138	268	134	21
Pt	126	360	141	67
Au	\	\	\	7

TOF: mol_{H_2} libéré pour un rendement en H_2 de 10%/[molcatalyseur $_{total}$ × temps de réaction (min)] pour tous les atomes, l'unité du TOF est mol_{H_2} mol_{cat}^{-1} min^{-1}.

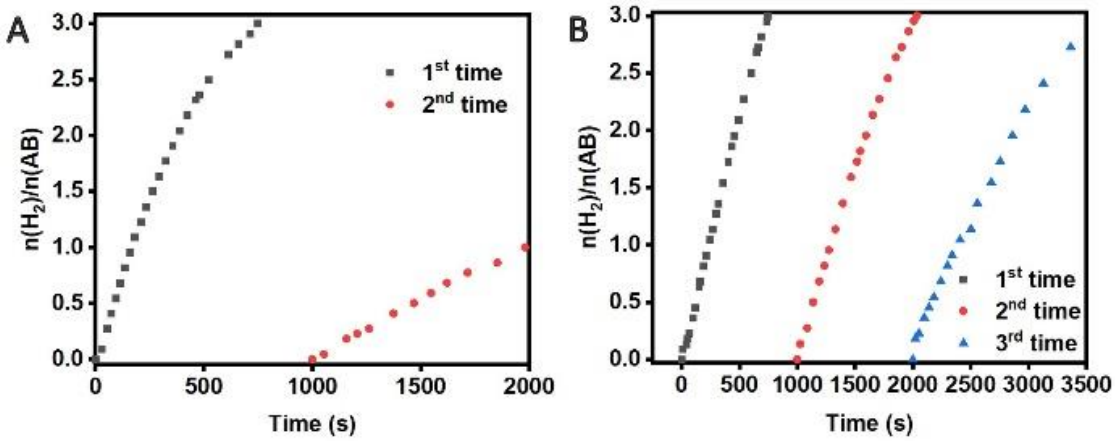

Figure 11. Diagrammes temporels de l'évolution de H_2 à partir de l'hydrolyse de AB catalysée par RhNP (A) et RhNP*; (B) dans le test de réutilisation.

Les études cinétiques, l'expérience isotopique et les réactions en tandem ont été réalisées lors de l'hydrolyse catalytique de AB, révélant le clivage de la liaison O-H comme l'étape déterminant la vitesse de réaction. Elles montrent aussi que et l'un des 2 atomes H de H_2 produit provient de l'eau et l'autre de AB. Enfin, une proposition de mécanisme d'hydrolyse catalytique de l'AB est présentée ici (**Figure 12**) . En raison de la propriété hydrurique de la liaison B-H, l'eau a tendance à produire une liaison hydrogène [NH_3BH_2H] --- H-OH avec NH_3BH_3, ce qui affaiblit la liaison B-H hydrurique de AB et la liaison O-H acide de l'eau. Le transfert d'hydrure de AB à la surface du nanocatalyseur entraîne la rupture de la liaison B-H et la formation d'une espèce M-H de surface chargée négativement. La liaison H mentionnée ci-dessus avec l'eau amène l'eau à proximité de la surface du nanocatalyseur, ce qui facilite grandement le clivage O-H de l'eau (étape déterminant la vitesse de réaction), et ce d'autant plus que la densité électronique dans cette liaison est affaiblie par cette liaison hydrogène et que la NP est plus active lors de

l'addition oxydante en raison de la densité électronique plus élevée apportée par la charge négative. En conséquence, la première molécule H_2 est produite par élimination réductrice de deux hydrures de surface, laissant à la surface de la NP deux fragments, $NH_3BH_2^-$ et OH^- qui s'éliminent également de manière réductrice pour la surface, ce qui fournit l'intermédiaire réactionnel NH_3BH_2OH (**Figure 12**). La répétition de ce processus conduit finalement à l'évolution de 3 équiv. de H_2.[19]

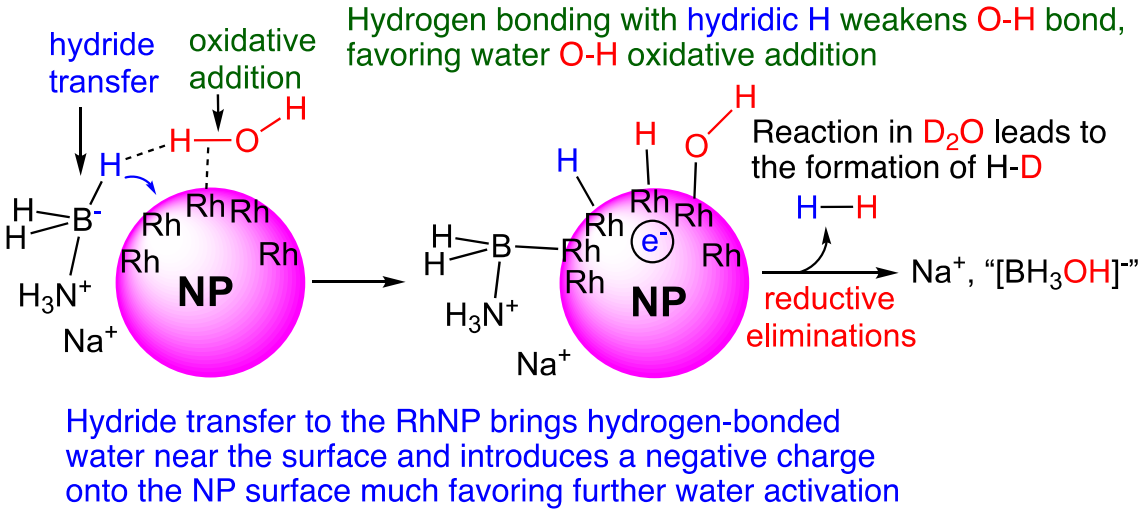

Figure 12. Mécanisme schématisé pour la formation de la première molécule de H_2 lors de l'hydrolyse AB catalysée par RhNP.

Dans le **Chapitre 4**, une série de complexes réservoirs d'hydrure dérivés du cobaltocène avec différents degrés et localisations des perméthylations de Cp, [CoCp(η^4-C_5H_6)], **1H**, [CoCp*(η^4-C_5H_6)], **2H**, [CoCp*(η^4-C_5Me_5H)], **3H**, a été préparée en utilisant le réducteur riche en hydrure $NaBH_4$ (**Figure 13**). Les complexes sont étudiés pour la génération de H_2 et comme donneur d'hydrure pour l'hydrogénation catalysée des oléfines dans le méthanol.

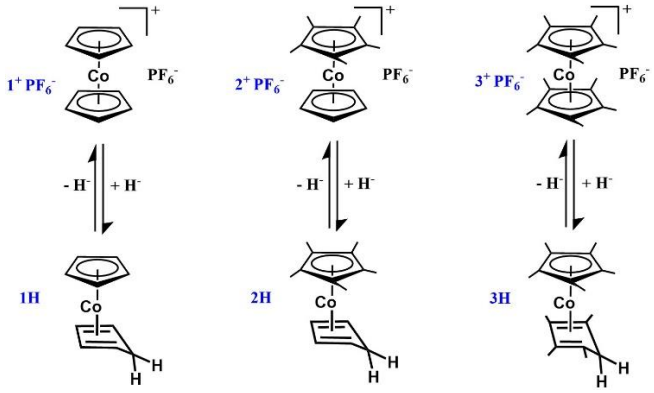

Figure 13. Propriétés de réservoir d'hydrure des complexes de Co(I) [Co(η^5-C_5H_5)(η^4-C_5H_6)], **1H**, [Co(η^5-C_5Me_5)(η^4-C_5H_6)], **2H**, [Co(η^5-C_5Me_5)(η^4-C_5Me_5H)], **3H** et les structures correspondantes des complexes de Co(III) à réservoir d'hydrure vide [Co(η^5-C_5H_5)$_2$]$^+PF_6^-$, **$1^+PF_6^-$**, [Co(η^5-C_5H_5)(η^5-C_5Me_5)]$^+PF_6^-$, **$2^+PF_6^-$**, [Co(η^5-C_5Me_5)$_2$]$^+PF_6^-$, **$3^+PF_6^-$**.

Tableau 2. Résumé de l'évolution de H_2 à partir de **1H**, **2H**, **3H** en 1minute à température ambiante

Conditions	production de H_2 à partir de **1H**		production de H_2 à partir de **2H**		production de H_2 à partir de **3H**	
	In MeOH	In EtOH	In MeOH	In EtOH	In MeOH	In EtOH
Avec Pd/C	Yes	Yes	Yes	Yes	Non	\
Sans Pd/C	Yes	Yes	Yes	Yes	\	\
Recyclabilité	Non	Non	Yes	Yes	Yes	\

Lors de l'évolution de H_2 evolution, lorsque l'on mélange les complexes **2H** (ou **1H**) avec le methanol (ou ethanol), une quantité stœchiométrique d' hydrogène est produite. (**Table 2**) Lors de l'evaporation du solvant, **2H** est obtenu comme un solide rouge. Par addition de HPF_6 aqueux, le solide rouge devient un précipité jaune qui est filté . On confirme par RMN ^1H qu'il s'agit de **$2^+PF_6^-$**. À cette fin, une voie de transformation de **2H** en **$2^+PF_6^-$** en présence de méthanol est proposée ici (**Figure 14**). Après la génération de H_2, un

intermédiaire dans le complexe de paire d'ions [Cp*CoCp^{+}, MeO^{-}] est possiblement produit, résultant en la formation du complexe rouge pour lequel la structure est supposée être [Cp*Co(η^4-C_5H_5OMe)], ce qui devra être confirmé par une caractérisation spectroscopique et analytique. Cette hypothèse structurelle est basée sur le fait que ce complexe (i) est presque de la même couleur que le complexe **2H** de Co(I) (donc, possiblement de structure apparentée) (ii) est ensuite lentement oxydé par l'air et/ou ensuite précipité par l'addition de HPF_6 aqueux, résultant en la formation de **$2^{+}PF_6^{-}$.** La représentation proposée du processus global est illustrée dans la **Figure 14**. Le mécanisme exact de la formation du couple d'ions intermédiaire n'est pas claire. L'hypothèse la plus vraissemblable et énergétiquement la plus réaliste implique une attaque nucléophile directe de la liaison O-H de l'alcool par l'atome H hydrurique (situé en *exo*) de **2H** pour former **H_2** et RO^{-}.

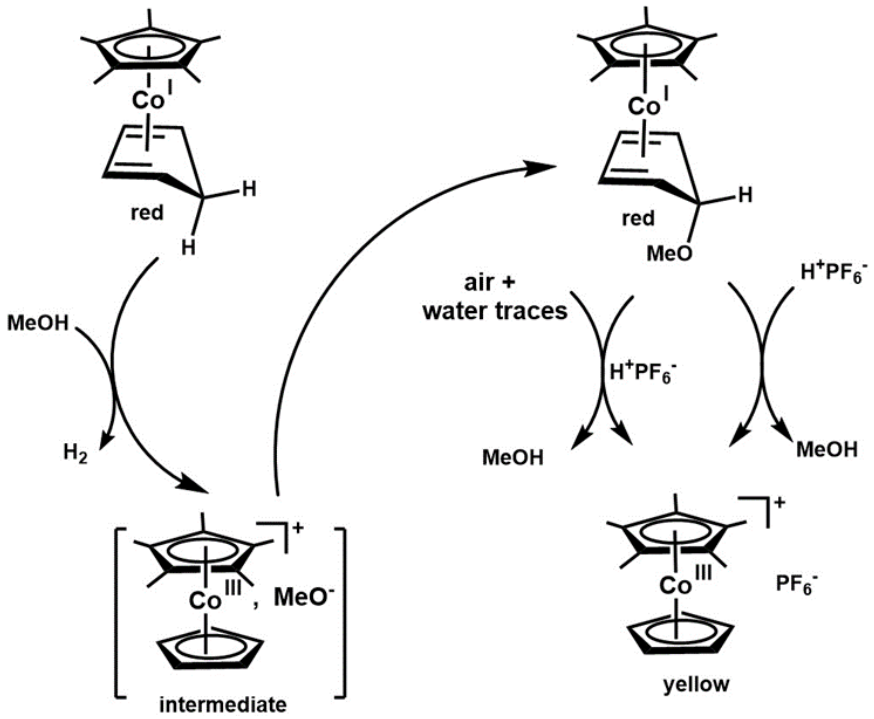

Figure 14. Mécanisme proposé pour la génération de H_2 à partir du méthanol et du complexe réservoir d'hydrure **2H**.

Ensuite, les complexes sont utilisés *in situ* pour l'hydrogénation des oléfines. Ici, on utilise un alcène inactivé et stériquement encombré, le 1,1-diphényléthylène. La réaction de **2H** (0,5 mmol) avec MeOH est utilisée pour l'hydrogénation du 1,1-diphényléthylène (0,2 mmol) en présence de 5 % molaire de Pd/C; 18h de réaction plus tard, à température ambiante (25 ˚C) et extraction, une conversion de 100% du 1,1-diphényléthylène est obtenue. Après la réaction d'hydrogénation, en dissolvant le résidu **2H** dans l'eau, le complexe sandwich cationique peut être récupéré lors de l'ajout de HPF_6. (**Figure 15**)

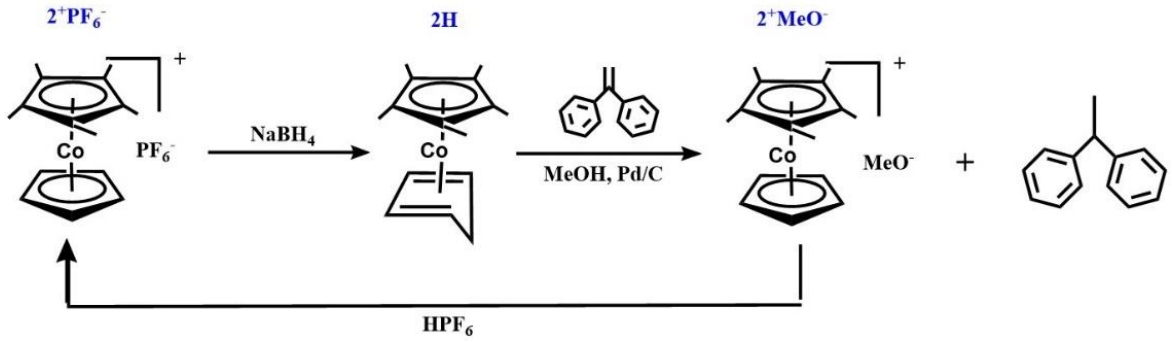

Figure 15. Système recyclé de **2H** dans l'hydrogénation du 1,1-diphényléthylène.

Cependant, en augmentant la température de réaction à 50˚C dans l'hydrogénation du 1,1-diphényléthylène en utilisant **2H**, on constate que la conversion est de 74,3% (**Figure 16**) . Ensuite, **1H** a été appliqué à la réaction, montrant une conversion de 100% à 0 ˚C et 79,4% à 25 ˚C. Contrairement à **1H**, **3H** produit une conversion de 100% à 50 ˚C et 0% de conversion à 25 ˚C. Les résultats sont résumés dans le **Tableau 3**.

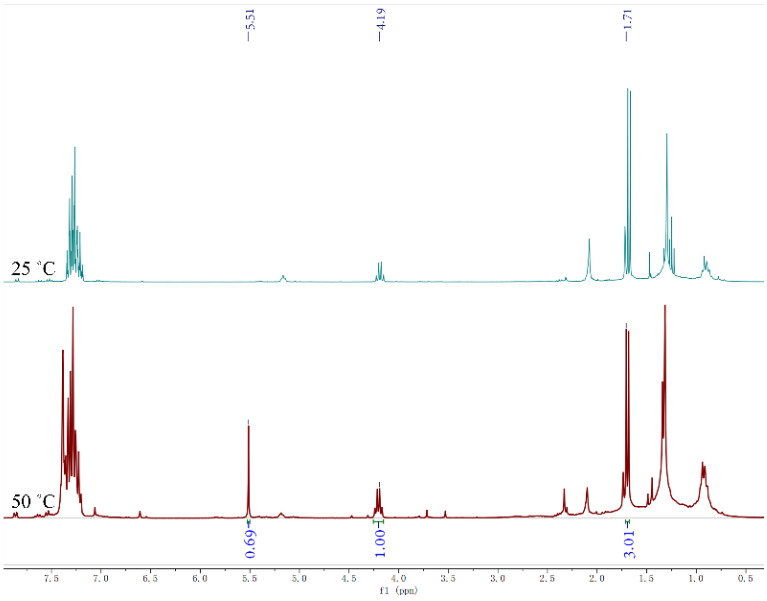

Figure 16. Spectre ^{1}H NMR du 1,1-diphénylméthane dans l'hydrogénation du 1,1-diphényléthylène en utilisant **2H** à 50 ˚C et 25 ˚C. RMN de 1H (300 Hz, $CDCl_3$).

Tableau 3. Résumé de l'hydrogénation catalysée du 1,1-diphényléthylène à l'aide de H_2 formé à partir de **1H, 2H et 3H** à différentes températures**.**

Température	**1H**	**2H**	**3H**
50 ˚C	\	74.3%	100%
25 ˚C	79.4%	100%	0
0 ˚C	100%	\	\
Recyclabilité	Non	Oui	Oui

En conclusion, **2H** apparaît comme le meilleur candidat parmi les trois complexes pour son évolution rapide de H_2 avec une grande capacité de don d'hydrure à température ambiante et une recyclabilité par réaction de $\mathbf{2^{+}PF_6^{-}}$

avec $NaBH_4$. **1H** montre une capacité comparable pour l'évolution de H_2, mais il ne présente pas une stabilité suffisante pour une récupération facile. **3H** montre une activité favorable dans l'hydrogénation du 1,1-diphényléthylène à une température plus élevée que **1H** et **2H**. Ces variations de comportement des complexes **1H**, **2H**, **3H** résultent de la différence de degré et localisation de la perméthylation du ligand cyclopentadiényle. La présence de groupes méthyles dans les ligands Cp* augmente la densité électronique du métal central Co, et l'angle de cône beaucoup plus grand de Cp* par rapport à Cp implique une stabilisation stérique supplémentaire dans les complexes Cp*, ce qui entraîne un ordre de stabilité croissant: **1H < 2H < 3H. 3H** présente trop d'encombrement stérique près de l'atome H hydrurique *exo*, ralentissant ou inhibant la réaction malgré une densité électronique accrue de l'atome Co par rapport aux analogues **1H** et **2H**. Pour **3H**, la production de H_2 lors de la réaction avec l'alcool peut être anticipée seulement à des températures significativement plus élevées que la température ambiante.

Afin d'étudier l'origine des atomes d'hydrogène dans la réaction d'hydrogénation, l'hydrogénation du 1,1-diphényléthylène est réalisée en utilisant la réaction de **2H** avec le méthanol deutéré (CH_3OD) et de $\mathbf{2H_D}$ deutéré (D en *exo*) avec le méthanol non deutéré, respectivement. Dans les deux cas, on observe l'existence de 1,1-diphénylméthane monodeutéré par RMN ^1H et spectrométrie de masse, ce qui montre bien que le méthanol est la source d' un atome H de H_2 formé et **2H** la source de l'autre atome H de H_2 lors de la réaction d'hydrogénation.

Enfin, une réaction en tandem a été réalisée pour vérifier l'origine des atomes de H dans la réaction de dégagement de H_2 entre **2H** et le méthanol. (**Figure 17**) Lorsque 10 équiv. de **2H** sont utilisés dans le tube de gauche pour

l'hydrogénation d'un équiv. de styrène dans le tube de droite, on constate une conversion de 100 % du styrène. Cela confirme également le dégagement d'hydrogène lors du mélange de **2H** avec de méthanol. D'autre part, l'éthylbenzène produit est deutéré, ceci qui est montré par intégration des pics en RMN ^{1}H, ce qui confirme que le méthanol est la source de l'un des deux atomes H de H_2 produit.

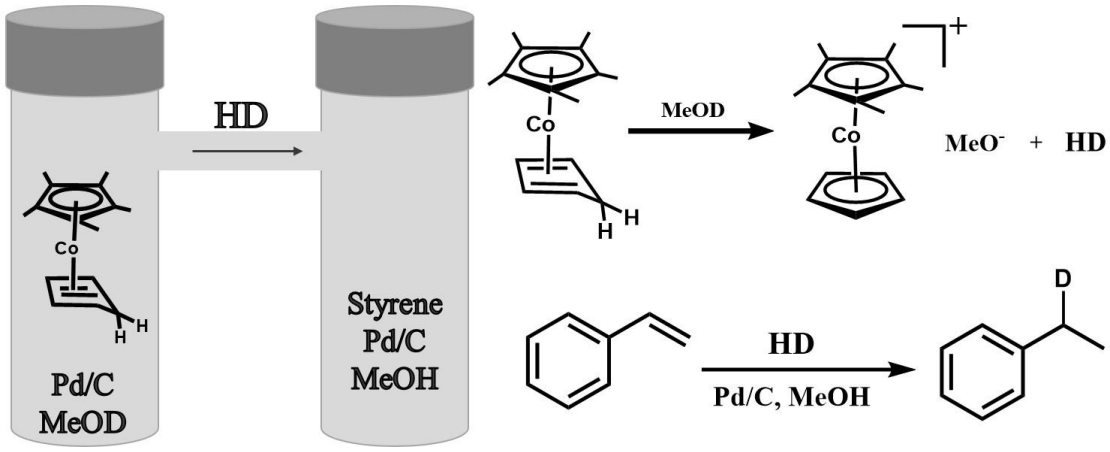

Figure 17. Hydrogénation du styrène dans un système de réaction en tandem utilisant **2H**.

En résumé, notre travail de thèse a permis d'avancer dans le développement des connaissances actuelles concernant les applications catalytiques des complexes de métaux de transition de droite et des complexes sandwichs comportant un atome d' hydrogène à caractère hydrurique. Grâce aux études des TMNP stabilisées par des dendrimères click, nous avons une bonne compréhension de la relation entre la stabilité, les performance catalytiques des nanoparticules et la structure des dendrimères (triazoles intradendritiques stabilisant et protégeant les NP). L'étude des NP de métaux de transition stabilisées par des complexes métallocénium comportant un atome H à

caractère hydrurique a fourni une nouvelle stratégie pour la préparation de nanocatalyseurs efficaces. Les réactions d'évolution de l'hydrogène et d'hydrogénation se produisant en présence des complexes organométalliques comportant un atome H à caractère hydrurique offrent une possibilité pour le développement de systèmes recyclables. Grâce à la recherche doctorale, nous avons atteint une bonne compréhension des paramètres guidant la stabilisation des NPs et leur efficacité catalytique, et nous avons amélioré notre compréhension des ligands qui modulent l'activité des complexes sandwich en chimie organométallique des éléments de transition situés à droite dans le tableau périodique.

Références

1. REN21 Renewables 2018 Global Status Report. **2018,** *http://www.ren21.net/about-ren21/about-us/*.

2. Chu, S.; Majumdar, A. Opportunities and challenges for a sustainable energy future. *Nature* **2012,** *488*, 294-303.

3. Zhu, J.; Hu, L.; Zhao, P.; Lee, L. Y. S.; Wong, K. Y. Recent Advances in Electrocatalytic Hydrogen Evolution Using Nanoparticles. *Chem. Rev.* **2020,** *120*, 851-918.

4. Lewis, N. S.; Nocera, D. G. Powering the planet: Chemical challenges in solar energy utilization. *Proc. Natl. Acad. Sci. U.S.A.* **2006,** *103*, 15729-15735.

5. Haryanto, A.; Fernando, S.; Murali, N.; Adhikari, S. Current Status of Hydrogen Production Techniques by Steam Reforming of Ethanol: A Review. *Energy & Fuels* **2005,** *19*, 2098-2106.

6. Chandra, M.; Xu, Q. A high-performance hydrogen generation system: Transition metal-catalyzed dissociation and hydrolysis of ammonia–borane. *J. Power Sources* **2006,** *156*, 190-194.

7. Staubitz, A.; Robertson, A. P. M.; Manners, I. Ammonia-Borane and Related Compounds as Dihydrogen Sources. *Chem. Rev.* **2010,** *110*, 4079-4124.

8. Chen, W.; Shen, J.; Huang, Y.; Liu, X.; Astruc, D. Catalyzed Hydrolysis of Tetrahydroxydiboron by Graphene Quantum Dot-Stabilized Transition-Metal Nanoparticles for Hydrogen Evolution. *ACS Sustain. Chem. Eng.* **2020,** *8*, 7513-7522.

9. Fu, F.; Wang, C.; Wang, Q.; Martinez-Villacorta, A. M.; Escobar, A.; Chong, H.; Wang, X.; Moya, S.; Salmon, L.; Fouquet, E.; Ruiz, J.; Astruc, D. Highly Selective and Sharp Volcano-type Synergistic Ni_2Pt@ZIF-8-Catalyzed Hydrogen Evolution from Ammonia Borane Hydrolysis. *J. Am. Chem. Soc.* **2018,** *140*, 10034-10042.

10. Singh, A. K.; Xu, Q. Synergistic Catalysis over Bimetallic Alloy Nanoparticles. *ChemCatChem* **2013,** *5*, 652-676.

11. Chen, T.; Rodionov, V. O. Controllable Catalysis with Nanoparticles: Bimetallic Alloy Systems and Surface Adsorbates. *ACS Catal.* **2016,** *6*, 4025-4033.

12. Gelle, A.; Jin, T.; de la Garza, L.; Price, G. D.; Besteiro, L. V.; Moores, A. Applications of Plasmon-Enhanced Nanocatalysis to Organic Transformations. *Chem. Rev.* **2020,** *120*, 986-1041.

13. Ruiz, J.; Lafuente, G.; Marcen, S.; Ornelas, C.; Lazare, S.; Cloutet, E.; Blais, J.-C.; Astruc, D. Construction of Giant Dendrimers Using a Tripodal Building Block. *J. Am. Chem. Soc.* **2003,** *125*, 7250-7257.

14. Astruc, D.; Boisselier, E.; Ornelas, C. Dendrimers Designed for Functions: From Physical, Photophysical, and Supramolecular Properties to Applications in Sensing, Catalysis, Molecular Electronics, Photonics, and Nanomedicine. *Chem. Rev.* **2010,** *110*, 1857-1959.

15. Astruc, D. Electron-transfer processes in dendrimers and their implication in biology, catalysis, sensing and nanotechnology. *Nature Chemistry* **2012,** *4*, 255-267.

16. Akbayrak, S.; Tonbul, Y.; Özkar, S. Ceria supported rhodium nanoparticles: Superb catalytic activity in hydrogen generation from the hydrolysis of ammonia borane. *Appl. Catal. B* **2016,** *198*, 162-170.

17. Cummings, S. P.; Le, T. N.; Fernandez, G. E.; Quiambao, L. G.; Stokes, B. J. Tetrahydroxydiboron-Mediated Palladium-Catalyzed Transfer Hydrogenation and Deuteriation of Alkenes and Alkynes Using Water as the Stoichiometric H or D Atom Donor. *J. Am. Chem. Soc.* **2016,** *138*, 6107-6110.

18. Astruc, D. *Organometallic chemistry and catalysis*. Berlin: Springer: 2007 (édition Française augmentée: *Chimie Organométallique et Catalyse*, EDP Sciences, Les Ulis, 2013).

19. Wang, Q.; Fu, F.; Yang, S.; Martinez Moro, M.; Ramirez, M. d. l. A.; Moya, S.; Salmon, L.; Ruiz, J.; Astruc, D. Dramatic Synergy in CoPt Nanocatalysts Stabilized by “Click” Dendrimers for Evolution of Hydrogen from Hydrolysis of Ammonia Borane. *ACS Catal.* **2018,** *9*, 1110-1119.

Chapter 1. General Introduction

1.1. Introduction of hydrogen as a key green energy source

Hydrogen (H_2) is regarded as the most promising green energy carrier with ‘‘great potential for clean, efficient power in stationary, portable and transport applications’’,[1-2] owing to its high-energy density (142 MJ kg^{-1}), earth abundance and sustainability.[3] Actually, the topic of hydrogen as potential energy of the future economy has been the theme of research in the field since the mid’ 1970s.[4] The past decades have witnessed the great progress in transformation of hydrogen-powered technologies from science fictions to realities. For, instance, the Japanese company Toyota Mirai and Hudai Nexo have developed hydrogen-based commercial cars since 2014 and 2017 respectively, the hydrogen-based blue taxis of the Hype company are well visible in Paris (**Figure 1.1**) and will reach 10 000 vehicles within the next two years, Mercedes-Benz has also started development of personal hydrogen-powered cars, and China declared its world’s first commercial hydrogen-powered tram in 2017.[5]

Figure 1.1. Hydrogen-energy-based taxis of the Hype company in Paris

However, main issues of this "hydrogen economy" lie in the hydrogen production efficiency and the demand for the mass distribution of hydrogen-powered technologies. Currently, 96% H_2 production is originated from the reforming of fossil fuels at high temperatures, which is associated with the emission of greenhouse gases and dramatic pollution with dust and radioactive materials.[6] Therefore, considerable efforts have been made to develop new technologies and materials for the implementation of a hydrogen economy.[7]

Here we briefly summarize two methods of hydrogen generation: (i) the so-called Hydrogen Evolution Reaction (HER) that is the cathodic part of water electrolysis, the other one, the anodic part being the oxygen evolution reaction, (OER, not discussed here); (ii) hydrogen generation from hydrogen-rich compounds.

1.1.1. Hydrogen evolution reaction (HER)

Presently, electrochemical water splitting (electrolysis), in which both hydrogen source (H_2O) and products (O_2 and H_2) are environmental-friendly, is much-favored method for H_2 evolution, as it fully fulfills the concept of clean energy.[8] However, an unavoidable obstacle that hinders water electrolysis for mass H_2 evolution is its high electric power consumption. The electrolysis of water (H_2O (l) $\rightarrow$ H_2 (g) + 1/2 O_2 (g), $\Delta G°$ = +237.2 kJ mol^{-1}, $\Delta E°$ = 1.23 V vs. normal hydrogen electrode (NHE)) involves two half-cell reactions: the hydrogen evolution reaction (HER, $2H^+$ (aq) + $2e^-$ $\rightarrow$ H_2 (g)) and the oxygen evolution reaction (OER, $2H_2O$ (l) $\rightarrow$ $4e^-$ + $4H^+$ (aq) + O_2 (g)) as shown in **Figure 1.2**.[9] For instance, Valenti *et al* reported a hybrid HER catalyst, **f-MWCNTs@Pd/TiO$_2$**, based on the combination of functionalized multi-walled carbon nanotubes (f-MWCNTs) and Pd nanoparticles that were

mutually integrated within a titanium dioxide (TiO_2) shell, exhibiting an excellent HER rate at neutral pH with zero overpotential.[10]

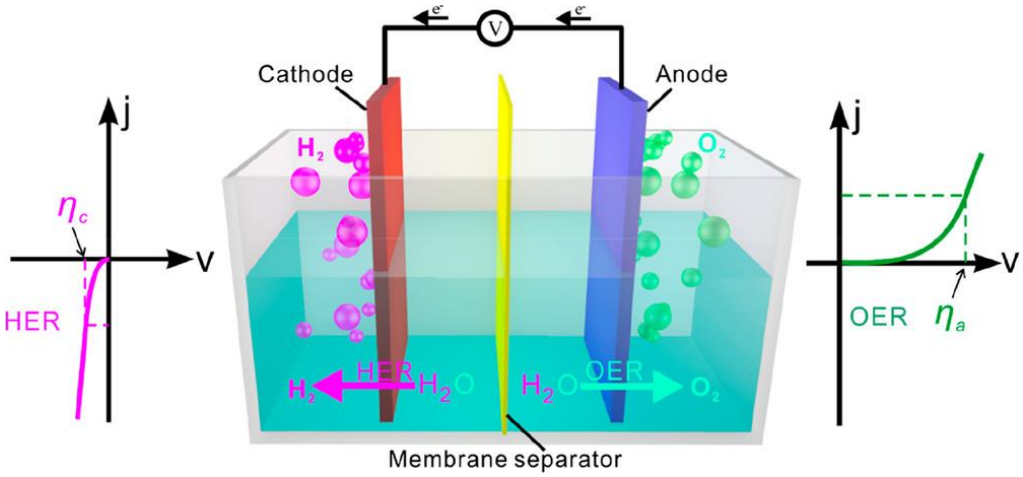

Figure 1.2. Hydrogen evolution reaction and oxygen evolution reaction of electrocatalytic water splitting.[9]

1.1.2. Photocatalytic hydrogen evolution

The photocatalytic process is also an alternative for water splitting, since solar irradiation can be regarded as an endless natural energy without charge.[11] Especially, located surface plasmon resonance (LSPR) induced photocatalytic hydrogen production has fascinated a lot of attention, owing their substantial electromagnetic field.[12] Liu *et al*. reported a plasmonic AuPd alloy nanoparticles supported on super small carbon nitride nanospheres (AuxPdy/CNS) that exhibit a high turnover frequency (TOF) value of 1017.8 h^{-1} under visible-light irradiation (λ>420 nm) at 298 K in the hydrogen evolution from formic acid (**Figure 1.3**). This remarkable photocatalytic activity is mainly attributed to the optimized electronic structure of Pd in the AuPd/CNS composite, which result in an acceleration of the electron transfer from photoresponsive super small carbon nitride nanospheres and plasmonic Au to the active Pd sites.[13]

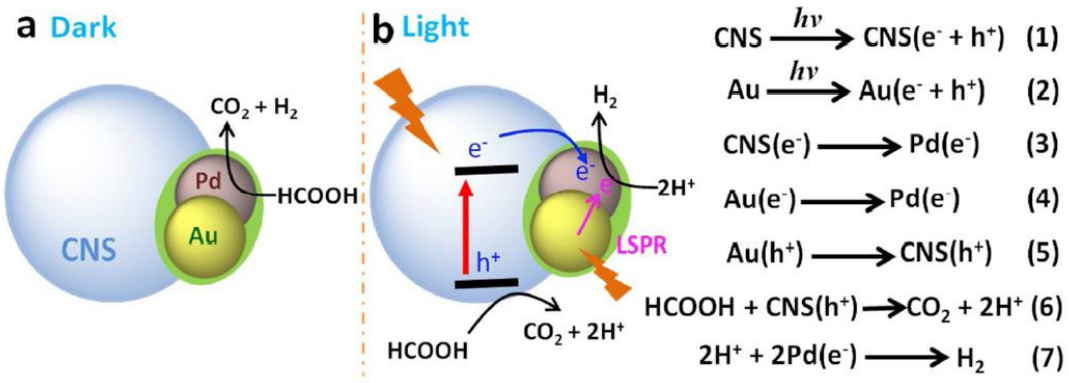

Figure 1.3. Schematic illustration of photocatalytic hydrogen evolution from formic acid for AuPd/CNS (a) under dark and (b) light.[13]

Furthermore, chemocatalytic HER is an alternative option, where hydrogen is generated through chemocatalytic decomposition of hydrogen precursors, such as ammonia borane, hydrazine monohydrate, and sodium borohydride.[5]

1.2. Hydrogen evolution from hydrolysis of hydrogen-storage materials

Hydrogen-storage materials should be with high hydrogen content, high stability in the solid state and solution under ambient conditions, nontoxicity, and high solubility.[3] Generally, there are three kinds of hydrogen in compounds, hydride H^-, neutral hydrogen atoms H^0 and proton H^+. Boron and aluminum form negative charged molecular hydride (B–H, Al–H) based on the electronegativity difference, whereas carbon and nitrogen form positively charged molecular hydrides, and transition metals, such as Ti, V, Zr, Pd, La, Ce form little-polarized hydrides.[14] For the sake of safety and stability, borane hydride, such as sodium borohydride, ammonia borane and their derivatives are recognized as promising options for HER.[15]

1.2.1 Hydrolysis of sodium borohydride ($NaBH_4$)

$NaBH_4$ is by far longest-known hydrogen carrier owing to its high hydrogen-storage capacity (10.8 wt %) and easy solubility in alkaline aqueous solution for safe, stable and long periods of storage (except its slow reaction with water).[3] Typically, hydrogen generation from $NaBH_4$ proceeds via thermo-decomposition pathways or a hydrolysis pathway.[16] In the case of hydrogen production by thermo-decomposition, high temperatures (>500 ˚C) are required due to the high thermo-stability of $NaBH_4$, and the thermo-decomposition process is very complex, mainly due to the formation of several intermediates and gases.[17] $NaBH_4$ reacts slowly with water under ambient conditions, and therefore it is not an ideal H_2 source, but $NaBH_4$ hydrolysis has still long been considered upon catalysis. The seminal study by Schlesinger *et al*. in 1953 already showed the capability of releasing 4 *equiv*. hydrogen in the acidic homogeneous catalytic hydrolysis of $NaBH_4$ in water (**Equation 1.1**).[18]

$$NaBH_4 + 2H_2O \rightarrow NaBO_2 + 4H_2 \qquad (\mathbf{1.1})$$

This route is very attractive, because it produces only hydrogen gas that can be directly used in a proton exchange membrane fuel cell. Excess of water is needed, however, due to the moderate $NaBH_4$ solubility and the hydrolysis of $NaBH_4$ usually forming mixtures of hydrated sodium metaborates (**Equation 1.2**).

$$NaBH_4 + (2 + x)\, H_2O \rightarrow NaBO_2 \cdot xH_2O + 4H_2 \qquad (\mathbf{1.2})$$

Thus, under such conditions, the gravimetric hydrogen storage capacity of $NaBH_4$ is far lower than the theoretical value (10.8 wt%). Accordingly, two possible means are proposed in order to release the hydrogen from the

stabilized solution: (1) lowering the pH value of the reaction solution by addition of a strong acid; and (2) catalytic hydrolysis by adding a catalyst, which would allow hydrogen release on demand.[19] Yang *et al*. reported an effective hydrogen evolution with lower activation energy (47.4 kJ mol^{-1}) based on the hydrolysis of alkalized $NaBH_4$ solution. (**Figure 1.4**) This high performance is mainly ascribed to the ultrasmall Pt atomic clusters, which have more active sites to adsorb and break the B–H bonds in BH_4^- ions for the generation of negative charged H^- via electron transfer, and then H^- can immediately combine with the positive charged H^+ to rapidly produce H_2.[20] Our group also reported a "click"-dendrimer-supported metal catalyst for catalytic $NaBH_4$ hydrolysis, exhibit a remarkable synergy between Pt and Co when the Pt/Co proportion is 1:1.[21]

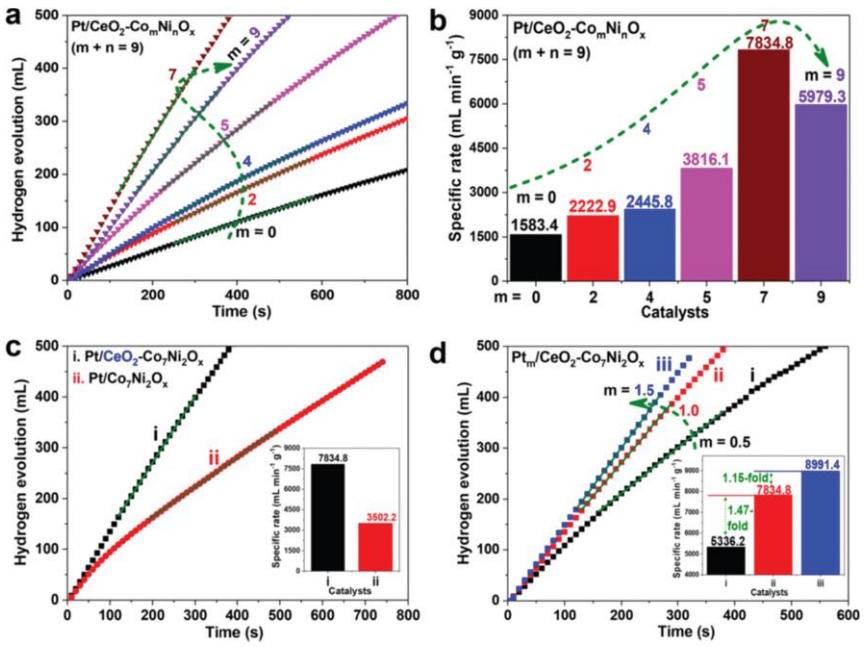

Figure 1.4. Hydrogen generation on Pt/Ce–Co–Ni catalysts for $NaBH_4$ hydrolysis.[20]

1.2.2. Hydrolysis of ammonia borane (AB)

Ammonia borane (NH_3BH_3, AB) is a stable solid at room temperature with a density of 0.780 g cm^{-3} and a melting point of 112–114 °C.[22] Owing to its high hydrogen content (19.6 wt%), low molecular weight (30.9 g mol^{-1}), and nontoxic and environmentally friendly nature, NH_3BH_3 has been considered as a promising hydrogen storage material.[23-25] Generally, hydrogen release from NH_3BH_3 follows either a thermal decomposition in the solid phase or catalytic solvolysis (hydrolysis and methanolysis) under mild conditions.[23, 26] As high temperature is required in the thermal decomposition of NH_3BH_3 (>200˚C),[25] the hydrolytic (**Equation 1.3**) or metanalytic (**Equation 1.4**) dehydrogenation of NH_3BH_3 are more favorable methods for HER.[27-28]

$$NH_3BH_3 + 2H_2O \rightarrow NH_4BO_2 + 3H_2 \qquad (\mathbf{1.3})$$

$$NH_3BH_3 + 4MeOH \rightarrow NH_4B(OMe)_4 + 3H_2 \qquad (\mathbf{1.4})$$

Considerable investigations have been involved in the catalytic dehydrogenation of NH_3BH_3 for HER. Xu's group pioneered the hydrolysis of AB using efficient noble metal catalysts (Pt, Rh, Pd, Ru).[23] Subsequently, a series of excellent works have been reported, demonstrating ammonia-borane as a potential hydrogen storage material comparing favorably with many other hydrogen storage materials.[29-33]. In our group, a series of transition metal nanocatalysts have been applied for the AB hydrolysis to produce hydrogen,[21, 34-38] and their mechanism has been investigated, revealing the

oxidative addition of the water O−H bond as rate-determining step in catalytic AB dehydrogenation (**Figure 1.5**).[37]

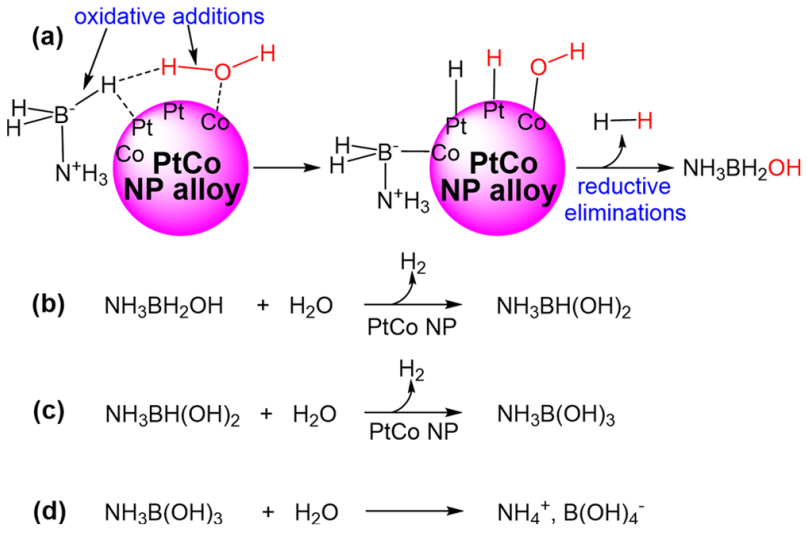

Figure 1.5. Suggested mechanism for the AB hydrolysis reaction catalyzed by Pt_1Co_1/dendrimer.[37]

1.2.3. Hydrolysis of diboronic acid ($B_2(OH)_4$)

Diboronic acid (tetrahydroxydiboron, $B_2(OH)_4$) is not of hydrogen containing materials contrary to all the others described here, but upon its hydrolysis, water is the H-containing material in this case as will be shown in this thesis. Diboronic acid is usually regarded as a borylation or reducing agent. It has recently been reported as an active substrate for various transfer hydrogenation reactions and hydrogen evolution reactions.[39-44] For instance, Stokes *et al*. reported the tetrahydroxydiboron-mediated transfer hydrogenation of alkenes and alkynes from water.[41] Hydrogen evolution from tetrahydroxydiboron has also been reported when catalyzed by a serious graphene quantum dot (GQD) stabilized nanoparticles.[45] (**Figure 1.6**) Isotopic experiment along with kinetic studies confirmed that water is the only

hydrogen source in the hydrolysis of $B_2(OH)_4$, which reveals the reaction formula as follows:

$$B_2(OH)_4 + 2\,H_2O \rightarrow 2\,B(OH)_3 + H_2\uparrow \qquad (\mathbf{1.5})$$

In contrast with the hydrolysis of NH_3BH_3 or $NaBH_4$ for which one H atom of H_2 formed is provided by H_2O and the other one by the boron compound, both H atom atoms of the produced H_2 are originated from water upon tetrahydroxydiboron hydrolysis, which offers a novel strategy for the hydrogen evolution reaction. Here, although tetrahydroxydiboron is not H source for H_2 formation, but it promotes the O-H bond cleavage of water in the presence of a nanocatalyst.

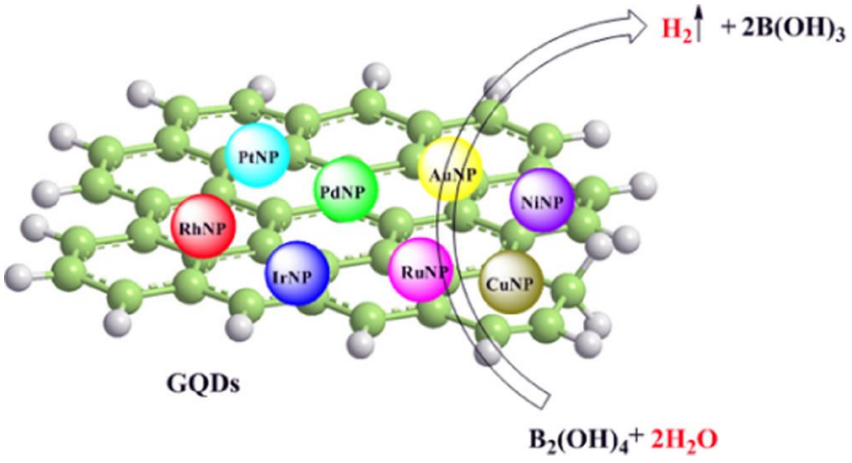

Figure 1.6. H_2 evolution from the hydrolysis of $B_2(OH)_4$.[45]

1.2.4. Hydrolysis of other hydride-rich compounds

Besides the popular boron-based materials, metal hydrides, liquid organic hydrides are also promising candidate for hydrogen evolution.[3] Metal hydrides, with great advantage for high gravimetric capacity ($Mg(BH_4)_2$:14.9 wt % and $LiBH_4$:18.5 wt %)[46] for hydrogen storage in a quite safe, efficient, compact and repeatedly reversible way, has gained intensive attention for

HER.[47] In general, metal hydrides are always nanostructured, which can be grouped into three large classes: (1) binary hydrides MH_x (M = main-group or transition metal, such as in LiH, MgH_2, $PdH_{0.6}$, TiH_2); (2) intermetallic hydrides, AB_xH_y (A is typically the hydriding metal and B is the nonhydriding metal, such as $TiFeH_x$, $TiMn_2H_x$, and $LaNi_5H_x$); and (3) complex metal hydrides, MEH_x (E = boron (borohydrides, e.g., $LiBH_4$, $Mg(BH_4)_2$); nitrogen (amides, e.g., $LiNH_2$, $Mg(NH_2)_2$), aluminum (alanates, e.g., $NaAlH_4$, $Mg(AlH_4)_2$)).[47]

1.3. Catalysts for H_2 production

Besides hydrogen carriers, nanocatalysts for catalytic hydrogen evolution are a significant field that facilitate stable hydrogen release with great safety and thus makes it accessible for terminal applications. Nanocatalysts, especially metal transition nanoparticles, have experienced explosive growth during the last few decades because they combine the merits of high turnover in homogeneous catalysis and recyclability in heterogeneous catalysis.[48]

1.3.1. Monometallic transition metal nanocatalysts

Transition metal nanoparticles (TMNPs) hold great promise in catalytic hydrogen evolution reactions because of their high surface-to-volume ratio, rich active surface atoms, and unique electronic structures as compared with their bulk counterparts. However, the very active surface atoms make nanoparticles being unstable during the course of catalysis. Thus, the nature of catalytic metal species and TMNPs supports are the two main aspects needing investigations for hydrogen evolution reactions.

As for metal species, the second- and third-row late transition metals (**Figure 1.7**), especially Pd, Au, Pt, Ru and Ag, have been extensively exploited in NP catalysis, and a large variety of hydrogen production reactions have been investigated using NPs based on these metals.[48] RhNPs are currently the most active catalysts for H_2 generation upon AB hydrolysis, showing a high TOF value of 2010 min^{-1} when confined by nanoceria (Rh/CeO_2).[49] Pt is the state-of-the-art electrocatalysts for HER, but its high price and low abundance in the earth's crust limits its large-scale application. Thus, many strategies are proposed to develop high-performance noble metal-free catalysts with low-cost transition metals. For examples, Laasonen et al. reported the fabrication of single shell carbon-encapsulated Fe nanoparticles decorated on single-walled carbon nanotubes (SWNTs) via an aerosol chemical vapor deposition method, showing a comparable electrocatalytic performance as that of Pt.[50]

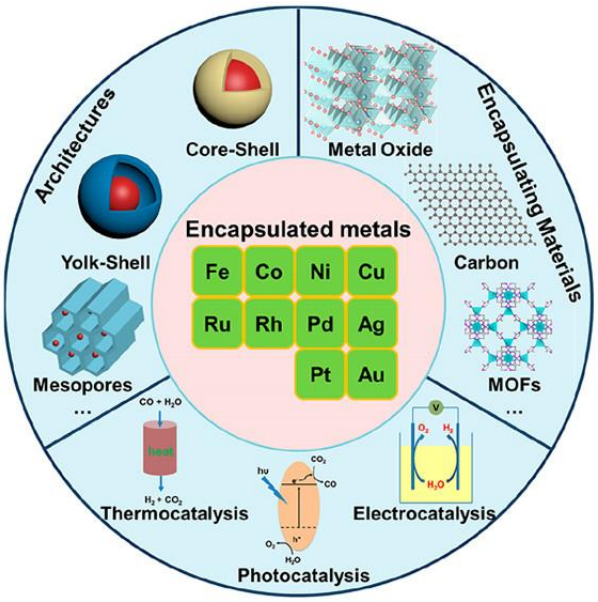

Figure 1.7. Encapsulated transition metal nanoparticles with different architectures for catalytic applications.[51]

1.3.2. Bimetallic TMNPS

Bimetallic metal nanoparticles, composing of two different metal species, usually show novel electronic, optical, catalytic or photocatalytic properties, and thus distinguish themselves from their monometallic counterparts.[52-54] Upon the introduction of a secondary metal element, the bimetallic TMNPs can show not only the combination of the properties related to the presence of two individual metals, but also new properties due to a synergy between two metals, and thus result in a high-performance catalysts for hydrogen evolution reaction.[55] Yang *et al*. synthesized a star-shaped decahedra Au-RhNPs with core-shell structure (**Figure 1.8**), founding that Au atoms functions to optimize binding energy while Rh atoms role in active sites in electrochemical HER. Also, electronic structure changes are observed which is the result of the tensile strain deriving from twinned Au/Rh structure and lattice mismatch.[56] Besides, the use of metals, such as Ni, Fe, and Co in combination with noble metals can decrease the content of expensive noble metals, thereby affording low-cost catalysts. Previous work in our lab have revealed a sharp volcano-shape Synergy between Ni-Pt and Co-Pt.[34, 37]

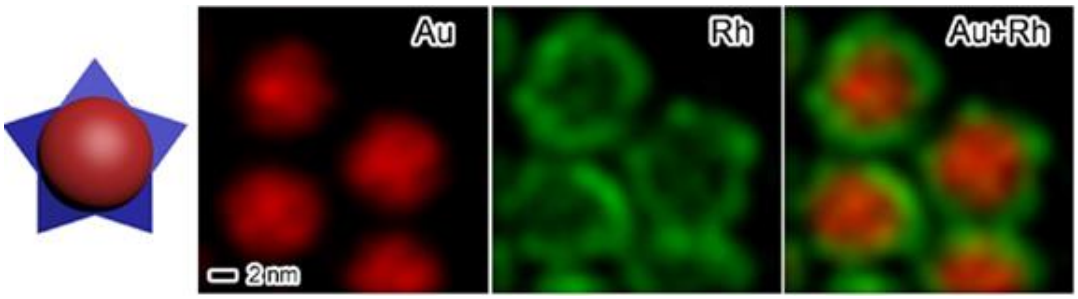

Figure 1.8. Structural, and compositional characterizations of the Au-Rh core-shell star-shaped decahedra.[56]

1.4. Supports for H_2 production nano-catalysts

Owing to the high surface energy, transition metal nanoparticles (TMNPs) are thermodynamically unstable and prone to migration and coalescence during catalysis, which is always accompanied by a critical decline of catalytic stability. Thus, encapsulating metal nanoparticles in nanoshells or nanopores becomes one of the most promising strategies to overcome the stability issue of the metal nanoparticles. TMNPs supports, which serve to isolate the metal nanoparticles and hinder them from aggregation, play an important role in the modification of the electron density of TMNPs and modulation of metal surface, and finally influence the catalytic activity.[57-60] The TMNPs supports can be categorized into inorganic oxides (SiO_2, TiO_2, CeO_2, etc.) and carbon, porous materials (mesoporous materials, metal–organic frameworks, and covalent organic frameworks), and organic capsules (dendrimers and metal organic cages).[51]

1.4.1. "Click" dendrimers

"Click" dendrimers containing 1,2,3-triazole ligands and triethylene glycol (TEG) termini, are known effective support for various TMNPs (Pd, Pt, Ru, Rh, Au, Ag, Cu, Co, Ni).[37, 61-63] They are originated from the "click" reaction between the terminal azido groups of dendrimer cores and dendrons containing an alkyne group at their focal points (or the reverse), and thus called "click" dendrimers. Thanks to the hydrophilic TEG termini, the "click" dendrimers are highly soluble in aqueous solution. The intradendritic triazole rings loosely coordinates to and activates the NP surface atoms, owing to their stereoelectronic effects including the electronic donicity of the ligands and the drastic steric constraints of the intradendritic environment.[21] As a result, these

"click" dendrimer-encapsulated TMNPs exhibit desirable catalytic performances in various chemical transformations, and especially for hydrogen evolution reaction. For example, bimetallic CoPt nanoparticles supported by "click" dendrimers exhibit a remarkable positive synergy between Co and Pt, and thus give an excellent catalytic performance in AB hydrolysis with TOF of 303 mol_{H_2} mol_{cat}^{-1} min^{-1}.[37] A series of Au-based alloyed nanocatalysts Au−LTMNPs (LTM = Ru, Co, Rh, Ni, and Pt) have also be reported to be well supported by the "Click" dendrimer (**Figure 1.9**).[35] These plasmonic TMNPs are distinguished for their visible light boosted hydrogen evolution in the catalytic hydrolysis of AB and $NaBH_4$. "Click" dendrimers are found to play an important role in facilitating the capture of visible light by coordination to the Au atoms.[35]

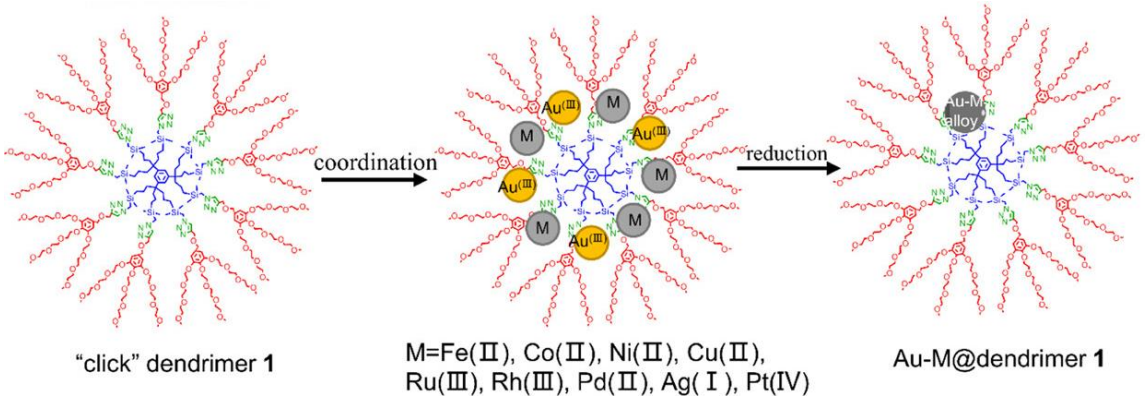

Figure 1.9. visible-light boosted H_2 evolution catalyzed by Au-LTMNPs @ "Click" dendrimer.[35]

1.4.2. Metal–organic frameworks (MOFs)

Metal–organic frameworks (MOFs), as multidimensional porous materials consisting of metal ions or clusters coordinated to multidentate organic ligands, have become one of the most popular research areas in the chemical and materials sciences due to their large surface areas, tunable pore sizes and

versatile architectures.[5, 64-65] Featuring these outstanding instincts, MOFs enable active guest species to be introduced into the pores/cages/channels and allow substrates to access the internal active sites, and thus turn to be excellent porous nanomaterials for the encapsulation of TMNPs catalyst.[65] Besides, the combination of catalytically active TMNPs and MOFs can introduce surprising synergistic effects, thus leading to much improved performances compared to that of either host or guest material in hydrogen evolution reactions. For example, Su et al. reported a series of nonprecious metal nanoparticles (NPs) supported by the metal–organic framework MIL-101, showing a very high turnover frequency (TOF) of 51.7 mol_{H_2} mol_{cat}^{-1} min^{-1} toward the hydrolytic dehydrogenation of NH_3BH_3. This high-performance of the catalyst is ascribed to synergistic effect of crystallinity and size of metal NPs, which is confined by the porous MOF MIL-101.

Zeolitic imidazolate frameworks (ZIFs), as important members in the MOF family, have attracted intensive attention due to their ease of synthesis and extraordinary high thermal stability and remarkable chemical resistance to boiling water and organic solvents.[66] ZIFs are porous hybrid materials with structures analogous to zeolites that are built upon 4-connected nets of tetrahedral units, wherein metal ions, such as Zn^{2+} or Co^{2+}, are linked through N atoms in ditopic imidazolate anions.[66-68] Among the ZIFs, ZIF-8 ($Zn(mIM)_2$, mIM = 2-methylimidazolate) (**Figure 1.10**) exhibits a soft topology comprised of 1.16 nm cages connected through six-membered windows, 0.34 nm in size, and is currently the most widely investigated ZIF material for a range of applications.[69-70] In our group, non-noble Ni metal nanoparticles were first prepared for hydrogen evolution upon hydrolysis of ammonia borane, achieving the TOF value of 85.7 mol_{H_2} mol_{cat}^{-1} min^{-1} at room temperature,

which is the highest total turnover frequency among these first-row late transition metals.[36] This result thus motivated our further investigation on ZIF-8 encapsulated TMNPs for HER. Then, a series of bimetallic NiPt@ZIF-8 nanocatalyst with various Ni/Pt proportion was introduced. (**Figure 1.10**) By optimizing transition metal ratios, a sharp positive synergy between 2/3 Ni and 1/3 Pt was found, exhibiting a remarkable catalytic efficiency with TOF of 600 mol_{H_2} mol_{cat}^{-1} min^{-1} under ambient conditions, which overtook performances of previous Pt-base catalysts.

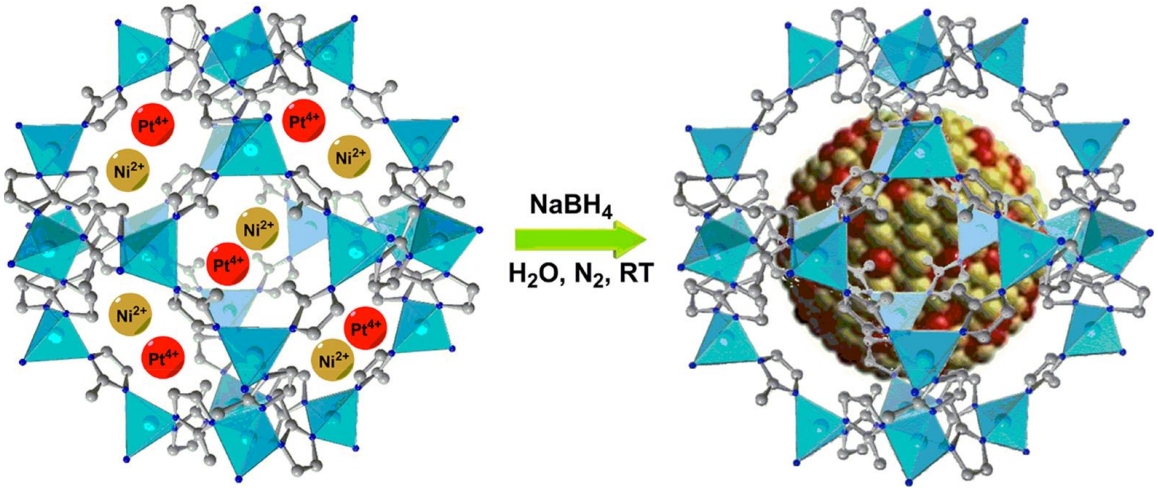

Figure 1.10. Synthesis of the NiPt@ZIF-8 NPs.[34]

1.4.3. Other supports

Besides the porous materials, *e. g.* MOF, and organic capsules, *e. g.* "click" dendrimer, inorganic oxides and carbon are also desirable candidates for TMNPs in hydrogen evolution reaction. For instance, Basset's group[71] reported the synthesis of photocatalytic Pt/CN/KCC-1 for hydrogen evolution, where porous fibrous silica KCC-1[72] was also beneficial for improving photocatalytic stability. Cheng et. al. reported the synthesis of well dispersed 2.4 nm Rh nanoparticles (NPs) supported on graphene via a one-step in situ

procedure by using methylamine borane (MeAB) as the reducing agent. Compared with other conventional supports, such as carbon black, SiO_2, γ-Al_2O_3, and the physical mixture of Rh and graphene, the as-prepared Rh NPs supported on graphene exhibit superior catalytic activity towards the hydrolysis of ammonia borane, exhibiting a high TOF value of 325 min^{-1}.[73] Additionally, organometallic materials play an important role in catalysis, in particular, Basset's surface organometallic catalysis (SOMCat).[74] Our group reported that the organometallic sandwich cobaltocene serves as both the reductant and stabilizer for the preparation of TMNPs, giving a well-confined AgNPs and CuNPs with a narrow size distribution without any other ligand or support.[75] (**Figure 1.11**)

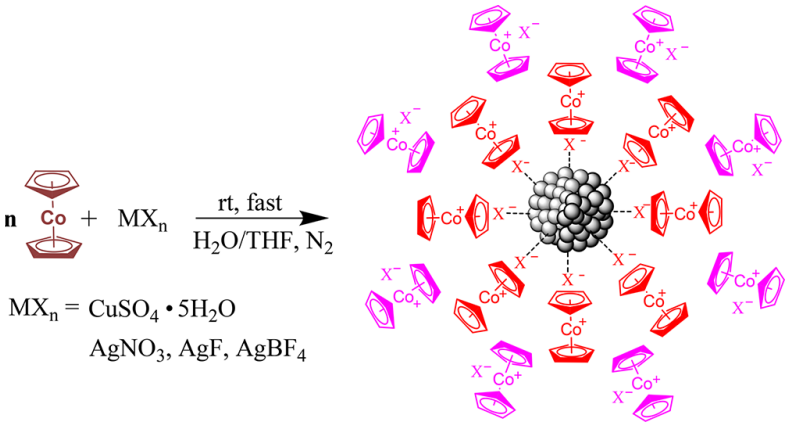

Figure 1.11. Synthesis of CuNPs and AgNPs by Reaction of $CuSO_4 \cdot 5H_2O$ or a Ag Salt with Cobaltocene.[75]

1.5. Summary of the PhD work and Plan

As a part of our current research on the development of new TMNP nanocatalysts, this thesis manuscript is divided into 4 chapters. It begins with the introduction of the development of catalytic hydrogen evolution in

Chapter 1, followed by 3 chapters presenting the preparation of TMNPs in hydrogen evolution reaction.

In **Chapter 2**, the mono-metallic and bimetallic transition metal NPs, stabilized by 27 triethylene glycol (TEG)-terminated "click" dendrimers, were prepared for H_2 evolution upon $B_2(OH)_4$ hydrolysis. Several gold-containing bimetallic nano-catalytic systems, Au_x-Rh_y, have been exploited with various Au/Rh ratios, showing a remarkable bimetallic synergy between Au and Rh at metal proportion of 4:1. The photocatalytic activities of Au-Rh nanocatalyst are also investigated, involving a unique located surface plasmon resonance effect. Tandem reaction and kinetic studies are examined, confirming our proposal of catalytic mechanism of $B_2(OH)_4$ hydrolysis.

In **Chapter 3**, the versatile hydride-rich neutral organometallics [CoCp(η^4-C_5H_6)] (Cp= η^5-C_5H_5), **1H**, and [CoCp*(η^4-C_5H_6)] (Cp* = η^5-C_5Me_5), **2H**, are used as both a reductant and stabilizer for a series of Transition Metal Nano Particles, abbreviated TMNP, originated from **1H**, and TMNP* originated from **2H**. It is well recognized that permethylation of Cp ligand stabilizes metallocenes and other organometallics owing to the stereo-electronic influence of the five methyl substituents in Cp*. With the perspective of this comparison, the catalytic activity of TMNP and TMNP* are investigated for the hydrolysis of $B_2(OH)_4$ and ammonia borane.

In **Chapter 4**, a series of cobaltocene-derived hydride-reservoir complexes with different Cp methylation, [CoCp(η^4-C_5H_6)], **1H**, [CoCp*(η^4-C_5H_6)], **2H**, [CoCp*(η^4-C_5Me_5H)], **3H**, were prepared using the reductant $NaBH_4$. The complexes are investigated for H_2 generation and as hydride donors towards the hydrogenation of olefins in methanol. The results show that **2H** with one Cp* ligand exhibits optimized stereo-electronic properties, i. e. high

thermodynamic stability as well as good hydride donor capacity in the model hydrogenation of 1,1-diphenylethylene catalyzed by Pd/C. Given its robust 18-electron sandwich structure (empty hydride reservoir), the cationic form of **2H**, $\mathbf{2^{+}PF_6^{-}}$, is easily recycled upon precipitation of $\mathbf{2^{+}}$ using HPF_6. The isotope experiment and tandem reaction show that the two H atoms in the produced 1,1- diphenylethane are provided from **2H** and the methanol solvent.

Finally, conclusion and perspectives of the thesis are provided.

1.6. References

1. He, T.; Pachfule, P.; Wu, H.; Xu, Q.; Chen, P. Hydrogen carriers. *Nat. Rev. Mater.* **2016,** *1*, 16059.

2. Hirscher, M.; Yartys, V. A.; Baricco, M.; Bellosta von Colbe, J.; Blanchard, D.; Bowman, R. C.; Broom, D. P.; Buckley, C. E.; Chang, F.; Chen, P.; Cho, Y. W.; Crivello, J.-C.; Cuevas, F.; David, W. I. F.; de Jongh, P. E.; Denys, R. V.; Dornheim, M.; Felderhoff, M.; Filinchuk, Y.; Froudakis, G. E.; Grant, D. M.; Gray, E. M.; Hauback, B. C.; He, T.; Humphries, T. D.; Jensen, T. R.; Kim, S.; Kojima, Y.; Latroche, M.; Li, H.-W.; Lototskyy, M. V.; Makepeace, J. W.; Møller, K. T.; Naheed, L.; Ngene, P.; Noréus, D.; Nygård, M. M.; Orimo, S.-i.; Paskevicius, M.; Pasquini, L.; Ravnsbæk, D. B.; Veronica Sofianos, M.; Udovic, T. J.; Vegge, T.; Walker, G. S.; Webb, C. J.; Weidenthaler, C.; Zlotea, C. Materials for hydrogen-based energy storage – past, recent progress and future outlook. *J. Alloys Compd.* **2020,** *827*, 153548.

3. Wang, C.; Astruc, D. Recent developments of nanocatalyzed liquid-phase hydrogen generation. *Chem. Soc. Rev.* **2021,** *50*, 3437-3484.

4. Abe, J. O.; Popoola, A. P. I.; Ajenifuja, E.; Popoola, O. M. Hydrogen energy, economy and storage: Review and recommendation. *Int. J. Hydrog. Energy* **2019,** *44*, 15072-15086.

5. Zhu, B.; Zou, R.; Xu, Q. Metal–Organic Framework Based Catalysts for Hydrogen Evolution. *Advanced Energy Materials* **2018,** *8*, 1801193.

6. Haryanto, A.; Fernando, S.; Murali, N.; Adhikari, S. Current Status of Hydrogen Production Techniques by Steam Reforming of Ethanol: A Review. *Energy & Fuels* **2005,** *19*, 2098-2106.

7. Yu, X.; Tang, Z.; Sun, D.; Ouyang, L.; Zhu, M. Recent advances and remaining challenges of nanostructured materials for hydrogen storage applications. *Prog. Mater Sci.* **2017,** *88*, 1-48.

8. Xiao, P.; Chen, W.; Wang, X. A Review of Phosphide-Based Materials for Electrocatalytic Hydrogen Evolution. *Advanced Energy Materials* **2015,** *5*, 1500985.

9. Zhu, J.; Hu, L.; Zhao, P.; Lee, L. Y. S.; Wong, K. Y. Recent Advances in Electrocatalytic Hydrogen Evolution Using Nanoparticles. *Chem. Rev.* **2020,** *120*, 851-918.

10. Valenti, G.; Boni, A.; Melchionna, M.; Cargnello, M.; Nasi, L.; Bertoni, G.; Gorte, R. J.; Marcaccio, M.; Rapino, S.; Bonchio, M.; Fornasiero, P.; Prato, M.; Paolucci, F. Co-axial heterostructures integrating palladium/titanium dioxide with carbon nanotubes for efficient electrocatalytic hydrogen evolution. *Nat. Commun.* **2016,** *7*, 13549.

11. Zada, A.; Muhammad, P.; Ahmad, W.; Hussain, Z.; Ali, S.; Khan, M.; Khan, Q.; Maqbool, M. Surface Plasmonic‐Assisted Photocatalysis and Optoelectronic Devices with Noble Metal Nanocrystals: Design, Synthesis, and Applications. *Adv. Funct. Mater.* **2019,** *30*, 1906744.

12. Gelle, A.; Jin, T.; de la Garza, L.; Price, G. D.; Besteiro, L. V.; Moores, A. Applications of Plasmon-Enhanced Nanocatalysis to Organic Transformations. *Chem. Rev.* **2020,** *120*, 986-1041.

13. Zhang, S.; Li, M.; Zhao, J.; Wang, H.; Zhu, X.; Han, J.; Liu, X. Plasmonic AuPd-based Mott-Schottky Photocatalyst for Synergistically Enhanced Hydrogen Evolution from Formic Acid and Aldehyde. *Appl. Catal. B-Environ.* **2019,** *252*, 24-32.

14. Kojima, Y. Hydrogen storage materials for hydrogen and energy carriers. *Int. J. Hydrog. Energy* **2019,** *44*, 18179-18192.

15. Metin, Ö.; Özkar, S. Hydrogen Generation from the Hydrolysis of Ammonia-borane and Sodium Borohydride Using Water-soluble Polymer-stabilized Cobalt(0) Nanoclusters Catalyst. *Energy & Fuels* **2009,** *23*, 3517-3526.

16. Muir, S. S.; Yao, X. Progress in sodium borohydride as a hydrogen storage material: Development of hydrolysis catalysts and reaction systems. *Int. J. Hydrog. Energy* **2011,** *36*, 5983-5997.

17. Makepeace, J. W.; He, T.; Weidenthaler, C.; Jensen, T. R.; Chang, F.; Vegge, T.; Ngene, P.; Kojima, Y.; de Jongh, P. E.; Chen, P.; David, W. I. F. Reversible ammonia-based and liquid organic hydrogen carriers for high-density hydrogen storage: Recent progress. *Int. J. Hydrog. Energy* **2019,** *44*, 7746-7767.

18. Schlesinger, H. I.; Brown, H. C.; Finholt, A. E.; Gilbreath, J. R.; Hoekstra, H. R.; Hyde, E. K. Sodium Borohydride, Its Hydrolysis and its Use as a Reducing Agent and in the Generation of Hydrogen1. *J. Am. Chem. Soc.* **1953,** *75*, 215-219.

19. Brack, P.; Dann, S. E.; Wijayantha, K. G. U. Heterogeneous and homogenous catalysts for hydrogen generation by hydrolysis of aqueous sodium borohydride (NaBH4) solutions. *Energy Science & Engineering* **2015,** *3*, 174-188.

20. Wu, C.; Zhang, J.; Guo, J.; Sun, L.; Ming, J.; Dong, H.; Zhao, Y.; Tian, J.; Yang, X. Ceria-Induced Strategy To Tailor Pt Atomic Clusters on Cobalt–Nickel Oxide and the Synergetic Effect for Superior Hydrogen Generation. *ACS Sustain. Chem. Eng.* **2018,** *6*, 7451-7457.

21. Kang, N.; Djeda, R.; Wang, Q.; Fu, F.; Ruiz, J.; Pozzo, J. L.; Astruc, D. Efficient "Click"-Dendrimer-Supported Synergistic Bimetallic Nanocatalysis for Hydrogen Evolution by Sodium Borohydride Hydrolysis. *ChemCatChem* **2019,** *11*, 2341-2349.

22. Staubitz, A.; Robertson, A. P. M.; Manners, I. Ammonia-Borane and Related Compounds as Dihydrogen Sources. *Chem. Rev.* **2010,** *110*, 4079-4124.

23. Chandra, M.; Xu, Q. A high-performance hydrogen generation system: Transition metal-catalyzed dissociation and hydrolysis of ammonia–borane. *J. Power Sources* **2006,** *156*, 190-194.

24. Chen, Y.-Z.; Liang, L.; Yang, Q.; Hong, M.; Xu, Q.; Yu, S.-H.; Jiang, H.-L. A seed-mediated approach to the general and mild synthesis of non-noble metal nanoparticles stabilized by a metal–organic framework for highly efficient catalysis. *Materials Horizons* **2015,** *2*, 606-612.

25. Yao, Q.; Ding, Y.; Lu, Z.-H. Noble-metal-free nanocatalysts for hydrogen generation from boron- and nitrogen-based hydrides. *Inorganic Chemistry Frontiers* **2020,** *7*, 3837-3874.

26. Blaquiere, N.; Diallo-Garcia, S.; Gorelsky, S. I.; Black, D. A.; Fagnou, K. Ruthenium-Catalyzed Dehydrogenation of Ammonia Boranes. *J. Am. Chem. Soc.* **2008,** *130*, 14034-14035.

27. Zhan, W.-W.; Zhu, Q.-L.; Xu, Q. Dehydrogenation of Ammonia Borane by Metal Nanoparticle Catalysts. *ACS Catal.* **2016,** *6*, 6892-6905.

28. Ramachandran, P. V.; Gagare, P. D. Preparation of Ammonia Borane in High Yield and Purity, Methanolysis, and Regeneration. *Inorg. Chem.* **2007,** *46*, 7810-7817.

29. Marder, T. B. Will We Soon Be Fueling our Automobiles with Ammonia–Borane? *Angew. Chem. Int. Ed.* **2007,** *46*, 8116-8118.

30. Lu, Z.-H.; Jiang, H.-L.; Yadav, M.; Aranishi, K.; Xu, Q. Synergistic catalysis of Au-Co@SiO2 nanospheres in hydrolytic dehydrogenation of ammonia borane for chemical hydrogen storage. *J. Mater. Chem.* **2012,** *22*, 5065-5071.

31. Sun, D.; Mazumder, V.; Metin, Ö.; Sun, S. Catalytic Hydrolysis of Ammonia Borane via Cobalt Palladium Nanoparticles. *ACS Nano* **2011,** *5*, 6458-6464.

32. Yan, J.-M.; Zhang, X.-B.; Akita, T.; Haruta, M.; Xu, Q. One-Step Seeding Growth of Magnetically Recyclable Au@Co Core−Shell Nanoparticles: Highly Efficient Catalyst for Hydrolytic Dehydrogenation of Ammonia Borane. *J. Am. Chem. Soc.* **2010,** *132*, 5326-5327.

33. Xi, P.; Chen, F.; Xie, G.; Ma, C.; Liu, H.; Shao, C.; Wang, J.; Xu, Z.; Xu, X.; Zeng, Z. Surfactant free RGO/Pd nanocomposites as highly active heterogeneous catalysts for the hydrolytic dehydrogenation of ammonia borane for chemical hydrogen storage. *Nanoscale* **2012,** *4*, 5597-5601.

34. Fu, F.; Wang, C.; Wang, Q.; Martinez-Villacorta, A. M.; Escobar, A.; Chong, H.; Wang, X.; Moya, S.; Salmon, L.; Fouquet, E.; Ruiz, J.; Astruc, D. Highly Selective and Sharp Volcano-type Synergistic Ni_2Pt@ZIF-8-Catalyzed Hydrogen Evolution from Ammonia Borane Hydrolysis. *J. Am. Chem. Soc.* **2018,** *140*, 10034-10042.

35. Kang, N.; Wang, Q.; Djeda, R.; Wang, W.; Fu, F.; Moro, M. M.; Ramirez, M. d. l. A.; Moya, S.; Coy, E.; Salmon, L.; Pozzo, J.-L.; Astruc, D. Visible-Light Acceleration of H_2 Evolution from Aqueous Solutions of Inorganic Hydrides Catalyzed by Gold-Transition-Metal Nanoalloys. *ACS Appl. Mater. Interfaces* **2020,** *12*, 53816-53826.

36. Wang, C.; Tuninetti, J.; Wang, Z.; Zhang, C.; Ciganda, R.; Salmon, L.; Moya, S.; Ruiz, J.; Astruc, D. Hydrolysis of Ammonia-Borane over Ni/ZIF-8 Nanocatalyst: High Efficiency, Mechanism, and Controlled Hydrogen Release. *J. Am. Chem. Soc.* **2017,** *139*, 11610-11615.

37. Wang, Q.; Fu, F.; Yang, S.; Martinez Moro, M.; Ramirez, M. d. l. A.; Moya, S.; Salmon, L.; Ruiz, J.; Astruc, D. Dramatic Synergy in CoPt Nanocatalysts Stabilized by "Click" Dendrimers for Evolution of Hydrogen from Hydrolysis of Ammonia Borane. *ACS Catal.* **2018,** *9*, 1110-1119.

38. Zhao, Q.; Kang, N.; Martínez Moro, M.; Guisasola, E.; Moya, S.; Coy, E.; Salmon, L.; Liu, X.; Astruc, D. Sharp Volcano-Type Synergy and Visible Light Acceleration in H_2 Release upon $B_2(OH)_4$ Hydrolysis Catalyzed by Au-Rh@Click-Dendrimer Nanozymes. *ACS A.E.M* **2022,** *5*, 3834–3844.

39. Liu, S. S.; Zhou, Y. M.; Sui, Y. B.; Liu, H.; Zhou, H. F. $B_2(OH)_4$-Mediated One-Pot Synthesis of Tetrahydroquinoxalines from 2-Amino(nitro)anilines and 1,2-Dicarbonyl Compounds in Water. *Org. Chem. Front.* **2017,** *4*, 2175-2178.

40. Zhou, J.; Huang, Y.; Shen, J.; Liu, X. Pd/C-Catalyzed H2 Evolution from Tetrahydroxydiboron Hydrolysis. *Catal. Lett.* **2021,** *151*, 3004-3010.

41. Cummings, S. P.; Le, T. N.; Fernandez, G. E.; Quiambao, L. G.; Stokes, B. J. Tetrahydroxydiboron-Mediated Palladium-Catalyzed Transfer Hydrogenation and Deuteriation of Alkenes and Alkynes Using Water as the Stoichiometric H or D Atom Donor. *J. Am. Chem. Soc.* **2016,** *138*, 6107-6110.

42. Molander, G. A.; Cavalcanti, L. N.; Garcia-Garcia, C. Nickel-Catalyzed Borylation of Halides and Pseudohalides with Tetrahydroxydiboron $B_2(OH)_4$. *J. Org. Chem.* **2013,** *78*, 6427-6439.

43. Londregan, A. T.; Piotrowski, D. W.; Xiao, J. Rapid and Selective in situ Reduction of Pyridine-N-oxides with Tetrahydroxydiboron. *Synlett* **2013,** *24*, 2695-2700.

44. Gurung, S. R.; Mitchell, C.; Huang, J.; Jonas, M.; Strawser, J. D.; Daia, E.; Hardy, A.; O'Brien, E.; Hicks, F.; Papageorgiou, C. D. Development and Scale-up of an Efficient Miyaura Borylation Process Using Tetrahydroxydiboron. *Org. Process Res. Dev.* **2017,** *21*, 65-74.

45. Chen, W.; Shen, J.; Huang, Y.; Liu, X.; Astruc, D. Catalyzed Hydrolysis of Tetrahydroxydiboron by Graphene Quantum Dot-Stabilized Transition-Metal Nanoparticles for Hydrogen Evolution. *ACS Sustain. Chem. Eng.* **2020,** *8*, 7513-7522.

46. Orimo, S.-i.; Nakamori, Y.; Eliseo, J. R.; Züttel, A.; Jensen, C. M. Complex Hydrides for Hydrogen Storage. *Chem. Rev.* **2007,** *107*, 4111-4132.

47. Schneemann, A.; White, J. L.; Kang, S.; Jeong, S.; Wan, L. F.; Cho, E. S.; Heo, T. W.; Prendergast, D.; Urban, J. J.; Wood, B. C.; Allendorf, M. D.; Stavila, V. Nanostructured Metal Hydrides for Hydrogen Storage. *Chem. Rev.* **2018,** *118*, 10775-10839.

48. Wang, D.; Astruc, D. The recent development of efficient Earth-abundant transition-metal nanocatalysts. *Chem. Soc. Rev.* **2017,** *46*, 816-854.

49. Akbayrak, S.; Tonbul, Y.; Özkar, S. Ceria supported rhodium nanoparticles: Superb catalytic activity in hydrogen generation from the hydrolysis of ammonia borane. *Appl. Catal. B* **2016,** *198*, 162-170.

50. Tavakkoli, M.; Kallio, T.; Reynaud, O.; Nasibulin, A. G.; Johans, C.; Sainio, J.; Jiang, H.; Kauppinen, E. I.; Laasonen, K. Single-Shell Carbon-Encapsulated Iron Nanoparticles: Synthesis and High Electrocatalytic Activity for Hydrogen Evolution Reaction. *Angew. Chem. Int. Ed.* **2015,** *54*, 4535-4538.

51. Gao, C.; Lyu, F.; Yin, Y. Encapsulated Metal Nanoparticles for Catalysis. *Chem. Rev.* **2021,** *121*, 834-881.

52. Singh, A. K.; Xu, Q. Synergistic Catalysis over Bimetallic Alloy Nanoparticles. *ChemCatChem* **2013,** *5*, 652-676.

53. Verma, P.; Yuan, K.; Kuwahara, Y.; Mori, K.; Yamashita, H. Enhancement of Plasmonic Activity by Pt/Ag Bimetallic Nanocatalyst Supported on Mesoporous Silica in the Hydrogen Production from Hydrogen Storage Material. *Appl. Catal. B-Environ.* **2018,** *223*, 10-15.

54. Chen, T.; Rodionov, V. O. Controllable Catalysis with Nanoparticles: Bimetallic Alloy Systems and Surface Adsorbates. *ACS Catal.* **2016,** *6*, 4025-4033.

55. Zaleska-Medynska, A.; Marchelek, M.; Diak, M.; Grabowska, E. Noble metal-based bimetallic nanoparticles: the effect of the structure on the optical, catalytic and photocatalytic properties. *Adv. Colloid Interface Sci.* **2016,** *229*, 80-107.

56. Bian, T.; Xiao, B.; Sun, B.; Huang, L.; Su, S.; Jiang, Y.; Xiao, J.; Yuan, A.; Zhang, H.; Yang, D. Local epitaxial growth of Au-Rh core-shell star-shaped decahedra: A case for studying electronic and ensemble effects in hydrogen evolution reaction. *Appl. Catal. B* **2020,** *263*, 118255.

57. Zhu, Q.-L.; Xu, Q. Immobilization of Ultrafine Metal Nanoparticles to High-Surface-Area Materials and Their Catalytic Applications. *Chem* **2016,** *1*, 220-245.

58. Zhang, Q.; Lee, I.; Joo, J. B.; Zaera, F.; Yin, Y. Core–Shell Nanostructured Catalysts. *Acc. Chem. Res.* **2013,** *46*, 1816-1824.

59. Wang, N.; Sun, Q.; Yu, J. Ultrasmall Metal Nanoparticles Confined within Crystalline Nanoporous Materials: A Fascinating Class of Nanocatalysts. *Adv. Mater.* **2019,** *31*, 1803966.

60. Navalon, S.; Dhakshinamoorthy, A.; Alvaro, M.; Garcia, H. Metal nanoparticles supported on two-dimensional graphenes as heterogeneous catalysts. *Coord. Chem. Rev.* **2016,** *312*, 99-148.

61. Boisselier, E.; Diallo, A. K.; Salmon, L.; Ornelas, C.; Ruiz, J.; Astruc, D. Encapsulation and Stabilization of Gold Nanoparticles with "Click" Polyethyleneglycol Dendrimers. *J. Am. Chem. Soc.* **2010,** *132*, 2729-2742.

62. Deraedt, C.; Salmon, L.; Etienne, L.; Ruiz, J.; Astruc, D. "Click" dendrimers as efficient nanoreactors in aqueous solvent: Pd nanoparticle stabilization for sub-ppm Pd catalysis of Suzuki–Miyaura reactions of aryl bromides. *Chem. Commun.* **2013,** *49*, 8169-8171.

63. Liu, X.; Gregurec, D.; Irigoyen, J.; Martinez, A.; Moya, S.; Ciganda, R.; Hermange, P.; Ruiz, J.; Astruc, D. Precise Localization of Metal Nanoparticles in Dendrimer Nanosnakes or Inner Periphery and Consequences in Catalysis. *Nat. Commun.* **2016,** *7*, 13152.

64. Yang, Q.; Xu, Q.; Jiang, H. L. Metal-organic frameworks meet metal nanoparticles: synergistic effect for enhanced catalysis. *Chem. Soc. Rev.* **2017,** *46*, 4774-4808.

65. Huang, Y. B.; Liang, J.; Wang, X. S.; Cao, R. Multifunctional metal-organic framework catalysts: synergistic catalysis and tandem reactions. *Chem. Soc. Rev.* **2017,** *46*, 126-157.

66. Park, K. S.; Ni, Z.; Côté, A. P.; Choi, J. Y.; Huang, R.; Uribe-Romo, F. J.; Chae, H. K.; O'Keeffe, M.; Yaghi, O. M. Exceptional chemical and thermal stability of zeolitic imidazolate frameworks. *Proc. Natl. Acad. Sci. U.S.A.* **2006,** *103*, 10186-10191.

67. Banerjee, R.; Phan, A.; Wang, B.; Knobler, C.; Furukawa, H.; O'Keeffe, M.; Yaghi, O. M. High-Throughput Synthesis of Zeolitic Imidazolate

Frameworks and Application to CO₂ Capture. *Science* **2008,** *319*, 939-943.

68. Lee, Y.-R.; Jang, M.-S.; Cho, H.-Y.; Kwon, H.-J.; Kim, S.; Ahn, W.-S. ZIF-8: A comparison of synthesis methods. *Chem. Eng. J.* **2015,** *271*, 276-280.

69. Bhattacharjee, S.; Jang, M.-S.; Kwon, H.-J.; Ahn, W.-S. Zeolitic Imidazolate Frameworks: Synthesis, Functionalization, and Catalytic/Adsorption Applications. *Catalysis Surveys from Asia* **2014,** *18*, 101-127.

70. Zhang, T.; Zhang, X.; Yan, X.; Lin, L.; Liu, H.; Qiu, J.; Yeung, K. L. Core–shell Pd/ZSM-5@ZIF-8 membrane micro-reactors with size selectivity properties for alkene hydrogenation. *Catal. Today* **2014,** *236*, 41-48.

71. Bhunia, M. K.; Melissen, S.; Parida, M. R.; Sarawade, P.; Basset, J.-M.; Anjum, D. H.; Mohammed, O. F.; Sautet, P.; Le Bahers, T.; Takanabe, K. Dendritic Tip-on Polytriazine-Based Carbon Nitride Photocatalyst with High Hydrogen Evolution Activity. *Chem. Mater.* **2015,** *27*, 8237-8247.

72. Polshettiwar, V.; Cha, D.; Zhang, X.; Basset, J. M. High-Surface-Area Silica Nanospheres (KCC-1) with a Fibrous Morphology. *Angew. Chem. Int. Ed.* **2010,** *49*, 9652-9656.

73. Shen, J.; Yang, L.; Hu, K.; Luo, W.; Cheng, G. Rh nanoparticles supported on graphene as efficient catalyst for hydrolytic dehydrogenation of amine boranes for chemical hydrogen storage. *Int. J. Hydrog. Energy* **2015,** *40*, 1062-1070.

74. Samantaray, M. K.; D'Elia, V.; Pump, E.; Falivene, L.; Harb, M.; Ould Chikh, S.; Cavallo, L.; Basset, J.-M. The Comparison between Single Atom Catalysis and Surface Organometallic Catalysis. *Chem. Rev.* **2020,** *120*, 734-813.

75. Fu, F.; Ciganda, R.; Wang, Q.; Tabey, A.; Wang, C.; Escobar, A.; Martinez-Villacorta, A. M.; Hernández, R.; Moya, S.; Fouquet, E.; Ruiz, J.; Astruc, D. Cobaltocene Reduction of Cu and Ag Salts and Catalytic Behavior of the Nanoparticles Formed. *ACS Catal*. **2018,** *8*, 8100-8106.

Chapter 2. Sharp Volcano-Type Synergy and Visible-Light Acceleration in H_2 Release upon $B_2(OH)_4$ Hydrolysis Catalyzed by Au-Rh@click-dendrimer Nanozymes

2.1. Introduction

We report oxygen atom uptake from H_2O producing H_2 upon reaction with $B_2(OH)_4$ catalyzed under ambient condition by bimetallic Au-Rh nano-particles (NPs) encapsulated in a "click"-dendrimer. These nano catalysts of metallo-macromolecular type play the role of "nanozymes" (NZs), a general term currently utilized for artificial nanomaterials with catalytic activities resembling those of enzymes.[1] In the present case, we will show some resemblance of these nanocatalysts[2] with hydrogenase that catalyze the formation of H_2 from water protons, including mechanistic results.[3,4] $B_2(OH)_4$, a useful borylation agent, sometimes used in hydrogenation reactions,[5-8] is potentially usable for H_2 generation upon hydrolysis according to **Equation 2.1**:

$$\mathbf{B_2(OH)_4 + 2\,H_2O \rightarrow 2\,B(OH)_3 + H_2\uparrow} \qquad \mathbf{(2.1)}$$

Transfer hydrogenation[9] of unsaturated hydrocarbon using catalytic $B_2(OH)_4$ hydrolysis was pioneered in 2016 by Stokes and his group who reported that this reaction could be used for hydrogenation and deuteration of a variety of alkenes and alkynes and showed that both hydrogen atoms of water were transferred to the unsaturated substrates.[5] A catalytic mechanism was suggested without H_2 formation involving the intermediacy of a Pd-H species in which the unsaturated hydrocarbon inserted to end up with its hydrogenation. It has also been shown that H_2 formation proceeded upon Pd-catalyzed hydrolysis of $B_2(OH)_4$.[9] For comparison, ammonia borane (AB) hydrolysis is a well-known classic method of H_2 generation in which one of the generated H_2 atoms (the "hydridic" one) is provided by hydrogen-rich AB and the other one (the "acidic" one) from water.[10] On the other hand, $B_2(OH)_4$ only contains acidic hydrogen atoms, and apparently both hydrogen atoms of

produced H_2 seem to come from water (*vide infra*), thus none would come from $B_2(OH)_4$. Consequently, $B_2(OH)_4$ is not a hydrogen storage material, contrary to AB and its derivatives. By the way, the fact that water behaves as a hydrogen storage source upon utilizing $B_2(OH)_4$ hydrolysis offers a D_2 production method from D_2O, applicable for the deuteration of unsaturated compounds of extensive utility in mechanism studies,[11] and analytical chemistry.[12,13]

$B_2(OH)_4$ is stable in water at room temperature, and thus a catalyst is required for its hydrolysis to H_2 according to **Equation 2.1**. Formation of H_2 would be of interest given the considerable application in its production as a long-term sustainable energy supply.[14-19] Given the absence of reasonably practical loop to recycle $B_2(OH)_4$ from the reaction product $B(OH)_3$, however, **Equation 2.1** can rather be considered as a test reaction and a useful and fast way to produce H_2 or D_2 on the laboratory scale under ambient conditions. Bimetallic NPs, constituted of two distinct metal elements, often show an enhanced chemical performance compared to those of their monometallic counterparts.[20] The presence of a second metal indeed usually provokes a modification of the electronic state of each metal in the NP and consequently modifies the catalytic activity of the bimetallic nanocatalysts. Besides, the second metal induces a geometric effect often reducing the number of multiple adsorption sites by partially blocking the surface or facilitating access to more active sites owing to specific atomic arrangement.[21] This frequently positive synergistic effect has received much attention in optical, catalytic, and photocatalytic applications.[20]

Photocatalysis is regarded as a prominent approach utilizing the endless and diffuse solar energy.[22] The plasmonic metal NPs (PMNPs)[23] have drawn much attention owing to their surface plasmonic resonant (SPR) effect that is

utilized for plasmonic photocatalytic hydrogen evolution. Light excitation provokes hot charge transfer to the nearby substrate for a few tenths of fs, which reduces the activation energy of the reaction of the adsorbed substrate.[24] Therefore, PMNP morphology, size and structure control the efficiency of the photocatalytic system.[25,26]

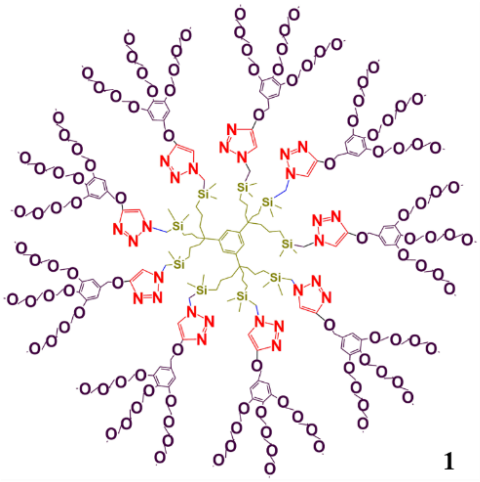

Figure 2.1 "Click" dendrimer **1**.

Dendrimer-RNA NPs are known to provide protective immunity against several lethal viruses,[27] and polyamidoamine (PAMAM) dendrimers encapsulating NPs have functioned as catalysts.[28,29] Dendrimers of "click" type are known as effective nanocatalyst encapsulating supports for a variety of reactions.[30] They contain intradendritic 1,2,3-triazolyl groups resulting from "click" reactions. They are therefore called "click" dendrimers (**Figure 2.1**), because they result from the Cu(I)-catalyzed Huisgen 1,3-dipolar azide-alkyne cycloaddition (CuAAC, the most known so-called "click" reaction[31]) of the terminal azido groups of dendrimer cores with dendrons containing an alkyne group at their focal points. These "click" dendrimers, such as **1** (**Figure 2.1**), are of micellar type, due to their hydrophobic interior and the presence of hydrophilic triethylene glycol (TEG) terminal groups. They are

dendritic amphiphilic unimolecular micelles allowing coordination, to their intradendritic triazole groups, of transition-metal ions and, more mildly, NPs.[31] These intradendritically coordinated metal cations and NPs are stabilized by protection, due to the bulk of the "click" dendrimer periphery. Therefore, here, "click"-dendrimer-encapsulated, mono-metallic and bimetallic transition metal NPs including Au have been prepared, tested and compared towards H_2 evolution upon $B_2(OH)_4$ hydrolysis under both dark and visible-light illumination conditions. Several gold-containing bimetallic nanocatalytic systems, Au_x-Rh_y have been selected and examined with various metal ratios, allowing to determine the optimized metal ratios in the dark, light-induced acceleration, and combined effects. From these results, the benefits of bimetallic synergy and visible light illumination are analyzed and discussed. Finally, hydrolysis experiments using D_2O instead of H_2O including determination of the kinetic isotope effect (KIE) are carried out in order to contribute to a mechanistic proposal concerning the AuRh NZ-catalyzed $B_2(OH)_4$ hydrolysis.

2.2. Synthesis and characterization of the “click” dendrimer-encapsulated Au-Rh NZs

2.2.1 Materials

The precursors used for the click-dendrimer-encapsulated NP preparations, $RhCl_3$, $KAuCl_4 \cdot xH_2O$, $NaBH_4$ and $B_2(OH)_4$ were purchased from Sigma-Aldrich and are analytical grade. All flasks were washed with aqua regia (HCl: HNO_3 = 3:1) before usage to avoid the presence of metal residues. Milli-Q water (18.2 MΩ, Thermo Fischer Scientific Inc., USA) was used in the process of NP fabrication and catalytic reactions.

2.2.2. Synthesis of the "click" dendrimer-encapsulated Au-Rh NZs

The "click" dendrimer (**Figure 2.1** and **Figure S2.1**, **Experimental Section**) containing nine 1,2,3-triazole ligands on the tethers and 27 water-solubilizing triethylene glycol termini was fabricated via a method previously reported.[32] Taking advantage of the presence of nitrogen-rich 1,2,3-triazoles along the "click" dendrimer tethers, Rh (III) and Au (III) were coordinated to the intra-dendritic 1,2,3-triazoles upon blending together their precursor metal derivatives with the dendrimer under N_2. Then, the Au-Rh NPs were generated upon addition of a freshly-prepared solution of the reductant $NaBH_4$ to the dendrimer-metal (III) assembly (**Scheme 2.1**).[33] The composition of Au and Rh in the bimetallic NPs is termed as Au_xRh_y, where x and y indicate the molar ratio of Au and Rh, for example Au_4Rh_1 for an Au-Rh NZ containing 80% mol Au and 20% mol Rh. Various Au_xRh_y NPs were prepared upon varying the proportions x/y of the metal precursors from 0.5 to 6.

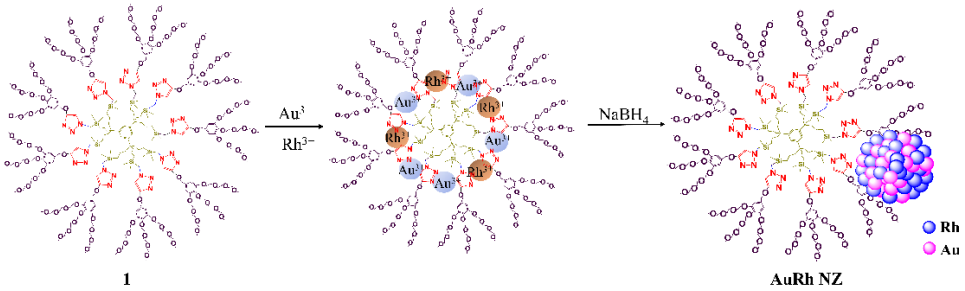

Scheme 2.1. Synthesis of various Au-Rh NZs supported by the "click" dendrimer 1.

2.2.3. Au-Rh NZ characterizations

The overall characterizations of the Au-Rh @click-dendrimer NZs were carried out using NMR and UV-vis. spectroscopies, transmission electron

microscopy (TEM), high-resolution TEM (HRTEM), Energy-Dispersive X-ray Spectroscopy (EDS), X-ray Photoelectron Spectroscopy (XPS) and chromatography-mass spectrometry (GC-MS). Bruker AC 300 MHz was used for the NMR spectra with all chemical shifts in parts per million (δ, ppm) referring to TMS at room temperature. UV- vis. spectra were recorded using a Perkin-Elmer Lambda 19 UV-vis. spectrometer. TEM images were recorded on TEM JEOL JEM 1400 (120 kV) - 2100F. HRTEM images were recorded by Jéol JEM-ARM200f -200 kV with a probe corrector, which was also equipped with a STEM HAADF system (Scanning Transmission Electron Microscopy Hight Angle Annular Dark Field) and energy-dispersive X-ray Spectroscopy (EDS) analysis system. XPS experiments were performed in a SPECS Sage HR 100 spectrometer with a non-monochromatic X-ray source (magnesium Kα line of 1253.6 eV energy and 252 W)

2.2.4. Catalytic reactions

The catalytic hydrolysis of $B_2(OH)_4$ was carried out at 25 ± 1 °C. In a typical experiment, 0.1 % mmol Au-Rh NZ dissolved in 4 ml deionized water was placed in a 50-ml round bottom flask with two outlets. Then, $B_2(OH)_4$ (1mmol, 90 mg) dissolved in 5 ml deionized water was added under vigorous stirring. The measurement of the produced H_2 gas was conducted in a typical water-filled gas burette. A 7-W visible LED lamp (Sunshine Lighting Limited, France) with a light intensity of 1540 lx was used for the light irradiation. The temperature of the reaction was measured using an electronic thermometer.

2.3. Results and discussions

2.3.1 Au-Rh NZ characterizations

The microstructure and size distribution of the metal NPs were investigated by TEM and high-resolution TEM (HRTEM). The as-prepared mono- and bimetallic NPs are homogeneously dispersed with a narrow small size distribution (**Figure 2.2** and **Figure S 2.2** to **Figure S 2.14**, **Experimental Section**). For Au_4Rh_1 NPs, a very fine diameter size distribution of 1.5 ± 0.4 nm is observed (**Figure S 2.4**, **Experimental Section**). This good confinement of the NPs is attributed to the stabilization effect of the intradendritic triazole ligands that coordinate to the gold and rhodium atoms. The intra- dendritic NPs make these nano-assemblies resemble metalloenzymes in their sizes, inner

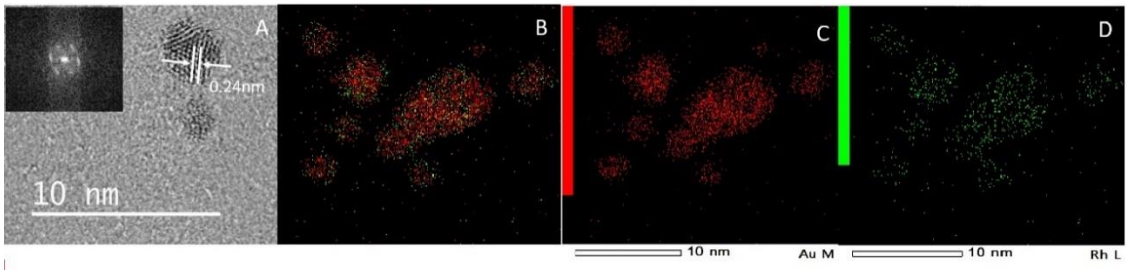

Figure 2.2 Transmission Electron Microscopy for Au_4Rh_1 NZs. HRTEM images; inset: corresponding Fast-Fourier transform (FFT) pattern (A). EDX elemental mapping images of the overlapped Au and Rh (B), and Au mapping (C) and Rh mapping (D)

catalytic site localization, transition-metal catalysts and hydrogenase-like function (*vide infra*, mechanistic section).[3, 28] **Figure 2.2A** exhibits clear lattice fringes with a space of 0.24 nm, which confirms the crystallinity of the Au_4Rh_1 NPs. A diffraction pattern with six-fold rotational symmetry in the inset fast-Fourier transform pattern evidences the (111) facets of Au and Rh.[34]

The element mapping of Au and Rh by EDS (**Figure 2.2B**, **2.2C**, **2.2D**) shows the alloy structure of the Au_4Rh_1 NZ. The Au element is more concentrated in the core of the NPs, which is also evidenced by the distribution of Au and Rh along the cross-section (**Figure S 2.9**, **Experimental Section**).

In order to investigate the surface electronic structure, XPS was recorded for the dendritic and the Au-Rh alloy NZ parts. As shown in **Figure 2.3**, comparing to the binding energy of pure AuNPs (87.38 eV and 83.70 eV) and pure RhNPs (312.63 eV and 307.96 eV), the alloyed Au_4Rh_1NZs exhibits a small upshift of 0.14 and 0.16 eV for Au^0 and a large upshift of 2.02 and 2.25 eV for Rh^0. The XPS data show that the Au atoms are not much perturbed upon alloying, whereas the Rh 3d orbitals are shifted to higher energy upon alloying Rh with Au, which means that the Rh atoms undergo some decrease of electron density in the Au-Rh alloy upon atom redistribution.[35,36]

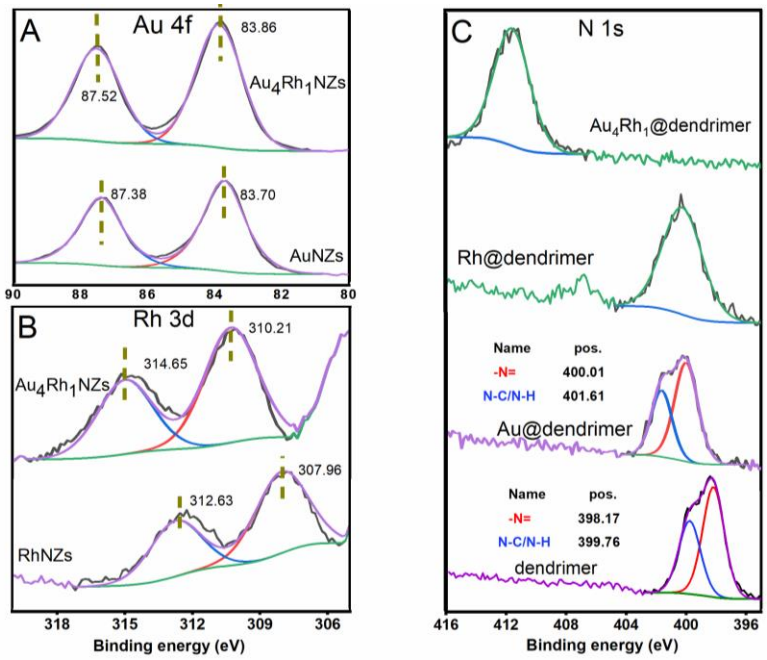

Figure 2.3. XPS patterns of the Au 4f (A), Rh 3d (B) for AuNZs, RhNZs, Au_4Rh_1NZs and N 1s for dendrimer, RhNPs@dendrimer, AuNPs@dendrimer and Au_4Rh_1NPs @dendrimer.

Let us now examine the shifts occurring for the dendritic triazole N 1s band upon dendrimer coordination to the alloyed metal atoms. The N 1s region of the dendrimer has two components centered at 398.17 and 399.76 eV that are assigned to -N=C- and -N-C/N-H of the triazole ligand in the dendrimer (**Figure 2.3**).[37,38] After loading the metal NPs in the dendrimer, the N 1s bands shift towards higher binding energies, exhibiting peaks at 400.01eV and 401.61eV for the monometallic AuNPs, 400.27eV for the monometallic RhNPs and 411.56 eV for the Au_4Rh_1NPs, which discloses significant electronic interactions between the NPs and the triazole ligand. The significance of the higher binding energy values in the NZ compared to the dendrimer alone is a decreased electron density on the dendritic N atoms upon coordination to the metals due to the N ligand electronic donation to these metal atoms.

Let us now consider the reduction by $NaBH_4$ of the two intra-dendritically coordinated metal cations to metal (0) NPs. Au^{3+} has a higher reduction potential than Rh^{3+} and, based on this consideration only, the Marcus theory region for exergonic electron transfer would dictate faster Au NP formation compared to Rh NP formation.[39] The coordination of chlorides and heteroatom ligands of the dendrimer, including in particular triazoles, changes the reduction potentials of the metal cations, however. Then, another factor that affects the relative rates of formation of the two NPs is the nucleation kinetics. Altogether, there is still a preference for the faster Au NP formation compared to the Rh NP formation, and the result may then be either formation of an Au@Rh core-shell NP or an alloy with an Au-enriched core. For instance, a related case was reported by Tsang's group with Ag@Pd NPs that catalyzed H_2 production from formic acid.[40] From EDX data obtained through the cross-section line element mapping (**Figure S 2.9** and **S 2.10**, **Experimental Section**), it is concluded that the alloy structure preferably contains Rh atoms located at the periphery of these bimetallic NPs and preferably Au atoms at the center. When the Au proportion is dominant, however, the introduction of a small amount of Rh is envisioned to tune the electron distribution of Au and Rh and generate defect sites at the surface of the Au-Rh NPs.[34]

2.3.2. Volcano-type synergistic effects in Au-Rh nanozymes for $B_2(OH)_4$ hydrolysis

A series of "click" dendrimer-supported Au_xRh_y NPs with diverse Au and Rh proportions (Rh mole content varying from 0 to 100%) were applied as NZs for the hydrolysis of $B_2(OH)_4$ at 25 ± 1 °C. The time profile plots of H_2 evolution and TOF_s values of Au-Rh nanozyme-catalyzed $B_2(OH)_4$ hydrolysis

are presented in **Figure 2.4**. The catalytic performance of H_2 evolution is determined by the reaction time at 10% $B_2(OH)_4$ conversion. Thus, the TOF_s value here is defined as mole of generated H_2 divided by the total number of surface atoms over the time span of 10% $B_2(OH)_4$ conversion.[41] When 1 mmol $B_2(OH)_4$ is consumed, 1 equiv. H_2 is produced in $B_2(OH)_4$ hydrolysis (**Equation 2.1**). The monometallic Au and Rh NZs are valuable catalysts providing TOF_s values of 1500 and 570 mol_{H_2} mol_{cata}^{-1} min^{-1} (**Table 2.1**), respectively, which indicates that the Au NZ is more active than Rh NZ. This result is opposite to those reported for NPs supported by graphene quantum dots (GQDs) reported by Jang *et al*, demonstrating a dramatic effect of the support on the nanocatalysts.[9] However, a dramatic rise of the TOF_s value was observed when Rh was introduced to form Au-Rh NZs. As shown in **Figure 2.4B**, the alloyed Au-Rh NZs displayed an enhanced catalytic activity compared to the monometallic counterparts, with a TOF_s value of 3700 mol_{H_2} mol_{cata}^{-1} min^{-1} for Au_6Rh_1, 5100 mol_{H_2} mol_{cata}^{-1} min^{-1} for Au_4Rh_1, 3200 mol_{H_2} mol_{cata}^{-1} min^{-1} for Au_2Rh_1, and 1900 mol_{H_2} mol_{cata}^{-1} min^{-1} for Au_1Rh_2, respectively (**Table 2.1**).

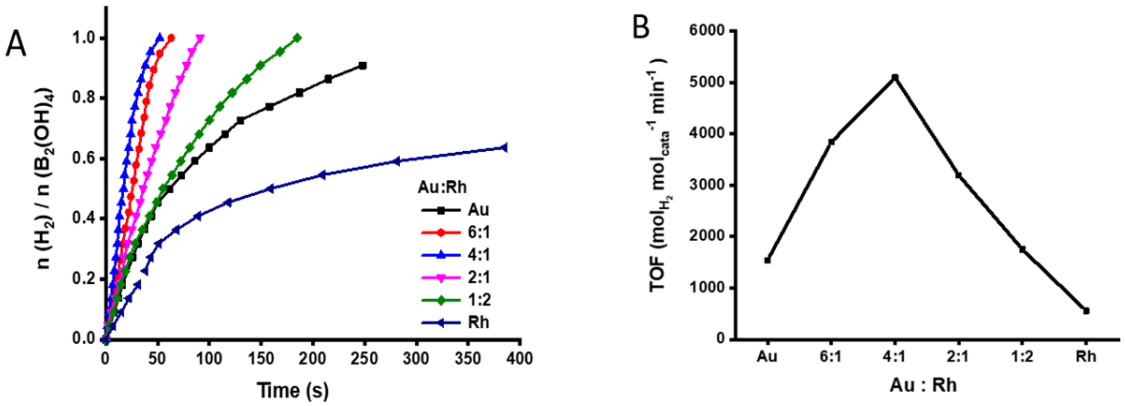

Figure 2.4. (A) Time profile plots of H_2 evolution and (B) TOF_s value of $B_2(OH)_4$ hydrolysis catalyzed by 0.1 mol % Au-Rh NZs with different Au/Rh molar ratios in the dark at 25± 1 ˚C

Among all the NZs, Au_4Rh_1 NZ exhibited the highest enhancement with a 3.4-time higher TOF_s value compared to pristine Au NZ under the same conditions. All these results reveal an impressive volcano-type synergistic effect between the Au and Rh components. To verify the bimetallic synergy between Au and Rh, a mixture of 80% monometallic Au NZ and 20% monometallic Rh NZ was conducted for $B_2(OH)_4$ hydrolysis, and the result (**Figure S 2.17A**, **Experimental Section**) indicates that there is no additional efficiency upon physically blending these two monometallic NZs. Besides, the recyclability of the best Au_4Rh_1NZ shows completion of quantitative hydrolysis during 4 cycles in dark, requiring progressively increased reaction time along these cycles, however (**Figure 2.5A**). There is slightly reduced efficiency of this NZ catalyst upon recycling. Catalytic AuRh NZ efficiency is demonstrated upon $B_2(OH)_4$ hydrolysis in the absence of catalyst (**Figure S 2.20**, **Experimental Section**) at 25˚C, 50˚C and 90˚C, which indicates that catalysis at 25˚C even with Au_1Rh_2 NZ that shows the least synergy is faster than $B_2(OH)_4$ hydrolysis alone at 90˚C. It is known that the substrate adsorption and product desorption step impact the efficiency of the catalyst.[34,42] When Au alloys with Rh, tuning the Au and Rh composition, Au_4Rh_1NZ and Au_1Rh_2NZ exhibit different Rh exposures of NP surfaces (**Figure 2.2**, **Figure S 2.8**, **Experimental Section**), which results in a diversity of active sites, and thus different catalytic performances. Additionally, electronic effects also impact the catalytic $B_2(OH)_4$ hydrolysis as indicated by the XPS data (**Figure 2.3**) involving Au and Rh in the alloyed Au_4Rh_1 NZs that exhibit an upshift of binding energy compared to the monometallic Au and Rh NZs.[42]

Table 2.1 TOF values of Au-Rh NZ catalysts with various molar ratios under dark and light conditions at 25 ±1 ºC unless noted otherwise.

catalyst	Au_1Rh_0	Au_6Rh_1	Au_4Rh_1	Au_2Rh_1	Au_1Rh_2	Au_1Rh_2 28±1˚C	Au_0Rh_1
Time(s)-dark	248±5	63±2	52±2	91±2	185±2	153±2	385±8
TOF_t-dark	410±30	1200±80	1800±180	820±40	530±20	600±40	132±4
TOF_s-dark	1500±100	3700±300	5100±400	3200±300	1900±300	2000±300	570±70
Time (s)-light	237±5	52±2	39±2	69±2	131±2	-	379±8
TOF_t-light	410±40	1300±150	2100±400	1100±100	735±50	-	134±4
TOF_s-light	1500±500	4000±300	6000±400	4300±300	2600±500	-	580±70
R_{atom}(nm)	0.135	0.135	0.135	0.135	0.135	-	0.135
R_L/R_D	1.0	1.1	1.2	1.3	1.4		1.0
Size(nm)	2.0±0.4	1.7±0.2	1.5±0.4	2.1 ±0.5	1.9±0.2	-	2.3+0.2

$TOF_t = mol_{H_2\ produced} / [mol_{catt} \times$ reaction time (min)], where mol_{catt} is the mole of the total atoms of the catalyst, calculated at 10% conversion of $B_2(OH)_4$ hydrolysis.

$TOF_s = mol_{H_2\ produced} / [mol_{cats} \times$ reaction time], where mol_{cats} the turnover mole of the surface atoms of the catalyst, calculated at 10% conversion of $B_2(OH)_4$ hydrolysis.

The unit of TOF_t and TOF_s is $mol_{H_2}\ mol_{cat}^{-1}\ min^{-1}$. R_{atom} is the radius of the atom. N_s and N are the numbers of surface atoms and total atoms of the catalyst, respectively. R_L/R_D is the light enhancement rate.

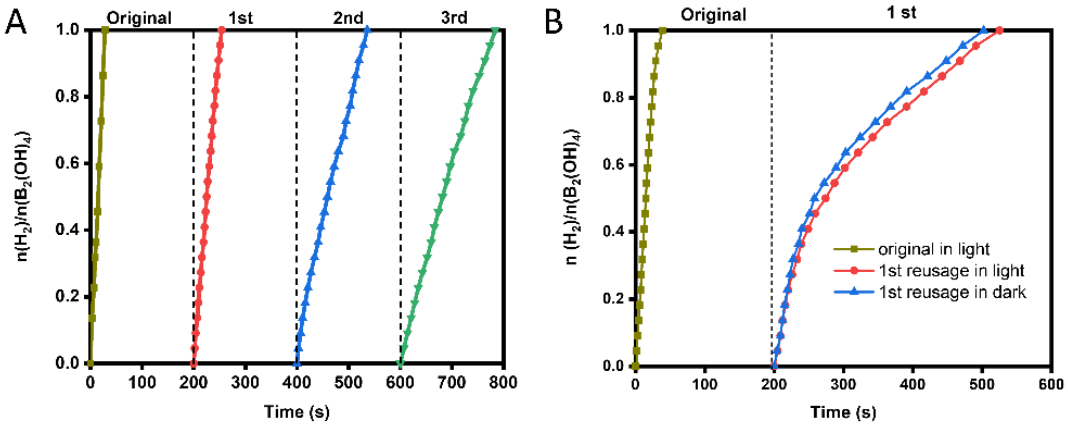

Figure 2.5. (A) Time plots of H_2 evolution for $B_2(OH)_4$ hydrolysis catalyzed by 1 mol % Au_4Rh_1NZ in the original, and 1st, 2nd and 3rd recycling tests in dark. (B) Time plots of H_2 evolution from $B_2(OH)_4$ hydrolysis catalyzed by 0.1 mol % Au_4Rh_1NZs under light (original) including 1st recycling under light and dark conditions. After photocatalysis, reused Au_4Rh_1NZs shows a TOF in dark or light of 1300 ± 200 $mol_{H_2}\ mol_{cat}^{-1}\ min^{-1}$)

2.3.3. Photocatalytic $B_2(OH)_4$ hydrolysis by the Au-Rh NZs

In order to explore the photocatalytic activity of the Au-Rh NZs, a low-power white-light LED was used to irradiate the reaction medium. Such a low-intensity light should avoid the participation of a significant photothermal effect (*vide infra*). As shown in **Figure 2.6** and **Figure S 2.16** (**Experimental Section**), the alloyed Au-Rh NZ clearly exhibits light-accelerated H_2 production, whereas the catalytic activities of the monometallic Au NZ and Rh NZ do not show any observable light-induced enhancement (**Figure S 2.19**, **Experimental Section**). Besides, the Au_4Rh_1 NZ possess the highest TOF_s value in both dark and light conditions, as a result of the cumulative effect of synergy in the dark and light-induced enhancement. In order to further investigate the efficiency of light irradiation, the light-enhancement rate (R_L / R_D) is introduced here, defined by simply dividing the TOF_s value of the catalyst under visible light (R_L) by that enhancement. The R_L / R_D value is 1.2 for the most effective nanocatalyst, Au_4Rh_1 NZ. Under dark conditions (R_D).[43]

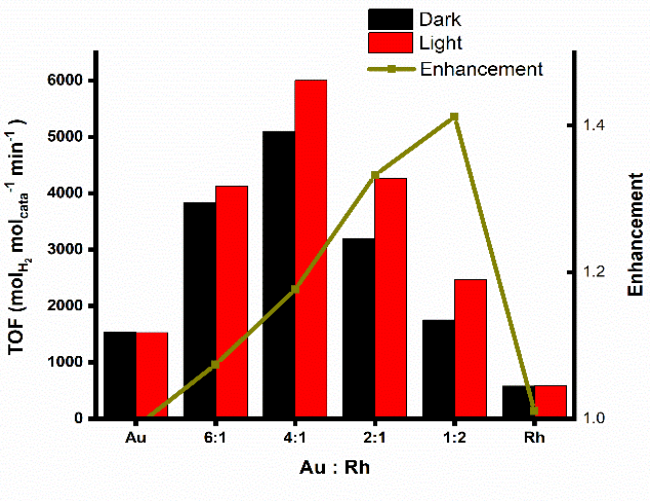

Figure 2.6. TOF_s value and enhancement rate (R_L/R_D) of $B_2(OH)_4$ hydrolysis photocatalyzed by 0.1 mol % Au-Rh NPs with various Au/Rh molar ratios at 25± 1˚C.

Many efforts have been devoted to the explanations of the photocatalysis mechanisms in the literature. For plasmonic metal NPs of Au and Ag, the surface plasmon resonance (SPR) effect is supposed to be the main factor responsible for the photocatalytic activity.[22, 24-26] Besides, it has been suggested that the photothermal effect is also involved in the light enhancement.[44] As the Au_1Rh_2 NZ exhibited the highest light-induced enhancement (**Figure 2.6** and **Table 2.1**), it was selected for photocatalytic investigations. In order to search any photothermal effect, the temperature of the Au_1Rh_2 NZ catalyst was monitored during the light irradiation period. Specifically, the temperature change was recorded by a thermometer that was inserted in a sealed vial containing 4 ml catalyst under light illumination. The results (**Figure S 2.17B**, **Experimental Section**) indicate that there is only 1.6 ^{o}C temperature increase during 10 minutes of visible-light illumination, which shows only modest heat generation under such light irradiation under these conditions. Aiming at this clarification, the catalytic reaction was carried out, when the reaction vial was covered by tin foil, but still exposed to light illumination. In this case, the catalytic system was still influenced by the light-induced heating, but there was no visible-light available for SPR-related acceleration. The results shown in **Figure S 2.18A** (**Experimental Section**) reveal that there is no significant catalytic efficiency variation between dark and tin foil-covered situations. Although there is heat release under light irradiation, the heating scale is negligible, because the catalytic reaction finishes within 3 min for Au_1Rh_2 NZs, which can only cause ~0.5˚C temperature increase under this light irradiation (**Figure S 2.17B**, **Experimental Section**). The time plot in **Figure S 2.16D** (**Experimental Section**) shows that H_2 generation in dark at 28˚C is less efficient than that in

light at 25 ˚C. Besides, the temperature change of the catalytic reaction in light underwent almost the same route as that under dark conditions (**Figure S 2.18B**, **Experimental Section**). All these results reveal that the photothermal effect in only an extremely minor component, if any, of the reason for the light-induced acceleration.

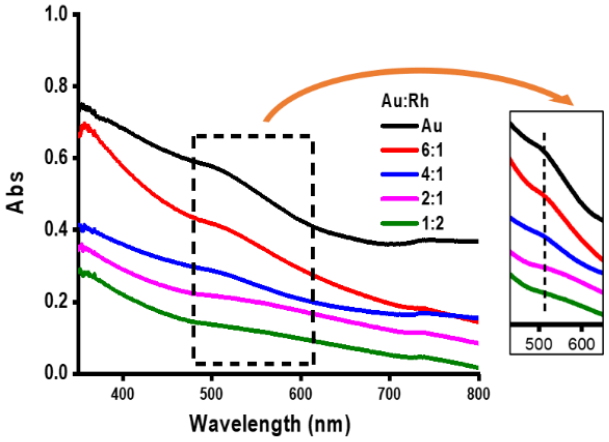

Figure 2.7. UV-vis. spectra of Au and Au-Rh NZs

On the other hand, the intrinsic plasmonic property of the prepared Au-Rh NPs is shown in **Figure 2.7**. Au NZ and Au-Rh NZ show a wide plasmon band around 500-540 nm, and the Au plasmonic absorption weakens as the percentage of Rh increases. This is ascribed to the shielding of the plasmon excitation of Au by Rh in the outer surface of the NP.[45,46] Previous studies have demonstrated that the integration of a plasmonic metal, such as Cu, Au, or Ag, and a catalytically active noble metal (e.g., Rh, Ru, Pd, or Pt) in a bimetallic system could be attributed to photocatalytic chemical transformations.[26] For instance, Ye et al reported a Rh-Au- $SrTiO_3$ photocatalyst for the synthesis of syngas using the CO_2 and H_2O under visible-light illumination.[47]

In the presence of light, the coherent electron oscillation of plasmonic Au nonradiative dephase results in the generation of hot electron carriers owing to the SPR effect.[24] Subsequently, giving a lower work function of Au (4.45 eV) than that of Rh (5.0 eV),[48] the active hot electrons resulting from the SPR of Au are driven to migrate to Rh sites. This equilibrates the Fermi level of a Au/Rh alloy within a few fs, causing an electron transfer from Au to Rh. The resulting enrichment of the Rh site favors oxidative addition cleavage of a water O-H bond that is involved in the rate-determining step (*vide infra*). Therefore, the catalytic efficiency of $B_2(OH)_4$ hydrolysis is enhanced under light illumination.[43] Besides, the recyclability of Au_1Rh_2 NZ after photocatalysis is investigated. As shown in **Figure 2.5B**, after photocatalysis, reused Au_4Rh_1NZs shows a TOF in dark and light of 1300 ± 200 $mol_{H_2}\,mol_{cat}^{-1}\,min^{-1}$). There is almost no light-induced enhancement after photocatalysis for Au_1Rh_2NZs, probably indicating an atomic rearrangement of Au and Rh in the alloy,[49] which need further investigation.

In order to verify the role of the SPR in photocatalysis, lights with wavelengths of 520 nm and 450 nm were employed to conduct catalytic $B_2(OH)_4$ hydrolysis. Photon fluxes at different wavelength are calculated here for the analysis of photons on photocatalysis.[50] The result shown in **Figure S 2.24** (**Experimental Section**) indicates that 520 nm, which is near the SPR peak of Au/Rh NZs, is more efficient than 450 nm irradiation as indicated by the TOF_s comparison. On the other hand, photon flux, calculated following a standard ferrioxalate actinometry,[51] reveals that 450 nm irradiation (2.92×10^{-9} einsteins.s^{-1}) possesses a higher photon flux than 520 nm (2.34×10^{-9} einsteins·s^{-1}). This result indicates that irradiation by more photons does not necessarily lead to an increased efficiency, because it is selectively the light

corresponding to the surface plasmon band of Au/Rh NZs that provides enhanced catalytic efficiency.[52]

In conclusion, Au_4Rh_1 NZ is the best nanocatalyst for this reaction both in the dark and under light illumination while Au_1Rh_2 NZs exhibit the highest light enhancement rate among a series of Au-Rh NZs. This result indicates the great significance of the metal proportions in an alloy and also demonstrates that Au is beneficial to this catalytic reaction in two cumulative ways: volcano-type synergy in dark and plasmonic effect under light illumination.

2.3.4. Kinetic study

In order to gain in-depth understanding of $B_2(OH)_4$ hydrolysis catalyzed by the Au-Rh NZs, the kinetics with Au_4Rh_1 NZ, the best catalyst in term of TOF_s, was investigated for catalytic H_2 generation under various catalysts, $B_2(OH)_4$ concentration and temperatures.

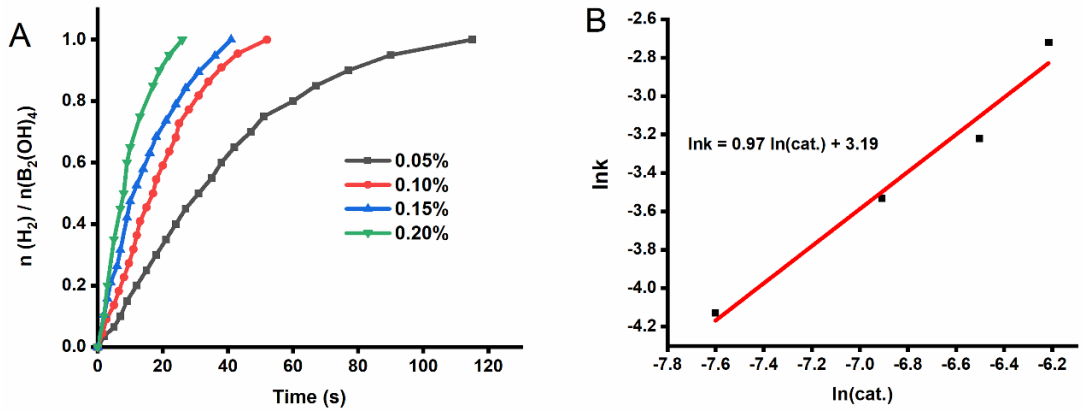

Figure 2.8. (A) Time plots of H_2 generation in the hydrolysis of $B_2(OH)_4$ catalyzed by various concentration of Au_4Rh_1 NZ catalyst in dark. (B) Plot of H_2 evolution rate vs. catalyst concentration ($R^2 = 0.96$).

Figure 2.8A shows the time plot of H_2 generation catalyzed by 0.05 mol %-0.2 mol % Au_4Rh_1 NZ at 25 ± 1 ºC. The hydrogen evolution exhibited a linear increase with respect to reaction time in the initial period. Based on

the slope of the fitted linear portions of the plots, all the reaction rate constants (*k*) were calculated, providing the plot of the logarithm of H_2 evolution vs. Au_4Rh_1 NZ concentration in **Figure 2.8B**. The slope of the logarithmic plot was 0.97, indicating that the $B_2(OH)_4$ hydrolysis reaction is first order with respect to the catalyst concentration.[10]

The time plot of H_2 evolution at different concentrations of $B_2(OH)_4$ is shown in **Figure 2.9A**. The slope of the logarithmic plot of H_2 evolution vs. $B_2(OH)_4$ amount in **Figure 2.9B** is 0.107, demonstrating that H_2 generation closely follows zero-order kinetics in $B_2(OH)_4$ amount.

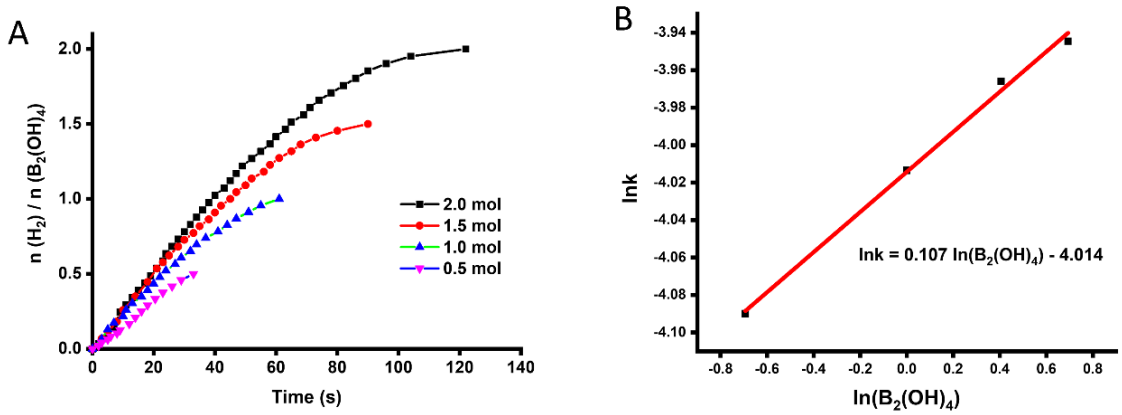

Figure 2.9. (A) Time plots of H_2 generation catalyzed by 0.1 mol % Au_4Rh_1 NZs with various $B_2(OH)_4$ amounts in the dark. (B) Plot of H_2 evolution rate vs. $B_2(OH)_4$ amount ($R^2 = 0.99$).

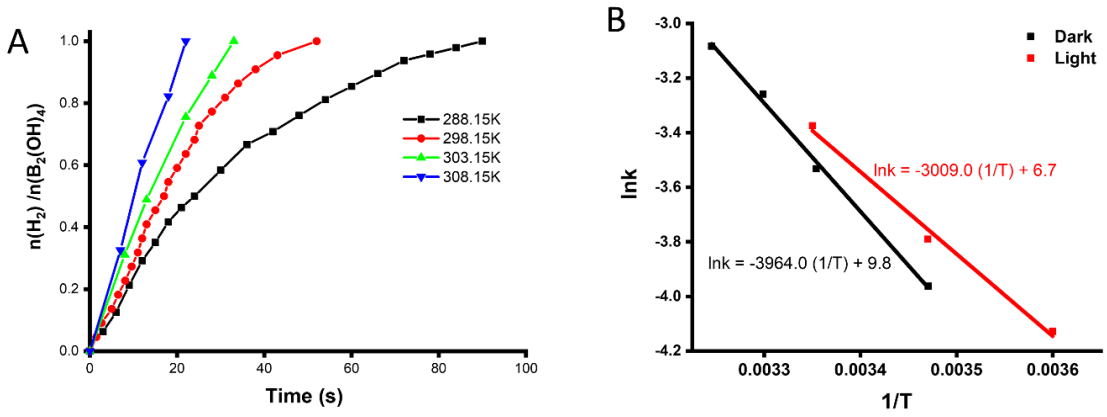

Figure 2.10. (A) Time plots of H_2 generation in the hydrolysis of $B_2(OH)_4$ catalyzed by 0.1 mol % Au_4Rh_1 NZs at various temperatures in the dark. (B) Arrhenius plots in the dark (R^2 = 0.99) and light (R^2 = 0.98) according to H_2 generation vs. time at different temperatures.

The time dependence of H_2 evolution catalyzed by 0.1 mol % Au_4Rh_1 NZ at different temperatures is illustrated in **Figure 2.10A**. As the reaction rate constant *k* is related to the activation energy (E_a) by the Arrhenius Equation,[33] the Arrhenius plots of ln *k* vs. 1/T (**Figure 2.10B**) is depicted in accordance with the fitted linear parts of the plots in **Figure 2.10A**. The activation energy (E_a) is calculated to be 32.9 ± 1.4 kJ/mol in the dark and 25.0 ± 2.0 kJ/mol with visible light irradiation according to the Arrhenius equation (**Equation S 2.1**, **Experimental Section**). The reduced activation energy in light illumination may also be an indicator of the SPR-induced catalytic enhancement of H_2 evolution.

2.3.5. Mechanistic study

In order to confirm the hydrogen source of the produced H_2 gas, D_2O was used instead of H_2O as solvent in the hydrolysis of $B_2(OH)_4$ catalyzed by

Au_4Rh_1. As shown in **Figure 2.11**, the catalysis in mixture dissolved in D_2O exhibits a lower slope in the time plot of H_2 generation, exhibiting a k_H/k_D value of 2.52 in dark. This result indicates a kinetic isotope effect (KIE)[11] showing that the cleavage of an O-H bond in water is involved in the rate-determining step of the $B_2(OH)_4$ hydrolysis process. The low KIE value is the result of a concerted process involving the O-H oxidative addition. Besides, the k_H/k_D value obtained upon light irradiation is 2.94 (**Figure 2.11**), higher than that in dark, which shows the increased role of O-H oxidative addition in the rate-limiting step compared to that upon reaction in the dark. This is in agreement with the electronic enrichment of the Rh site facilitating this O-H oxidative addition step.

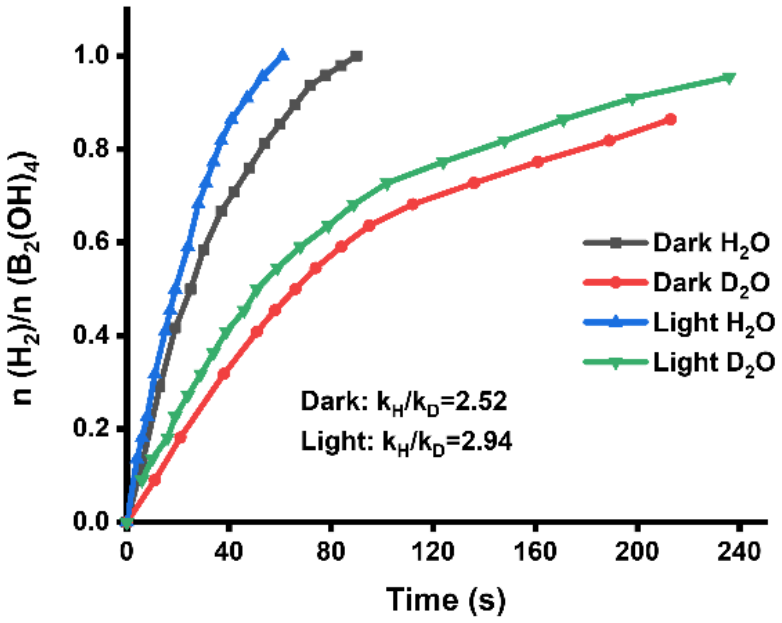

Figure 2.11. Time plot of hydrogen evolution catalyzed by 0.1 mol % Au_4Rh_1NPs in H_2O and D_2O in dark and light at 15 ±1˚C.

Successive reactions, in which the hydrolysis of $B_2(OH)_4$ and the hydrogenation of styrene utilizing the H_2 gas produced in the former step,

were conducted in the same system. These experiments were then carried out in order to investigate the fate of the deuterium atoms. D_2 gas evolution occurred upon hydrolysis of $B_2(OH)_4$ catalyzed by Au_4Rh_1 NZ in D_2O in the left tube, meanwhile this gas was directed to the right tube to initiate the hydrogenation of styrene in CD_3OD in the presence of commercial Pd/C at room temperature (**Figure S 2.21**, **Experimental Section**). Hydrogenation of styrene occurs in methanol, while the nanocatalyst was in aqueous solution. The solid heterogeneous Pd/C hydrogenation catalyst was employed in the right tube. The product in the right tube was collected 24 h later, for analysis by ^{1}H NMR spectroscopy and gas chromatography–mass spectrometry. In the ^{1}H NMR spectra (**Figure S 2.22**, **Experimental Section**), a cluster of peaks at 7.11-7.28 ppm with 5-H integration reflects the existence of aromatic H atoms. No signals appear at 5~7ppm, indicating 100% conversion of styrene to deuterated ethylbenzene. Compared to normal ethylbenzene, reduced integration values of the peaks at 2.6 and 1.22-1.17 ppm were observed, showing deuteration of ethylbenzene in the right tube. Besides, in the mass spectrum (**Figure S 2.23**, **Experimental Section**), there were three peaks at around 107, 108 and 109 m/z corresponding to substitution of one, two and three H atom by D atoms in deuterated ethylbenzene. The mass spectrum of deuterated ethylbenzene contains not only the peak corresponding to bis-deuterated ethylbenzene as expected, but also minor peaks corresponding to mono- and tris-deuterated ethylbenzene. The presence of these odd numbers of D atoms in the ethylbenzene product is due to the stability of the styryl radical intermediate Ph-CH·-CH_3 (or deuterated analogues) that can exchange H (or D) atoms with the Pd_n-H or Pd_n-D catalytic species, Pd_n-H species being formed by reaction of partly deuterated ethylbenzene with the Pd_n catalyst, and Pd-D by oxidative addition of D_2 on Pd_n (Experimental Section). The

formula found is Ph-$CH_{0.08}D_{1.92}$-$CH_{2.71}D_{0.29}$, in which the total number of D atoms in the deuterated ethylbenzene obtained is 2.2 ± 0.2 for 2 D expected. Between $B_2(OH)_4$ and D_2O, fast H/D exchange occurs between these two oxo-acids, but D_2O is in such a very large molar excess (450/1), so that the final proportion of H atoms in D_2 formed is negligeable.

All these results confirm those obtained by direct alkene hydrogenation[5] and verify that both hydrogen atoms of the produced hydrogen gas are originated from water. Accordingly, a mechanism of $B_2(OH)_4$ hydrolysis catalyzed by Au-Rh NZs is proposed here (**Figure 2.12**). In the first step of the catalytic cycle, $B_2(OH)_4$ is adsorbed onto the catalyst surface to give the intermediate I. Subsequently, the intermediate II is obtained following oxidative addition of the B-B bond onto the metal surface.[5,9] Owing to the electron-deficiency of the Lewis-acidic B-containing species, two H_2O molecules obviously act as Lewis base to coordinate two boron atoms giving the intermediate III. At this point, the oxidative addition of an O-H bond of H_2O is facilitated by the initial H_2O coordination to the boron atoms bringing these O-H bonds close to the catalyst surface. The result is the formation of the two NP-H bonds, as shown by the D_2O experiments, and the release of 2 $B(OH)_3$ whose formation was demonstrated earlier,[9] giving intermediate IV. Finally, the generated hydride-[M]-hydride intermediate IV produces H_2 upon reductive elimination.[53]

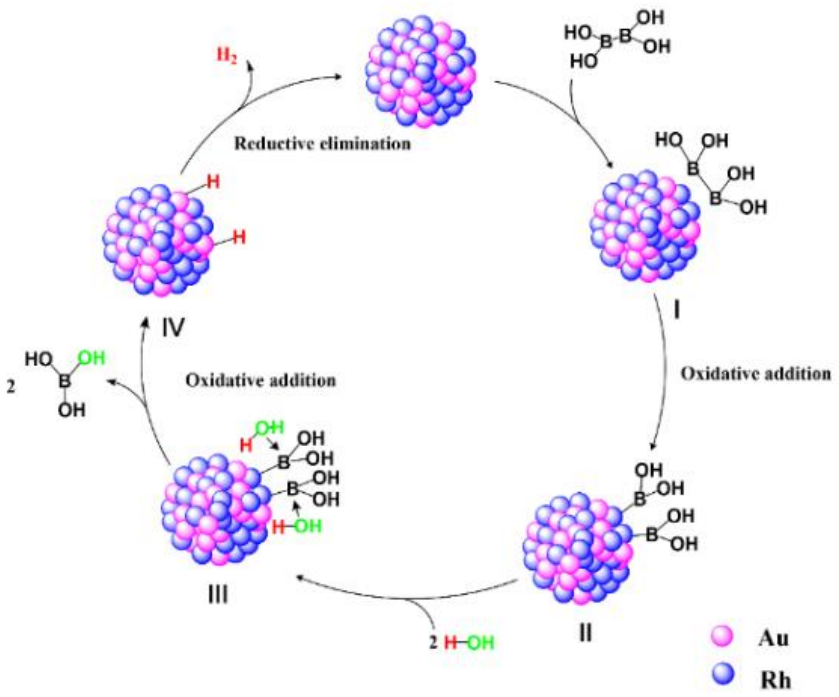

Figure 2.12. Schematic illustration of the confirmed mechanism of the $B_2(OH)_4$ dehydrogenation catalyzed by the nanozyme catalysts Au-RhNZ @click dendrimer.

As indicated in the introduction, there are similarities between this mechanism and that of hydrogenase including, first, the origin (water) of both atoms forming H_2. Then, mechanistically, in hydrogenase, two water protons are successively transferred to heteroatoms of the ligand bound to the metal site together with electrons, before their transfer to the metal site, followed by reductive elimination to yield H_2. Here, the metal site of the NZs is played by the bimetallic NP. The two water protons are transferred via the two boron species before subsequent transfer to the NP, which is also followed by reductive elimination like in the hydrogenase enzyme. These mechanistic features are in sharp contrast with those involved in borohydride or ammonia-borane hydrolysis, whereby first a hydride is transferred from the borane precursor followed by proton transfer from water in the second step. The

beneficial use of visible light for the NZs is compatible with the same $B_2(OH)_4$ hydrolysis mechanism, just clearly accelerating the last step, reductive elimination, by increasing the electron density on Rh through electronic donation upon transfer from the plasmonic metal, Au.

2.4. Conclusion

A series of alloyed Au-Rh NP catalysts supported and encapsulated by a "click" dendrimer (called nanozymes, NZs) were prepared, extensively characterized, then utilized for H_2 production upon $B_2(OH)_4$ hydrolysis and convenient hydrogenation reactions with produced H_2. These Au-Rh NZs with different molar ratios of the two metals in the alloys were shown to exhibit different catalytic efficiencies, the optimized composition being Au_4Rh_1 with sharp volcano-type synergies of 3.4-fold and 8.9-fold increased TOF_s compared to the monometallic Au and Rh NZs, respectively. The plasmonic Au-Rh NZs also exhibit remarkable additional enhancement of catalytic activity under visible-light illumination provoking what appears to be hot electron injection from plasmonic Au to Rh-adsorbed substrates at the nearby Rh atom and giving the highest light enhancement rate of 1.4 for Au_1Rh_2 NZ. Although the synergistic sharp volcano-type enhancement in the dark and light-induced enhancements show their maxima for distinct proportions of the two metals in the alloy, the two effects are cumulative, and the maximum combined enhancement effect is obtained for the Au_4Rh_1 NZ. In the alloy, Au plays both roles of most efficient partner in the synergistic volcano-type effect and source of plasmonic charge transfer, which explains why the percentage of the part of Au atoms among the two metals is much larger than the Rh part in the optimized catalyst, Au_4Rh_1 NZ. Kinetic and

isotopic studies along with successive reactions confirm the mechanism of $B_2(OH)_4$ hydrolysis, indicating that both hydrogen atoms of formed H_2 are coming from water (contrary to ammonia borane), like with hydrogenase. This work illustrates a rational design of the function of plasmonic metal in light-accelerated bimetallic photo-catalysis and a facile strategy for H_2 (or D_2) evolution from H_2O (resp. D_2O) based on $B_2(OH)_4$ hydrolysis together with application of H_2 (resp. D_2) formed.

2.5. Experimental Section

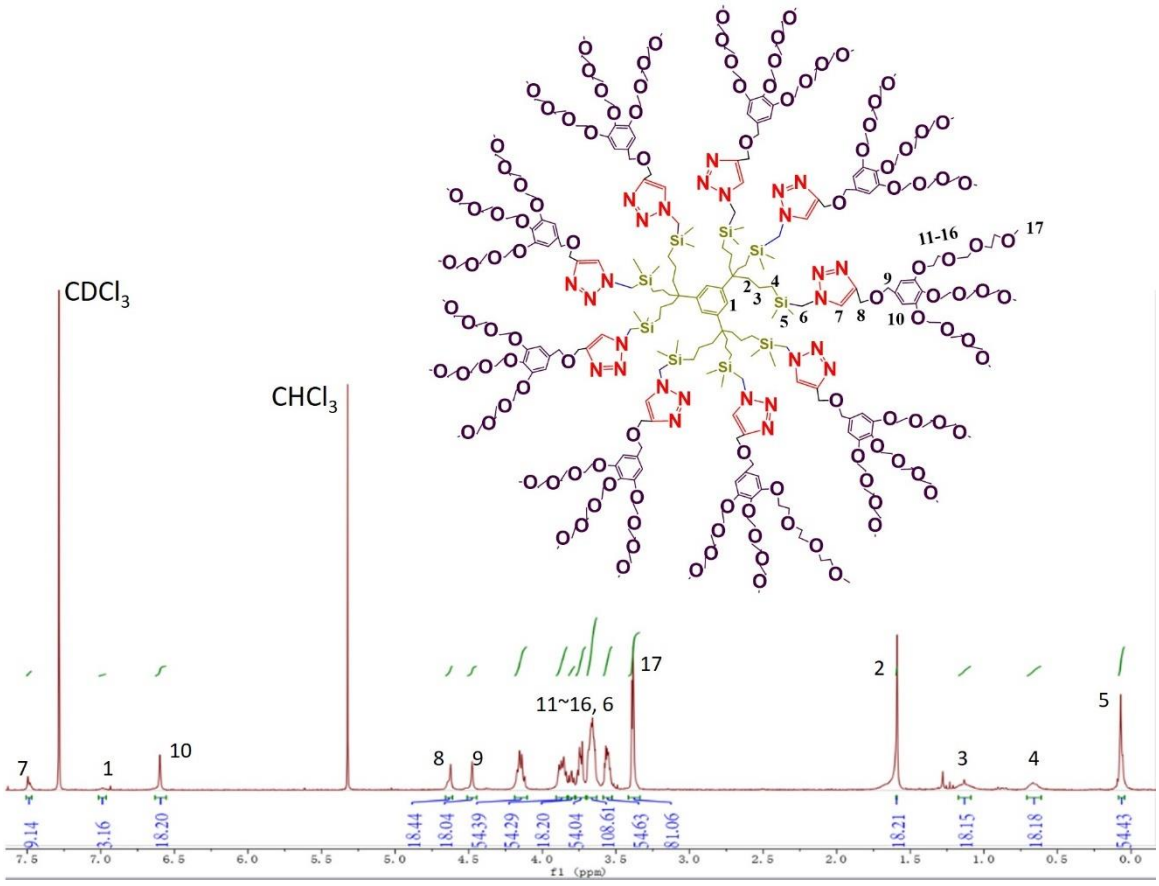

Figure S 2.1. ^{1}H NMR spectrum of the triazole-containing dendrimer in $CDCl_3$. ppm: 7.51 (CH-triazole), 6.99 (CH-arom. intern), 6.60 (CH-arom. extern), 4.63 (triazole-CH2-O), 4.48 (O-CH_2-arom. extern), 3.85-4.15 (CH_2CH_2O-arom. extern), 3.80 (Si-CH_2-triazole), 3.53-3.77 (OCH_2CH_2O), 3.37-3.40 (CH_3O), 1.70 ($CH_2CH_2CH_2Si$), 1.13 ($CH_2CH_2CH_2Si$), 0.66 ($CH_2CH_2CH_2Si$), 0.07 ($Si(CH_3)_2$).

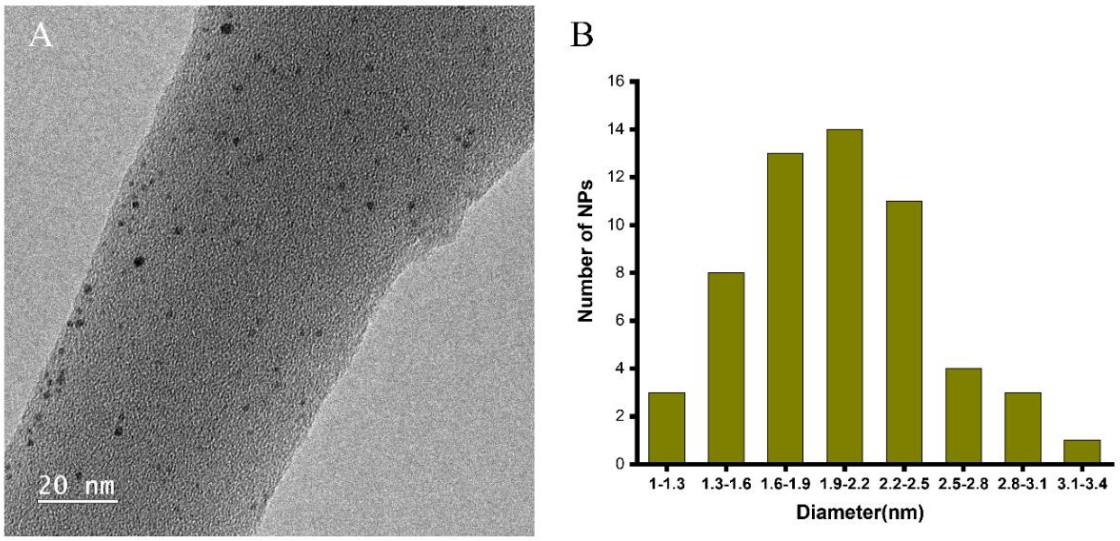

Figure S 2.2. TEM images (A) and size distribution (B) of Au NZs

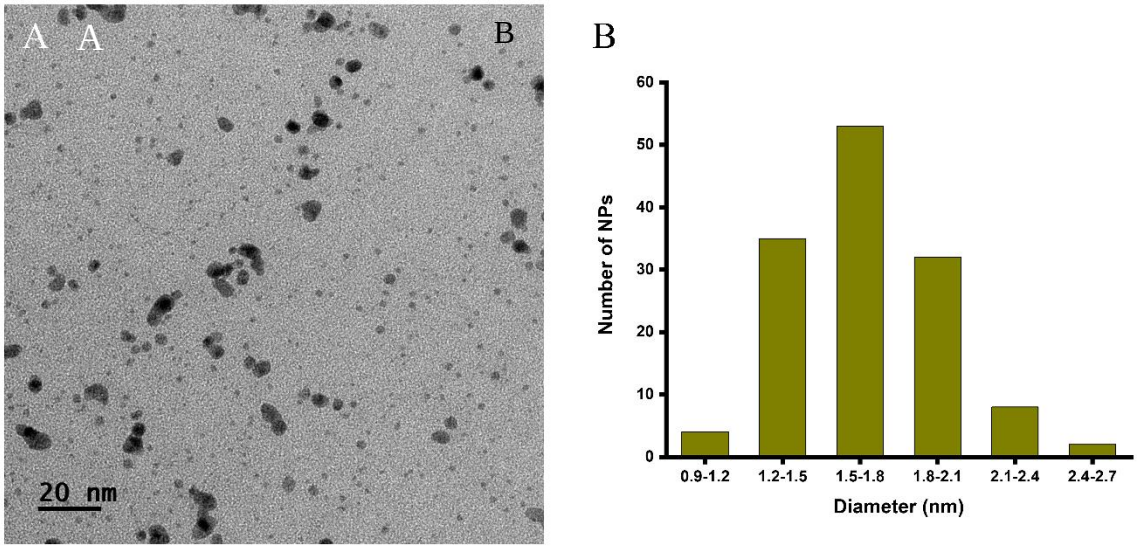

Figure S 2.3. TEM images (A) and size distribution (B) of Au_6Rh_1 NZs

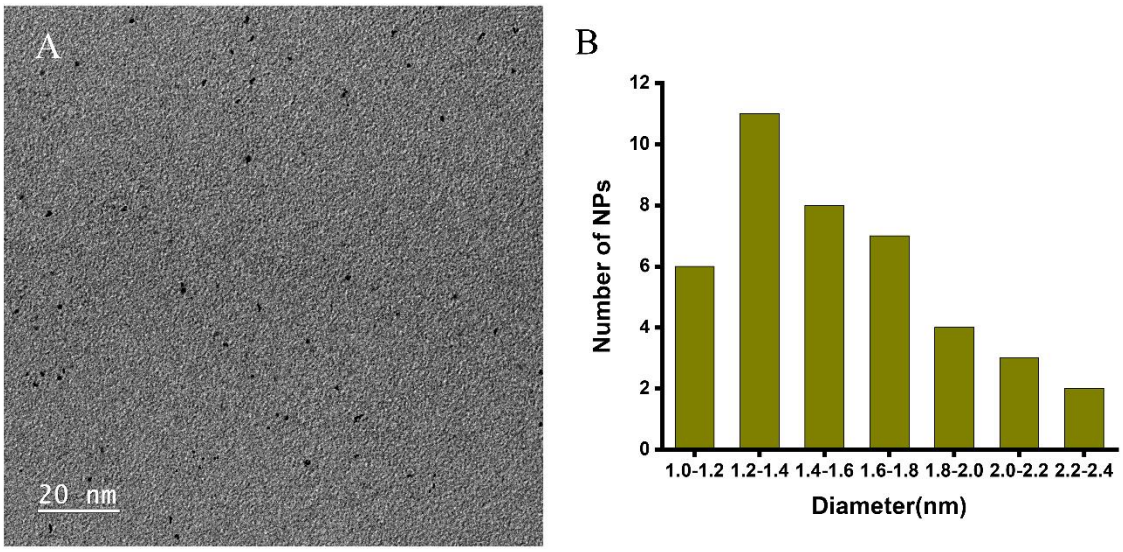

Figure S 2.4. TEM images (A) and size distribution (B) of Au_4Rh_1 NZs

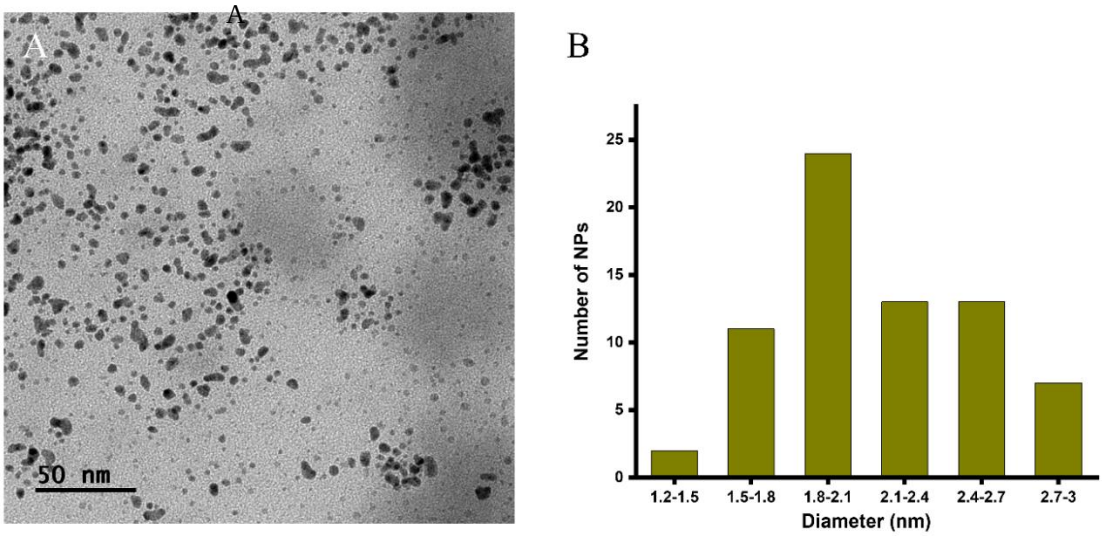

Figure S 2.5. TEM images (A) and size distribution (B) of Au_2Rh_1 NZs

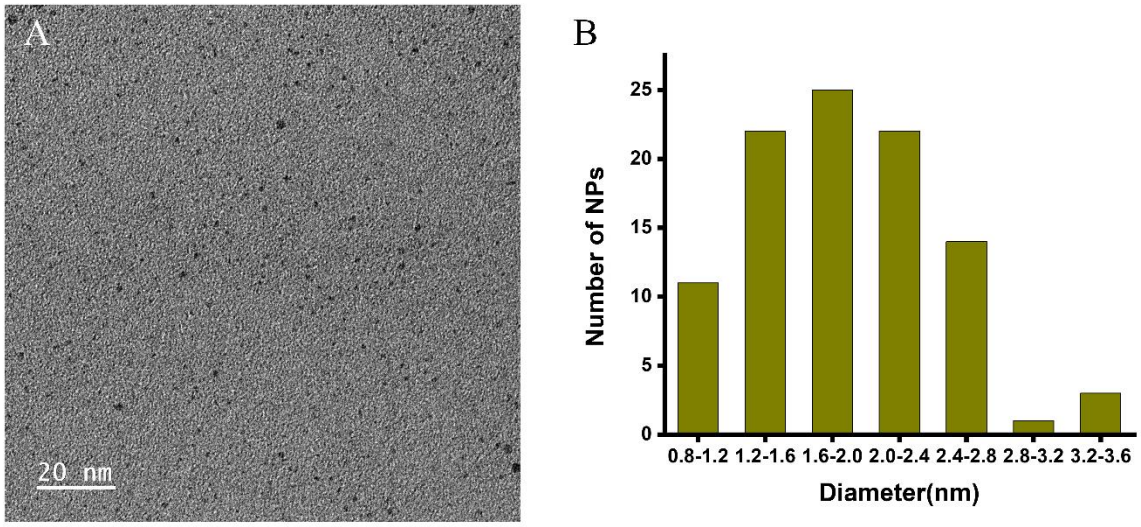

Figure S 2.6. TEM images (A) and size distribution (B) of Au_1Rh_2 NZs

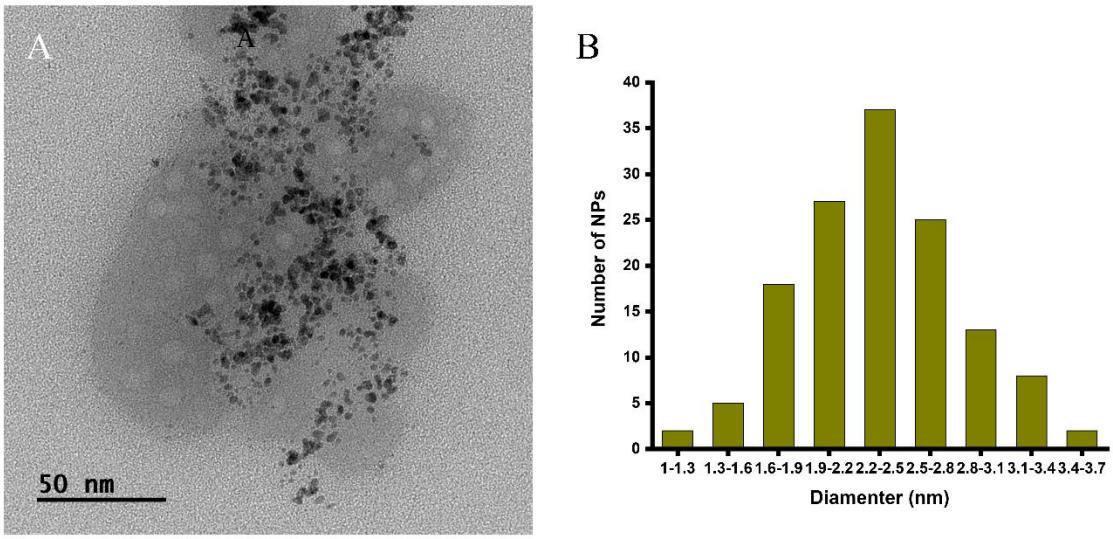

Figure S 2.7. TEM images (A) and size distribution (B) of RhNZs

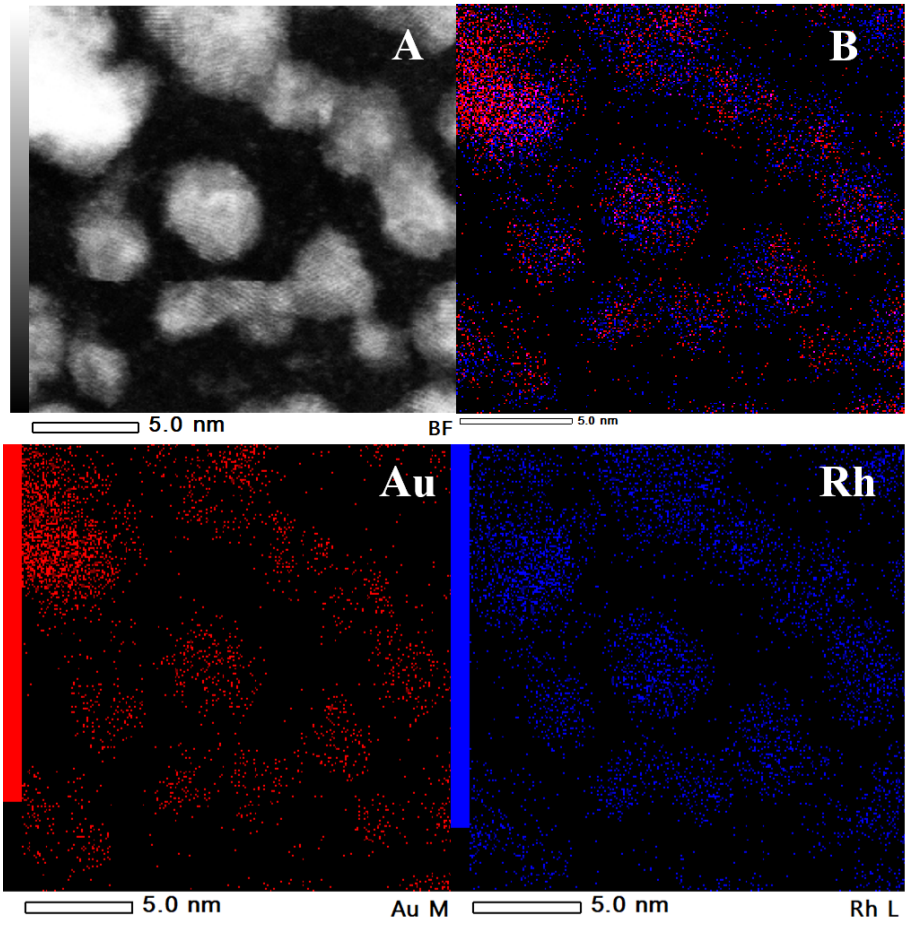

Figure S 2.8. HRTEM image (A), EDX elemental mapping images of the overlapped Au and Rh in Au_1Rh_2 NZs (B) and Au mapping (Au) and Rh mapping (Rh)

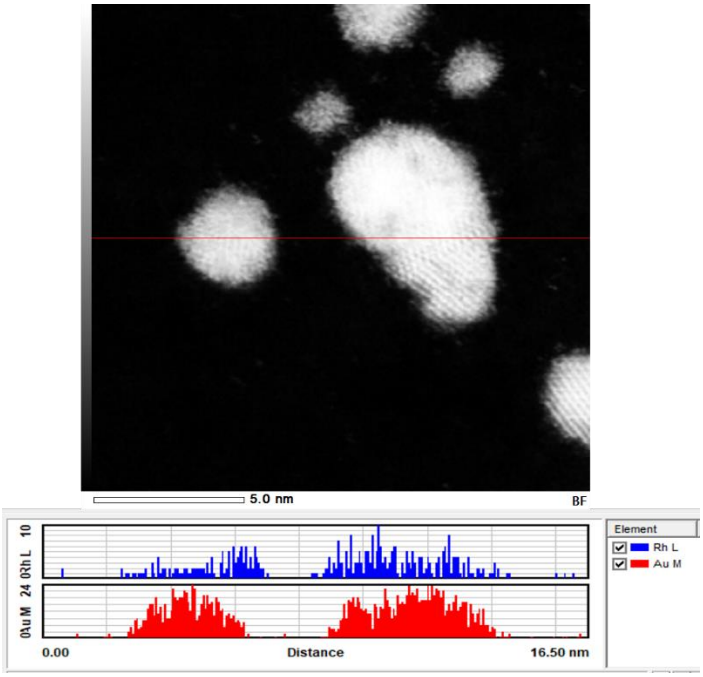

Figure S 2.9. Distribution of Au and Rh along cross-section line for Au_4Rh_1 NZs

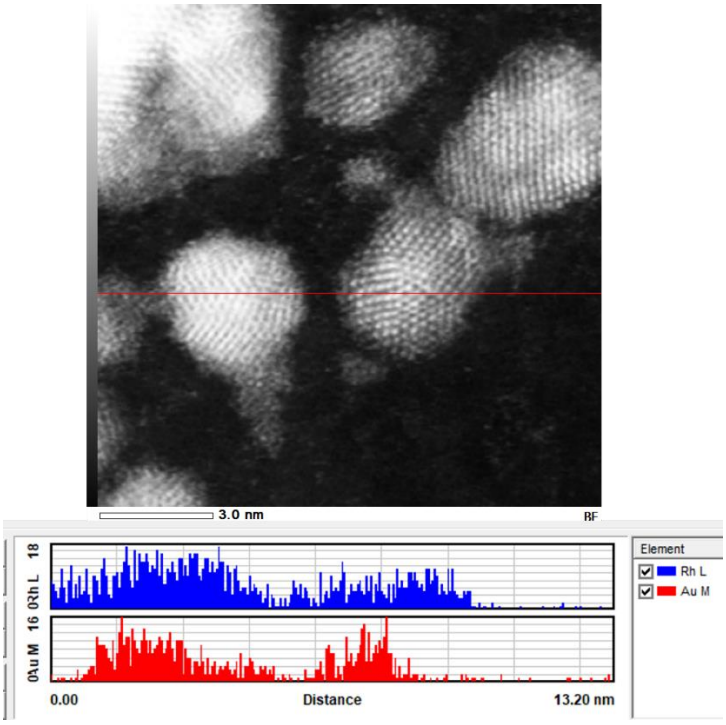

Figure S 2.10. Distribution of Au and Rh along cross-section line for Au_1Rh_2 NZs

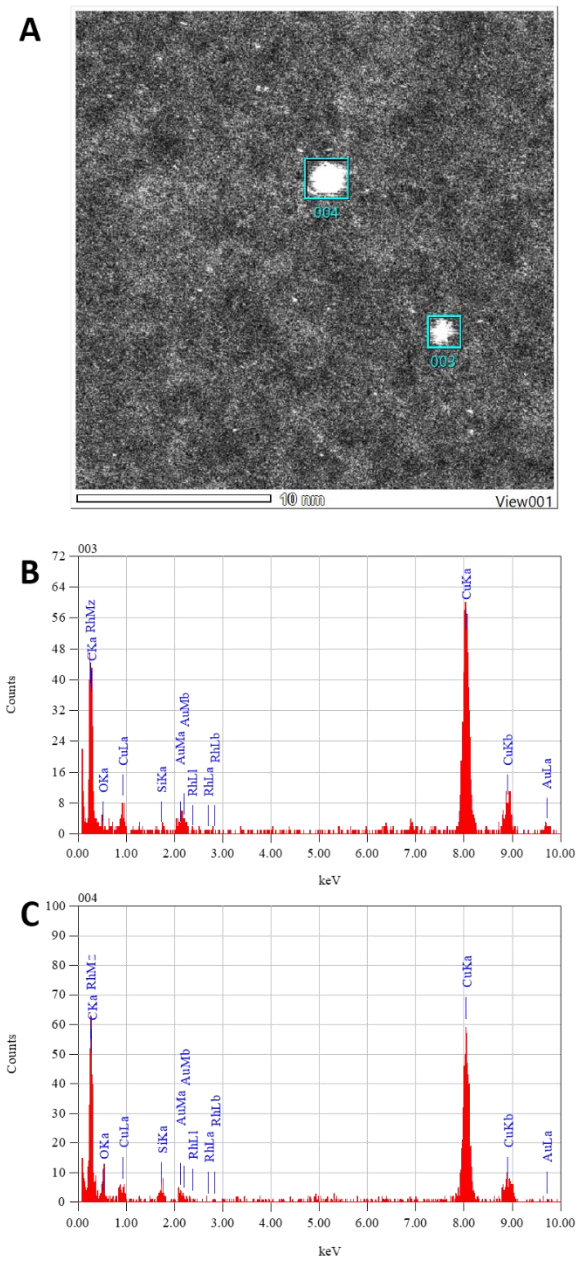

Figure S 2.11. HRTEM-EDX image of Au_4Rh_1 NZs (A), element distribution of 003 area (B) and 004 area (C).

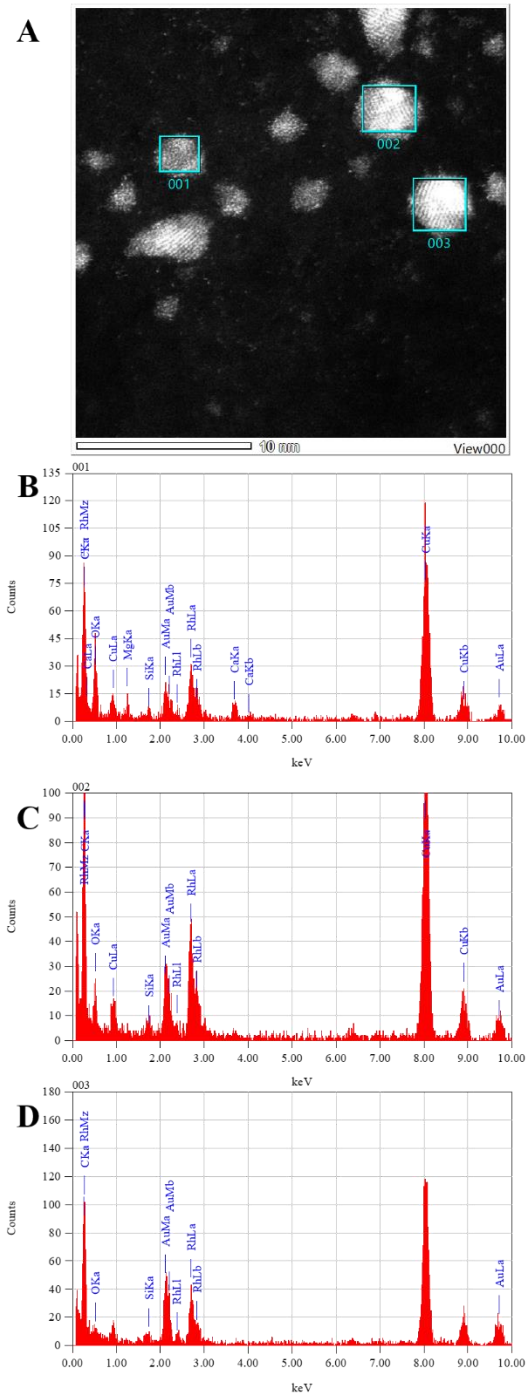

Figure S 2.12. HRTEM-EDX image of Au_1Rh_2 NZs (A), element distribution of 001 area (B), 002 area (C) and 003

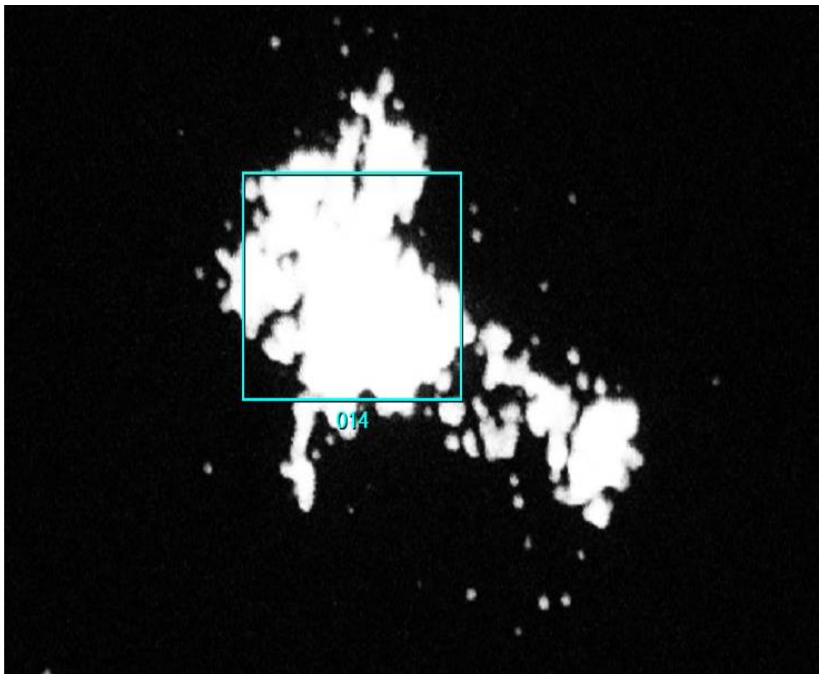

Thin Film Standardless Standardless Quantitative Analysis

Fitting Coefficient: 0.0734

Element	(keV)	Mass%	Counts	Sigma	Atom%	Compound	Mass%	Cation	K
C K*	(Excluded)		ND			ND			
O K*	(Excluded)		ND			ND			
Si K*	(Excluded)		ND			ND			
Cu K*	(Excluded)		ND			ND			
Rh L		2.696	13.04	1132.21	0.59	22.29			0.9805
Au M	(Ref.)	2.120	86.96	7406.10	1.57	77.71			1.0000
Total			100.00			100.00			

Figure S 2.13. Element analysis of the selected area 014 by EDS of Au_4Rh_1NZs

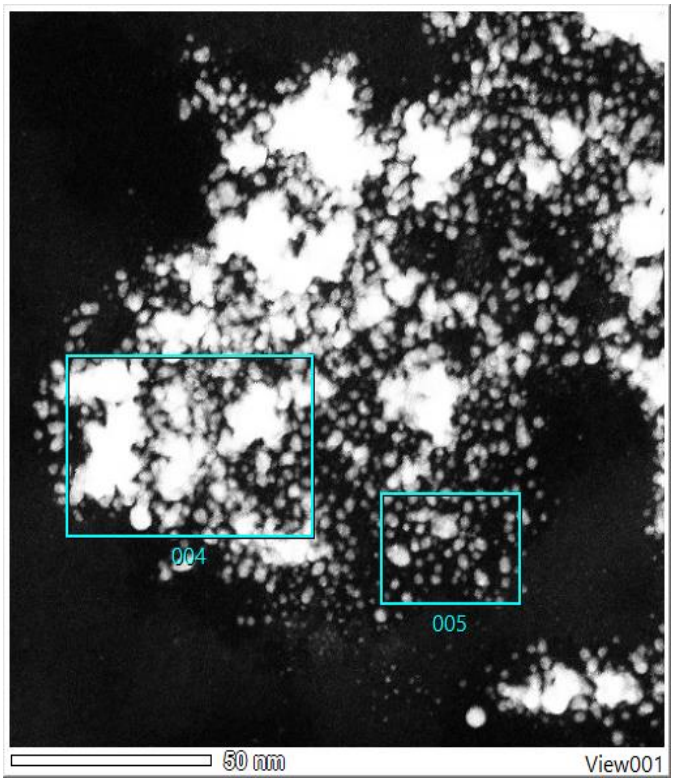

Thin Film Standardless Standardless Quantitative Analysis

Fitting Coefficient : 0.1083

Element	(keV)	Mass%	Counts	Sigma	Atom%	Compound	Mass%	Cation	K
C K*	(Excluded)		ND			ND			
N K*	(Excluded)		ND			ND			
O K*	(Excluded)		ND			ND			
Si K*	(Excluded)		ND			ND			
Cu K*	(Excluded)		ND			ND			
Rh L		2.696	44.90	1238.20	1.85	60.94			0.9805
Au M	(Ref.)	2.120	55.10	1489.62	2.25	39.06			1.0000
Total			100.00			100.00			

Figure S 2.14. Element analysis of the selected area 004 by EDS of Au_1Rh_2NZs

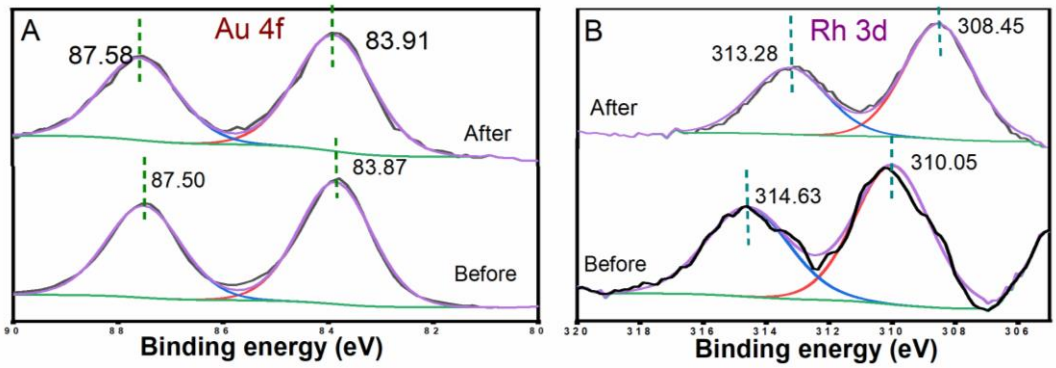

Figure S 2.15. XPS patterns of the Au 4f (A) and Rh 3d (B) for Au_1Rh_2NZs before catalysis and after photocatalysis.

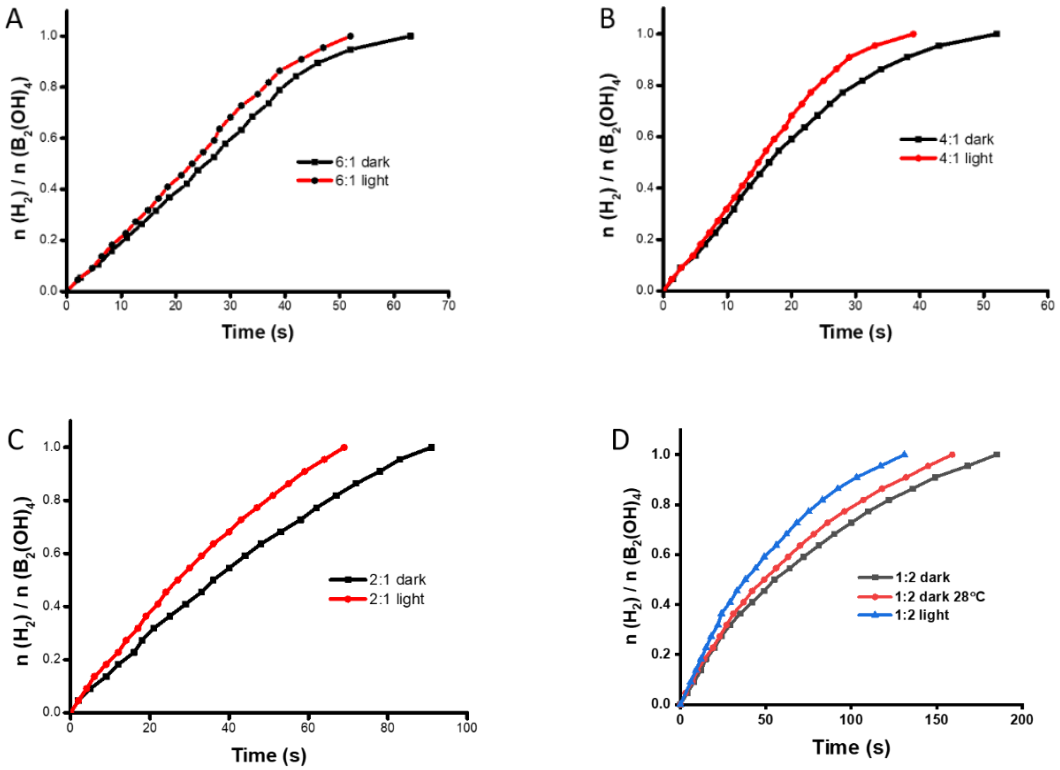

Figure S 2.16. Time plots of H_2 generation in the hydrolysis of $B_2(OH)_4$ catalyzed by 0.1mol % Au_6Rh_1 (A), Au_4Rh_1(B), Au_2Rh_1 (C) in dark and light at 25±1˚C. The time plot of H_2 generation in the hydrolysis of $B_2(OH)_4$ catalyzed by Au_1Rh_2 in dark and light at 25±1˚C and in dark at 28 ± 1 °C. (D)

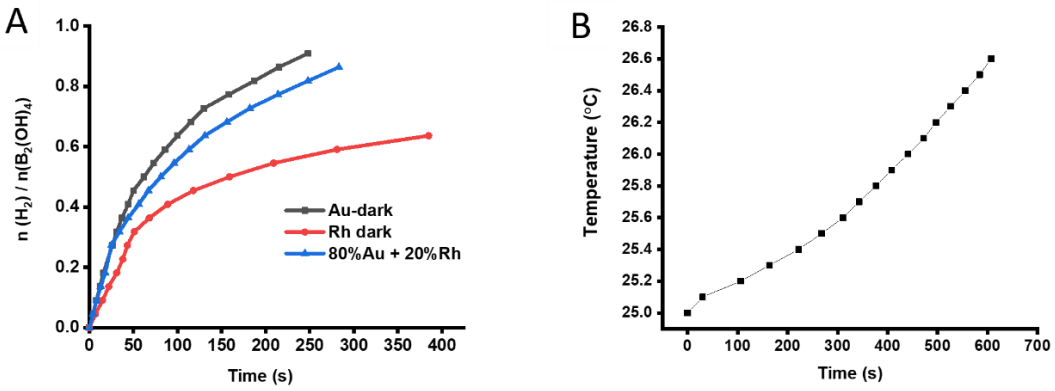

Figure S 2.17. (A) Time plots of hydrogen generation without catalyst and catalyzed by AuNZs, RhNZs, the mixture of 80%AuNZs and 20% RhNZs in dark. (B) Temperature increases of the catalyst under visible-light illumination.

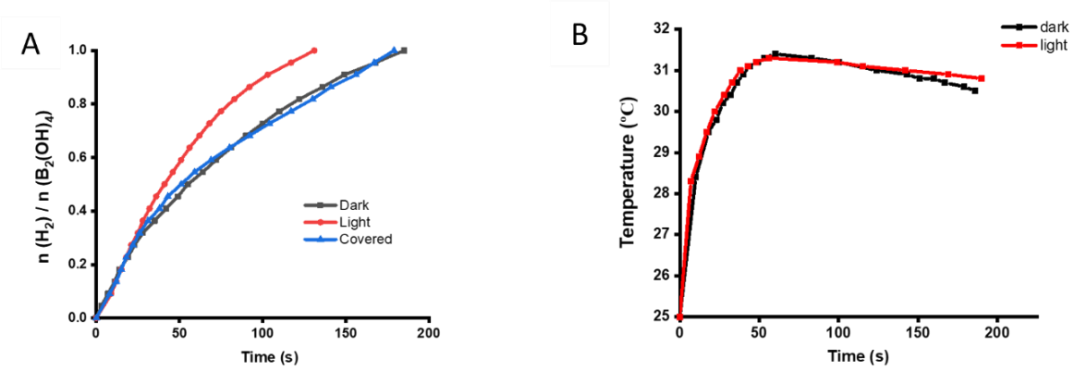

Figure S 2.18. (A) Time plots of hydrogen generation catalyzed by Au_1Rh_2NZs in dark, in light and in a situation when the reaction system is covered by tin foil but still under light irradiation. (B) Temperature increase in the catalytic $B_2(OH)_4$ hydrolysis system catalyzed by Au_1Rh_2NZs under dark and visible-light illumination.

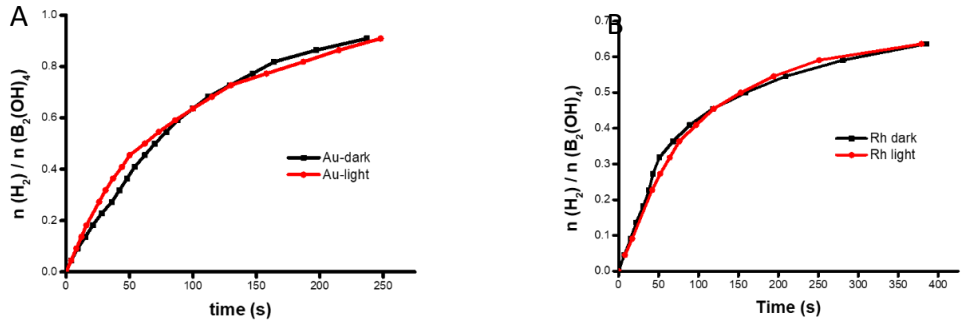

Figure S 2.19. Time plots of hydrogen generation catalyzed by Au (A) and Rh (B) under dark and light condition at 25± 1 °C

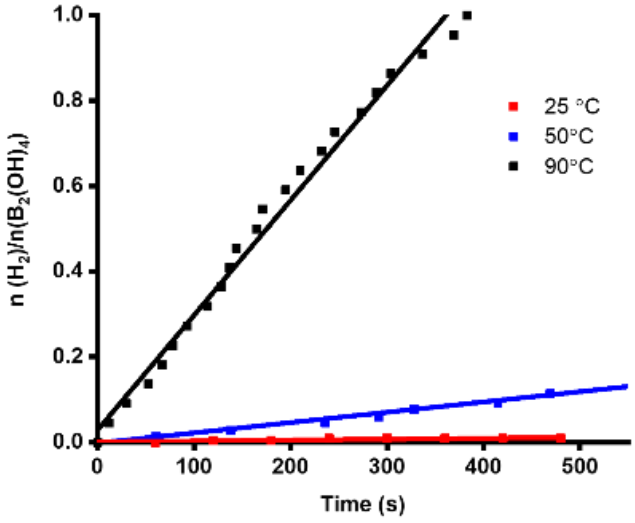

Figure S 2.20. Time plots of H_2 evolution from $B_2(OH)_4$ hydrolysis without catalyst at 25˚C, 50 ˚C and 90 ˚C.

Calculation of activation energy

The activation energy (E_a) was calculated using the Arrhenius equation:

$$\ln k = \ln A - \frac{E_a}{RT} \qquad \textbf{(S2.1)}$$

Where k is reaction rate, A is the pre-exponential factor, E_a is the activation energy, R is the universal gas constant, and T is the absolute temperature.

Calculation of TOF_t and TOF_s

$$\boldsymbol{TOF_t = \frac{n_{H_2}}{n_{cat_t} \cdot time}} \quad \textbf{(S2.2)}$$

$$\boldsymbol{TOF_s = \frac{n_{H_2}}{n_{cat_s} \cdot time}} \quad \textbf{(S2.3)}$$

Where, TOF_t is the turnover frequency of the total atoms. TOF_s is the turnover frequency of the surface atoms. $\boldsymbol{n_{H_2}}$ is mole of produced H_2. Time is reaction time (min). $\boldsymbol{n_{cat_t}}$ is mole of total atoms. $\boldsymbol{n_{cat_s}}$ is mole of surface atoms.

When number of surface atoms $\boldsymbol{N_s}$ and the number of total atoms $\boldsymbol{N_t}$ is introduced here,

$$\boldsymbol{\frac{n_{cat_s}}{n_{cat_t}} = \frac{N_s}{N_t}} \quad \textbf{(S2.4)}$$

On the other hand,

$$\boldsymbol{N_t = \frac{\frac{4}{3}\pi {R_{NP}}^3}{\frac{4}{3}\pi {R_{atom}}^3}} \quad \textbf{(S2.5)}$$

$$\boldsymbol{N_s = \frac{4\pi {R_{NP}}^2}{\pi {R_{atom}}^2}} \quad \textbf{(S2.6)}$$

Where $\boldsymbol{R_{atom}}$ is the radius of metal atom, $\boldsymbol{R_{NP}}$ is the radius of nanoparticles. Thus,

$$\boldsymbol{TOF_s = \frac{TOF_t \cdot R_{NP}}{4R_{atom}}} \quad \textbf{(S2.7)}$$

Successive reactions

The successive reactions were conducted in a sealed system as shown in **Figure S 2.21.** Successive reaction of B2(OH)$_4$ dehydrogenation in D2O and hydrogenation of styrene in CD3OD. The hydrolysis of $B_2(OH)_4$ and the hydrogenation of styrene in a sealed system constituted the successive reaction.

The hydrolysis of $B_2(OH)_4$ catalyzed by Au_4Rh_1 NZs was conducted in D_2O in the left flask. The produced hydrogen gas was then transported to the right flask vis the connected rubber tube to initiate the hydrogenation of styrene.

In the right flask, the commercial Pd/C catalyst (10 mmol% per styrene) was applied to catalyze the hydrogenation of styrene (0.5 mmol) in CD_3OD at 25ºC for 12h. When the reaction was finished, the resulting compound in the right tube was collected and centrifugated for ^{1}H NMR and GC-MS analysis (**Figure S 2.** and **Figure S 2.23**).

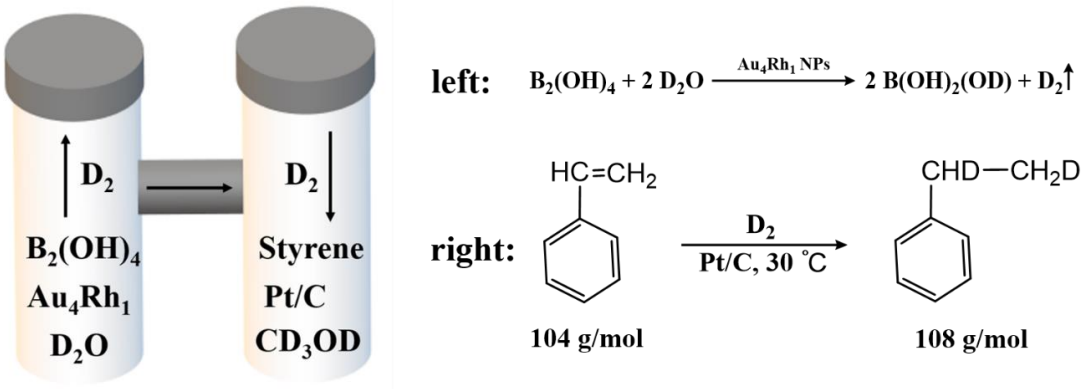

Figure S 2.21. Successive reaction of $B_2(OH)^4$ dehydrogenation in D_2O and hydrogenation of styrene in CD_3OD

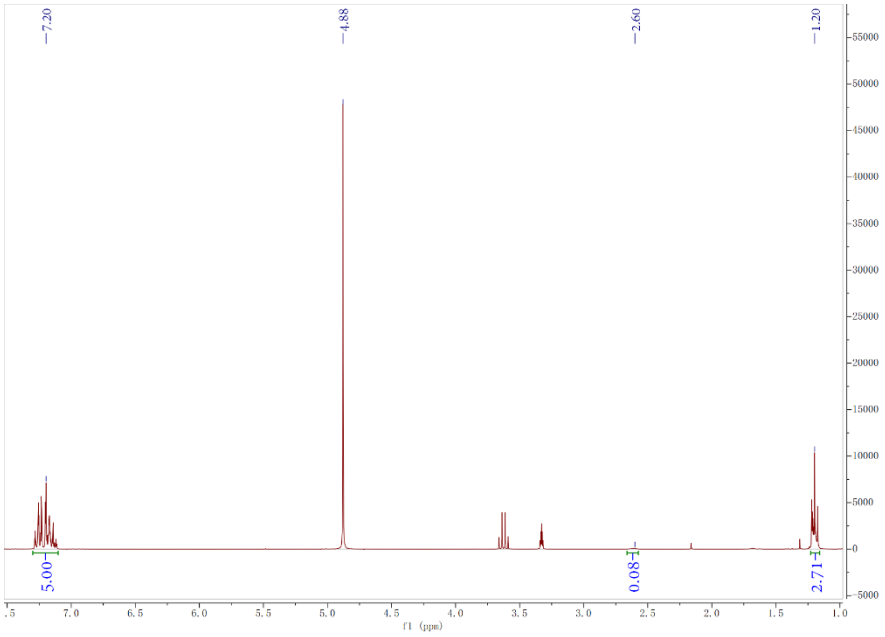

Figure S 2.22. ^{1}H NMR spectrum of ethylbenzene generated from the hydrogenation of styrene in successive reaction in CD_3OD. ^{1}H NMR (300MHz), δ 7.28-7.11 (aromatic H, 5H), 2.60 (-CH_2, 0.08H), 1.22-1.17 (-CH_3, 2.71H)

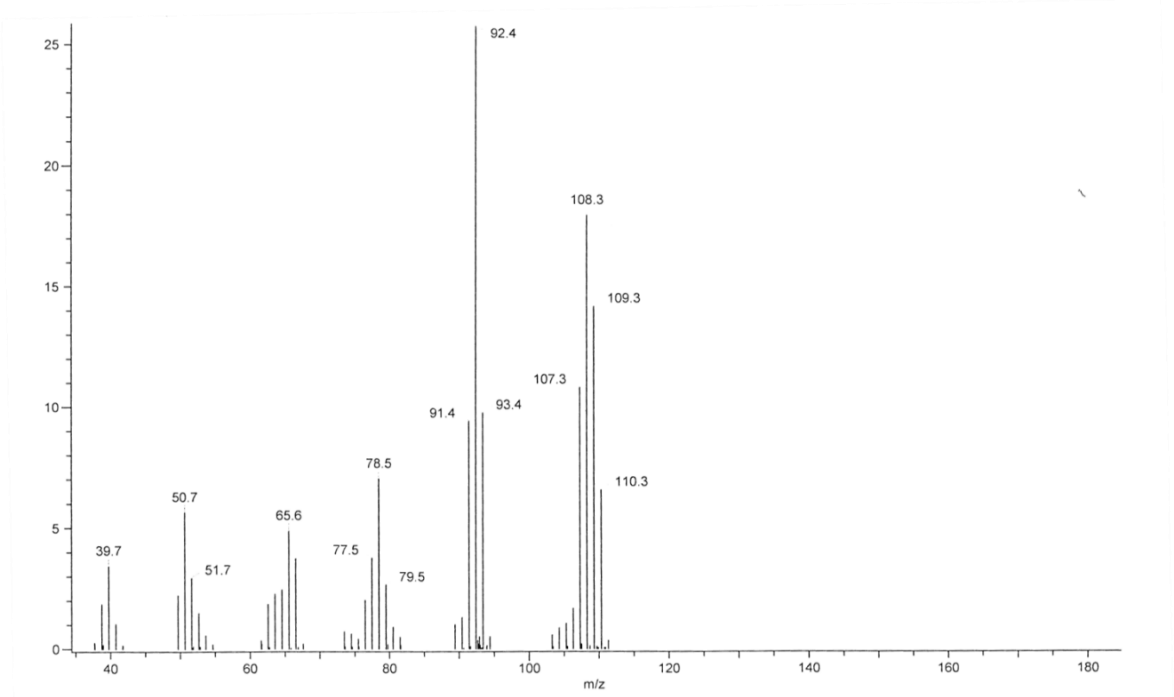

Figure S 2.23. The GC-MS spectrum of the hydrogenation product of styrene. m/z 107.3 ($C_6H_5CHDCH_3$, $C_6H_5CHCH_2D$), 108.3 ($C_6H_5CHDCH_2D$), 109.3 ($C_6H_5CD_2CH_2D$)

Formation of deuterated ethylbenzene

1) Formation of deuterated catalytic species $Pd(D)_2$:
$Pd_n + D_2 \leftrightharpoons Pd(D)_2$

2) Formation of dideuterated ethylbenzene:
$PhCH{=}CH_2 + Pd(D)_2 \leftrightharpoons PhCHDCH_2D$

3) Formation of hydrogenated catalytic species Pd_n-H:
$PhCHDCH_2D + Pd_n \leftrightharpoons PhCD\cdot CH_2D + Pd_n\text{-}H$

4) Formation of monodeuterated ethylbenzene:
$PhCHDCH_2D + Pd_n \leftrightharpoons PhCH\cdot CH_2D + Pd_n\text{-}D$
$PhCH\cdot CH_2D + Pd_n\text{-}H \leftrightharpoons PhCH_2CH_2D + Pd_n$

5) Formation of trideuterated ethylbenzene:
$PhCHDCH_2D + Pd_{n.} \leftrightharpoons PhCD\cdot CH_2D + Pd_n\text{-}H$
$PhCD\cdot CH_2D + Pd_n\text{-}D \leftrightharpoons PhCD_2CH_2D + Pd_n$

6) The final ethylbenzenes calculated from ^{1}H NMR (**Figure S 2.23**) integrations can be $Ph\text{-}CH_{0.08}D_{1.92}\text{-}CH_{2.71}D_{0.29}$.

Calculation of photon flux

Photon flux received during the reaction is analyzed by standard ferrioxalate actinometry[54,55] Typically, potassium ferrioxalate hydrate (1.2mmol, 590mg) is dissolved in 100ml H_2SO_4 (0.05M), giving a 0.012mmol/L ferrioxalate solutions which is stored in dark. A buffered solution of 1,10-phenanthroline was prepared by dissolving 1,10-phenanthroline (100 mg) and sodium acetate (22.52 mg) in H_2SO_4 (100 mL, 0.5 M), and the solution is also stored in dark.

To measure the photon flux of the LED lamp, 2ml ferrioxalate solution is injected into a quartz cuvette (l = 1 cm) and illuminated for 90s. After irradiation, 0.35ml phenanthroline solution is added to the cuvette under

stirring. 1h later, the solution is applied for UV-Vis spectrum and its concentration is determined by the absorbance at 510 nm. At the same time, a sample without irradiation is also prepared and tested for UV-Vis spectrum. Au/RhNZs exhibit a wide plasmon band around 500-540 nm, indicating that the main photon flux received by the NZs corresponds to 500-540 nm. Thus, lights with two different wavelengths (λ_{max}= 520 nm and λ_{mas}= 450nm) are measured here.

The amount of produced Fe^{2+} is determined as:

$$\boldsymbol{mol\ Fe^{2+} = \frac{V.\Delta A(510\ nm)}{l \times \varepsilon}} \quad \text{(S2.8)}$$

Where V is the volume of irradiation (0.00235 L), $\boldsymbol{\Delta A(510\ nm)}$ is the absorbance increase owing to the formation of $\boldsymbol{Fe^{2+}}$ (**Figure S 2.25**), ε is the molar extinction coefficient of $[Fe(Phen)_3]^{2+}$ complex (11100 $L \cdot mol^{-1} \cdot cm^{-1}$), l is optical path-length of the cuvette (1 cm).

Photon flux is determined as:

$$\boldsymbol{Photon\ flux = \frac{mol\ Fe^{2+}}{\Phi \times t \times f}} \quad \textbf{(S2.9)}$$

Where Φ is quantum yield for the ferrioxalate (0.71 at λ_{max}=520 nm, 0.96 at λ_{max}=450 nm)[56], t is the reaction time (90s), f is the fraction of light absorbed at λ_{max}= 520 nm or 450 nm. This value is calculated using $f = 1-10^{-A(520\ nm\ or\ 450\ nm)}$, A(520 nm or 450 nm) is the absorbance of the ferrioxalate solution at 520 nm (or 450 nm).

Thus, photon flux was determined to be $2.34\times10^{\wedge(-9)}$ einsteins$\cdot s^{-1}$ for light with λ_{max}=520 nm (average of three experiments), and $2.92\times10^{\wedge(-9)}$ einsteins.s^{-1} for light with λ_{mas}= 450nm (average of three experiments). However, time plots of H_2 evolution shown in **Figure S 2.24** indicates that more photon flux (λ_{mas}= 450nm) cannot give rise to a higher TOF value when comparing with light with λ_{mas}= 520nm.

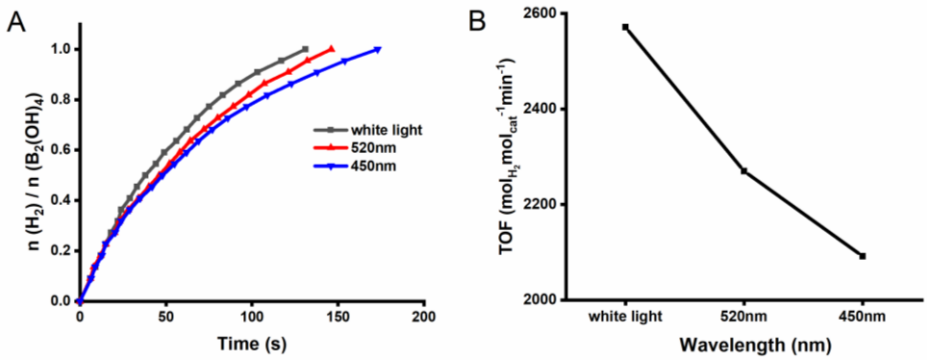

Figure S 2.24. (A)time plot and (B) TOF value of $B_2(OH)_4$ hydrolysis catalyzed by 0.1 mol % Au_1Rh_2NZs under different light illumination

Table S 2.2. Catalytic activity of the reported catalysts for $B_2(OH)_4$ hydrolysis.

Catalysts	Catalyst/ $B_2(OH)_4$ molar ratio	Temperature ˚C	Size (nm)	TOF_t	TOF_s	Reference
RhNPs/GQD	0.04%	30	1.9	1925	3658	[57]
PtNPs/GQD	0.04%	30	2.7	1773	4603	[57]
AuNPs/GQD	0.04%	30	4	455	1698	[57]
PdNPs/GQD	0.04%	30	3.8	216	802	[57]
IrNPs/GQD	0.04%	30	1.9	99	185	[57]
RuNPs/GQD	0.04%	30	2.4	53	127	[57]
PtNPs/Glucan	0.04%	30	2.5	348	830	[57]
PtNPs/TiO_2	0.04%	30	3.4	206	681	[57]
Pt/C	0.04%	30	2.2	144	300	[57]
Au@dendrimer	0.10%	25	2	220	819	This work
Rh@dendrimer	0.10%	25	2.3	99	427	This work
Au_4Rh_1@dendrimer	0.10%	25	1.5	1154	3227	This work

TOF_t is the turnover frequency for total atoms. TOF_s is the turnover frequency for surface atoms. The unit of TOF is $mol_{H2}\ mol_{cat}^{-1}\ min^{-1}$

2.6. References

1. Huang, Y.; Re, J.; Qu, X. Nanozymes: Classification, Catalytic Mechanisms, Activity Regulation, and Applications. *Chem. Rev*. 2019, *119*, 4357-4412.

2. Astruc, D. Introduction: Nanoparticles in Catalysis. *Chem. Rev*. 2020, *120*, 461-463.

3. Lubitz, W.; Ogata, H,; Rudiger, O.; Reijerse, E. Hydrogenases. *Chem. Rev*. 2014, *114*, 4081-4148.

4. Amaro-Gahete, J.; Pavliuk, M. V.; Tian, H. N.; Esquivel, D.; Romero-Salguero, F. J.; Ott, S. Catalytic Systems mimicking the [Fe-Fe]-hydrogenase active site for visible-light hydrogen production. *Coord. Chem. Rev*. 2021, *448*, 214172.

5. Cummings, S. P.; Le, T. N.; Fernandez, G. E.; Quiambao, L. G.; Stokes, B. J. Tetrahydroxydiboron-Mediated Palladium-Catalyzed Transfer Hydrogenation and Deuteriation of Alkenes and Alkynes Using Water as the Stoichiometric H or D Atom Donor. *J. Am. Chem. Soc.* 2016, *138*, 6107-6110.

6. Zhou, Y. Huang, J. Shen, X. Liu, Pd/C-Catalyzed H_2 Evolution from Tetrahydroxydiboron Hydrolysis, Catal. Letters 2021, *151*, 3004-3010.

7. Jang, M.; Lim, T.; Park, B. Y.; Han, M. S. Metal-Free, Rapid, and Highly Chemoselective Reduction of Aromatic Nitro Compounds at Room Temperature, *J. Org. Chem*. 2022, *87*, 910-919.

8. Chen, W.; Shen, J.; Huang, Y.; Liu, X.; Astruc, D. Catalyzed Hydrolysis of Tetrahydroxydiboron by Graphene Quantum Dot-Stabilized Transition-Metal Nanoparticles for Hydrogen Evolution. *ACS Sustain. Chem. Eng.* 2020, *8*, 7513-7522.

9. Wang, D.; Astruc, D. The Golden Age of Transfer Hydrogenation. *Chem. Rev.* 2015, *115*, 6621-6686;

10. Fu, F.; Wang, C.; Wang, Q.; Martinez-Villacorta, A. M.; Escobar, A.; Chong, H.; Wang, X.; Moya, S.; Salmon, L.; Fouquet, E.; Ruiz, J.; Astruc, D. Highly Selective and Sharp Volcano-type Synergistic Ni_2Pt@ZIF-8-Catalyzed Hydrogen Evolution from Ammonia Borane Hydrolysis. *J. Am. Chem. Soc.* 2018, *140*, 10034-10042.

11. Gómez-Gallego, M.; Sierra, M. A. Kinetic Isotope Effects in the Study of Organometallic Reaction Mechanisms. *Chem. Rev.* 2011, *111*, 4857-4963.

12. Atzrodt, J.; Derdau, V. Pd- and Pt-catalyzed H/D exchange methods and their application for internal MS standard preparation from a Sanofi-Aventis perspective. *J. Labelled Compd. Radiopharm.* 2010, *53*, 674-685.

13. Sloane, S. E.; Reyes, A.; Vang, Z. P.; Li, L.; Behlow, K. T.; Clark, J. R. Copper-Catalyzed Formal Transfer Hydrogenation/Deuteration of Aryl Alkynes. *Org. Lett.* 2020, *22*, 9139-9144.

14. Chu, S.; Cui, Y.; Liu, N. The path towards sustainable energy, *Nat. Mater.* 2017, *16*, 16-20.

15. Zhu, Y.; Ouyang, L.; Zhong, H.; Liu, J.; Wang, H.; Shao, H.; Huang, Z.; Zhu, M. Closing the Loop for Hydrogen Storage: Facile Regeneration of $NaBH_4$ from its Hydrolytic Product, *Angew. Chem. Int. Ed.* 2020, *59*, 8623-8629.

16. Liu, C. C.; Gong, T.; Zhang, J.; Zheng, X. R.; Mao, J.; Liu, H.; Li, Y.; Hao, Q. Y., Engineering Ni_2P-$NiSe_2$ heterostructure interface for highly efficient alkaline hydrogen evolution. *Appl. Catal. B-Environ.* 2020, *262*.

17. Wang, H. F.; Chen, L. Y.; Pang, H.; Kaskel, S.; Xu, Q., MOF-derived electrocatalysts for oxygen reduction, oxygen evolution and hydrogen evolution reactions. *Chem. Soc. Rev.* 2020, *49* (5), 1414-1448.

18. Lin, Y.; Sun, K. A.; Chen, X. M.; Chen, C.; Pan, Y.; Li, X. Y.; Zhang, J., High-precision regulation synthesis of Fe-doped Co_2P nanorod bundles as efficient electrocatalysts for hydrogen evolution in all-pH range and seawater. *Journal of Energy Chemistry* 2021, *55*, 92-101.

19. Zhu, J.; Hu, L. S.; Zhao, P. X.; Lee, L. Y. S.; Wong, K. Y., Recent Advances in Electrocatalytic Hydrogen Evolution Using Nanoparticles. *Chem. Rev.* 2020, *120* (2), 851-918.

20. Zaleska-Medynska, A.; Marchelek, M.; Diak, M.; Grabowska, E. Noble metal-based bimetallic nanoparticles: the effect of the structure on the optical, catalytic and photocatalytic properties. *Adv. Colloid Interface Sci.* 2016, *229*, 80-107.

21. Gilroy, K. D.; Ruditskiy, A.; Peng, H.-C.; Qin, D.; Xia, Y. Bimetallic Nanocrystals: Syntheses, Properties, and Applications. *Chem. Rev.* 2016, *116*, 10414-10472.

22. Wang, C.; Astruc, D. Nanogold plasmonic photocatalysis for organic synthesis and clean energy conversion. *Chem. Soc. Rev.* 2014, *43*, 7188-7216.

23. Daniel, M-C.; Astruc, D., Gold Nanoparticles: Assembly, Supramolecular Chemistry, Quantum-size Related Properties, and Applications towards Biology, Catalysis and Nanotechnology, *Chem. Rev.* 2004, *104*, 293-346.

24. Zada, A.; Muhammad, P.; Ahmad, W.; Hussain, Z.; Ali, S.; Khan, M.; Khan, Q.; Maqbool, M. Surface Plasmonic-Assisted Photocatalysis and

Optoelectronic Devices with Noble Metal Nanocrystals: Design, Synthesis, and Applications. *Adv. Funct. Mater.* 2019, *30*, 1906744.

25. Gelle, A.; Jin, T.; de la Garza, L.; Price, G. D.; Besteiro, L. V.; Moores, A. Applications of Plasmon-Enhanced Nanocatalysis to Organic Transformations. *Chem. Rev*. 2020, *120*, 986-1041.

26. Verma, P.; Kuwahara, Y.; Mori, K.; Yamashita, H. Pd/Ag and Pd/Au bimetallic nanocatalysts on mesoporous silica for plasmon-mediated enhanced catalytic activity under visible light irradiation. *J. Mater. Chem. A* 2016, *4*, 10142-10150.

27. J. S. Chahal, O. F. Khan, C. L. Cooper, J. S. McPartlan, J. K. Tsosie, L. D. Tilley, S. M. Sidik, S. Lourido, R. Langer, S. Bavari, H. Ploegh and D. G. Anderson. Dendrimer-RNA Nanoparticles Generate Protective Immunity Against Iethal Ebola, H1N1 Influenza, and Toxoplasma Gondii Challenges with a Single Dose, *Proc. Natl. Acad. Sci. USA*, 2016, *113*, E4133–4142.

28. R. W. Scott, O. M. Wilson and R. M. Crooks, Synthesis, Characterization, and Applications of Dendrimer-Encapsulated Nanoparticles, *J. Phys. Chem. B*, 2005, *109*, 692-704.

29. V. S. Myers, M. G. Weir, E. V. Carino, D. F. Yancey S. Pande and R. M. Crooks. Dendrimer-encapsulated Nanoparticles : New Synthetic and Characterization Methods and Catalytic Applications, *Chem. Sci*., 2011, *2*, 1632-1646

30. Astruc, D.; Boisselier, E.; Ornelas, C. Dendrimers Designed for Functions: From Physical, Photophysical, and Supramolecular Properties to Applications in Sensing, Catalysis, Molecular Electronics, Photonics, and Nanomedicine. *Chem. Rev.* 2010, *110*, 1857-1959.

31. Wang, C.; Ikhlef, D.; Kahlal, S.; Saillard, J.-Y.; Astruc, D. Metal-Catalyzed Azide-Alkyne "Click" Reactions: Mechanistic Overview and Recent Trends. *Coord. Chem. Rev.* 2016, *316*, 1-20.

32. Astruc, D.; Heuzé, K.; Gatard, S.; Méry, D.; Nlate, S.; Plault, L. Metallodendritic Catalysis for Redox and Carbon-Carbon Bond Formation Reactions: A Step towards Green Chemistry. *Adv. Synth. Catal*. 2005, *347*, 329-338.

33. Wang, Q.; Fu, F.; Yang, S.; Martinez Moro, M.; Ramirez, M. d. l. A.; Moya, S.; Salmon, L.; Ruiz, J.; Astruc, D. Dramatic Synergy in CoPt Nanocatalysts Stabilized by "Click" Dendrimers for Evolution of Hydrogen from Hydrolysis of Ammonia Borane. *ACS Catal*. 2019, *9*, 1110-1119.

34. Bian, T.; Xiao, B.; Sun, B.; Huang, L.; Su, S.; Jiang, Y.; Xiao, J.; Yuan, A.; Zhang, H.; Yang, D. Local epitaxial growth of Au-Rh core-shell star-shaped decahedra: A case for studying electronic and ensemble effects in hydrogen evolution reaction. *Appl. Catal. B* 2020, *263*, 118255.

35. Kang, Y. Q.; Xue, Q.; Peng, R. L.; Jin, P. J.; Zeng, J. H.; Jiang, J. X.; Chen, Y. Bimetallic AuRh nanodendrites consisting of Au icosahedron cores and atomically ultrathin Rh nanoplate shells: synthesis and light-enhanced catalytic activity. *NPG Asia Mater*. 2017, *9*.

36. Ding, J.; Li, X.; Chen, L.; Zhang, X.; Tian, X. Photocatalytic hydrogen production over plasmonic AuCu/$CaIn_2S_4$ composites with different AuCu atomic arrangements. *Appl. Catal. B* 2018, *224*, 322-329.

37. Saad, A.; Vard, C.; Abderrabba, M.; Chehimi, M. M. Triazole/Triazine-Functionalized Mesoporous Silica As a Hybrid Material Support for Palladium Nanocatalyst. *Langmuir* 2017, *33*, 7137-7146.

38. Moulder, J.F.; Stickle, W.F.; Sobol, P.E.; Bomben, K.D. Handbook of X ray Photoelectron Spectroscopy, *Physical Electronics*, 1995

39. Marcus, R. A. On the Theory of Oxidation-Reduction Reactions Involving Electron Transfer. I. *J. Chem. Phys.* 1956, *24*, 966-978.

40. Tedsree, K.; Li, T.; Jones, S.; Chan, C. W.; Yu, K. M.; Bagot, P. A.; Marquis, E. A.; Smith, G. D.; Tsang, S. C. Hydrogen production from formic acid decomposition at room temperature using a Ag-Pd core-shell nanocatalyst. *Nat. Nanotechnol.* 2011, *6*, 302-307.

41. Schüth, F.; Ward, M. D.; Buriak, J. M. Common Pitfalls of Catalysis Manuscripts Submitted to Chemistry of Materials. *Chem. Mater.* 2018, *30*, 3599-3600.

42. Gao, F.; Goodman, D. W. Pd–Au bimetallic catalysts: understanding alloy effects from planar models and (supported) nanoparticles. *Chem. Soc. Rev.* 2012, *41*, 8009-8020.

43. Verma, P.; Yuan, K.; Kuwahara, Y.; Mori, K.; Yamashita, H. Enhancement of plasmonic activity by Pt/Ag bimetallic nanocatalyst supported on mesoporous silica in the hydrogen production from hydrogen storage material. *Appl. Catal. B-Environ.* 2018, *223*, 10-15.

44. Dubi, Y.; Un, I. W.; Sivan, Y. Thermal effects – an alternative mechanism for plasmon-assisted photocatalysis. *Chem. Sci.* 2020, *11*, 5017-5027.

45. Yin, Z.; Wang, Y.; Song, C.; Zheng, L.; Ma, N.; Liu, X.; Li, S.; Lin, L.; Li, M.; Xu, Y.; Li, W.; Hu, G.; Fang, Z.; Ma, D. Hybrid Au–Ag Nanostructures for Enhanced Plasmon-Driven Catalytic Selective Hydrogenation through Visible Light Irradiation and Surface-Enhanced Raman Scattering. *J. Am. Chem. Soc.* 2018, *140*, 864-867.

46. Ma, Y.; Li, W.; Cho, E. C.; Li, Z.; Yu, T.; Zeng, J.; Xie, Z.; Xia, Y. Au@Ag Core−Shell Nanocubes with Finely Tuned and Well-Controlled Sizes, Shell Thicknesses, and Optical Properties. *ACS Nano* 2010, *4*, 6725-6734.

47. Li, D.; Ouyang, S.; Xu, H.; Lu, D.; Zhao, M.; Zhang, X.; Ye, J. Synergistic effect of Au and Rh on $SrTiO_3$ in significantly promoting visible-light-driven syngas production from CO_2 and H_2O. *Chem. Commun*. 2016, *52*, 5989-5992.

48. Trasatti, S. Work function, electronegativity, and electrochemical behaviour of metals: II. Potentials of zero charge and "electrochemical" work functions. *J. Electroanal. Chem.* 1971, *33*, 351-378.

49. Kang, N.; Wang, Q.; Djeda, R.; Wang, W.; Fu, F.; Moro, M. M.; Ramirez, M. d. l. A.; Moya, S.; Coy, E.; Salmon, L.; Pozzo, J.-L.; Astruc, D., Visible-Light Acceleration of H_2 Evolution from Aqueous Solutions of Inorganic Hydrides Catalyzed by Gold-Transition-Metal Nanoalloys. *ACS Appl. Mater. Interfaces* 2020, *12* (48), 53816-53826.

50. Qureshi, M.; Takanabe, K., Insights on Measuring and Reporting Heterogeneous Photocatalysis: Efficiency Definitions and Setup Examples. *Chem. Mater.* 2017, *29* (1), 158-167

51. Cornilleau, T.; Hermange, P.; Fouquet, E., Gold-catalysed cross-coupling between aryldiazonium salts and arylboronic acids: probing the usefulness of photoredox conditions. *Chem. Commun.* 2016, *52* (65), 10040-10043.

52. Xu, P.; Lu, W.; Zhang, J.; Zhang, L., Efficient Hydrolysis of Ammonia Borane for Hydrogen Evolution Catalyzed by Plasmonic Ag@Pd Core–Shell Nanocubes. *ACS Sustain. Chem. Eng.* 2020, *8* (33), 12366-12377.

53. Astruc, D. *Organometallic Chemistry and Catalysis*. Springer, Berlin, 2007, pp 87-95.

54. Aillet, T.; Loubière, K.; Dechy-Cabaret, O.; Prat, L., Accurate Measurement of the Photon Flux Received Inside Two Continuous Flow Microphotoreactors by Actinometry. *International Int. J. Chem. React. Eng.* 2014, *12*, 257 - 269.

55. Cornilleau, T.; Hermange, P.; Fouquet, E., Gold-catalysed cross-coupling between aryldiazonium salts and arylboronic acids: probing the usefulness of photoredox conditions. *Chem. Commun.* 2016, *52* (65), 10040-10043.

56. Greenberg, J. W.; Malhotra, V.; Ennever, J. F., Wavelength dependence of the quantum yield for the structural isomerization of bilirubin. *Photochem. Photobiol.* 1987, *46* (4), 453-456.

57. Chen, W.; Shen, J.; Huang, Y.; Liu, X.; Astruc, D. Catalyzed Hydrolysis of Tetrahydroxydiboron by Graphene Quantum Dot-Stabilized Transition-Metal Nanoparticles for Hydrogen Evolution. *ACS Sustain. Chem. Eng.* 2020, *8*, 7513-7522.

Chapter 3. Cobalt sandwich-stabilized rhodium nanocatalysts for ammonia borane and tetrahydroxydiboron hydrolysis

3.1. Introduction

The conventional fossil fuels (coal, petroleum oil, and natural gas, etc.) produce dangerous greenhouse gas and considerable pollution, and therefore there is a huge demand for clean and sustainable energy sources.[1-5] Hydrogen gas (H_2) is regarded as the most attractive green energy source because of its high gravimetric energy density and lack of pollution due to its combustion product, water.[6-11] However, giving the dangers of explosion, large-scale application of H_2 involves transformation and storage issues. H_2 evolution from stable hydrogen storage materials appears as a valuable option. Boron chemistry contains hydrogen-rich compounds with hydridic hydrogen atoms,[12] and its role in energy-related processes has been very recently emphasized.[10] In particular, ammonia borane (AB) has attracted intensive attention owing to its high hydrogen content (19.6 wt%), high solubility and stability in aqueous solution.[13-32] Given the very low reaction rate of AB hydrolysis under ambient conditions, acceleration by catalysts is regarded as a promising way, and intensive efforts have been achieved to exploit efficient catalysts. It has been proposed that one of the hydrogen atoms of H_2 formed is provided by the borane group of AB, and the other one from water. Besides, the hydrolysis of tetrahydroxydiboron, $B_2(OH)_4$, is also promising for H_2 evolution as reported in the literature, but in this case it has been shown that both H atoms of H_2 are provided by water.[33-35] $B_2(OH)_4$ was first reported in 1955 by hydrolysis of B_2Cl_4 and $B_2(NMe_2)_4$.[36,37] Initially, the borylation of vinyl cyclopropane, vinyl aziridine, and allyl acetate substrates using $B_2(OH)_4$ was reported.[38] $B_2(OH)_4$ also serves as a reducing reagent, for example, for the reduction of pyridine-N-oxides[39] and nitro-aromatics.[40] Stokes and co-workers pioneered transfer hydrogenation of unsaturated

hydrocarbons utilizing catalytic $B_2(OH)_4$ hydrolysis. Mechanistic studies revealed that $B_2(OH)_4$ facilitated the transfer of H atoms from water giving the intermediate Pd-H species, in which the unsaturated hydrocarbon inserted to complete its hydrogenation, and no H_2 gas was observed during the process. [41] Thus, $B_2(OH)_4$ plays the role of abstracting H atoms from water, rather than hydrogen storage material like AB. [34,42]

Transition-metal (TM) nanoparticles (NP) have multiple applications in optics, sensing and especially catalysis.[1,43-53] Active sites on their surface play a key role in binding substrate atoms due to their composition, size dispersity, morphology and coordination by ligands.[54,55] The nanocatalysts are generally fabricated by reduction of TM salt precursors using a reducing agent such as $NaBH_4$, H_2, Mg, Li, Na naphthalene, *etc.*, in a presence of protecting ligand.[26, 56-58] In this process, the oxidized form of the reductant is retained in an uncertain state, which is prone to disturb the coordination type between the nanocatalyst and ligands, consequently impacting the nanocatalyst activity and reliability.[59]

Hydride-rich organometallic complexes, obtained through reduction of 18-electron organometallic sandwich cations using sodium borohydride, have been studied as hydride-donating reagents for various chemical transformations.[60,61] For example, the hydride-rich complex [$RhCp(\eta^4\text{-}C_5H_6)$] was converted to rhodicenium cation in the presence of the hydride-accepting trityl (Ph_3C^+) cation via an initial electron-transfer step, followed by hydrogen-atom transfer, instead of a concerted hydride transfer.[60] Such a process is known in iron-sandwich chemistry.[62] The reverse has also long been known: reduction using $NaBH_4$ can proceed by electron transfer followed by H-atom transfer.[63] Barlow et al reported two classes of organometallic hydride

donors as *n*-dopants for organic semiconductors.[64] In cyclic voltammetry, organometallic hydrides undergo irreversible oxidation that presumably involve single-electron oxidation followed by H atom transfer.[36,65]

Here, the hydride-rich neutral organometallics [Co(η^5-C_5H_5)(η^4-C_5H_6)], **1H**, and [Co(η^5-C_5Me_5)(η^4-C_5H_6)], **2H**, are used as reductants of transition metal chlorides, because upon reduction reactions these organocobalt complexes form cobalticenium chloride $\mathbf{1^+Cl^-}$, resp. pentamethylcobalticenium chloride $\mathbf{2^+Cl^-}$ that are well-characterized robust compounds. In the reduction process, they are expected to play both the role of reductants of M^{n+} to M^0 and that of NP stabilizer located around the NP periphery. NP stabilization is also insured by polyvinylpyrrolidone (PVP) 10000. The resulting nanocatalysts are abbreviated TMNP (stabilized by **1H**) and TMNP* (stabilized by **2H**), respectively. A series of electron-reservoir and hydride-reservoir complexes [$CoCp_2$], [$FeCp_2$], [FeCp(η^5-C_6H_6)], [FeCp(η^5-C_6Me_6)], [CoCp(η^4-C_5H_6)], [FeCp(η^5-C_6H_7)], [FeCp(η^5-C_6Me_6H)], with Cp = η^5-C_5H_5, have already previously been used to stabilize AuNPs and PdNPs by their oxidized form.[66] It was concluded that [CoCp(η^4-C_5H_6)] gave better results than the above 19-electron electron-reservoir complexes and other 18-electron hydride-reservoir complexes in the catalysed reduction of 4-nitrophenol by AuNP and Suzuki-Miyaura coupling reaction catalysed by PdNP. We have retained the idea that hydride transfer appears superior to electron transfer for the catalytic efficacy of the generated NPs, and we are applying it for the first time to H_2 formation reactions. Another trend that we are investigating here is whether the use of the ligand η^5-C_5Me_5 (Cp*) in the Co complex instead of parent Cp is beneficial to catalysis. It is well known that permethylation of at least one Cp ligand stabilizes metallocenes and other

organometallics because of the stereo-electronic influence of the five methyl substituents in Cp*. Indeed, Cp* is not only much bulkier than the parent Cp, but also a much stronger electron-releasing ligand.[67] Here the synthesis of a series of nanomaterials TMNP* (TM = Rh, Pt, Pd, Au) using **2H** as precursor for the reduction of TM chlorides is reported as well as their comparison with the related TMNP, prepared using **1H**, in these two catalytic hydrogen evolution reactions.

3.2. Results and Discussion

3.2.1. Preparation of TMNP and TMNP*

Metal precursors, for example, $RhCl_3$ (0.42 mg, 0.002 mmol), and PVP, 2 equiv, are dissolved in Milli-Q water (5 ml) under N_2 in a standard Schlenk flask and stirred for 30 min. Then, the freshly prepared complex [Co(η^5-C_5Me_5)(η^4-C_5H_6)], **2H** (0.03 mmol, see **Experimental Section**) dissolved in THF is injected into the flask under N_2 atmosphere, and the color of the solution changes immediately from colorless to dark brown, indicating the formation of TMNP* (**Equation 3.1** and **Figure 3.1**). After stirring for 30 min, the NPs are used in catalysis. The TMNP catalysts are prepared using the same method (**Experimental Section**). For $PtCl_4$ and $PdCl_2$, the produces are the same.

The reaction (**Equation 3.1**) produces H_2, but both H atoms of H_2 in this case are provided by the hydridic atom of **2H** (resp. **1H**) previously added to $[Cp^*CoCp]^+$) (resp. $[CpCp_2]^+$) upon reaction with $NaBH_4$.

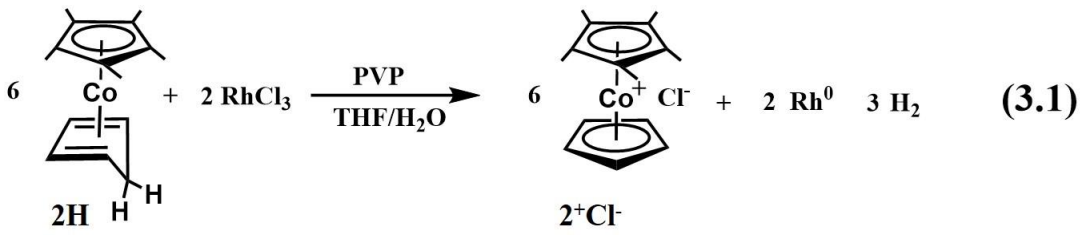

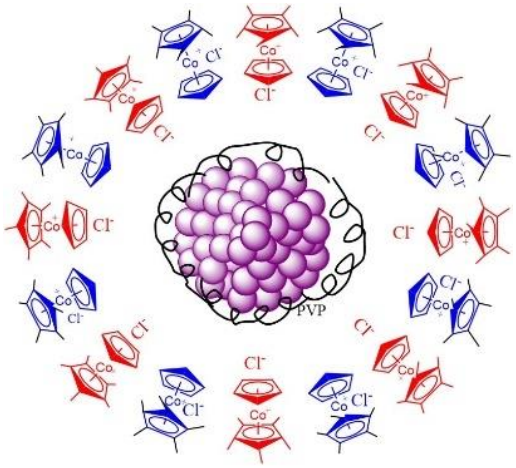

Figure 3.1. Schematic illustration of the RhNP* catalyst synthesized upon reduction of $RhCl_3$ by [CoCp*(η^4-C_5H_6)]. The red colour shows coordination of Cl^- to the NP core, and the blue colour illustrates metallocenyl chloride without coordination, corresponding to Rh atoms in the core (that are thus not surface atoms).

We suggest that in first instance **1H** (resp. **2 H**) is oxidized by M^{n+} according to a single electron transfer yielding the isostructural, yet unstable, 17-electron complex $\mathbf{1}^+$ (resp. $\mathbf{2}^+$). There is then a considerable driving force for transient $\mathbf{1}^+$ (resp. $\mathbf{2}^+$) to give the robust 18-electron cation $[CoCp_2]^+$, (resp. $[CoCp^*Cp]^+$), upon H-atom transfer probably to $M^{(n-1)+}$ in the course of its reduction process. The final H_2 formation might then result from reductive elimination from a $Rh(H)_2$ species formed by two successive H-atom transfers from two $\mathbf{1}^+$ (resp. $\mathbf{2}^+$) species. The alternative use of both electrons of the hydride to reduce M^{n+} while forming H^+ is energetically highly unlikely and

finally experimentally discarded by the reaction stoichiometry, the evidence of H_2 formation, and the lack of acidity of the final aqueous medium.

These cobalt complexes and PVP function cooperatively to stabilize the NPs. Without PVP, the metal NPs immediately precipitate upon addition of the cobalt complex; thus, PVP serves as a NP steric stabilizer. The cationic cobalt complex serves as a NP electrostatic stabilizer (in conjunction with surface-coordinated Cl^-) and in the same time as a complementary remote steric protector of the NP surface. In a previous work, it was shown that, after the dialysis of the AuNP, the cobalt complex can be removed, because it is water soluble, and thus only PVP was left for the protection of Au nanoparticles. In that later case, however, AuNP that were only stabilized by PVP showed a sharply decreased catalytic activity (reaction rate declined from 22.7×10^{-3} s^{-1} to 3.1×10^{-3} s^{-1} in 4-nitrophenol reduction), because of the loss of this electrostatic protection by $[CoCp_2]^+Cl^-$.[66]

3.2.2. Characterization of the nanoparticles

The microstructure and the size distribution of the TMNP* were investigated by transmission electron microscopy (TEM), and the typical catalysts RhNP* and AuNP* were examined. The characterization of this type of TMNP (including RhNP, but not RhNP*) is also accessible elsewhere.[66,68] As shown in **Figure 3.2A**, the nanocatalyst RhNP* exhibits a diameter size of 2.5 ± 1.5 nm, while RhNP shows a larger diameter size of 3.0 ± 1.1 nm (**Figure S 3.6**, **Experimental Section**). As shown in **Figure 3.1**, the small RhNP* are protected by ionic interactions between pentamethylcobalticenium chloride, $\mathbf{2^+Cl^-}$, and the NPs surface. Faster reduction due to the better reducing agent with the strong donor Cp* compared to Cp is responsible for the formation of smaller RhNP* compared to RhNP.

The small AuNP* exhibit a diameter size distribution of 7.1 ± 3.5 nm. (**Figure S 3.7**, **Experimental Section**). The CuNP* show a diameter of 10.1 ± 2.3 nm (**Figure S 3.8, Experimental Section**), which is the sign of the known weaker stability of the late first row TM NPs compared to the noble metal NP.

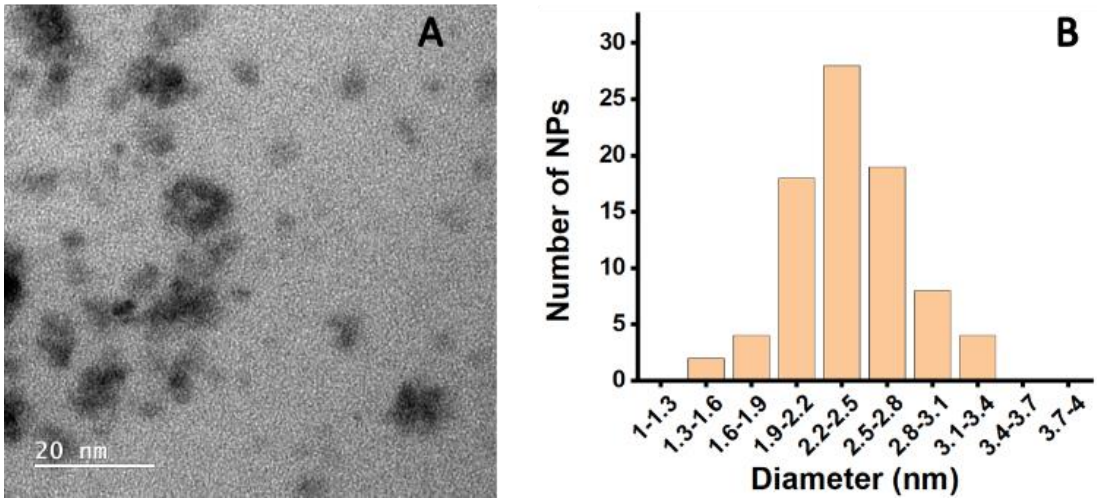

Figure 3.2. TEM image (A) and size distribution (B) of the RhNPs*.

X-ray photoelectron spectroscopy (XPS) of RhNP* shows a bonding energy of 308.2 eV and 312.8 eV, which is assigned to Rh $3d_{5/2}$ and $3d_{3/2}$, respectively, indicating that Rh atoms at the surface of RhNP* are exclusively zero valent (**Figure 3.3**). These Rh (0) values are close to those reported in the literature.[68,69] Very slightly higher values obtained here compared to the literature are attributable to the strong electrostatic effect provided by the ions of the organocobalt chloride complex surrounding the NP. In the UV-vis. spectra of RhNP*, a band appears at 410 nm, corresponding to the pentamethylcobalticenium moiety, also indicating that organometallic reductants are oxidized by the Rh cations to form $\mathbf{2^+Cl^-}$ and Rh (0) NPs (**Figure S 3.9, Experimental Section**).[66] As for AuNP*, besides the

pentamethylcobalticenium peak at 410 nm, there is a broad absorbance at 520 nm corresponding to the surface plasmon band (SPB) of the AuNP*.

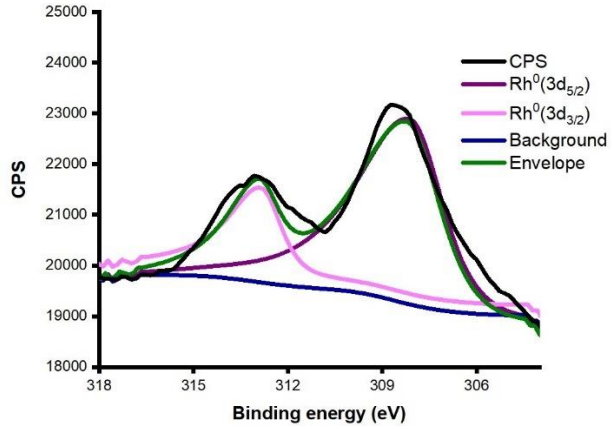

Figure 3.3. XPS spectrum of the RhNP* (CPS: counts per second).

3.3. Catalytic performances of TMNP and TMNP* in the hydrolysis of $B_2(OH)_4$ and ammonia borane (AB)

3.3.1. Hydrolysis of $B_2(OH)_4$ catalyzed by TMNP and TMNP*

Here, 0.2 mol% TMNP and TMNP* are used for $B_2(OH)_4$ hydrolysis. When 1 equiv. $B_2(OH)_4$ (90 mg) is consumed, 1 equiv. H_2 is produced, corresponding to 22.4 ml replacement of water in a typical water-filled gas burette at atmospheric pressure and room temperature (**Equation 3.2**).[20]

$$B_2(OH)_4 + 2\,H - OH \rightarrow 2\,B(OH)_3 + H_2\uparrow \qquad (\mathbf{3.2})$$

The TMNP (TM = Rh, Pd, Pt) produced from **1H**, termed RhNP, PdNP and PtNP, respectively **(Figure 3.4A**), and the TMNP*, produced from **2H** (**Figure 3.4C**), are very active catalysts for $B_2(OH)_4$ hydrolysis. To compare

the catalytic efficiency, the turnover frequency (TOF) is introduced here, defined as the number of moles of generated H_2 dividing by the total number of surface atoms over the time span of 10% substrate conversion. The calculated TOF values are 579 mol_{H_2} mol_{cat}^{-1} min^{-1} for RhNP, 138 mol_{H_2} mol_{cat}^{-1} min^{-1} for PdNP and 126 mol_{H_2} mol_{cat}^{-1} min^{-1} for PtNP, respectively (**Figure 3.4B**), whereas the values are 1364 mol_{H_2} mol_{cat}^{-1} min^{-1} for RhNP*, 268 mol_{H_2} mol_{cat}^{-1} min^{-1} for PdNP* and 360 mol_{H_2} mol_{cat}^{-1} min^{-1} for PtNP*, respectively (**Figure 3.4D**). The TOFs calculated by surface Rh atom (**Table S 3.1, Experimental Section**) compare to those obtained with other stabilizers shown (**Table S 3.2, Experimental Section**), revealing the very good activity of these RhNP*. Also, the results demonstrate that TMNP* exhibit a higher catalytic efficiency than their larger TMNP analogues. Besides, Rh is always the most active metal here among all the metals studied for catalytic $B_2(OH)_4$ hydrolysis with both organocobalt precursors.

The suggested mechanism in **Scheme 3.1** follows the literature proposal involving oxidative addition of the B-B bond onto the NP surface followed by water coordination, β-H elimination and reductive elimination of the two hydride ligands to form H_2 in which both atoms come from water (**Scheme 3.1**).[34]

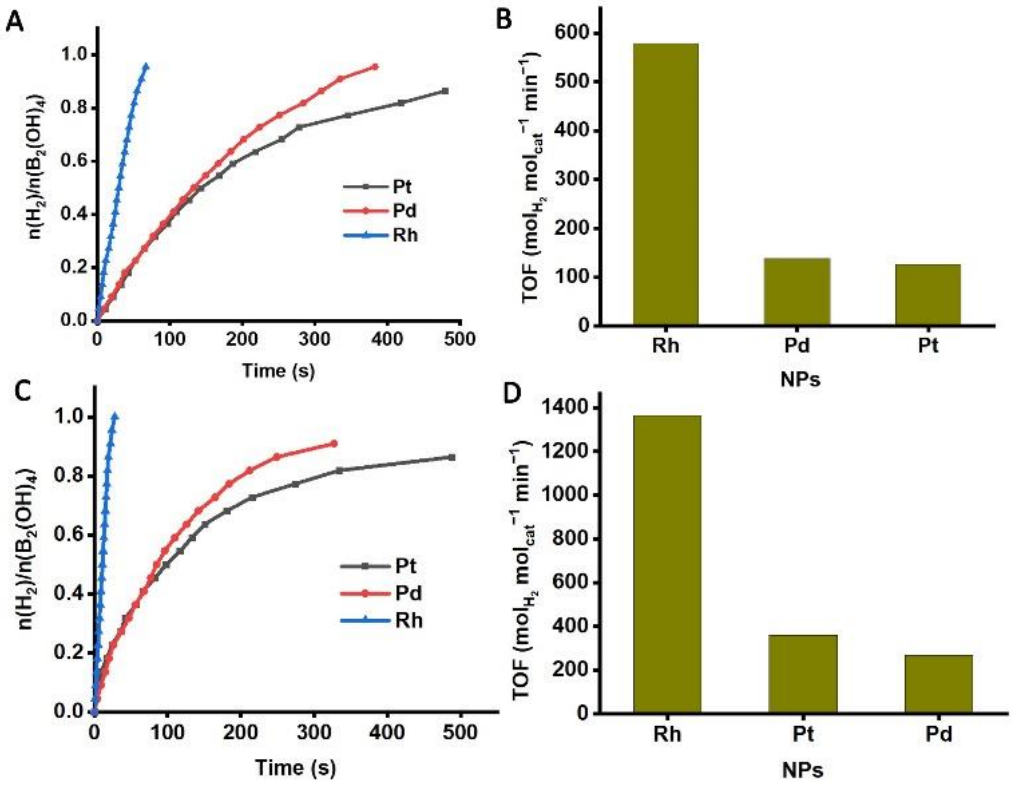

Figure 3.4. Time plot of H_2 evolution from the hydrolysis of $B_2(OH)_4$ catalysed by TMNP (A) and TMNP* (C). TOF values of $B_2(OH)_4$ hydrolysis catalysed by TMNP (B) and TMNP* (D).

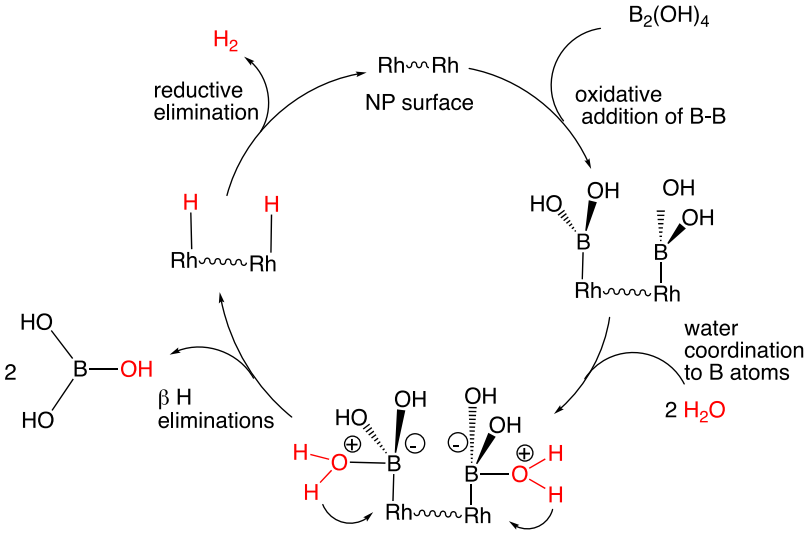

Scheme 3.1 Proposed mechanism for H_2 evolution upon RhNP*-catalyzed hydrolysis of $B_2(OH)_4$.

3.3.2. Ammonia borane hydrolysis catalysed by TMNP and TMNP*

To further compare the catalytic activities, the two groups of catalysts, TMNP and TMNP*, were then used for the hydrolysis of AB. AB is isoelectronic with gaseous ethane, but it shows different characteristics owing to the dipole moment between the N and B atoms. Its NH_3 and BH_3 fragments possess three protic $H^{\delta+}$ and three hydridic $H^{\delta-}$ hydrogens, respectively, which facilitates the intra-/inter-molecular $H^{\delta+}$ - $H^{\delta-}$ interactions. Besides, AB is a solid under ambient conditions, which is attributed to the heteropolar dihydrogen bonding, making AB implementable as chemical hydrogen storage materials.[19] Typically, when 1 equiv. AB (31 mg) is hydrolysed with the assistance of 0.2 mol% catalyst loading in our case, 3 equiv. H_2 are produced (**Equation 3.3**), resulting in 67 ml replacement of water in a water-filled gas burette at atmospheric pressure and room temperature.

$$NH_3BH_3 + 4\,H - \mathrm{OH} \rightarrow \mathrm{N}H_4^+\mathrm{B}(OH)_4^- + 3\mathrm{H}_2\uparrow \quad (\mathbf{3.3})$$

Time plots of H_2 evolution catalysed by TMNP are shown in **Figure 3.5A**. Like for the catalytic $B_2(OH)_4$ hydrolysis, TMNP are also active for NH_3BH_3 hydrolysis, showing a TOF value of 165 mol_{H_2} mol_{cat}^{-1} min^{-1} for RhNP, 134 mol_{H_2} mol_{cat}^{-1} min^{-1} for PdNP and 141 mol_{H_2} mol_{cat}^{-1} min^{-1} for PtNP, respectively (**Figure 3.5B**). For TMNP*, the TOF values are 125 mol_{H_2} mol_{cat}^{-1} min^{-1} for RhNP*, 21 mol_{H_2} mol_{cat}^{-1} min^{-1} for PdNP* and 67 mol_{H_2} mol_{cat}^{-1} min^{-1} PtNP*, respectively, i. e. somewhat lower for each metal compared with TMNP (**Figure 3.5C** and **3.5D**, **Table 3.1**), which is assigned to the protecting steric Cp* bulk decreasing the rate of substrate access to the NP surface. This order of catalytic activity at the beginning of the reactions,

defined by the TOFs, between TMNP and TMNP* is opposite to that of the catalytic $B_2(OH)_4$ hydrolysis. On the other hand, when comparing the time plot of H_2 evolution **in Figure 3.5A** and **3.5C**, for example, RhNPs, the curve of RhNP bends with time going on, while the curve of RhNP* proceeds almost linearly during catalysis, indicating an efficiency decline of the catalyst in the former case, and a relatively stable state of RhNP* in the latter case of catalytic hydrolysis of AB. PtNP* and PdNP* also show almost linear time plots (**Figure 3.5C**), whereas the time plot curves of PtNP and PdNP bend (**Figure 3.5A**), indicating comparatively more stable PtNP* and PdNP* than PtNP and PdNP, respectively .

Besides, AuNP* exhibits catalytic activity in AB hydrolysis (**Figure 3.5C**), whereas AuNP is inert at 0.2 mol% catalyst loading scale. In conclusion, although TMNP show a higher TOF value than TMNP* (except for Au), a better stability is obtained with TMNP*.

In sum, although the TMNP shows slightly higher TOF values than the TMNP* in AB hydrolysis (**Table 3.1** and **S 3.1, Experimental Section**), **2H** appears to be a preferred complex for the preparation of nanocatalysts, because it shows a fine balance between catalytic performance and stability. RhNP* favorably compares to the best state-of-the-art catalysts for AB hydrolysis in terms of TOF per surface atom, stability and recyclability (**Table S 3.3, Experimental Section**).

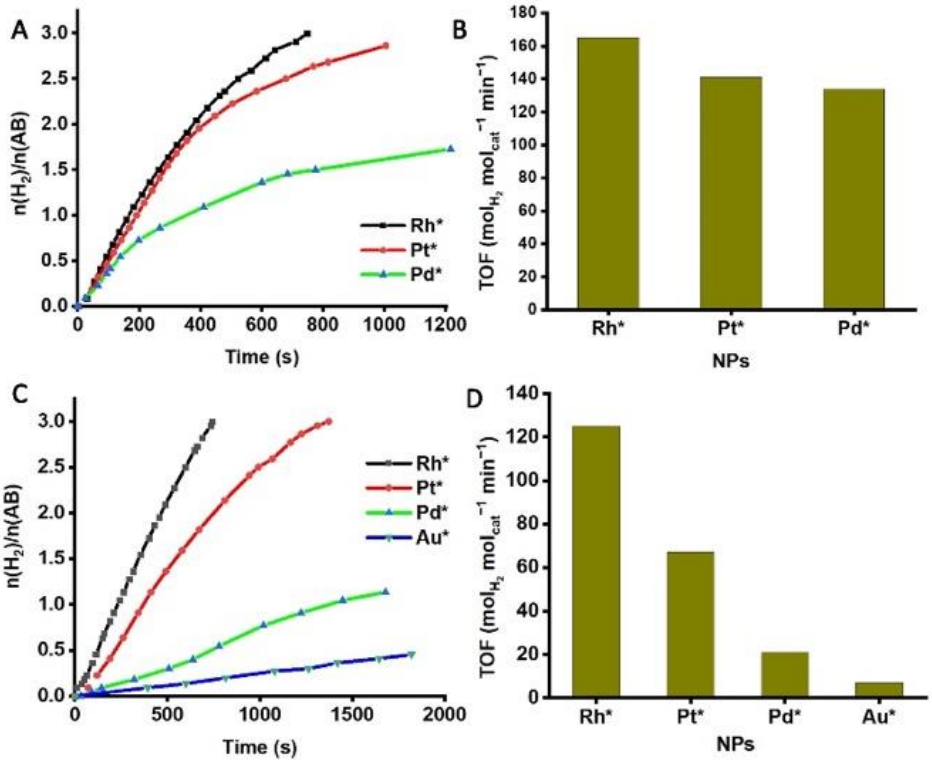

Figure 3.5. Time plot of H_2 evolution from the hydrolysis of AB catalysed by TMNP (A) and TMNP* (C). TOF values of catalytic AB hydrolysis catalysed by TMNP (B) and TMNP* (D).

Table 3.1. Compared TOFs for $B_2(OH)_4$ and AB hydrolysis catalysed by nanoparticles supported by $\mathbf{1}^+$ and $\mathbf{2}^+$, respectively.

	TOF $B_2(OH)_4$ hydrolysis		TOF AB hydrolysis	
	TMNP	TMNP*	TMNP	TMNP*
Rh	579	1364	165	125
Pd	138	268	134	21
Pt	126	360	141	67
Au	\	\	\	7

TOF: mol_{H_2} released at 10% H_2 yield/[total $mol_{catalyst}$ × reaction time (min)] for all atoms, the unit of TOF is $mol_{H_2}\ mol_{cat}^{-1}\ min^{-1}$.

These results also show that **2H** is a better choice than **1H** for the preparation of nanocatalysts. Subsequently, the reusability of the TMNP and TMNP* has been investigated. For the best RhNP in the parent TMNP family, the catalytic efficiency declined sharply in the second usage with only 1 mmol H_2 evolution in 1000 seconds along with precipitation of NPs in the hydrolysis of AB (**Figure 3.6A**). On the other hand, RhNP* has been recycled 3 times with progressively increased reaction time and, importantly, no NP precipitation was observed after 3 cycles (**Figure 3.6B**). These results confirm that the permethylated hydride reservoir complex **2H** gives rise to a more satisfying catalyst than the analogue complex **1H** concerning nanocatalyst stability and recyclability.

This difference of catalytic activity between TMNP and TMNP* can be ascribed to the methylation of the supporting ligands. In complex **2H**, the Cp* ligand (Cp* = η^5-C_5Me_5) is as a stronger electron-donor than Cp (Cp = η^5-C_5H_5) owing to the existence of the 5 electron-releasing methyl groups in Cp*, which increases the electronic density of the central metal Co. Besides, the bulk of Cp* is considerably larger than that of Cp, offering a better steric protection than Cp for the NP stabilization. As a result, after the reduction of metal precursors, the NPs stabilized by $\mathbf{2^+Cl^-}$ are more stable than those stabilized by $\mathbf{1^+Cl^-}$.[67] The better stability of RhNP* compared to RhNP is an additional reason explaining the better catalytic results obtained with RhNP*, aggregation of NPs being better prevented with $\mathbf{2^+Cl^-}$ than with $\mathbf{1^+Cl^-}$. Better catalytic performance of TMNP* supported by $\mathbf{2^+Cl^-}$ compared to TMNP supported by $\mathbf{1^+Cl^-}$ in the catalytic hydrolysis of AB and $B_2(OH)_4$ result overall from both smaller NP size and better stability during the catalytic process.

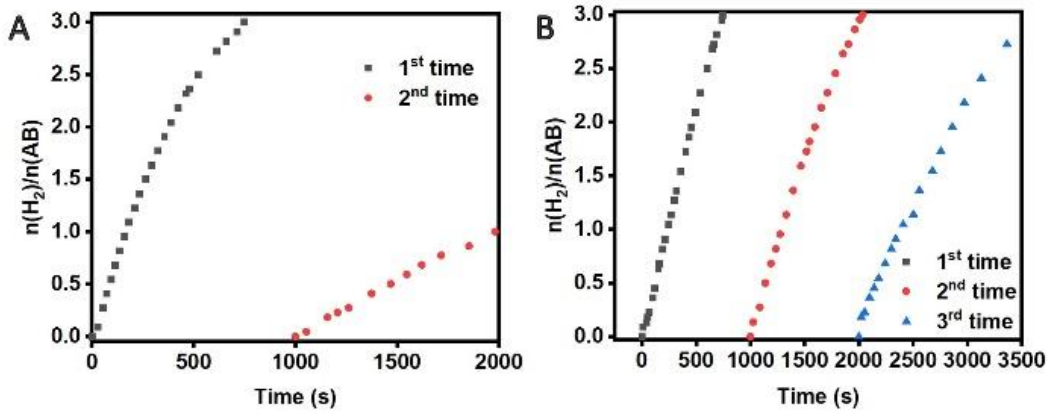

Figure 3.6. Time plots of H_2 evolution from the hydrolysis of AB catalysed by RhNP (A) and RhNP*; (B) in the reuse test

3.3.3. Kinetic studies and mechanism

In order to investigate the mechanism of AB hydrolysis catalysed by TMNP*, the best catalyst RhNP* was used for kinetic studies. **Figure 3.7A** shows the time plot of H_2 evolution in the presence of various concentrations of AB. The corresponding slop of logarithmic plot of H_2 evolution vs. AB concentration is 0.17 (**Figure 3.7B**), indicating a zero-order kinetics in AB concentration. This also reveals that AB activation is barely involved in the rate-determining steps.[24]

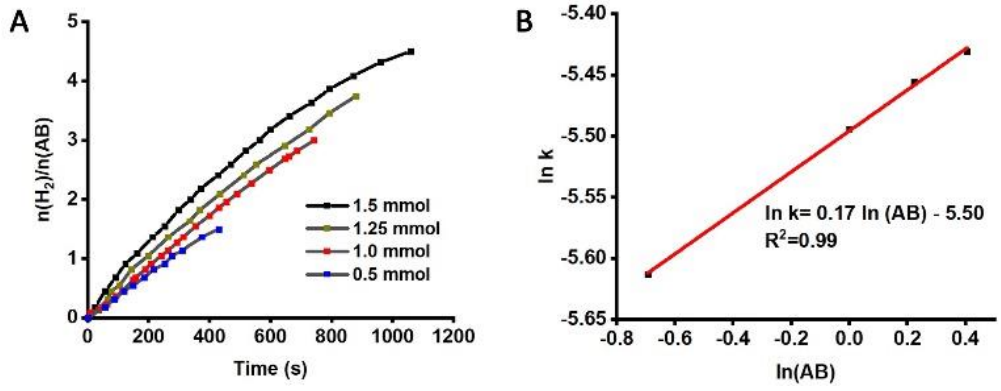

Figure 3.7. (A) Time plots of H_2 evolution catalysed by 0.2 mol% RhNP* and (B) Plots of the H_2 generation rate vs. AB concentration both on natural logarithmic scales.

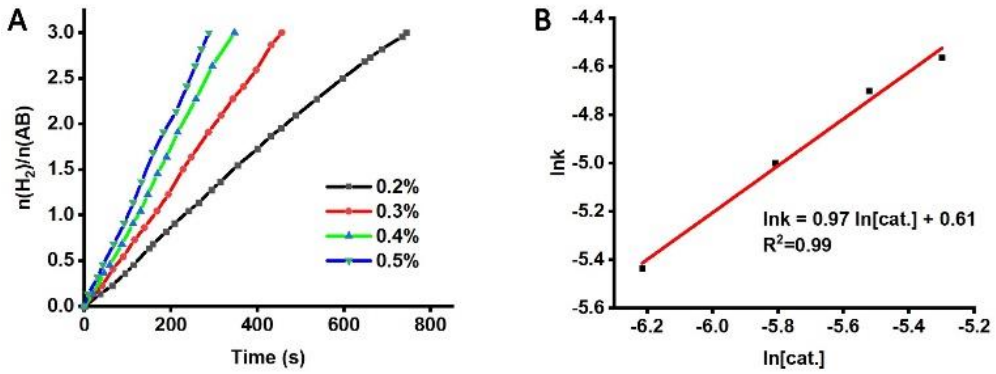

Figure 3.8. (A) Plots of the times of the AB hydrolytic dehydrogenation catalysed by the RhNP* nanocatalyst with various catalyst amounts. (B) Plots of the rates of H_2 generation vs. concentration of the RhNP* nanocatalyst both on natural logarithmic scales.

The time plot of hydrogen evolution from AB hydrolysis catalysed by various amount of RhNP* is shown in **Figure 3.8A**. Increasing the amount of catalyst is favorable for the acceleration of AB hydrolysis. The slop of logarithmic plot of H_2 generation vs. the amount of RhNP* is 0.97 (**Figure 3.8B**), indicating that the reaction is first order in catalyst amount.

Figure 3.9A depicts the temperature influence on AB hydrolysis catalysed by RhNP*; the H_2 evolution rate dramatically raises as the reaction temperature increases from 283K to 313K. From the Arrhenius plots in **Figure 3.9B**, the activation energy (*E*a) is calculated to be 26.1 KJ/mol according to the Arrhenius Equation (**Equation S 3.4**, **Experimental Section**).

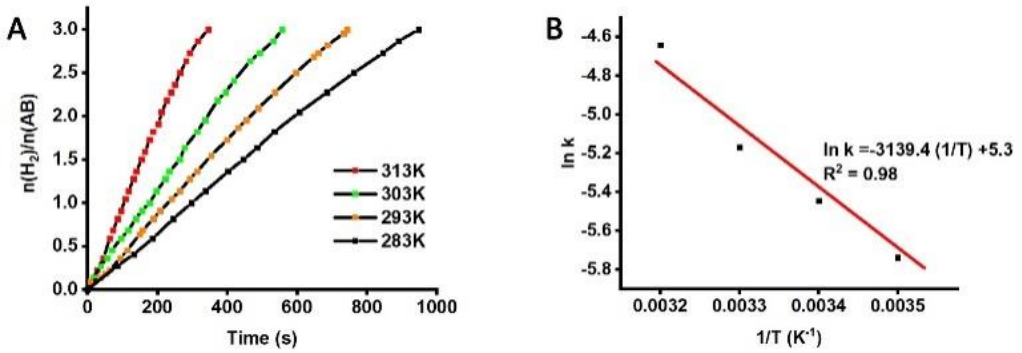

Figure 3.9. (A)Plots of the hydrogen evolution vs time for AB hydrolysis catalysed at various temperatures by 0.2 mol % RhNP* catalyst. (B) Kinetic data obtained from the Arrhenius plots.

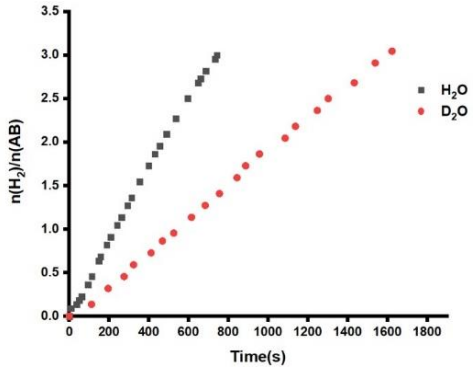

Figure 3.10. Evolution of H_2 upon NH_3BH_3 hydrolysis with H_2O and D_2O catalysed by 0.2 mol % RhNP* (KIE = 2.26).

When D_2O is used as solvent instead of H_2O for AB hydrolysis catalysed by 0.2% RhNP*, the result depicted in **Figure 3.10** shows a decreased reaction rate in D_2O, indicating a kinetic isotope effect (KIE = k_D/k_H)[20,42] of 2.3, suggesting that the cleavage of the O-H bond in water is highly involved in the rate-determining step.

As the KIE experiment indicated that an O-H bond of water was cleaved in the rate-determining step, deuterated water was used in tandem reaction for further investigation of the atomic composition of the H_2 gas produced. In a tandem reaction, two chambers for different reactions were

connected in a sealed system (**Figure 3.11**). H_2 evolution occurred in the left chamber in the presence of AB (31mg, 1mmol), RhNP* (0.2% mmol) and D_2O (2ml). Then, the produced H_2 gas transferred to the right chamber for the hydrogenation of styrene with the assistance of Pd/C and MeOD as solvent. After 24 h reaction at room temperature, the produced ethylbenzene was measured by ^1H NMR for confirmation. As shown in **Figure S 3.10 (Experimental Section)**, the integration of the ^1H NMR peaks at 7.12~7.28 ppm and 1.21~1.25 ppm is 5.00 and 3.03, respectively, corresponding to the phenyl and methyl groups. The peaks at 2.67~2.58 ppm, that are assigned to methylene group, show an integration of 0.84, less than the expected 2.00, indicating one D substitution in ethylbenzene. From the ^1H NMR of isotopic ethylbenzene, it is suggested that one H atom of the produced H_2 comes from water, and another H atom comes from AB in the hydrolysis of AB catalysed by RhNP*, confirming previous publications.

Based on the experimental result above, the mechanism confirms trends that were previously suggested. Owing to the hydridic property of B-H bond, water is prone to form $[NH_3BH_2H] \cdots$ H-OH complex with NH_3BH_3 via H bonding, which weakens the AB hydridic B-H bond and water O-H bond. Hydride transfer from AB to the nanocatalyst surface leads to B-H bond cleavage and formation of a negatively charged surface M-H species. The above H bonding with water bring water nearby the nanocatalyst surface, which very much facilitates water O-H cleavage (rate-determining step), and all the more so that electron density in this bond is weakened by this H bonding and the NP is more active in oxidative addition due to higher electron density brought by the negative charge. As a result, the first H_2 molecule is produced by reductive elimination of two surface hydrides, leaving on the NP

surface two fragments, $NH_3BH_2^-$ and OH^- that also reductively eliminate, which provides the reaction intermediate NH_3BH_2OH (**Figure 3.11**). Repetition of this process schematized in **Figure 3.11**, finally gives evolution of 3 equiv. H_2 (**Figure 3.12**).

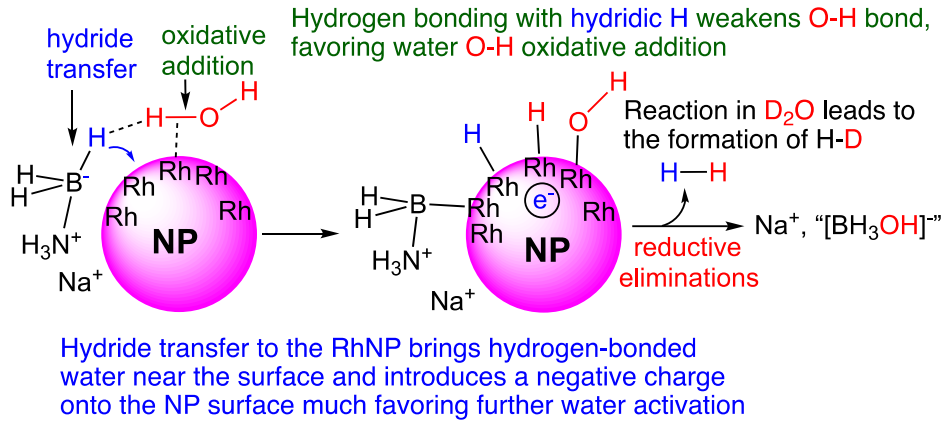

Figure 3.11. Schematized mechanism for the formation of the first H_2 molecule upon RhNP-catalyzed AB hydrolysis.

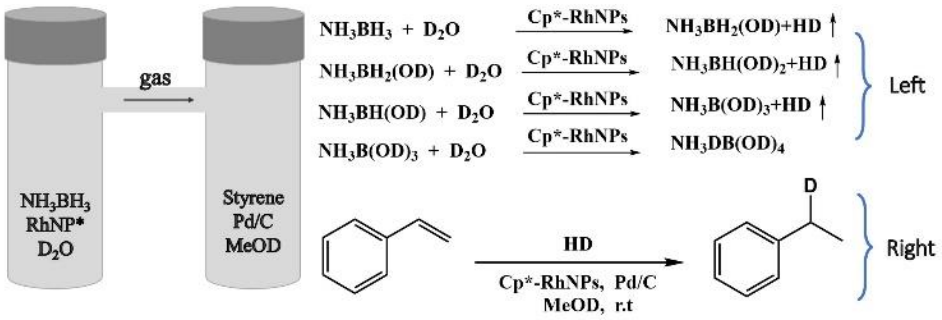

Figure 3.12 Tandem reaction of AB dehydrogenation in D_2O and hydrogenation of styrene in MeOD.

3.4. Conclusions

The TMNP and TMNP*, prepared from the reduction of late TM chloride salts by hydride-rich cobaltocene derivatives $[Co(\eta^5\text{-}C_5H_5)(\eta^4\text{-}C_5H_6)]$, **1H**, resp. $[Co(\eta^5\text{-}C_5Me_5)(\eta^4\text{-}C_5H_6)]$, **2H**, have been characterized.

They are used for the first time to carry out two catalytic H_2 evolution reactions using hydrolysis of both ammonia borane and $B_2(OH)_4$. The results reveal that the Rh nanocatalysts prepared in this way are among the best nanocatalysts for these reactions. For instance, they compare advantageously with previous nanocatalysts prepared using dendrimers[70,71] or metal organic frameworks.[53,72] RhNP* show a catalytic activity (TOF) superior to that of RhNP for $B_2(OH)_4$ hydrolysis, and this trend is opposite for AB hydrolysis whose reaction mechanism is very different (in AB hydrolysis, one H atom of H_2 comes from AB and the other ones from water, whereas in $B_2(OH)_4$ hydrolysis both H atoms of H_2 are provided by water). However, the activity of RhNP decreases in the course of the reactions due to lack of sufficient stability, and this RhNP is not recyclable due to aggregation. On the other hand, the TMNP* are stable nanocatalysts in the course of reactions, which is assigned to the steric bulk of the Cp* ligand of the organocobalt cation protecting the nanocatalyst surface. The RhNP* appear stable and recyclable at least three times without agglomeration; they are the best choice for the hydrolysis of both AB and $B_2(OH)_4$, and the catalytic results are good compared to the literature. Kinetic studies of AB dehydrogenation catalysed by RhNP* revealed that the reaction is zero order in AB concentration and first order in NP amount with a low activation energy E_a of 26.1 KJ/mol. The KIE value of 2.3 indicates that the O-H cleavage of water is highly involved in the rate-determining step, proposed to be much facilitated by H bonding between AB and water. This first and successful use of the new complex **2** to produce efficient nanocatalysts upon reduction of TM salts could in the future be extended to other catalytic systems. Great advantages of the use of these neutral hydridic cobalt complexes are their strong reducing power as hydride donors (still increased with the better electron donor ligand Cp*), their use as

both reductant and NP stabilizer with steric protection (still increased with the large Cp*), and the fact that their oxidized forms are fully stable and easily recovered as water soluble chloride salts. The catalytic performances are among the best ones compared to previous results, and this strategy should also allow further stabilization and catalytic use of the NPs on various other supports.

3.5. Experimental Section

Preparation of [Co(η^5-C_5Me_5) (η^4-C_5H_6)], 2H $NaBH_4$ (189.2 mg, 5 mmol) was added into the THF solution of Cp*CoCpPF_6 (202 mg, 0.5 mmol) in N_2 and subsequently, the color of the solution changed from yellow to orange to red, indicating the formation of the **2H** (**Equation S 3.1**). Overnight, THF was removed *in vacuo*, and 20 ml pentane was injected to dissolve **2H**. Finally, **2H** was purified by cannula filtration to get the product as red solid. The yield of **2H** is 90%. The formation of [Co(η^5-C_5Me_5)(η^4-C_5H_6)] is confirmed by ^{1}H NMR, ^{13}C NMR, FT-IR and Mass spectrum.

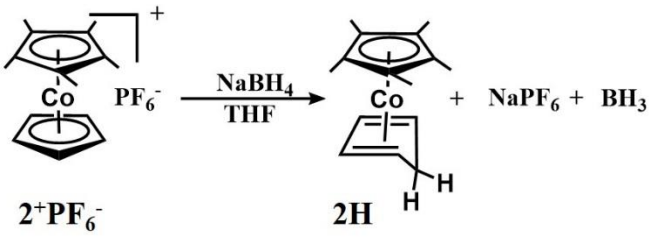

(S 3.1)

NMR of 2H A few accurate ^{1}H NNR spectra of π-cyclopentadiene complexes (bonded in a tetra-hapto fashion) have been published. To assign the proton peaks, deuterated [Co(η^5-C_5Me_5) (η^4-C_5H_5D)] was produced by reduction of **$2^+PF_6^-$** with $NaBD_4$ for comparison with **2H**. As shown in **Figure**

S 3.1, the signal at 1.55 ppm disappears for deuterated $\mathbf{2^D}$, indicating that the signal can be assigned to the *exo*-H (H_4) of the cobalt complex **2H**. Subsequently, the peaks at 4.33 ppm, 2.01 ppm, 1.53 ppm and 0.83 ppm are assigned to H_2, H_1, H_5 and H_3. (**Figure S 3.1**). The signal at 1.74 ppm is assigned to impurity. ^{13}C NMR in **Figure S 3.2** shows peaks at 80.49 ppm, 49.88 ppm, 17.47 ppm, 14.13 ppm, 11.98 ppm, corresponding to $-CH_3$, $-C_5Me_5$ and the three C signals in cyclopentadiene.

MS spectrum of 2H the mass spectrum shows a weak molecular peak at m/e 260.1 and the base peak at m/e 259.1. (**Figure S 3.3**) The former peak corresponds to the compound **2H**, while the latter peak is assigned to the hydride loss of compound **2H** and the formation of stable pentamethylcobalticenium cation $\mathbf{2^+}$.

FT-IR spectrum of 2H in the FT-IR spectrum of **2H**, there is a characteristic band of π-C_5H_5-metal groups, including a single C-H stretching band at 3097cm^{-1}. The bands at 2960 cm^{-1}, 2891 cm^{-1} corresponds to the aliphatic C-H stretching frequencies. Comparing with the cationic $\mathbf{2^+PF_6^-}$, **2H** shows an unusual band at 2736 cm^{-1} and 2614 cm^{-1}, attributed to the $C\text{-}H_{endo}$ and $C\text{-}H_{exo}$ stretching frequency, owing to a steric and electrostatic interactions between Co and H_{endo} / H_{exo}. The bands at 1443~1316 cm^{-1} are recognized as the C-C stretching frequency for the cyclopentadienyl ring. (**Figure S 3.4**)

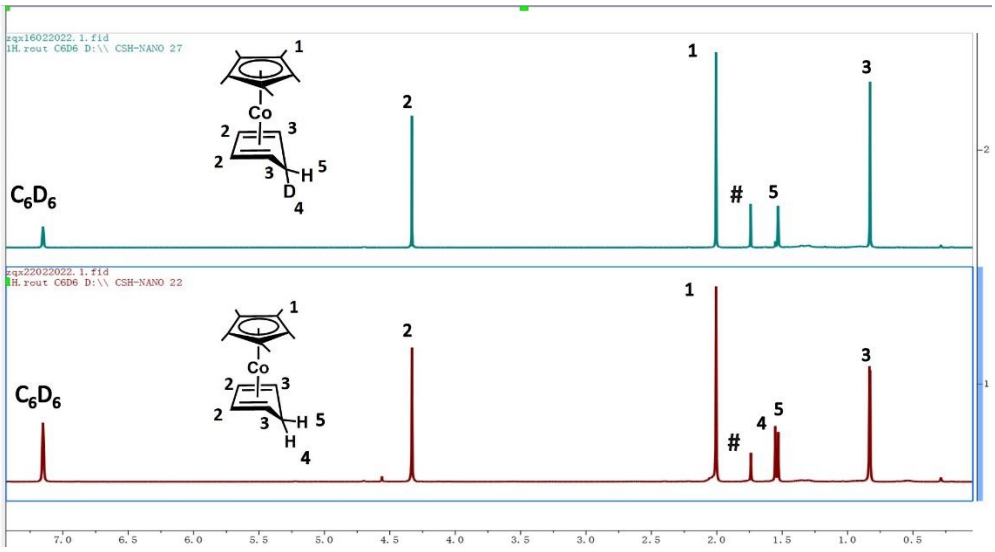

Figure S 3.1. ^{1}H NMR of [Co(η^5-C_5Me_5) (η^4-C_5H_6)] and [Co(η^5-C_5Me_5) (η^4-C_5H_5D)]: ^{1}H NMR (300 MHz, C_6D_6).

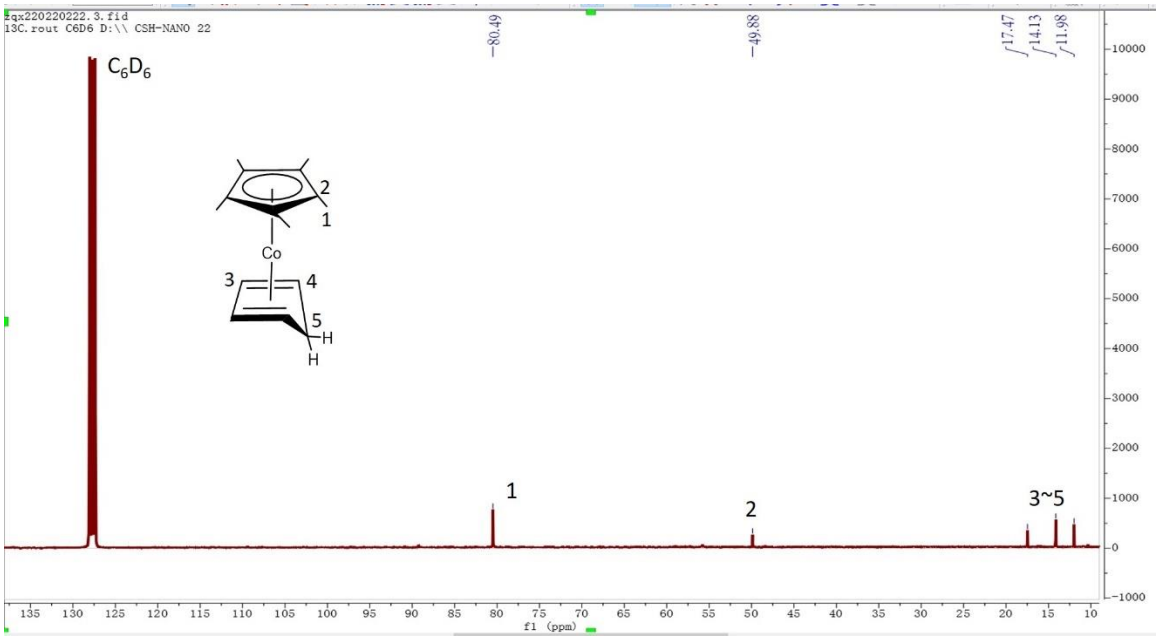

Figure S 3.2. ^{13}C NMR of [Co(η^5-C_5Me_5)(η^4-C_5H_6)], **2H**: ^{13}C NMR (300 MHz, C_6D_6).

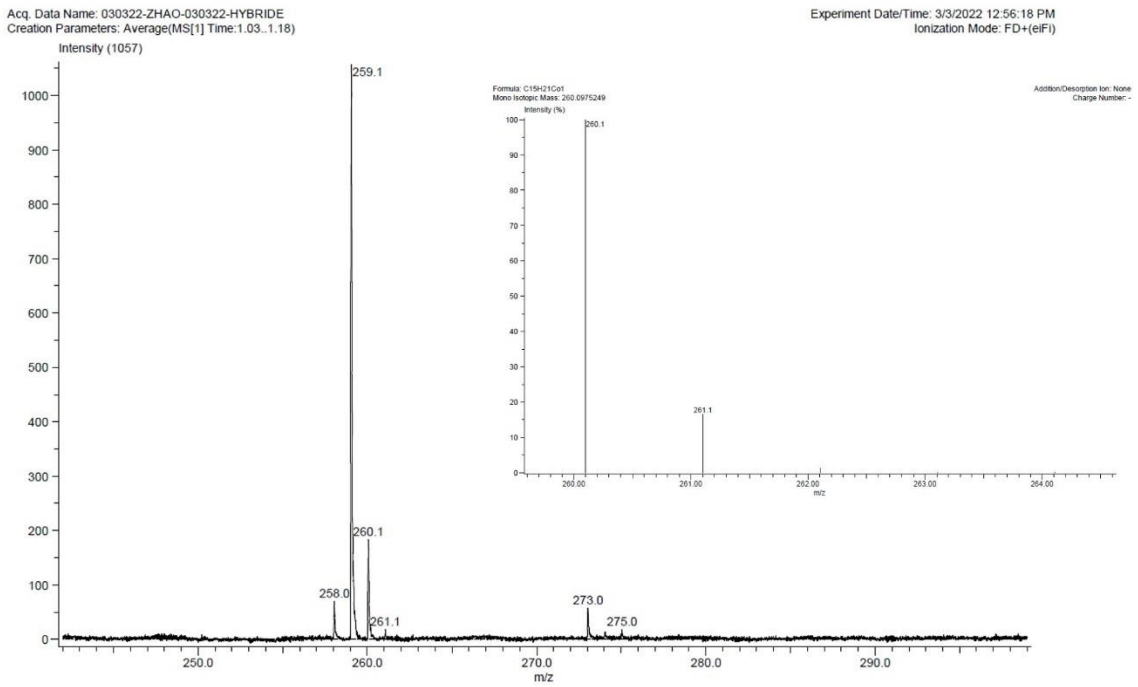

Figure S 3.3. MS spectrum of [Co(η^5-C_5Me_5)(η^4-C_5H_6)], **2H.** Inserted: the excepted MS spectrum of [Co(η^5-C_5Me_5)(η^4-C_5H_6)]

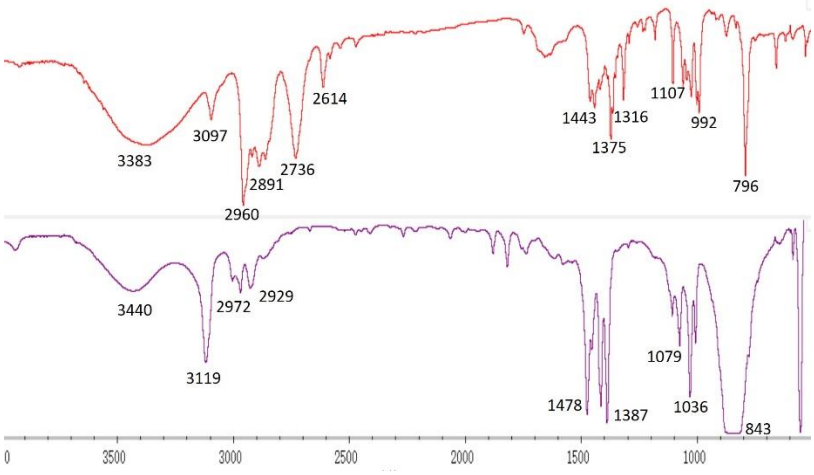

Figure S 3.4. FT-IR spectrum of [Co(η^5-C_5Me_5)(η^4-C_5H_6)], **2H**, (upper) and [Co(η^5-C_5Me_5)(η^5-C_5H_5)]$^+PF_6^-$, **$2^+PF_6^-$**, (bottom)

Preparation of [Co(η^5-C_5H_5)(η^4-C_5H_6)], 1H

$NaBH_4$ (189.2 mg, 5 mmol) was added into the THF solution of $CpCoCpPF_6$ (167 mg, 0.5 mmol)

in N_2 and, immediately, the color of the solution changed from yellow to red, indicating the formation of **1H** (**Equation S 3.2**). 2h later, THF was removed *in vacuo*, and 20 ml pentane was injected to dissolve **1H**. Finally, **1H** was purified by cannula filtration to get the compound as red solid. The yield of **1** was 90%.

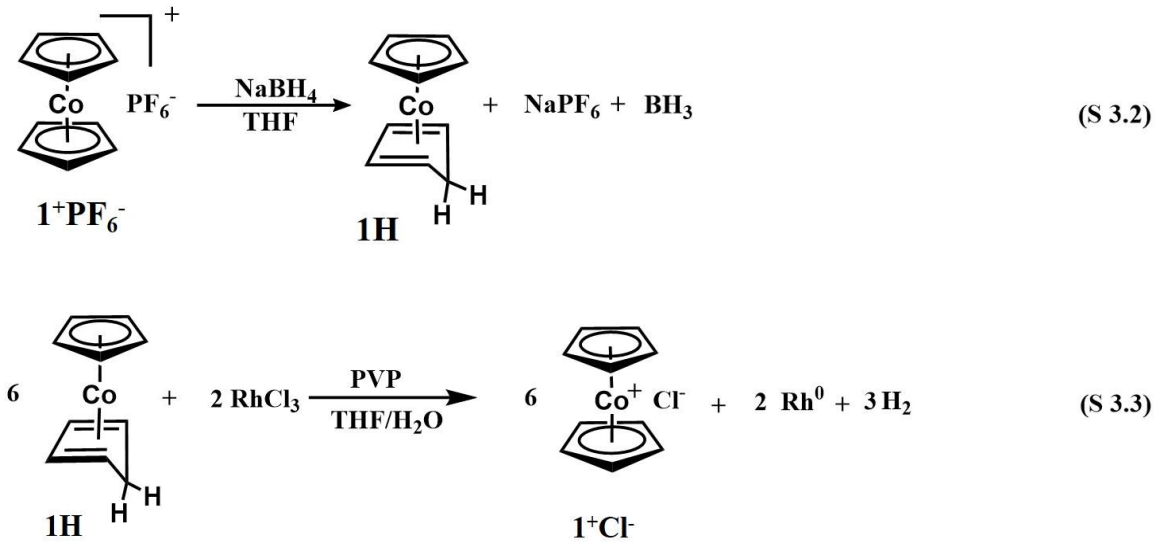

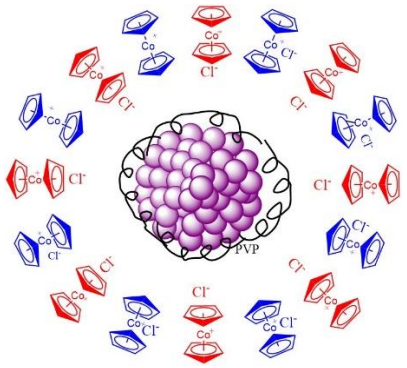

Figure S 3.5. Schematic illustration of RhNP upon reduction of $RhCl_3$ by [Co(η^5-C_5H_5)(η^4-C_5H_6)], **1**. The red color shows coordination of Cl^- to the NP core, and the blue color shows metallocenyl chloride without coordination (corresponding to Rh atoms in the core that are not surface atoms).

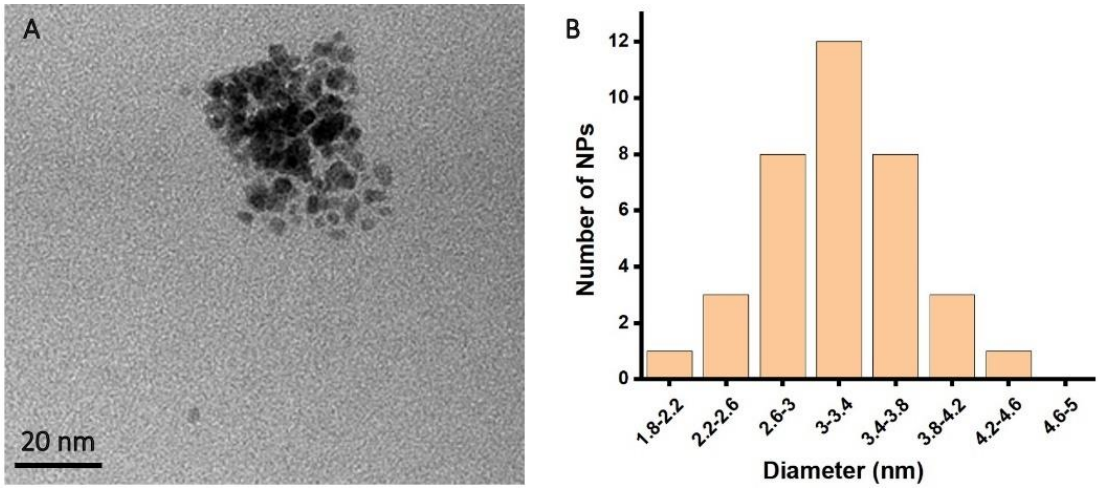

Figure S 3.6. TEM images and size distribution of the RhNP.

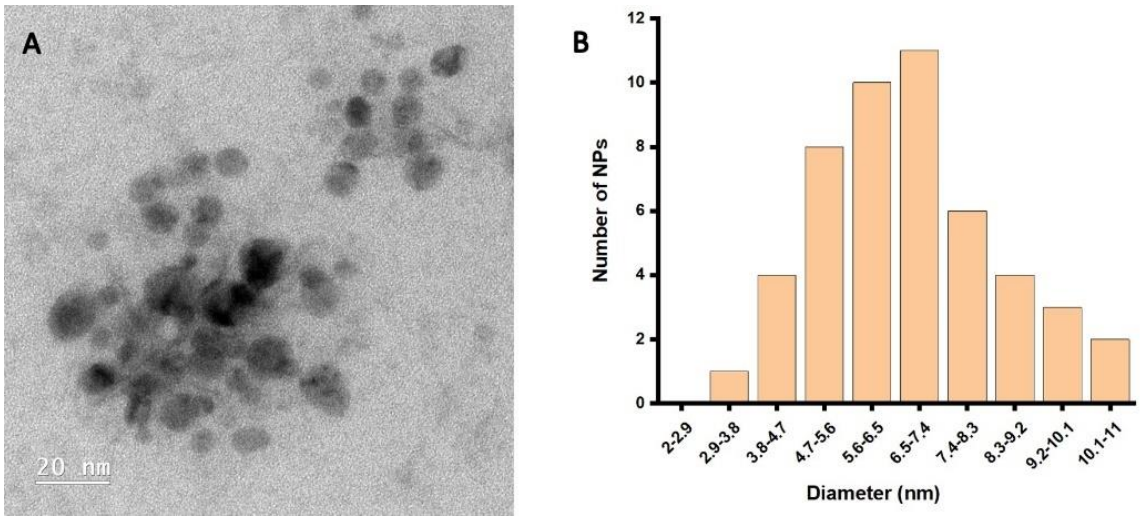

Figure S 3.7. TEM images and size distribution of the AuNPs*.

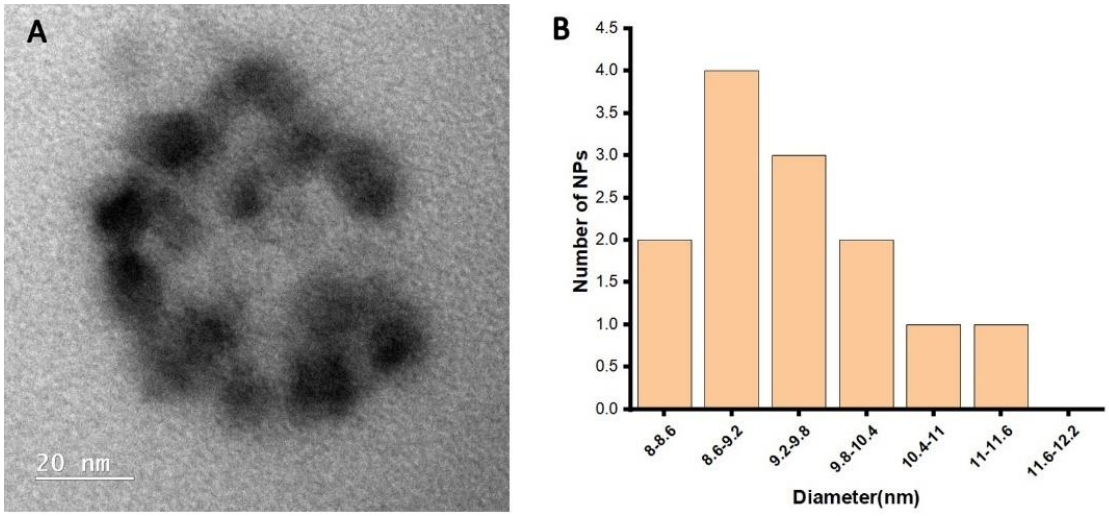

Figure S 3.8. TEM images and size distribution of the CuNPs*.

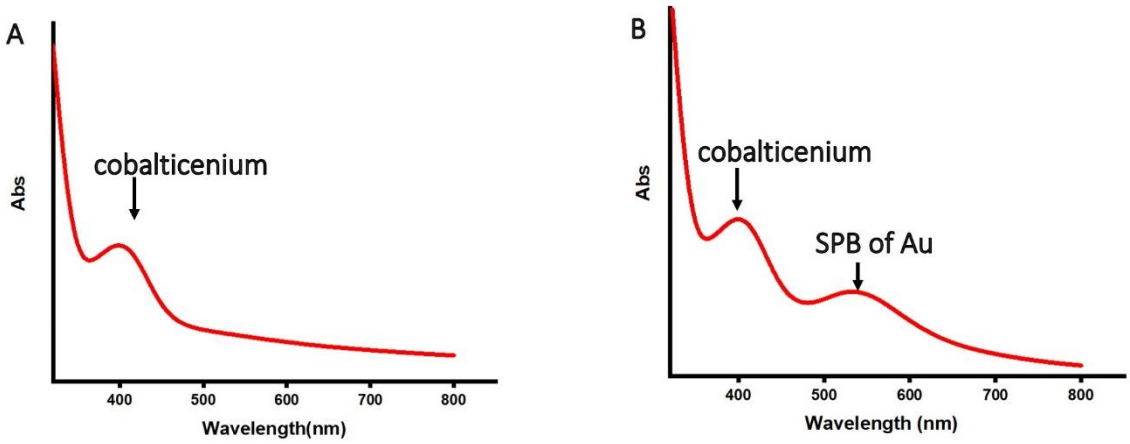

Figure S 3.9. UV-vis. spectra of RhNP* (A), AuNP* (B)

H_2 evolution from $B_2(OH)_4$ and AB hydrolysis catalysed by TMNP and TMNP* The catalytic hydrolysis of $B_2(OH)_4$ was carried out at 20 ± 1 °C. In a typical experiment, 0.2 % mmol RhNP* (5 ml H_2O + 1 ml THF) was placed in a 50 ml round bottom flask with two outlets. Then, $B_2(OH)_4$ (1 mmol, 90 mg) dissolved in 5 ml deionized water was added under

vigorous stirring. The measurement of the produced H_2 gas was conducted in a typical water-filled gas burette.

The catalytic hydrolysis of AB was carried out at 20 ± 1 °C. In a typical experiment, 0.2 % mmol RhNP* (5 ml H_2O + 1 ml THF) was placed in a 50ml round bottom flask with two outlets. Then, AB (1 mmol, 31 mg) dissolved in 1 ml deionized water was added under vigorous stirring. The measurement of the produced H_2 gas was conducted in a typical water-filled gas burette. The temperature of the reaction was measured using an electronic thermometer.

$$lnk = -\frac{Ea}{RT} + lnA \qquad (\boldsymbol{S\ 3.4})$$

Table S 3.1. TOF values of RhNP and RhNP* in $B_2(OH)_4$ and AB hydrolysis

	$B_2(OH)_4$		AB	
	RhNP	RhNP*	RhNP	RhNP*
NP diameter(nm)	3.0	2.5	3.0	2.5
Atom diameter(nm)	0.135	0.135	0.135	0.135
TOF_t	579	1364	165	125
TOF_s	3217	6315	917	578

the unit of TOF_t and TOF_s is $mol_{H_2}\ mol_{cat}^{-1}\ min^{-1}$.

Table S 3.2. Comparison of the catalytic performances of nanocatalysts in $B_2(OH)_4$ hydrolysis

Catalyst	Support	NPs loading	TOF [a]
RhNP*	pentamethylcobalticenium	0.2mol%	6315
RhNP	cobalticenium	0.2mol%	3217
RhNP[73]	graphene quantum dots	0.4 mol‰	3658
PtNP[73]	graphene quantum dots	0.4 mol‰	4603
AuNP[73]	graphene quantum dots	0.4 mol‰	1698
PdNP[73]	graphene quantum dots	0.4 mol‰	802
IrNP[73]	graphene quantum dots	0.4mol ‰	185
RuNP[73]	graphene quantum dots	0.4 mol‰	127
Glucan-PtNP[73]	Glucan	0.4 mol‰	830
TiO_2-PtNP[73]	TiO_2	3.66 wt %	681
Pt/C[73]	Carbon	5.0 wt %	300
Rh@dendrimer[74]	dendrimer	0.1mol%	132

[a] TOF = TOF_s= $mol_{H_2\ produced}$ / [surface mol_{cat_t}× reaction time (min)] the unit is $mol_{H_2}\ mol_{cat}^{-1}\ min^{-1}$.

Table S 3.3. Comparison of catalytic performance of RhNPs anchored on different supports in AB hydrolysis

Catalyst	Support	NPs loading	TOF [a]
RhNP*	pentamethylcobalticenium	0.2%	578
RhNP	cobalticenium	0.2%	917
RhNPs/dendrimer[75]	Dendrimer	1%	244
RhNPs/THPP[76]	THPP	0.2%	132
GQDs -RhNPs[77]	GQDs	0.4%	642
Rh_1/VO_2 [78]	VO_2 nanorods	0.2%	48
Rh^0/CeO_2[79]	CeO_2	0.8%	2010
Rh^0/SiO_2[79]	SiO_2	0.8%	112
Rh^0/Al_2O_3[79]	Al_2O_3	0.8%	195
Rh^0/TiO_2[79]	TiO_2	0.8%	105
Rh^0/ZrO_2[79]	ZrO_2	0.8%	102
Rh^0/HfO_2[79]	HfO_2	0.8%	24
Rh(0)/CNT[80]	CNT	0.25%	706
Rh/graphene[81]	Graphene	0.4%	325
Rh(0)@TiO_2[82]	TiO_2	0.116%	260

[a] TOF = $mol_{H_2\ produced}$ / [surface mol_{cat_t} × reaction time (min)], the unit is $mol_{H_2}\ mol_{cat}^{-1}\ min^{-1}$.

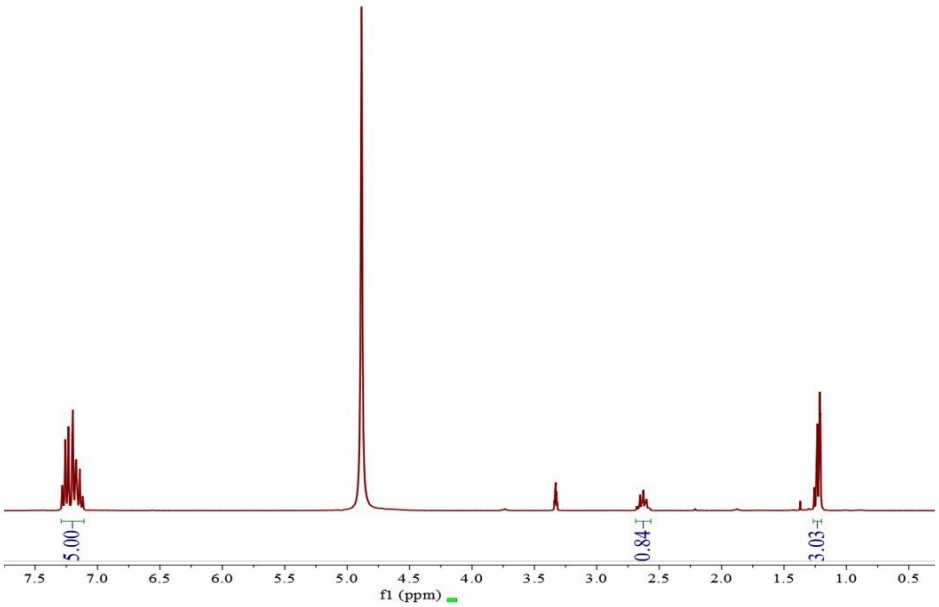

Figure S 3.10. ^{1}H NMR spectrum of the hydrogenation product of styrene in CD_3OD. 1H NMR (300 MHz, CD_3OD) δ 7.12~7.28 ppm (CH-arom, 5.00H), 2.67~2.58ppm (-CH2, 0.84H), 1.21~1.25 ppm (-CH3, 3.03H).

3.6. References

1. REN21, Renewables 2018 Global Status Report, 2018, **http://www.ren21.net/about-ren21/about-us/**.

2. S. Chu and A. Majumdar, Opportunities and challenges for a sustainable energy future, *Nature*, 2012, **488**, 294-303.

3. J. Zhu, L. Hu, P. Zhao, L. Y. S. Lee and K. Y. Wong, Recent Advances in Electrocatalytic Hydrogen Evolution Using Nanoparticles, *Chem. Rev.*, 2020, **120**, 851-918.

4. N. S. Lewis and D. G. Nocera, Powering the planet:

   Chemical challenges in solar energy utilization, *Proc. Natl. Acad. Sci. U.S.A.*, 2006, **103**, 15729-15735.

5. B. Ates, S. Koytepe, A. Ulu, C. Gurses and V. K. Thakur, Chemistry, Structures, and Advanced Applications of Nanocomposites from Biorenewable Resources, *Chem. Rev.*, 2020, **120**, 9304-9362.

6. T. He, P. Pachfule, H. Wu, Q. Xu and P. Chen, Hydrogen Carriers. *Nat. Rev. Mater.*, 2016, **1**, 16059.

7. Y. Tachibana, L. Vayssieres and J. R. Durrant, Artificial photosynthesis for solar water-splitting, *Nat. Photonics*, 2012, **6**, 511-518.

8. S. E. Hosseini and M. A. Wahid, Hydrogen production from renewable and sustainable energy resources: Promising green energy carrier for clean development, *Renew. Sustain. Energy Rev.*, 2016, **57**, 850-866.

9. P. Nikolaidis and A. Poullikkas, A comparative overview of hydrogen production processes, *Renew. Sustain. Energy Rev.*, 2017, **67**, 597-611.

10. Z. Huang, S. Wang, R. D. Dewhurst, N. V. Ignat'ev, M. Finze and H. Braunschweig, Boron: Its Role in Energy-Related Processes and Applications, *Angew. Chem. Int. Ed.*, 2020, **59**, 8800-8816.

11. J. Shen, W. Chen, G. Lv, Z. Yang, J. Yan, X. Liu and Z. Dai, Hydrolysis of NH_3BH_3 and $NaBH_4$ by graphene quantum dots-transition metal nanoparticles for highly effective hydrogen evolution, *Int. J. Hydrog. Energy*, 2021, **46**, 796-805.

12. Q. Zhao, R. D. Dewhurst, H. Braunschweig and X. Chen, A New Perspective on Borane Chemistry: The Nucleophilicity of the B−H Bonding Pair Electrons, *Angew. Chem., Int. Ed.*, 2019, **58**, 3268-3278.

13. A. Staubitz, A. P. M. Robertson and I. Manners, Ammonia-Borane and Related Compounds as Dihydrogen Sources, *Chem. Rev.*, 2010, **110**, 4079-4124.

14. Z. Li, T. He, D. Matsumura, S. Miao, A. Wu, L. Liu, G. Wu and P. Chen, Atomically Dispersed Pt on the Surface of Ni Particles: Synthesis and Catalytic Function in Hydrogen Generation from Aqueous Ammonia–Borane, *ACS Catal.*, 2017, **7**, 6762-6769.

15. D. W. Himmelberger, C. W. Yoon, M. E. Bluhm, P. J. Carroll and L. G. Sneddon, Base-Promoted Ammonia Borane Hydrogen-Release, *J. Am. Chem. Soc.*, 2009, **131**, 14101-14110.

16. H. Wu, Y. Cheng, B. Wang, Y. Wang, M. Wu, W. Li, B. Liu and S. Lu, Carbon dots-confined CoP-CoO nanoheterostructure with strong interfacial synergy triggered the robust hydrogen evolution from ammonia borane, *J. Energy Chem.*, 2021, **57**, 198-205.

17. W. Chen, X. Duan, G. Qian, D. Chen and X. Zhou, Carbon Nanotubes as Support in the Platinum-Catalyzed Hydrolytic Dehydrogenation of Ammonia Borane, *ChemSusChem*, 2015, **8**, 2927-2931.

18. S. Akbayrak, Y. Tonbul and S. Özkar, Ceria supported rhodium nanoparticles: Superb catalytic activity in hydrogen generation from the hydrolysis of ammonia borane, *Appl. Catal. B*, 2016, **198**, 162-170.

19. W. W. Zhan, Q. L. Zhu and Q. Xu, Dehydrogenation of Ammonia Borane by Metal Nanoparticle Catalysts, *ACS Catal.*, 2016, **6**, 6892-6905.

20. Q. Wang, F. Fu, S. Yang, M. Martinez Moro, M. d. l. A. Ramirez, S. Moya, L. Salmon, J. Ruiz and D. Astruc, Dramatic Synergy in CoPt Nanocatalysts Stabilized by "Click" Dendrimers for Evolution of Hydrogen from Hydrolysis of Ammonia Borane, *ACS Catal.*, 2018, **9**, 1110-1119.

21. P. Xu, W. Lu, J. Zhang and L. Zhang, Efficient Hydrolysis of Ammonia Borane for Hydrogen Evolution Catalyzed by Plasmonic Ag@Pd Core–Shell Nanocubes, *ACS Sustain. Chem. Eng.*, 2020, **8**, 12366-12377.

22. S. Rej, C. F. Hsia, T. Y. Chen, F. C. Lin, J. S. Huang and M. H. Huang, Facet-Dependent and Light-Assisted Efficient Hydrogen Evolution from Ammonia Borane Using Gold–Palladium Core–Shell Nanocatalysts, *Angew. Chem. Int. Ed.*, 2016, **55**, 7222-7226.

23. Y. Wu, Y. Sun, W. Fu, X. Meng, M. Zhu, S. Ramakrishna and Y. Dai, Graphene-Based Modulation on the Growth of Urchin-like $Na_2Ti_3O_7$ Microspheres for Photothermally Enhanced H_2 Generation from Ammonia Borane, *ACS Appl. Nano Mater.*, 2020, **3**, 2713-2722.

24. F. Fu, C. Wang, Q. Wang, A. M. Martinez-Villacorta, A. Escobar, H. Chong, X. Wang, S. Moya, L. Salmon, E. Fouquet, J. Ruiz and D. Astruc, Highly Selective and Sharp Volcano-type Synergistic Ni_2Pt@ZIF-8-Catalyzed Hydrogen Evolution from Ammonia Borane Hydrolysis, *J. Am. Chem. Soc.*, 2018, **140**, 10034-10042.

25. C. Wang, J. Tuninetti, Z. Wang, C. Zhang, R. Ciganda, L. Salmon, S. Moya, J. Ruiz and D. Astruc, Hydrolysis of Ammonia-Borane over Ni/ZIF-8 Nanocatalyst: High Efficiency, Mechanism, and Controlled Hydrogen Release, *J. Am. Chem. Soc.*, 2017, **139**, 11610-11615.

26. J. M. Yan, X. B. Zhang, S. Han, H. Shioyama and Q. Xu, Iron-nanoparticle-catalyzed hydrolytic dehydrogenation of ammonia borane for chemical hydrogen storage, *Angew. Chem. Int. Ed.*, 2008, **47**, 2287-2289.

27. W. Chen, D. Li, C. Peng, G. Qian, X. Duan, D. Chen and X. Zhou, Mechanistic and Kinetic Insights into the Pt-Ru Synergy during Hydrogen Generation from Ammonia Borane over PtRu/CNT Nanocatalysts, *J. Catal.*, 2017, **356**, 186-196.

28. K. Mori, K. Miyawaki and H. Yamashita, Ru and Ru-Ni Nanoparticles on TiO_2 Support as Extremely Active Catalysts for Hydrogen Production from Ammonia-Borane, *ACS Catal.*, 2016, **6**, 3128-3135.

29. L. Wang, H. Li, W. Zhang, X. Zhao, J. Qiu, A. Li, X. Zheng, Z. Hu, R. Si and J. Zeng, Supported Rhodium Catalysts for Ammonia–Borane Hydrolysis: Dependence of the Catalytic Activity on the Highest Occupied State of the Single Rhodium Atoms, *Angew. Chem. Int. Ed.*, 2017, **56**, 4712-4718.

30. H. Cheng, T. Kamegawa, K. Mori and H. Yamashita, Surfactant-free nonaqueous synthesis of plasmonic molybdenum oxide nanosheets with enhanced catalytic activity for hydrogen generation from ammonia borane under visible light, *Angew. Chem. Int. Ed.*, 2014, **53**, 2910-2914.

31. J. Zhang, W. Chen, H. Ge, C. Chen, W. Yan, Z. Gao, J. Gan, B. Zhang, X. Duan and Y. Qin, Synergistic Effects in Atomic-layer-deposited PtCox/CNTs Catalysts Enhancing Hydrolytic Dehydrogenation of ammonia Borane, *Appl. Catal. B-Environ.*, 2018, **235**, 256-263.

32. L. Yin, T. Zhang, K. Dai, B. Zhang, X. Xiang and H. Shang, Ultrafine PtCo Alloy Nanoclusters Confined in N-Doped Mesoporous Carbon Spheres for Efficient Ammonia Borane Hydrolysis, *ACS Sustain. Chem. Eng.*, 2021, **9**, 822-832.

33. Q. Zhao, N. Kang, M. Martínez Moro, E. Guisasola, S. Moya, E. Coy, L. Salmon, X. Liu and D. Astruc, Sharp Volcano-Type Synergy and Visible Light Acceleration in H_2 Release upon $B_2(OH)_4$ Hydrolysis Catalyzed by Au-Rh@Click-Dendrimer Nanozymes, *ACS A.E.M*, 2022, **5**, 3834–3844.

34. W. Chen, J. Shen, Y. Huang, X. Liu and D. Astruc, Catalyzed Hydrolysis of Tetrahydroxydiboron by Graphene Quantum Dot-Stabilized Transition-Metal Nanoparticles for Hydrogen Evolution, *ACS Sustain. Chem. Eng.*, 2020, **8**, 7513-7522.

35. J. Zhou, Y. Huang, J. Shen and X. Liu, Pd/C-Catalyzed H2 Evolution from Tetrahydroxydiboron Hydrolysis, *Catal. Lett.*, 2021, **151**, 3004-3010.

36. T. Wartik and E. F. Apple, A New Modification of Boron Monoxide, *J. Am. Chem. Soc.*, 1955, **77**, 6400-6401.

37. Z.-Y. Sun, S. Zhou, K. Yang, M. Guo, W. Zhao, X. Tang and G. Wang, Tetrahydroxydiboron-Promoted Radical Addition of Alkynols, *Org. Lett.*, 2020, **22**, 6214-6219.

38. S. Sebelius, V. J. Olsson and K. J. Szabó, Palladium Pincer Complex Catalyzed Substitution of Vinyl Cyclopropanes, Vinyl Aziridines, and Allyl Acetates with Tetrahydroxydiboron. An Efficient Route to Functionalized Allylboronic Acids and Potassium Trifluoro(allyl)borates, *J. Am. Chem. Soc.*, 2005, **127**, 10478-10479.

39. A. T. Londregan, D. W. Piotrowski and J. Xiao, Rapid and Selective in situ Reduction of Pyridine-N-oxides with Tetrahydroxydiboron, *Synlett*, 2013, **24**, 2695-2700.

40. D. Y. Chen, Y. M. Zhou, H. F. Zhou, S. S. Liu, Q. X. Liu, K. L. Zhang and Y. Uozumi, Metal-free Reduction of Nitro Aromatics to Amines with $B_2(OH)_4/H_2O$, *Synlett*, 2018, **29**, 1765-1768.

41. S. P. Cummings, T. N. Le, G. E. Fernandez, L. G. Quiambao and B. J. Stokes, Tetrahydroxydiboron-Mediated Palladium-Catalyzed Transfer Hydrogenation and Deuteriation of Alkenes and Alkynes Using Water as the Stoichiometric H or D Atom Donor, *J. Am. Chem. Soc.*, 2016, **138**, 6107-6110.

42. M. Gomez-Gallego and M. A. Sierra, Kinetic isotope effects in the study of organometallic reaction mechanisms, *Chem. Rev.*, 2011, **111**, 4857-4963.

43. C. B. M. and, C. R. Kagan and M. G. Bawendi, Synthesis and Characterization of Monodisperse Nanocrystals and Close-Packed Nanocrystal Assemblies, *Annu. Rev. Mater. Sci.*, 2000, **30**, 545-610.

44. M.-C. Daniel and D. Astruc, Gold Nanoparticles: Assembly, Supramolecular Chemistry, Quantum-Size-Related Properties, and Applications toward Biology, Catalysis, and Nanotechnology, *Chem. Rev.*, 2004, **104**, 293-346.

45. P. Hervés, M. Pérez-Lorenzo, L. M. Liz-Marzán, J. Dzubiella, Y. Lu and M. Ballauff, Catalysis by metallic nanoparticles in aqueous solution: model reactions, *Chem. Soc. Rev.*, 2012, **41**, 5577-5587.

46. X.-F. Yang, A. Wang, B. Qiao, J. Li, J. Liu and T. Zhang, Single-Atom Catalysts: A New Frontier in Heterogeneous Catalysis, *Acc. Chem. Res.*, 2013, **46**, 1740-1748.

47. D. Wang and D. Astruc, Fast-Growing Field of Magnetically Recyclable Nanocatalysts, *Chem. Rev.*, 2014, **114**, 6949-6985.

48. M. L. Brongersma, N. J. Halas and P. Nordlander, Plasmon-induced hot carrier science and technology, *Nat. Nanotechnol.*, 2015, **10**, 25-34.

49. D. Wang and D. Astruc, The recent development of efficient Earth-abundant transition-metal nanocatalysts, *Chem. Soc. Rev.*, 2017, **46**, 816-854.

50. L. Liu and A. Corma, Metal Catalysts for Heterogeneous Catalysis: From Single Atoms to Nanoclusters and Nanoparticles, *Chem. Rev.*, 2018, **118**, 4981-5079.

51. D. Astruc, Introduction: Nanoparticles in Catalysis, *Chem. Rev.*, 2020, **120**, 461-463.

52. S. Ji, Y. Chen, X. Wang, Z. Zhang, D. Wang and Y. Li, Chemical Synthesis of Single Atomic Site Catalysts, *Chem. Rev.*, 2020, **120**, 11900-11955.

53. Q. Wang and D. Astruc, State of the Art and Prospects in Metal-Organic Framework (MOF)-Based and MOF-Derived Nanocatalysis, *Chem. Rev.*, 2020, **120**, 1438-1511.

54. L. Nguyen, F. F. Tao, Y. Tang, J. Dou and X.-J. Bao, Understanding Catalyst Surfaces during Catalysis through Near Ambient Pressure X-ray Photoelectron Spectroscopy, *Chem. Rev.*, 2019, **119**, 6822-6905.

55. Z. Zheng, H. Li, T. Liu and R. Cao, Monodisperse noble metal nanoparticles stabilized in SBA-15: Synthesis, characterization and application in microwave-assisted Suzuki–Miyaura coupling reaction, *J. Catal.*, 2010, **270**, 268-274.

56. D. Astruc, F. Lu and J. R. Aranzaes, Nanoparticles as Recyclable Catalysts: The Frontier between Homogeneous and Heterogeneous Catalysis, *Angew. Chem. Int. Ed.*, 2005, **44**, 7852-7872.

57. C. Schöttle, P. Bockstaller, R. Popescu, D. Gerthsen and C. Feldmann, Sodium-Naphthalenide-Driven Synthesis of Base-Metal Nanoparticles and Follow-up Reactions, *Angew. Chem. Int. Ed.*, 2015, **54**, 9866-9870.

58. C. Schöttle, D. E. Doronkin, R. Popescu, D. Gerthsen, J.-D. Grunwaldt and C. Feldmann, Ti0 nanoparticles via lithium-naphthalenide-driven reduction, *Chem. Commun.*, 2016, **52**, 6316-6319.

59. F. Fu, R. Ciganda, Q. Wang, A. Tabey, C. Wang, A. Escobar, A. M. Martinez-Villacorta, R. Hernández, S. Moya, E. Fouquet, J. Ruiz and D.

Astruc, Cobaltocene Reduction of Cu and Ag Salts and Catalytic Behavior of the Nanoparticles Formed, *ACS Catal.*, 2018, **8**, 8100-8106.

60. S. Zhang, K. Moudgil, E. Jucov, C. Risko, T. V. Timofeeva, S. R. Marder and S. Barlow, Organometallic hydride-transfer agents as reductants for organic semiconductor molecules, *Inorg. Chim. Acta*, 2019, **489**, 67-77.

61. N. G. Connelly and W. E. Geiger, Chemical Redox Agents for Organometallic Chemistry, *Chem. Rev.*, 1996, **96**, 877-910.

62. D. Mandon, L.Toupet and D. Astruc, Electron-Transfer Pathways in the Hydride Abstraction by Ph_3C^+ from Exo-Substituted Cyclohexadiene Fe(0) Complexes : A Key in the Synthesis of Heterobifunctional Cyclohexadienes from Benzene, *J. Am. Chem. Soc.*, 1986, ***108***, 1320-1321.

63. P. Michaud, D. Astruc and J. H. Ammeter, Electon-Transfer Pathways in the Reduction of d^6 and d^7 Organo-Iron Cations by $LiAlH_4$ and $NaBH_4$, *J. Am. Chem. Soc.*, 1982, ***104***, 3755-3757.

64. B. D. Naab, S. Guo, S. Olthof, E. G. B. Evans, P. Wei, G. L. Millhauser, A. Kahn, S. Barlow, S. R. Marder and Z. Bao, Mechanistic Study on the Solution-Phase *n*-Doping of 1,3-Dimethyl-2-aryl-2,3-dihydro-1H-benzoimidazole Derivatives, *J. Am. Chem. Soc.*, 2013, **135**, 15018-15025.

65. X. Han, W. Hao, X.-Q. Zhu and V. D. Parker, A Thermodynamic and Kinetic Study of Hydride Transfer of a Caffeine Derivative, *J. Org. Chem.*, 2012, **77**, 6520-6529.

66. F. Fu, Q. Wang, R. Ciganda, A. M. Martinez-Villacorta, A. Escobar, S. Moya, E. Fouquet, J. Ruiz and D. Astruc, Electron- and Hydride-Reservoir

Organometallics as Precursors of Catalytically Efficient Transition Metal Nanoparticles in Water, *Chem. Eur. J*, 2018, **24**, 6645-6653.

67. X. Meng, C. Ma, L. Jiang, R. Si, X. Meng, , Y. Tu, , L. Yu, X. Bao and D. Deng, Distance Synergy of MoS_2-Confined Rhodium Atoms for Highly Efficient Hydrogen Evolution, *Angew. Chem. Int. Ed.*, 2020, **132**, 10588-10593

68. W. Wang, R. Ciganda, C. Wang, A. Escobar, A. M. Martinez-Villacorta, M. de los Angeles Ramirez, Ricardo Hernandez, S. E. Moya, J. Ruiz, J.-R. Hamon and D. Astruc, High catalytic activity of Rh nanoparticles generated from cobaltocene and RhCl3 in aqueous solution, ***Inorg. Chem. Front.,*** 2019, **6**, 2704-2708.

69. D. Astruc, *Organometallic Chemistry and Catalysis*, Berlin: Springer, 2007.

70. M. C. Daniel, J. Ruiz, N. Dro and D. Astruc, Synthesis of five generations of redox-sTable pentamethylamidoferrocenyl dendrimers, *Chem. Eur. J*. 2003, **9**, 4371-4379.

71. D. Astruc, Electron-transfer processes in dendrimers and their implication in biology, catalysis, sensing and nanotechnology, *Nat. Chem*. 2012, **4**, 255-267.

72. C. L. Wang, Q. Wang, F. Fu and D. Astruc, Hydrogen Generation upon Nanocatalyzed Hydrolysis of Hydrogen-Rich Boron Derivatives: Recent Developments, *Acc. Chem. Res*. 2020, **53**, 2483-2493.

73. W. Chen, J. Shen, Y. Huang, X. Liu and D. Astruc, Catalyzed Hydrolysis of Tetrahydroxydiboron by Graphene Quantum Dot-Stabilized Transition-

Metal Nanoparticles for Hydrogen Evolution, *ACS Sustain. Chem. Eng.*, 2020, **8**, 7513-7522.

74. Q. Zhao, N. Kang, M. Martínez Moro, E. Guisasola, S. Moya, E. Coy, L. Salmon, X. Liu and D. Astruc, Sharp Volcano-Type Synergy and Visible Light Acceleration in H_2 Release upon $B_2(OH)_4$ Hydrolysis Catalyzed by Au-Rh@Click-Dendrimer Nanozymes, *ACS A.E.M*, 2022, **5**, 3834–3844.

75. Q. Wang, F. Fu, A. Escobar, S. Moya, J. Ruiz and D. Astruc, "Click" Dendrimer-Stabilized Nanocatalysts for Efficient Hydrogen Release upon Ammonia-Borane Hydrolysis, *ChemCatChem*, 2018, **10**, 2673-2680.

76. N. Zhang, G. Liu, Y. Sun, Y. Wang, J. Yan and X. Liu, H_2 Evolution Upon Hydrolysis of Ammonia-Borane Catalyzed by Porphyrin Stabilized Nanocatalysts, *Catal. Lett.*, 2021, **151**, 2272-2278.

77. J. Shen, W. Chen, G. Lv, Z. Yang, J. Yan, X. Liu and Z. Dai, Hydrolysis of NH_3BH_3 and $NaBH_4$ by graphene quantum dots-transition metal nanoparticles for highly effective hydrogen evolution, *Int. J. Hydrog. Energy*, 2021, **46**, 796-805.

78. L. Wang, H. Li, W. Zhang, X. Zhao, J. Qiu, A. Li, X. Zheng, Z. Hu, R. Si and J. Zeng, Supported Rhodium Catalysts for Ammonia–Borane Hydrolysis: Dependence of the Catalytic Activity on the Highest Occupied State of the Single Rhodium Atoms, *Angew. Chem. Int. Ed.*, 2017, **56**, 4712-4718.

79. S. Akbayrak, Y. Tonbul and S. Özkar, Ceria supported rhodium nanoparticles: Superb catalytic activity in hydrogen generation from the hydrolysis of ammonia borane, *Appl. Catal. B*, 2016, **198**, 162-170.

80. D. W. Himmelberger, C. W. Yoon, M. E. Bluhm, P. J. Carroll and L. G. Sneddon, Base-Promoted Ammonia Borane Hydrogen-Release, *J. Am. Chem. Soc.*, 2009, **131**, 14101-14110.

81. J. Shen, L. Yang, K. Hu, W. Luo and G. Cheng, Rh nanoparticles supported on graphene as efficient catalyst for hydrolytic dehydrogenation of amine boranes for chemical hydrogen storage, *Int. J. Hydrog. Energy*, 2015, **40**, 1062-1070.

82. S. Akbayrak, S. Gençtürk, İ. Morkan and S. Özkar, Rhodium(0) nanoparticles supported on nanotitania as highly active catalyst in hydrogen generation from the hydrolysis of ammonia borane, *RSC Adv.*, 2014, **4**, 13742-13748

Chapter 4. Hydrogen Generation from Hydride-Reservoir Cobalt Sandwich Complexes in Alcohols and Tandem Olefin Hydrogenation

4.1. Introduction

Hydrogen is a crucial green energy source, and hydrogenation of unsaturated functionalities is regarded as one of the most fundamental subfields in chemical transformations with industrial applications spanning from fine chemicals to pharmaceuticals synthesis.[1-2] Conventional strategies for hydrogenation exploit gaseous H_2 with high pressure as hydrogen source. However, the utilization of explosive H_2 gas is always accompanied with concerns of storage and transportation issues, which hinders the application of hydrogenation reaction in non-elaborately equipped situations and also arise the investigations of non-H_2 hydrogen source. For example, Chirik *et al.* reported the bis(arylimidazol-2-ylidene) pyridine cobalt methyl complex, (^{iPr}CNC)$CoCH_3$, for the hydrogenation of inactivated, sterically hindered olefins. Spectroscopic observation reveals that it is the cobalt hydride complex, (^{iPr}CNC)CoH, obtained by hydrogenation of (^{iPr}CNC)$CoCH_3$, that facilitates the reaction.[3] Murakami *et al*. reported a solar-driven system to transfer hydrogen from ethanol to alkenes in the presence of aryl ketone. [4]

Hydride-rich organometallic complexes, obtained from the reduction of 18-electron organometallic sandwich cations, are of increasing research interest due to their roles in recent scientific advances as *n*-dopants for organic semiconductors, reducing reagents and hydride donors. [5-9] By transferring a hydride ion to an appropriate hydride abstractor substrate such as Ph_3C^+, the hydride-rich neutral complexes are converted to the corresponding cation via an initial two-electron, proton-coupled reaction in a concerted fashion.[10] Hydricity, which refers to the free energy required to cleave a metal-H bond, is the most commonly used parameter to describe the hydride donor ability.[11] Appel *et al*. reviewed the three primary methods for the determination of

thermodynamic hydricity of metal hydride, offering a valuable predictive tool for the prediction of chemical reactivity in a catalytic reaction[11] Glusac *et al*. reported the role of metal-free hydrides in catalysis and summarized the experimental and calculated hydricity values for more than 200 metal-free hydride donors, including carbon-, boron-, nitrogen- and silicon-based hydrides.[10] In transition-metal organometallic chemistry, penta-hapto cyclopentadienyl (Cp) ligands play an important role in stabilizing organometallic complexes by occupying three of the metal's coordination sites and by providing the metal center with five valence electrons.[12] The introduction of five methyl substituents on the Cp ligand provides in the C_5Me_5 (Cp*) electron-releasing ligand resulting in more stable complexes owing to the stereo-electronic stabilization benefitting from both an increased electronic density of the metal center and a large steric protection.[13]

Here, a series of cobaltocene-derived hydride-reservoir complexes with different Cp methylation, [CoCp(η^4-C_5H_6)], **1H**, [CoCp*(η^4-C_5H_6)], **2H**, [CoCp*(η^4-C_5Me_5H)], **3H**, was prepared using the hydride-rich (hydridic) reductant $NaBH_4$. (**Figure 4.1**) The complexes are investigated for H_2 generation and as hydride donor for the hydrogenation of olefins in methanol. The results show that **2H** with one Cp* ligand exhibits high thermodynamic stability as well as good hydride donor capacity in the model hydrogenation of 1,1-diphenylethylene catalyzed by Pd/C. Given the stable 18-electron sandwich structure, the cationic form of **2H**, $\mathbf{2^+PF_6^-}$, is easily recycled upon precipitation of $\mathbf{2^+}$ using HPF_6. The isotope experiment and tandem reaction disclose that the two H atoms in the produced 1,1- diphenylethane are provided from **2H** and the methanol solvent.

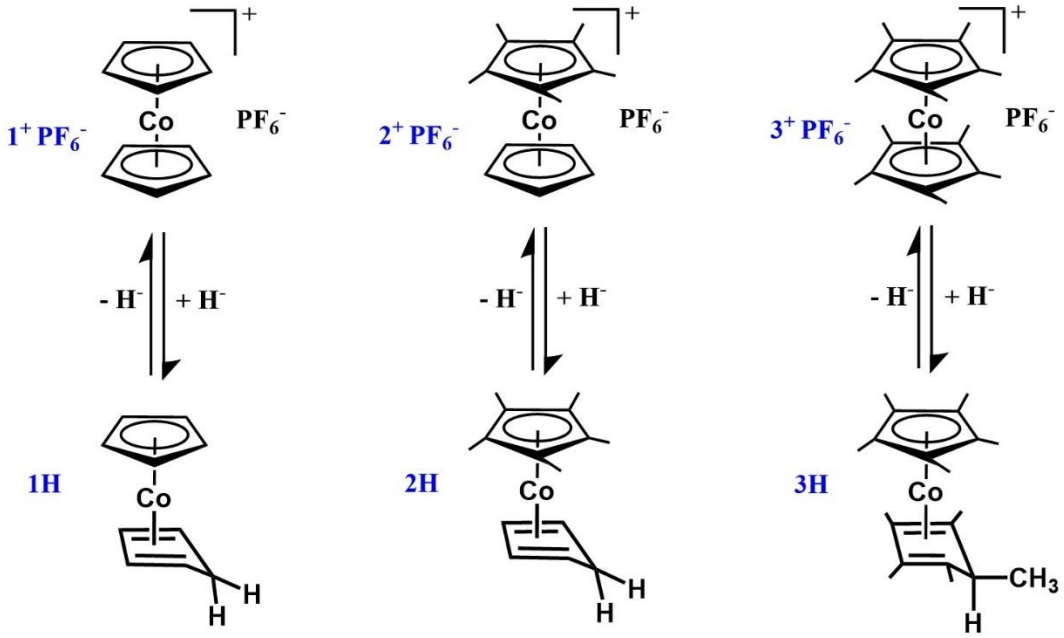

Figure 4.1. Hydride reservoir properties of the Co(I) complexes $[Co(\eta^5\text{-}C_5H_5)(\eta^4\text{-}C_5H_6)]$, **1H**, $[Co(\eta^5\text{-}C_5Me_5)(\eta^4\text{-}C_5H_6)]$, **2H**, $[Co(\eta^5\text{-}C_5Me_5)(\eta^4\text{-}C_5Me_5H)]$, **3H** and corresponding structures of the empty hydride reservoir Co(III) complexes $[Co(\eta^5\text{-}C_5H_5)_2]^+PF_6^-$, $\mathbf{1^+PF_6^-}$, $[Co(\eta^5\text{-}C_5H_5)(\eta^5\text{-}C_5Me_5)]^+PF_6^-$, $\mathbf{2^+PF_6^-}$, $[Co(\eta^5\text{-}C_5Me_5)_2]^+PF_6^-$, $\mathbf{3^+PF_6^-}$.

4.2. Results and discussion

4.2.1. H_2 evolution from 1H, 2H and 3H

The complexes **1H**, **2H** and **3H** were synthesized by reduction using $NaBH_4$ in THF of the salts $\mathbf{1^+PF_6^-}$, $\mathbf{2^+PF_6^-}$ and $\mathbf{3^+PF_6^-}$ respectively (**Chapter 3** and **Experimental Section**). The reaction of **1H** and **2H** with methanol or ethanol is fast (about one minute for completion) under ambient temperature. These reactions were first conducted in the presence of Pd/C, but later we found that these reactions proceeded as fast in the absence of catalyst. There is no reaction between **3H** with methanol or ethanol under these conditions, thus further research was conducted only with **1H** and **2H**. After H_2 evolution, the color of the solution resulting from the reaction of **2H** with MeOH remained

wine-red. Methanol was removed *in vacuo*, and a red solid was left. Upon the addition of aqueous HPF_6, the red solid dissolved therein, and at the same time, a yellow precipitate appeared, suggesting the formation of $\mathbf{2^+PF_6^-}$, which was further confirmed by ^1H NMR. (**Figure S 4.1**, **Experimental section**). Accordingly, a tentative transformation pathway of **2H** into $\mathbf{2^+PF_6^-}$ in the presence of methanol is proposed here (**Figure 4.2**). After the generation of H_2, an intermediate ion pair [Cp^*CoCp^+, MeO^-] complex was possibly produced, resulting in the formation of a red complex for which the structure is assumed to be $Cp^*Co(\eta^4\text{-}C_5H_5OMe)$, which will need to be confirmed by spectroscopic and analytical characterization. This structural assumption is based on the fact that this complex (i) is of almost the same color as the Co(I) complex **2H** (thus, of related structure) (ii) is then slowly oxidized by air and/or then precipitated by addition of aqueous HPF_6, resulting in the formation of $\mathbf{2^+\ PF_6^-}$**.** The proposed representation of the overall process is shown in **Figure 4.2**. The exact mechanism of the formation of the ion-pair intermediate is unclear. A first hypothesis would be electron transfer from **2H** to the alcohol giving RO^- and $H^\cdot$ followed by abstraction of the hydridic atom of **2H** by $H^\cdot$, but this involves unlikely high energy formation of $H^\cdot$. A second one energetically more realistic would involve direct nucleophilic attack of the O-H bond of the alcohol by the hydridic H atom of **2H** to form H_2 and RO^-.

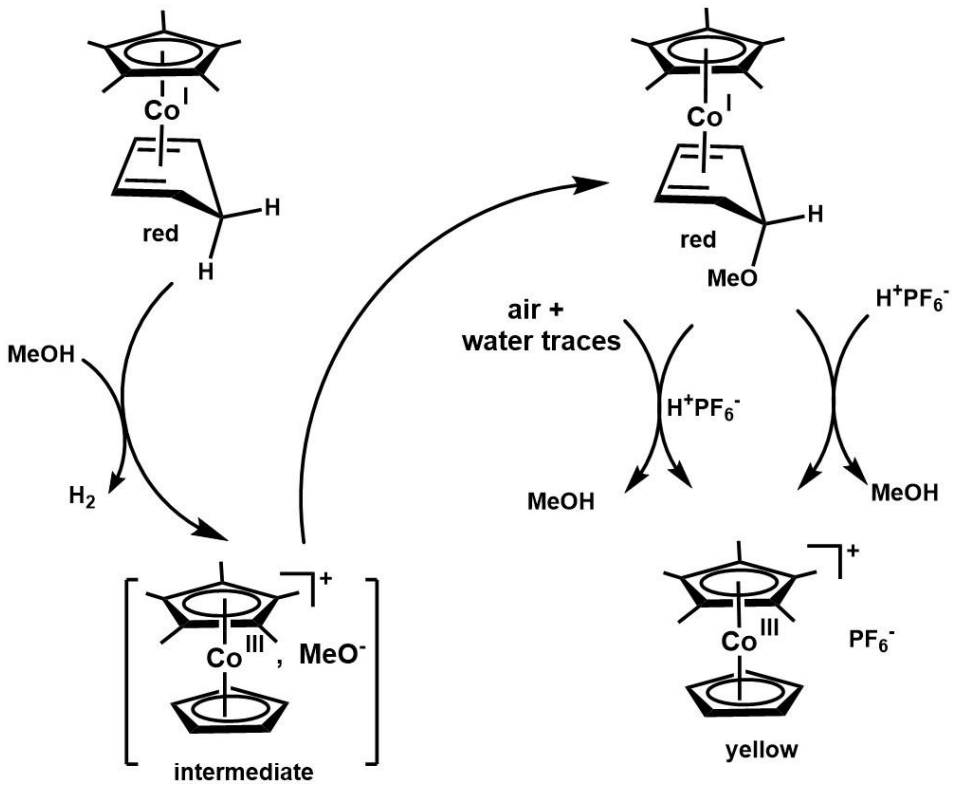

Figure 4.2. Proposed mechanism for H_2 generation from methanol and the hydride reservoir complex **2H**.

For, **1H**, the reaction with alcohols also produces H_2 gas within 1 min in both MeOH and EtOH. (**Table 4.1**) However, after H_2 production, the reaction residue cannot be recovered by precipitation with HPF_6 solution. The result of H_2 evolution from **1H**, **2H**, **3H** within 1 min at room temperature is summarized in **Table 4.1**.

From **Table 4.1**, **2H** appears as the best candidate among the three complexes for the given reaction, as it shows fast H_2 evolution, and it is recyclable by reaction of $\mathbf{2^+PF_6^-}$ with $NaBH_4$. **1H** exhibits a comparable ability for H_2 evolution, but it does not present a sufficient stability for a facile recovery. These variation of behavior of the complexes **1H**, **2H**, **3H** results from the

difference of degree of methylation of the cyclopentadienyl ligand. The presence of methyl groups in Cp* ligands increase the electronic density of the central metal Co, and the much larger cone angle of Cp* compared to Cp involves additional steric stabilization in Cp* complexes, resulting in increasing stability order: **1H** < **2H** < **3H**. **3H** presents too much bulk near the hydridic H atom slowing or inhibiting the reaction in spite of increased electronic density of the Co atom compared to the analogues **1H** and **2H**. In conclusion, for **3H**, H_2 production upon reaction with alcohol may be anticipated only at temperatures significantly higher than room temperature.

Table 4.1. Summary of H_2 evolution from **1H**, **2H**, **3H** within 1 min at room temperature.

Conditions	H_2 production from **1H**		H_2 production from **2H**		H_2 production from **3H**	
	In MeOH	In EtOH	In MeOH	In EtOH	In MeOH	In EtOH
With Pd/C	Yes	Yes	Yes	Yes	No	\
Without Pd/C	Yes	Yes	Yes	Yes	\	\
Recyclability	No	No	Yes	Yes	Yes	\

4.2.2. Hydrogenation of 1,1-diphenylethylene using 1H, 2H and 3H

H_2 production can be utilized *in situ* for the hydrogenation of olefins. Here, a sterically hindered, inactivated alkene, 1,1-diphenylethylene is used. The reaction of **2H** (0.5 mmol) with MeOH is utilized for the hydrogenation of 1,1-diphenylethylene (0.2 mmol) in the presence of 5 mol % Pd/C. After 18h of reaction at room temperature (25 ˚C) and extraction, the ^{1}H NMR of the organic compound allows analysis of the reactions, showing 100% conversion

of 1,1-diphenylethylene (**Figure 4.3**). However, when the reaction occurs at 50 ˚C, the conversion of 1,1- diphenylethylene turns out to be 74.3% according to the ^{1}H NMR in **Figure 4.3**.

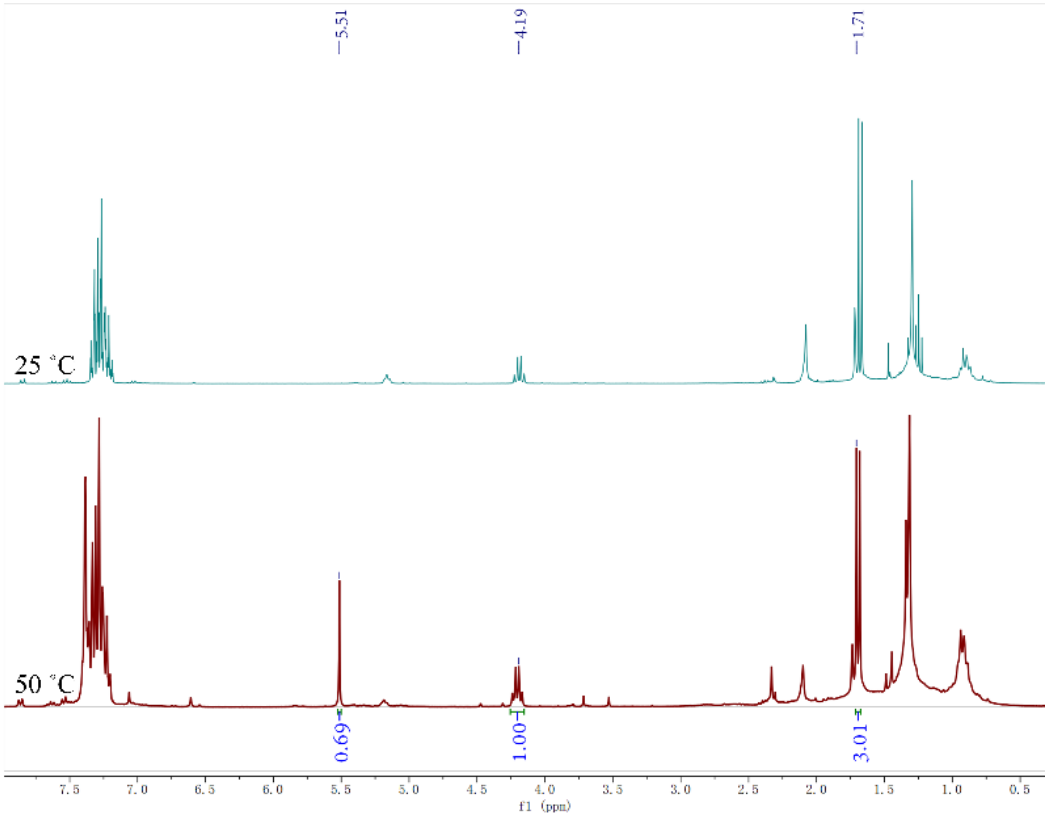

Figure 4.3. ^{1}H NMR spectrum of 1,1- diphenylethane in 1,1-diphenylethylene hydrogenation reaction using **2H** at 50 ˚C and 25 ˚C. ^{1}H NMR (300 MHz, $CDCl_3$)

The use of **1H** (5mmol) for the hydrogenation of 1,1-diphenylethylene (0.2 mmol), in the presence of 5 mol % Pd/C during 18h at 25 ˚C, shows decomposition and 79.4% conversion of 1,1-diphenylethylene according to the peak integration. However, reaction at 0 ˚C proceeds with 100% hydrogenation of 1,1-diphenylethylene, but the existence of impurity peaks

also reveals some decomposition of **1H** even at this low temperature. (**Figure 4.4**)

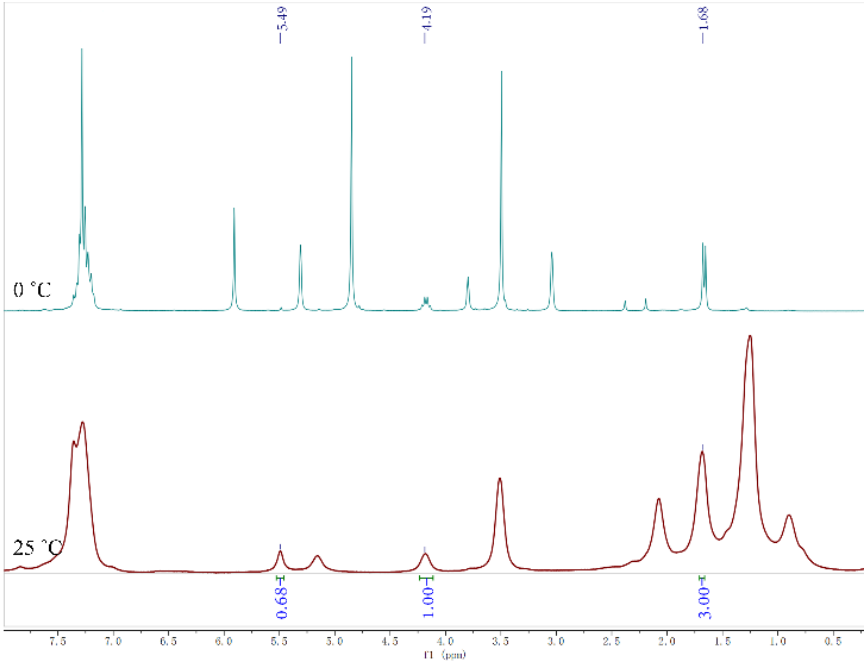

Figure 4.4. ^{1}H NMR spectrum of 1,1- diphenylethane in 1,1-diphenylethylene hydrogenation using **1H** at 25 ˚C and 0 ˚C. ^{1}H NMR (300 MHz, $CDCl_3$)

The use of **3H** (5mmol) for the hydrogenation of 1,1-diphenylethylene (0.2 mmol) in the presence of 5 mol % Pd/C, during 18h at 25 ˚C, shows zero conversion of 1,1-diphenylethylene according to the ^{1}H NMR spectrum (**Figure 4.5**). However, reaction at 50 ˚C proceeds with 100% hydrogenation of 1,1-diphenylethylene. After the hydrogenation reaction, the **3H** residue can be recovered by the precipitation upon addition of aqueous HPF_6. The structure of the recycled salt $\mathbf{3^{+}PF_6^{-}}$ is confirmed by the ^{1}H NMR spectrum (**Figure S 4.2**)

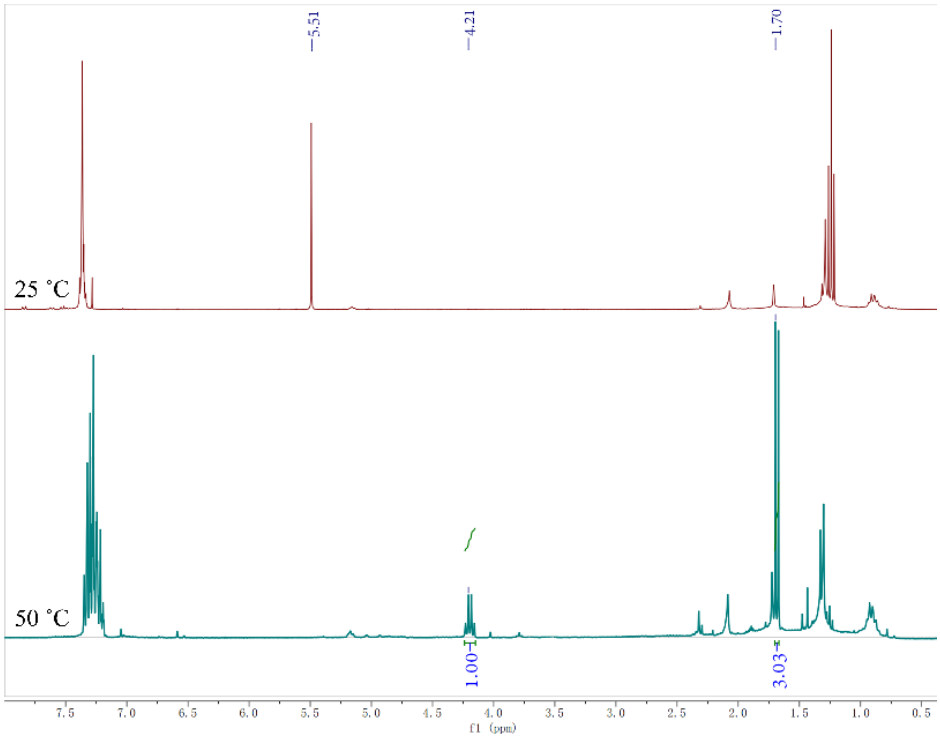

Figure 4.5. ^{1}H NMR spectrum of 1,1- diphenylethane in 1,1-diphenylethylene hydrogenation using **3H** at 50 ˚C and 25 ˚C. ^{1}H NMR (300 MHz, $CDCl_3$)

In summary, for the hydrogenation of 1,1-diphenylethylene, **3H** completes the reaction at 50 ˚C but not at all at 25 ˚C, **2H** completes the reaction at 25 ˚C, and **1H** completes the reaction at 0 ˚C (**Table 4.2**). These results can be ascribed to the hydricity of the hydride-reservoir complexes, which is highly affected by the structure–property relationships. For example, the strongest metal-free hydride donors can be found among boron-based anionic derivatives because of the negative charge on the B hydride. Boron-based hydrides anions thus have high hydride-donating capability.[10, 14] Here, with the increase of the ligand methylation degree, the thermodynamic stability of the sandwich complexes is enhanced.

Table 4.2. Summary of 1,1-diphenylethylene hydrogenation using H_2 formed from **1H**, **2H** and **3H** at different temperatures.

Temperature	**1H**	**2H**	**3H**
50 ˚C	\	74.3%	100%
25 ˚C	79.4%	100%	0
0 ˚C	100%	\	\
Recyclability	No	Yes	Yes

Although the hydrogenation of 1,1-diphenylethylene is completed using **2H**, the origin of the H atoms that are transferred to the olefin was investigated. To this end, 1.5 *equiv.* **2H** was used for the hydrogenation of 1.0 *equiv.* 1,1-diphenylethylene. The result shown in **Figure S 4.3** (**Experimental section**) reveals 100% conversion of 1,1- diphenylethane, indicating that **2H** is not the only H source for the hydrogenation reaction, as one **2H** molecule can only donate one hydride. This also corresponds to the fact that 1.0 *equiv.* H_2 is produced using 1.0 *equiv.* **2H**. (**Section 2.1**)

4.2.3. Deuteration studies

An isotopic experiment study was conducted here. First of all, 1.5 *equiv.* **2H** was utilized for the hydrogenation of 1.0 *equiv.*1,1-diphenylethylene in the presence of 5 mol % Pd/C, and methanol-D_4 used as solvent to investigate the deuteration of 1,1-diphenylethane produced. The ^{1}H NMR spectrum (**Figure S 4.4, Experimental section**) of 1,1-diphenylethane shows a quartet peak at 4.17 ppm with integration of 1 and a doublet peak at 1.68 ppm with integration of 2.64, which is less than expected 3, indicating the deuteration of 1,1-diphenylethane produced. Besides, 1,1-diphenylethane was also investigated

by mass spectrometry (MS). The result in **Figure S 4.5** (**Experimental section**) shows three main peaks with m/z at 182.1, 183.1, 184.1, which corresponds to zero, one and two deuterium atoms in 1,1-diphenylethane. As the only deuteration source is methanol in the system, it is reasonable to deduce that methanol provides one proton in the hydrogenation reaction, which can be ascribed to the one deuterated species observed by MS. The zero and two-atom deuteration peaks resulted from the H/D exchange at the surface of catalyst.

Also, deuterated **2H**, termed as $\mathbf{2H_D}$, was synthesized by reduction of the cationic precursor using $NaBD_4$ for the hydrogenation reaction. Location of the incoming D atom is assigned to the *exo* position (remote from Co) resulting from steroselective hydride attack. 1.5 *equiv.* $\mathbf{2H_D}$ was used for the hydrogenation of 1.0 *equiv.*1,1-diphenylethylene in the presence of 5 mol % Pd/C, and methanol was used as solvent. The ^{1}H NMR spectrum of the produced 1,1-diphenylethane shows two signals at 4.17 ppm with integration of 1 and 1.68 ppm with integration of 2.64. The mass spectrum of 1,1-diphenylethane also exhibits three typical peaks with m/z at 182.1, 183.1 and 184.1, corresponding to zero, one and two deuterations of 1,1-diphenylethane. (**Figure S 4.6** and **S 4.7**, **Experimental section**).

4.2.4. Hydrogenation of olefins using H_2 produced from 2H in tandem reactions

Tandem reaction consists of two or more successive independent reactions performed in one sealed system without separating and purifying the intermediates. They have been widely used for the investigation of the active site of catalytic reactions.[15] Here, a two-chamber tandem reaction was

conducted to investigate the origin of H atoms in H_2 evolution and 1,1-diphenylethylene hydrogenation using **2H**. In the tandem reaction (**Figure 4.6**), H_2 production proceeded in the left tube owing to the presence of **2H** and solvent, which was then transferred into the right tube for the hydrogenation of olefin.

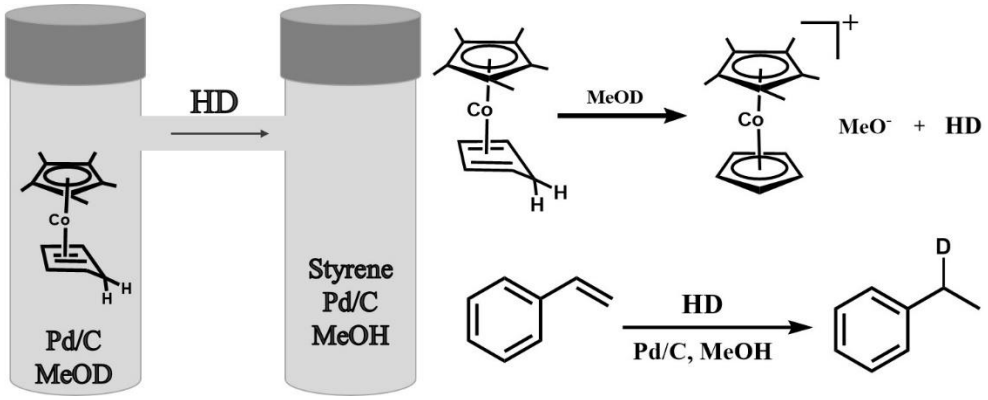

Figure 4.6. Hydrogenation of styrene in a tandem reaction system.

First of all, 2.5 *equiv*. **2H** and 5 mol % Pd/C were added into MeOD in the left tube, and 1.0 *equiv*. 1,1-diphenylethylene along with 5 mol % Pd/C dissolved in MeOH was injected in the right tube, which were the same amount as in the single-tube reaction. After 18h of reaction at 25˚C, no hydrogenation of 1,1-diphenylethylene occurred. Upon increasing the amount of **2H** to 10 *equiv*., there was no hydrogenation of 1.0 *equiv*. 1,1-diphenylethylene. (**Figure S 4.8**, **Experimental Section**) The result can be ascribed to the steric bulk barriers of 1,1-diphenylethylene hydrogenation. Therefore, an easily hydrogenated olefin, styrene, was used in the tandem reaction. (**Table 4.3**)

As shown in **Figure 4.6**, when 10 *equiv*. **2H** along with MeOD was used to produce H_2 in the left tube and 1.0 *equiv*. styrene was added in the right tube

along with the solvent MeOH and the catalyst Pd/C. ^{1}H NMR (**Figure S 4.9, Experimental section**) of the produced ethylbenzene shows a peak at 2.63 ppm with integration of 0.26 and a peak at 1.24 ppm with integration of 2.86. The integration of peak at 2.63 ppm is less than 1, revealing the deuteration of 1,1- diphenylethane, and the deuteration is originated from the solvent MeOD. Thus, methanol also provides one H for the produced H_2. On the other hand, there is no peaks in the region 5 ppm ~ 7 ppm in **Figure S 4.9** (**Experimental section**), revealing the full hydrogenation of styrene.

Our result revealed that 1.5 *equiv.* **2H** was enough for the hydrogenation of 1.0 *equiv.*1,1-diphenylethylene in a single-tube system, while the reaction was hindered in the presence of 10 *equiv.* **2H** in two-tube system. In later case, H_2 gas was produced and used separately, which resembles the commercial well-equipped hydrogenation reaction with high concentration and pressure H_2. However, in former case, it is close to stoichiometric transformations (1.5 *equiv.* **2H** vs. 1.0 *equiv.* olefin), which not only avoids the use of excessive gaseous H_2, but also improves efficiency of the hydrogenation reaction of sterically hindered, inactivated alkenes. Besides, **2H** can also be applied for other ethylene hydrogenation reactions, for example 2-vinylnaphthalene (**Figure S 4.10**, **Experimental section**), and phenyl vinyl sulfone (**Figure S 4.11**, **Experimental section**) as there are no olefin protons present at 5.0~7.0 ppm. The big difference of activity between the single-tube and two-tube reactions let highly suspect that the olefin hydrogenation mechanisms are distinct. The poor hydrogenation efficiency in the second tube of the two-tube reaction is due to the low H_2 concentration in a classic Pd-catalyzed olefin hydrogenation with H_2, whereas in the single-tube reaction, the high

efficiency seems to be due to direct hydride transfer from **2H** to the Pd catalyst on the way to olefin hydrogenation without intermediate formation of H_2.

Table 4.3. hydrogenation result of olefins in the tandem reaction.

Left （**2H**）	Right (1.0 *equiv.* olefin)	Conversion of olefin
1.5 *equiv.*	1,1-diphenylethylene	0
10.0 *equiv.*	1,1-diphenylethylene	0
10.0 *equiv.*	styrene	100%

Based on the experimental results above, a tentative mechanism for hydrogenation of olefin using hydride reservoir complex **2H** is proposed here (**Figure 4.7**). In the presence of Pd/C, the hydride of **2H** migrates to the surface of Pd_n, giving a negatively charged [Pd_n-H] and a cationic $\mathbf{2}^+$ (R^+ in **Figure 4.7**). The [Pd-H] serves as a Lewis base to attack the acidic MeOH, leading to the H^+ abstraction from MeOH and the formation of [H-Pd_n-H], which further undergoes the hydrogenation of olefin. On the other hand, MeO^- residue forms the red intermediate R-OMe with R^+, which has already been discussed in **Section 4.2.1**.

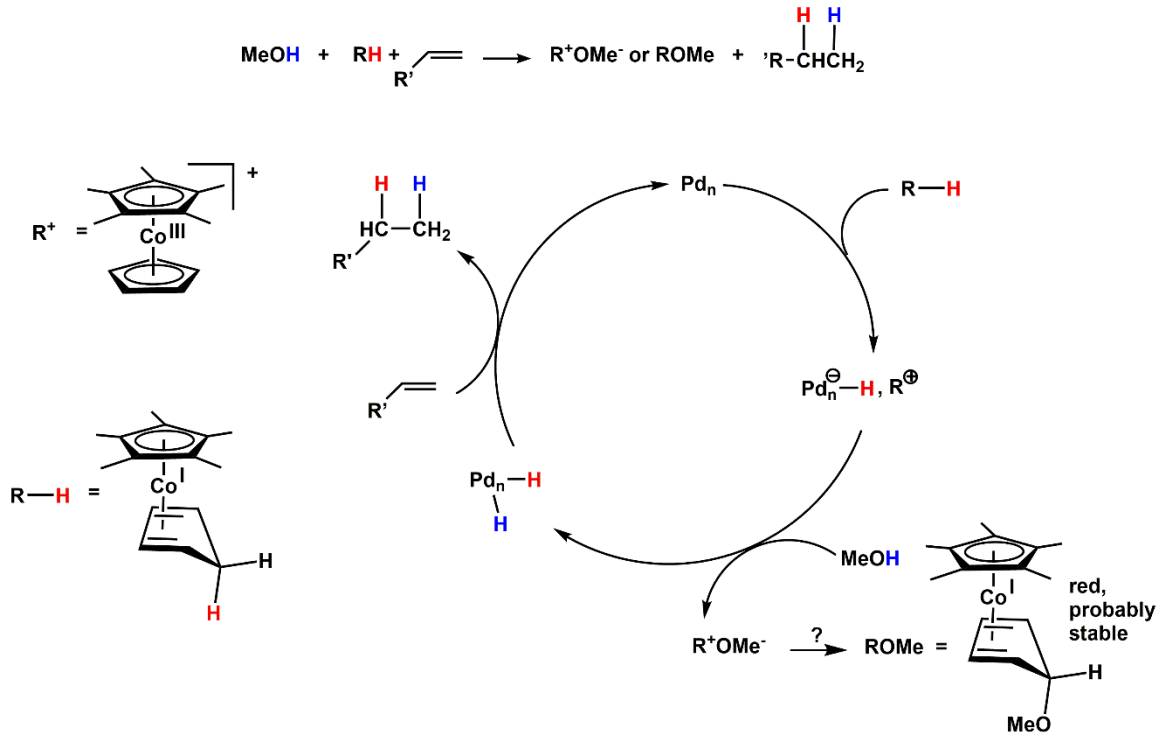

Figure 4.7. Proposed mechanism for hydrogenation of olefin using hydride reservoir complex **2H**.

4.3. Conclusion

In summary, a series of cobaltocene-derived hydride-reservoir complexes with different Cp methylation, [CoCp (η^4-C_5H_6)], **1H**, [CoCp*(η^4-C_5H_6)], **2H**, [CoCp*(η^4-C_5Me_5H)], **3H**, with Cp = η^5-C_5H_5 and Cp* = η^5-C_5Me_5, have been prepared and used for the hydrogenation of olefins as hydride-donors. The hydride-donating ability and stability of **1H**, **2H**, **3H** are compared in the hydrogenation of 1,1-diphenylethylene at different temperatures. In the interesting context of the nitrogen reduction reaction, it should be noted that **3H** has been found as an intermediate in the catalytic mechanism.[16,17] Among the three complexes, **2H** exhibits the best hydride-donating capability at room

temperature (25 ˚C). Besides, **2H** can be recycled upon precipitation of corresponding cationic $\mathbf{2^{+}Cl^{-}}$ owing to the stable sandwich structure of the later complex. The isotopic experiment revealed that **2H** donates one hydride and abstracts one acidic H atom for the hydrogenation reaction. This result offers a sustainable and safer system to hydrogenate alkenes. The use of single-tube *in situ* reaction presented technical advantages concerning stoichiometric reaction over two-tube reactions that, on the other hand, were informative concerning the H_2 formation reaction mechanism.

4.4. Experimental Section

The preparation of **1H**, **2H**, **3H** is shown in **Chapter 3** and our previous work.[5,18] The recycling process of the sandwich complexes is explained here using **2H** as an example. After hydrogenation reaction, **2H** residue and the organic compounds remains in methanol. Thus, solvent is firstly removed *in vacuo*. Then water and diethyl ether (1:1 in volume) is added into the flask. As a result, **2H** residue dissolves in water while the organic compounds is only soluble in ether. After extraction, the two phase are separated. Removing ether, the organic compounds are obtained for ^{1}H NMR without further purification. The **2H** residue is collected by precipitation upon the addition of HPF_6.

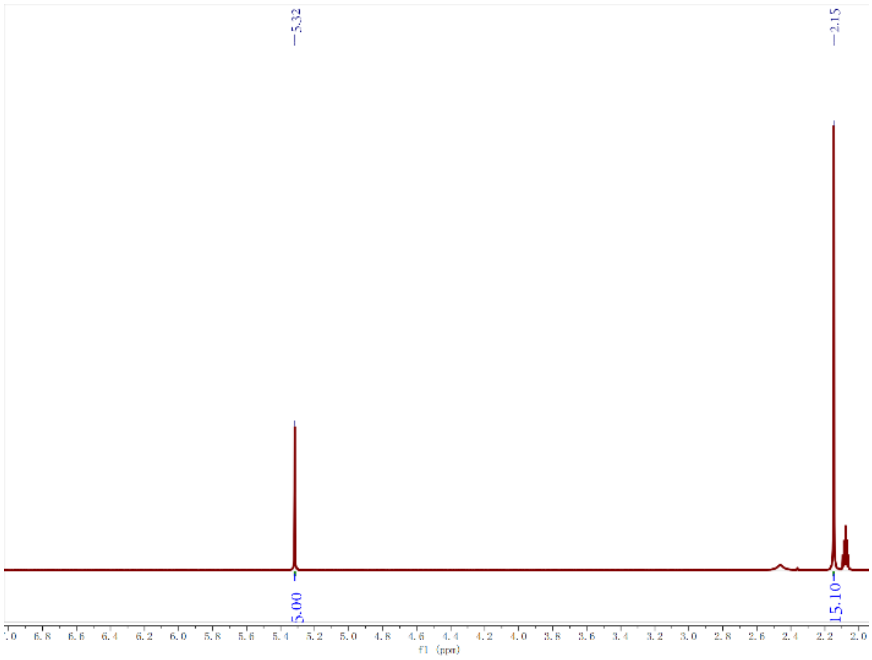

Figure S 4.1. ^{1}H NMR spectrum of recycled Cp*CoCpPF$_{6,}$ **2^{+}PF$_{6}^{-}$**. (300 MHz, acetone-D6)

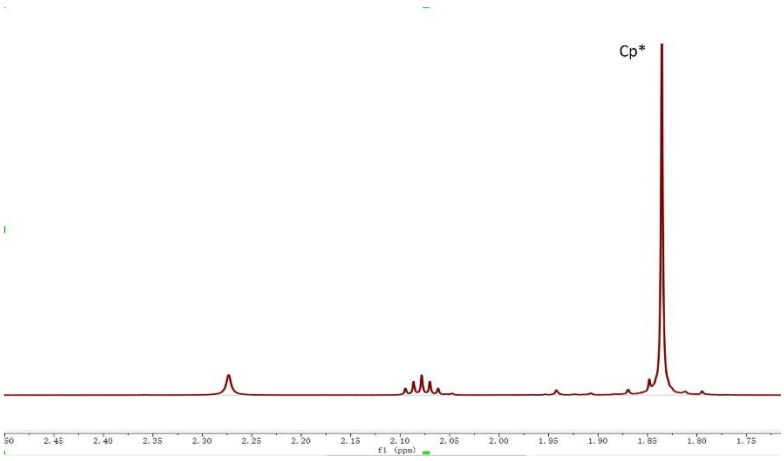

Figure S 4.2. ^{1}H NMR spectrum of recycled Cp*CoCp*PF$_{6,}$ **3^{+}PF$_{6}^{-}$**. (^{1}H NMR (300 MHz, Acetone-D6).

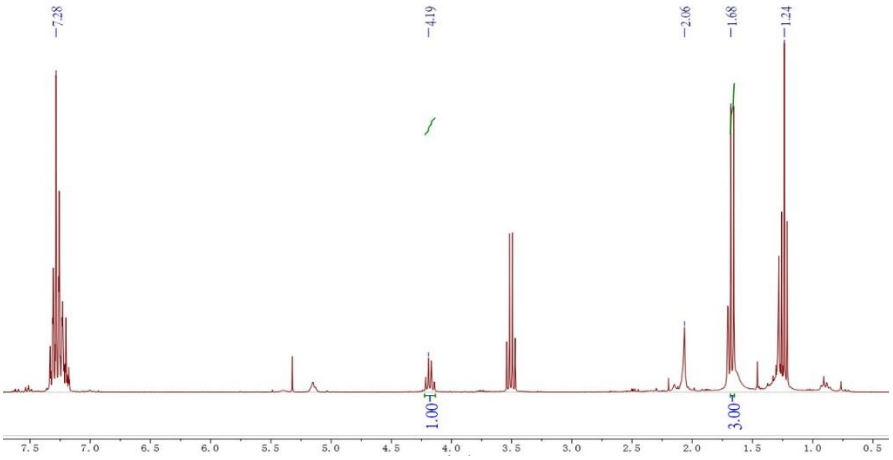

Figure S 4.3. ^{1}H NMR spectrum of 1,1- diphenylethane (*1.0 equiv.*) in 1,1-Diphenylethylene hydrogenation using **2H** (1.5 *equiv.*) at 25 ˚C. ^{1}H NMR (300 MHz, $CDCl_3$)

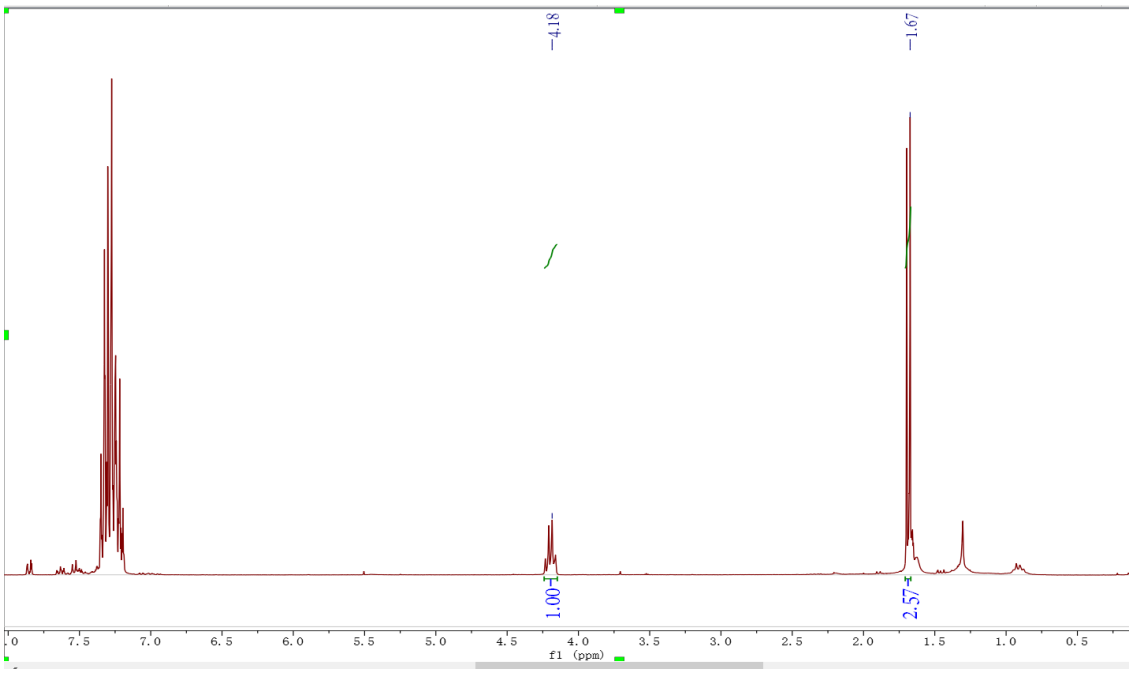

Figure S 4.4. ^{1}H NMR spectrum (300 MHz, $CDCl_3$)) of the hydrogenation of 1,1-diphenylethylene using **2H** and MeOD.

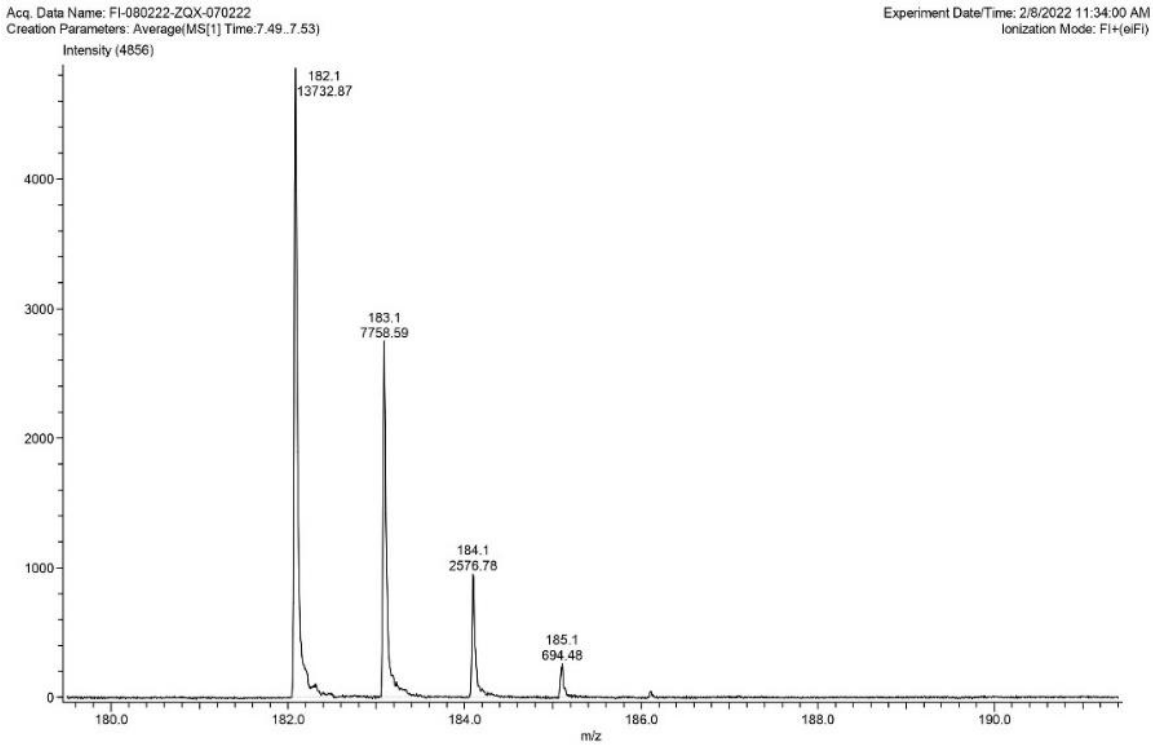

Figure S 4.5. GC-MS of deuterated 1,1-diphenylethane obtained using **2H** and MeOD

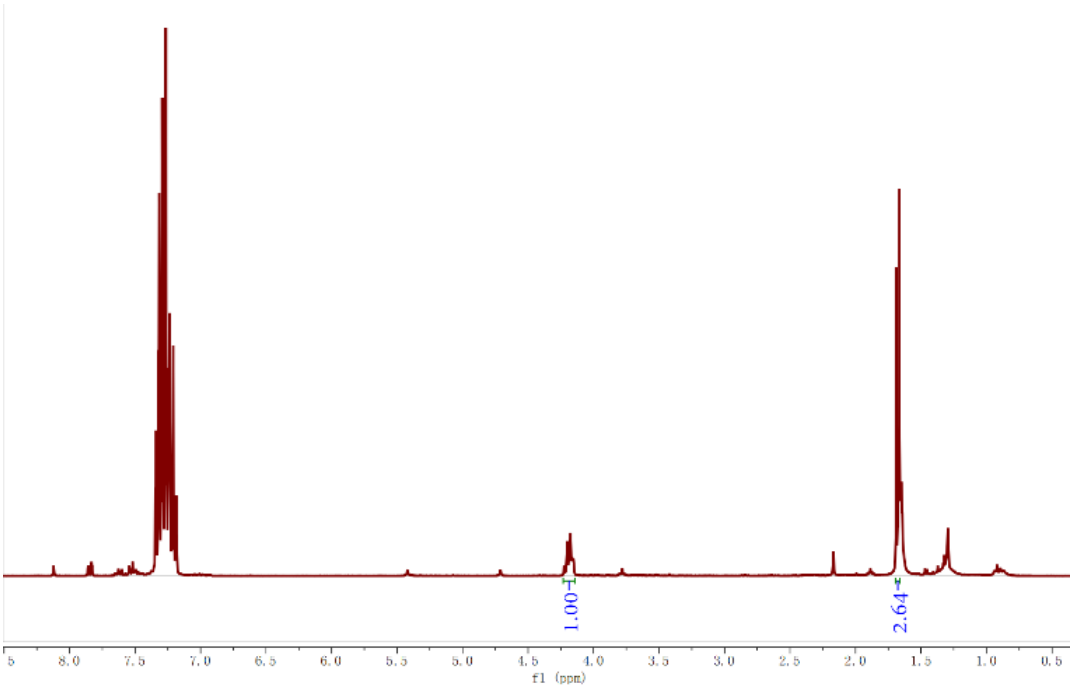

Figure S 4.6. ^{1}H NMR spectrum of hydrogenation of 1,1-diphenylethylene using **2H^{D}** and MeOH. (300 MHz, $CDCl_3$)

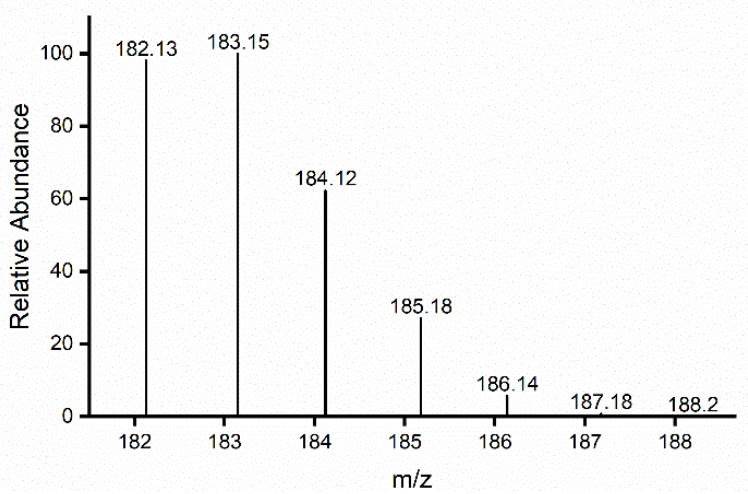

Figure S 4.7. GC-MS of deuterated 1,1-diphenylethane using **2H$_D$** and MeOH.

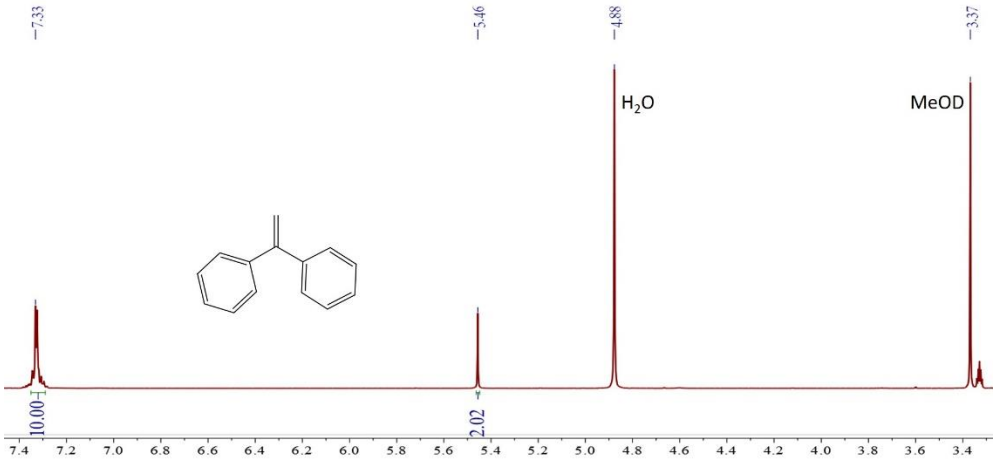

Figure S 4.8. ^{1}H NMR spectrum of hydrogenation of 1,1-diphenylethylene using *10 equiv.* **2H** and 1.0 *equiv*. 1,1-diphenylethylene in tandem reaction at 25˚C. ^{1}H NMR (300 MHz, MeOD)

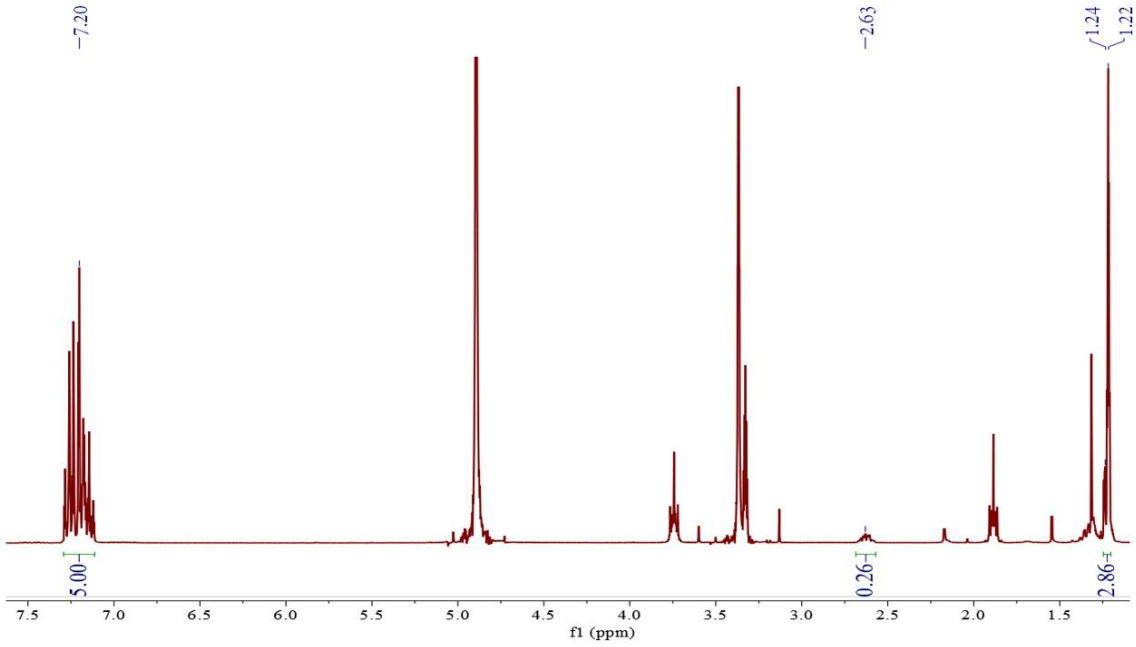

Figure S 4.9. Hydrogenation of styrene (*1.0 equiv*) using **2H** (*10.0 equiv.)* in a tandem reaction (300 MHz, MeOD)

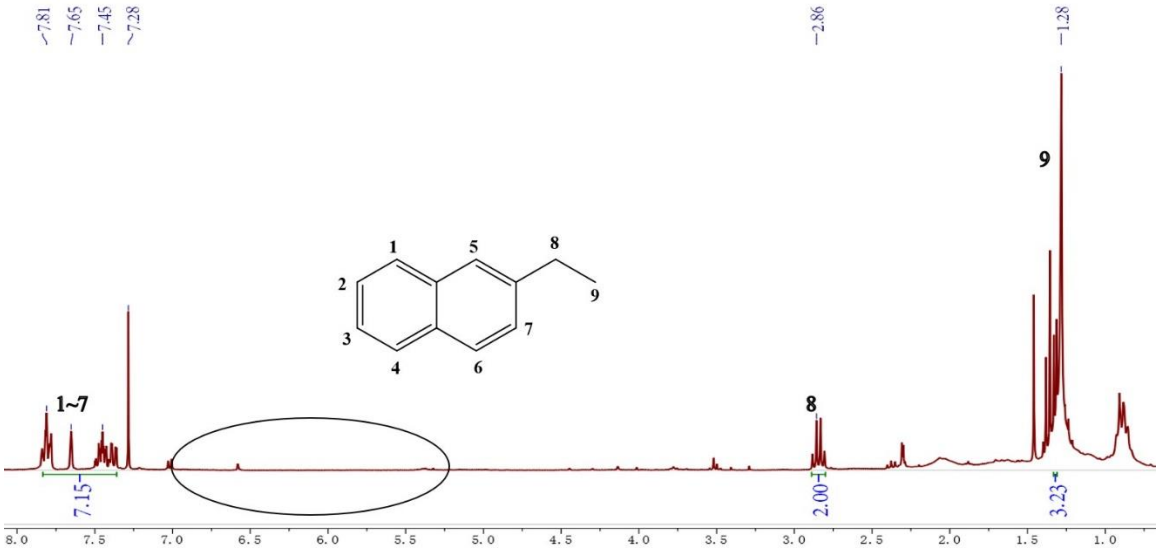

Figure S 4.10. ^{1}H NMR spectrum (300 MHz, $CDCl_3$) of the hydrogenation of 2-vinylnaphthalene

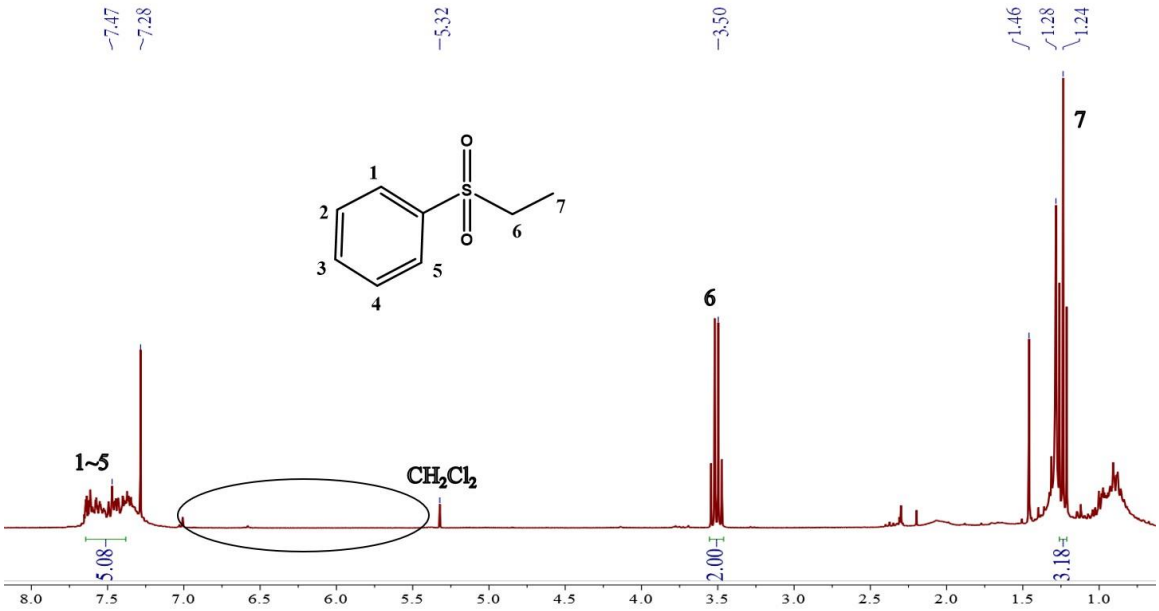

Figure S 4.11. ^{1}H NMR spectrum hydrogenation of phenyl vinyl sulfone (300 MHz, $CDCl_3$)

4.5. References

1. Wang, D.; Astruc, D. The Golden Age of Transfer Hydrogenation. *Chem. Rev.* **2015,** *115*, 6621-6686.

2. Zhang, G.; Scott, B. L.; Hanson, S. K. Mild and Homogeneous Cobalt-Catalyzed Hydrogenation of C=C, C=O, and C=N Bonds. *Angew. Chem. Int. Ed.* **2012,** *51*, 12102-12106.

3. Yu, R. P.; Darmon, J. M.; Milsmann, C.; Margulieux, G. W.; Stieber, S. C. E.; DeBeer, S.; Chirik, P. J. Catalytic Hydrogenation Activity and Electronic Structure Determination of Bis(arylimidazol-2-ylidene)pyridine Cobalt Alkyl and Hydride Complexes. *J. Am. Chem. Soc.* **2013,** *135*, 13168-13184.

4. Ishida, N.; Kamae, Y.; Ishizu, K.; Kamino, Y.; Naruse, H.; Murakami, M. Sustainable System for Hydrogenation Exploiting Energy Derived from Solar Light. *J. Am. Chem. Soc.* **2021,** *143*, 2217-2220.

5. Fu, F.; Wang, Q.; Ciganda, R.; Martinez-Villacorta, A. M.; Escobar, A.; Moya, S.; Fouquet, E.; Ruiz, J.; Astruc, D. Electron- and Hydride-Reservoir Organometallics as Precursors of Catalytically Efficient Transition Metal Nanoparticles in Water. *Chem. Eur. J* **2018,** *24*, 6645-6653.

6. Szajek, L. P.; Shapley, J. R. Unexpected synthesis of CpIr(.eta.4-C5H6) and a proton and carbon-13 NMR comparison with its cobalt and rhodium congeners. *Organometallics* **1991,** *10*, 2512-2515.

7. Pfeffer, M.; Grellier, M., 7.01 - Cobalt Organometallics. In *Comprehensive Organometallic Chemistry III*, Mingos, D. M. P.; Crabtree, R. H., Eds. Elsevier: Oxford, 2007; pp 1-119.

8. Koelle, U.; Fuss, B.; Rajasekharan, M. V.; Ramakrishna, B. L.; Ammeter, J. H.; Boehm, M. C. Pentamethylcyclopentadienyl transition-metal complexes. 7. Electrochemistry of transition-metal .pi.-complexes. 7. Cyclopentadienyl (arene)cobalt cations: preparation, electrochemical reduction, and spectroscopic investigation of the paramagnetic d7 monocations. *J. Am. Chem. Soc.* **1984,** *106*, 4152-4160.

9. Zhang, S.; Moudgil, K.; Jucov, E.; Risko, C.; Timofeeva, T. V.; Marder, S. R.; Barlow, S. Organometallic hydride-transfer agents as reductants for organic semiconductor molecules. *Inorg. Chim. Acta* **2019,** *489*, 67-77.

10. Ilic, S.; Alherz, A.; Musgrave, C. B.; Glusac, K. D. Thermodynamic and kinetic hydricities of metal-free hydrides. *Chem. Soc. Rev.* **2018,** *47*, 2809-2836.

11. Wiedner, E. S.; Chambers, M. B.; Pitman, C. L.; Bullock, R. M.; Miller, A. J. M.; Appel, A. M. Thermodynamic Hydricity of Transition Metal Hydrides. *Chem. Rev.* **2016,** *116*, 8655-8692.

12. Legzdins, P.; Reina, R.; Shaw, M. J.; Batchelor, R. J.; Einstein, F. W. B. Tetraphenylcyclopentadienyl nitrosyl complexes of molybdenum and tungsten. *Organometallics* **1993,** *12*, 1029-1037.

13. Astruc, D. *Organometallic chemistry and catalysis*. Berlin: Springer: 2007.

14. Heiden, Z. M.; Lathem, A. P. Establishing the Hydride Donor Abilities of Main Group Hydrides. *Organometallics* **2015,** *34*, 1818-1827.

15. Huang, Y. B.; Liang, J.; Wang, X. S.; Cao, R. Multifunctional metal-organic framework catalysts: synergistic catalysis and tandem reactions. *Chem. Soc. Rev.* **2017,** *46*, 126-157.

16. Chalkley, M. J.; Oyala, P. H.; Peters, J. C. Cp* Noninnocence Leads to a Remarkably Weak C−H Bond via Metallocene Protonation; J. Am. Chem. Soc. **2019**, 141, 4721−4729

17. Chalkley, M. J.; Castillo, T. J. D.; Matson, B. D.; Peters, J. C. Fe-Mediated Nitrogen Fixation with a Metallocene Mediator: Exploring pKa Effects and Demonstrating Electrocatalysis. J. Am. Chem. Soc. **2018**, 140, 6122−6129

18. Fu, F.; Dedieu, A.; Wang, W.; Chen, T.; Song, Y.; Fouquet, E.; Hamon, J. R.; Zhu, M.; Astruc, D. Stabilization of a new nanocomposite family by reduction of gold nanoclusters with electron-reservoir complexes. Chem. Commun. **2019**, 55, 10277-10280.

Conclusion and Perspectives

In this thesis, our investigations have concerned the design and catalytic applications of late transition-metal nanomaterials and hydride-reservoir sandwich complexes, specifically focusing on three aspects:

(i) The synthesis, optimization and catalytic properties of TMNPs stabilized by "click" TEG-dendrimers.

(ii) The design, synthesis and catalytic application of metallocenium stabilized TMNPs catalyst.

(iii) The design, synthesis of organometallic hydride-reservoir complexes for H_2 generation and the hydrogenation of olefins.

The investigation of TMNPs starts with the preparation of bimetallic Au-Rh nanoparticles with various Au/Rh proportion stabilized by "click" dendrimer. Fine monodispersed and alloy-structured TMNPs with a size range useful for catalytic applications (1.5-3.0 nm) were observed by TEM and applied for catalytic H_2 production upon hydrolysis of tetrahydroxydiboron, $B_2(OH)_4$. The optimized composition, Au_4Rh_1NPs, shows a sharp volcano-type synergies of 3.4-fold and 8.9-fold increased TOF_s (5100 $mol_{H_2}\, mol_{cat}^{-1}\, min^{-1}$) compared to the monometallic Au and Rh NPs. The plasmonic Au-Rh NPs also exhibit remarkable additional enhancement of catalytic activity under visible-light irradiation, giving the highest light enhancement rate of 1.4 for Au_1Rh_2 NPs. Kinetic experiments show that the reaction is first order in catalyst concentration and zero order in $B_2(OH)_4$ concentration. Cleavage of a water O−H bond in the rate-determining step is indicated by primary kinetic isotope effect. Tandem reaction using D_2O as solvent confirmed that the two

H atoms in the produced H_2 were originated from water. Taking all these experimental results into account, we assume that the enhanced efficiency of catalytic $B_2(OH)_4$ in light irradiation is attributed to the surface plasmon resonance of AuRhNPs, that favors hot electron migration from Au to Rh. As a result, the electron density of Rh sites is enriched which favors the promotion of the oxidative addition cleavage of a water O-H bond, thus facilitating the hydrogen evolution in catalytic $B_2(OH)_4$ hydrolysis.

Then, transition metal nanoparticles (Pt, Pd, Rh) supported by organometallic sandwich complexes was investigated. The hydride-rich neutral organometallics [Co(η^5-C_5H_5)(η^4-C_5H_6)], **1H**, and [Co(η^5-C_5Me_5)(η^4-C_5H_6)], **2H**, firstly served as a reductant converting the metal chlorides into metallic nanoparticles. Meanwhile, the produced nanoparticles, termed as TMNP (originated from **1H**) and TMNP*(originated from **2H**), were stabilized by the corresponding sandwich cations, respectively $\mathbf{1^+Cl^-}$ and $\mathbf{2^+Cl^-}$. Among the prepared nanocatalysts, Rh was found to be the most active metal species, and RhNP* exhibited the highest TOF values in the hydrolysis of $B_2(OH)_4$ (1364 $mol_{H_2}\ mol_{cat}^{-1}\ min^{-1}$). However, RhNP* (125 $mol_{H_2}\ mol_{cat}^{-1}\ min^{-1}$) showed a slightly lower TOF than RhNP (165 $mol_{H_2}\ mol_{cat}^{-1}\ min^{-1}$) in the hydrolysis of ammonia borane. The durability of the catalysts was also examined, revealing a better stability of RhNP* than RhNP. Thus, **2H** appears to be a preferred complex for the preparation of nanocatalysts, owing to its fine balance between catalytic performance and stability.

Finally, a series of cobaltocene-derived hydride-reservoir complexes with different Cp methylation, [CoCp(η^4-C_5H_6)], **1H**, [CoCp*(η^4-C_5H_6)], **2H**, [CoCp*(η^4-C_5Me_5H)], **3H**, were prepared using the hydride-rich (hydridic) reductant $NaBH_4$. Upon mixing the complexes with methanol, **2H** showed fast

H_2 evolution within 1 min. After H_2 evolution, **2H** residue can be recovered by the precipitation of HPF_6, giving the cationic $\mathbf{2^+PF_6^-}$. As for **1H**, fast H_2 evolution (within 1 min) was also observed when blending **1H** with methanol but it was not recyclable, indicating the decomposition of **1H** sandwich structure. On the contrary, **3H** was inert for hydrogen evolution but can be recycled after the mixing with methanol. The complexes were also investigated for the hydrogenation of 1,1-diphenylethylene as a model reaction in the presence of Pd/C catalyst. It was revealed that **2H** completes the rection at room temperature (25˚C) while **3H** needs higher temperature (50˚C) and **1H** oppositely required lower temperature (0 ˚C) to finish the reaction. The isotope experiment and tandem reaction using **2H** disclose that the two H atoms in the produced 1,1- diphenylethane are provided from **2H** and the methanol solvent. These results can be ascribed to the variation of thermodynamic stability and hydride donor capacity of the three complexes. It is well-known that permethylation of at least one Cp ligand stabilizes metallocenes and other organometallics because of the stereo-electronic influence of the five methyl substituents and a bulk steric protection of Cp*. Thus, for **2H** with one Cp* ligand, it bears with not only considerable thermodynamic stability owing the methylation of its Cp* ligands but also desirable chemical activity, which result in the best performance of **2H** among the three complexes in H_2 evolution and hydrogenation reaction at room temperature. **1H** with non-methylated ligands, possess chemical activity but loss the stability; **3H** with full-methylation of the ligands, is good at thermodynamic stability.

In summary, our thesis work has led to advances in the development of current knowledge of catalytic applications of late transition-metal nanomaterials and

hydride-rich sandwich complexes. Through the studies of dendrimers-stabilized TMNPs, we have a good understanding of the relationship between the stability, catalytic performance of nanoparticles and the structure of dendrimers. The study in transition metal NPs stabilized by hydride-rich metallocenium complexes provided a novel strategy for the preparation of efficient nanocatalysts. The hydrogen evolution and hydrogenation reactions occurred in the presence of the hydride-rich organometallic complexes offers a desirable idea for the development of recyclable systems. Through the PhD research we have reached a good understanding of the parameters that guide the stabilization of NPs and their catalytic efficiency in hydrogen evolution reaction, and enhanced our comprehension of ligands that modulate the activity of the sandwich complexes in organometallic chemistry.

Concerning Perspectives, in spite of tremendous studies on catalytic hydrogen evolution reactions, H_2 production from photocatalytic water splitting seems to be the most promising and sustainable tactic to achieve green energy as water is both the sole starting molecule and byproduct in the cycle of hydrogen economy where the H_2 combustion releases energy and produces water at the same time.[1] On the other hand, solar energy is the most attractive sustainable replacement for fossil fuels because it is plentiful, inexhaustible, and widely distributed energy.[2] The diffuse and intermittent intrinsic of solar irradiation motivates the demand for effective conversion of solar energy into chemical fuels that are storable, transportable, and usable. Thus, combining solar energy with water, a highly abundant resource, via photocatalytic water splitting provides an accessible strategy for hydrogen production. Photocatalytic water splitting consists of three consecutive steps: (i) absorption of photons with higher energies than the bandgap of the

photocatalysts, leading to the excitation of electron–hole pairs in the particles, (ii) charge separation and migration of these photoexcited carriers, and (iii) surface chemical reactions based on these carriers.[3] Thus, highly active photocatalysts are expected to have proper bandgap energies and band structures (i.e., the positions of the conduction-band minimum (CBM) and valence-band maximum (VBM)) to ensure the absorption of sufficient solar irradiation and realize overall solar water splitting.[4]

TiO_2, as a typical semiconductor photocatalyst, is the most diffuse one as it exhibits properties such as an outstanding stability toward photocorrosion, nontoxicity, low cost, and conduction and valence band edges (CB and VB, respectively) straddling the redox potentials of many sustainable chemical transformations. As a result, intensive research efforts have been made for the application of TiO_2-based catalyst for photocatalytic water splitting. Early works concentrate on doping TiO_2 with foreign atoms, such as transition metals (e.g., V, Cr, Mn, Fe and Cu) and nonmetal (e.g., N, C and S), to enhance the photocatalytic activities.[5] A benchmark progress is Pt decorated TiO_2 photocatalyst showing the solar H_2 evolution rate at ~41 mmol h^{-1} g_{cat}^{-1}.[6]

The design of plasmonic metal nanocatalysts is of significant importance for diverse range of applications such as water splitting and energy storage. Plasmonic metals (Au, Ag and Cu) produce a source of high-mobility of charge carriers and possess promoted optical absorption of solar spectrum due to their low excitation-energy requirements and consequently remarkable photoactivity, particularly under the visible light irradiation (>400 nm).[7] Dai *et al*. reported a novel Z-scheme Ag-C_3N_4/SnS_2 plasmonic heterojunction photocatalyst, showing excellent photocatalytic performances with highest reaction rate constant of 0.0201 min^{-1}, which was 7.2, 4.9 and 3.0 times higher

than those of the bare SnS_2, g-C_3N_4 and g-C_3N_4/SnS_2 respectively.[8] However, the ways of identification of suitable fabrication parameters with excellent reproducibility and incorporating plasmonic metals into devices remain to be challenging issues for photocatalytic H_2 evolution in future research.

References

1. Zhu, J.; Hu, L.; Zhao, P.; Lee, L. Y. S.; Wong, K. Y. Recent Advances in Electrocatalytic Hydrogen Evolution Using Nanoparticles. *Chem. Rev.* **2020,** *120*, 851-918.

2. Qi, J.; Zhang, W.; Cao, R. Solar-to-Hydrogen Energy Conversion Based on Water Splitting. *Advanced Energy Materials* **2018,** *8*, 1701620.

3. Wang, Q.; Domen, K. Particulate Photocatalysts for Light-Driven Water Splitting: Mechanisms, Challenges, and Design Strategies. *Chem. Rev.* **2020,** *120*, 919-985.

4. Zhang, P.; Wang, T.; Gong, J. Mechanistic Understanding of the Plasmonic Enhancement for Solar Water Splitting. *Adv. Mater.* **2015,** *27*, 5328-5342.

5. Naldoni, A.; Altomare, M.; Zoppellaro, G.; Liu, N.; Kment, Š.; Zbořil, R.; Schmuki, P. Photocatalysis with Reduced TiO_2: From Black TiO_2 to Cocatalyst-Free Hydrogen Production. *ACS Catal.* **2019,** *9*, 345-364.

6. Hernández, S.; Hidalgo, D.; Sacco, A.; Chiodoni, A.; Lamberti, A.; Cauda, V.; Tresso, E.; Saracco, G. Comparison of photocatalytic and transport properties of TiO_2 and ZnO nanostructures for solar-driven water splitting. *PCCP* **2015,** *17*, 7775-7786.

7. Zada, A.; Muhammad, P.; Ahmad, W.; Hussain, Z.; Ali, S.; Khan, M.; Khan, Q.; Maqbool, M. Surface Plasmonic‐Assisted Photocatalysis and Optoelectronic Devices with Noble Metal Nanocrystals: Design, Synthesis, and Applications. *Adv. Funct. Mater.* **2019,** *30*, 1906744.

8. Zhao, W.; Li, Y. J.; Zhao, P. S.; Zhang, L. L.; Dai, B. L.; Xu, J. M.; Huang, H. B.; He, Y. L.; Leung, D. Y. C. Novel Z-scheme Ag-C_3N_4/SnS_2 plasmonic heterojunction photocatalyst for degradation of tetracycline and H_2 production. *Chem. Eng. J.* **2021,** *405*.